Optimized transmon molecule for high fidelity quantum non demolition readout using cross-Kerr coupling

Vladimir Milchakov

THÈSE

Pour obtenir le grade de

DOCTEUR DE L'UNIVERSITÉ GRENOBLE ALPES

Spécialité : PHYSIQUE APPLIQUEE

Arrêté ministériel : 25 mai 2016

Présentée par

Vladimir MILCHAKOV

Thèse dirigée par **Olivier BUISSON**,chercheur, Université Grenoble Alpes

préparée au sein du **Laboratoire Institut Néel**
dans **l'École Doctorale Physique**

Molécule transmon optimisée pour une mesure quantique non destructrice en utilisant un couplage cross-Kerr

Optimized transmon molecule for high fidelity quantum non demolition readout using cross-Kerr coupling

Thèse soutenue publiquement le **28 mars 2022**,
devant le jury composé de :

Monsieur IOAN POP
Docteur en sciences, Karlsruhe Institut für Technologie, Rapporteur
Monsieur DENIS VION
Ingénieur HDR, CEA CENTRE DE PARIS-SACLAY, Rapporteur
Monsieur DOMINIQUE MAILLY
Directeur de recherche, CNRS DELEGATION ILE-DE-FRANCE SUD, Examinateur
Monsieur FRANCK BALESTRO
Professeur des Universités, UNIVERSITE GRENOBLE ALPES, Président
Monsieur VALERY RYAZANOV
Professeur, Moscow Institute of Physics & Technology, Examinateur

0.1. Acknowledgements

In the following lines, I would like to express my gratitude and appreciation for all the people without whom this work would not have been possible.

I would like to thank Dr. Ioan Pop and Dr. Denis Vion who carefully read my manuscript as reporters for their thoughtful comments and recommendations that gave me a fresh insight on my work and helped me to improve it. Thank you to Prof. Franck Balestro, Prof. Valery Ryazanov, Dr. Dominique Mailly for accepting the role of examiners: your feedback made this an inspiring experience for me and provoked a fruitful scientific discussion.

Special thanks to my supervisor, Olivier Buisson for his dedicated support and guidance. He was able to fascinate me with the idea of transmon molecule, giving me creative freedom and trusting my abilities to run this project. His cordial attitude and patience also helped me navigate in numerous professional and life situations during this time.

I am thankful to the Superconducting Quantum Circuits Team: Nicolas Roch for his expertise and strategic input, as well as Wiebke Guichard and Cécile Naud for valuable discussions.

I also acknowledge the ANR foundation for financial support of this project.

The contribution of my colleagues who helped me to undertake this research could not be overestimated. I am grateful to Remy Dassonneville, who taught me valuable things about experimental setup at the start of my PhD project and was available to participate in the project discussions afterwards.

I appreciate a brilliant work of our collaborators from Institute for Corpuscular Physics (Valencia, Spain): Tomas Ramos and Juan Jose Garcia-Ripoll for providing the solid theoretical foundation for this research.

Special thanks to Cyril Mori, who helped me a lot with measurements, data analysis and visualization. I am confident that the project is in good hands. Best of luck! I would like to thank Timothee Guerra, with whom we developed a comprehensive analysis of quantum trajectories; and Gonzalo Troncozo, who taught me to transfer liquid helium and became my good hiking companion.

My deep acknowledgement go to TWPA team: Luca Planat for his willingness and enthusiasm in providing his awesome amplifiers for the project on a short notice and a friendly atmosphere; as well as to Arpit Ranadive and Martina Esposito for the collaborative effort and sharing coffee breaks with me.

Furthermore, I would like to thank my colleagues who were so generous with their time in discussing this project: Farshad Foroughi for an invaluable help with HFSS modeling, circuits design, advises and thought-provoking discussions; Thibault Charpentier for teaching me the nanofab secrets in cleanroom and being a wonderful friend; Karthik Bharadwaj and Ilya Golokolenov for their help with Bluefors dilution fridge maintenance; Erica Fontana for help with SEM/EDS Analysis; Sebastian Pairis for SEM training and help; Guilliam Butseraen for making an AFM Analysis for me.

Many thanks to the fabrication team, including: Thierry Crozes for the consulting about EBL, Bruno Fernandez with special thanks for optical mask lithography and encouragement, Jean-Francois Motte, Gwenaelle Julie, Latifa Abbassi, Thierry Fournier, and Jeremie Viennot. Also, I would like to appreciate the kind attitude of Irene Peck.

Also, my acknowledgments go to IT-department of the Institute Neel, to Partick Belman and Julien Michel, who supported me with various problems and helped to

establish our data-server.

I would also like to express gratitude to the liquid factory team who have provided a 24/7 liquid helium source.

Finally, I would like to thank the people with whom I worked side by side every day and was able to discuss scientific questions or (and) just have fun. Thank you, Kazi Rafsanjani Amin, for your help with VNA as well as your company during hikes and other adventures! Thank you, Herman Edlbauer and Bernard Klemt, for a lot of fun we had together in cleanroom, as well as climbing, hiking, nordic skiing and making barbecue with "käseknacker". Thank you, Jovian Delaforce, for your sense of humor and our conversations during lunches. Thank you, Sebastian Leger, for the vivid atmosphere that you bring. Thank you, Ekaterina Al-Tavil, for your tremendous help with settling in Grenoble and your friendship.

I also appreciate the discussions with my ex-colleagues from Russia: Ivan Khrapach and Aleksandra Kulakova for their useful inputs on sample fabrication, as well as Gleb Fedorov and Kirill Shulga for fruitful discussions about physics and life.

And last but not least I want to thank my family and friends with special acknowledgement to my wife Ekaterina Milchakova who have been a great source of emotional support and encouragement during all this intense time.

Nobody ever figures out what life is all about, and it doesn't matter. Explore the world. Nearly everything is really interesting if you go into it deeply enough.

— Richard P. Feynman

(American theoretical physicist)

Keep in mind that if you do fast and badly, people will forget that you did fast and remember that you did badly. If you do it slowly and well, people will forget that you did it slowly and remember that you did it well!

— Sergei Korolev

(lead Soviet rocket engineer and spacecraft designer during the Space Race)

Contents

Chapter 1.

Introduction and summary

1.1. Introduction

1.1.1. Quantum computing

Quantum computing applies the principles of quantum mechanics to solve complex computational problems. These problems lie in the areas of quantum simulations, quantum linear algebra, quantum optimization and quantum factorization. In practice, progress in these areas will provide a leap forward in pharmacological and chemical research, AI and machine learning, traffic management and portfolio optimizations, cryptography etc. [1]. It is often called a Quantum Processing Unit (QPU) by analogy with the Graphics Processing Unit (GPU), which reflects the specificity of the tasks to be performed.

Historical overview

The idea of using quantum systems as components of a computing device was first formulated in 1980 in the independent works of Paul Binioff [2], Yuri Manin [3], and Richard Feynman [4] in 1982. The cited works discuss the possibility of using quantum computing devices as an alternative to the classical ones for simulations of quantum systems. The authors emphasize the inconsistency of describing quantum systems using classical computers due to the low capacity of the state space of classical systems in comparison to the state space of quantum systems. One of the main obstacles for simulating quantum systems by classical computers is the probabilistic nature of quantum phenomena, which is not typical for deterministic Turing machines.

In 1983 in the article “Conjugate Coding” [5], Stephen Wiesner introduced the concept of “qubit” - a quantum bit or a unit of quantum information. By analogy with the classical bit, a qubit has two eigenstates $|0\rangle$ and $|1\rangle$, and is capable to be in a state of their superposition. The state of the qubit is described by the expression: $|\psi\rangle = \alpha\,|0\rangle + \beta\,|1\rangle$, where α and β are arbitrary complex normalized factors. Later, the concept of the ”Quantum Computer” was proposed for a device that stores and processes information within a group of quantum systems, where information processing occurs as a result of coherent interactions of systems within this group [6].

Various types of qubits have been created. They are based on superconducting circuits [7, 8], states Rydberg atoms [9, 10, 11, 12, 13], orbital or spin states of electrons in quantum dots [14, 15], the direction of polarization of photons [16], spins of nuclei in NV centers of diamonds [17, 18] and spins of other nuclei and electrons.

There are two quantum algorithms, which are usually mentioned in a context of quantum computers. First, it is a Grover's quantum search algorithm [19] based on amplitude amplification. It was devised in 1996 and brought a significant speed-up to the process of enumerating a disorderly array of data. Its application would require only $\sqrt{N}$ actions against N actions to solve this problem by the classical method. Second, it is a Fourier transform-based Shor's algorithm [20]. It emerged in 1997 and allowed quantum computers to break RSA encryption [21] through rapid factorization, which has further fuelled the interest in the field of quantum computing. In addition, many other quantum algorithms were developed on basis of either quantum Fourier transform, or quantum amplitude amplification, or quantum walks.

Commercial use of superconducting quantum computers

The advantages of superconducting circuits include fast gate times, macroscopic size, and their ability to be manufactured in existing industrial microelectronics facilities.

Nowadays, quantum computers based on superconducting qubits have already been created. Although these systems have not yet surpassed the classical computers in solving practical problems, Google's Sycamore processor with 53 qubits has already demonstrated a supremacy [22] in a particular artificial task. Currently, there are several services, which provide access to cloud quantum computations: IBM Quantum [23], Rigetti Forest [24], Amazon Bracket [25], Microsoft's Azure Quantum [26] and others. Some companies as IQM [27] or D-WAVE [28] already sell off-the-shelf superconducting quantum computers to HPCs and R&Ds departments of business companies. Same time there are many other quantum hardware start-ups which are growing fast like AliceBob or NordQuantique. There are also many companies and start-ups which focuses on developing hardware useful for quantum computation such as Q-blox which provides room-temperature microwave electronics, Q-Devil which develops high quality cryogenic filters and cabling, Silent Waves which supplies quantum limited Josephson parametric amplifiers.

Although at this early stage QPUs are not yet superior, many experts expect, that quantum computers will soon become commercially applicable for some specific practical tasks as optimizations and certified randomness.

As the potential of quantum computers becomes clear, the amount of investment in the industry grows. According to the McKinsey report [1] published in December 2021, announced public investment reaches nearly $30 billion to this date. Private investors are not far behind: the total amount of private investments from 2001 to 2021 equaled more than $3.3 billion. The growing interest encourages scientific research to address the challenges provided by the industry.

Scientific problem

To carry out quantum computations, it is necessary to construct a circuit containing several interconnected qubits. We should be able to control and readout their state, as well as to protect the system from the influence of the environment. The requirements that this system should meet are known as "DiVincenzo's criteria" [29]:

1) A scalable physical system with well characterized qubit

2) The ability to initialize the state of the qubits to a simple fiducial state

3) Long relevant decoherence times

4) A "universal" set of quantum gates

5) A qubit-specific measurement capability

This project is an attempt to create a new type of superconducting qubit that better satisfies the above criteria, especially the readout criterion and state initialization. My PhD work was mainly focused on improving the coherence times and readout performance.

1.1.2. Decoherence of superconducting qubits

The decoherence of a quantum system can be presented as losses of quantum information. Any physical object interacting with a qubit will provoke its decoherence. To process and transfer quantum information, qubits must retain their prepared state for as long as possible, and it is their coherence time that determines the number of possible operations. That is why many efforts are aimed at isolating the qubit from the influence of the external environment to prolong its coherence time. In addition, it is important to retain the ability of the researcher to exert control over the qubit.

The main sources of decoherence for superconducting qubits are the following [30]: Two-Level Systems (TLS) [31, 32], radiation [33] and material losses [34], flux [35] and charge noise [36, 37], the Purcell effect [38, 39], and the quasiparticles [40, 41] which can be produced by ionizing radiation [42]. In each particular case, the main source of decoherence will vary depending on the qubit scheme. That is why several design innovations were introduced to reduce decoherence. The corresponding results are reflected in Fig. 1.1, which depicts the historical development of superconducting circuits [43].

The basic schemes of superconducting qubits were described in the overview paper [44]. Three types of superconducting qubits were defined depending on the way of storing quantum information: charge qubits [45, 46], flux qubits [47, 48], and phase qubits [49, 50, 51, 52]. The main characteristic, which helps to distinguish them, is $\frac{E_j}{E_c}$ ratio, where E_j is the Josephson energy and E_c the charging energy. In charge qubits the quantum information was encoded in the actual number of Cooper pairs, that occupy a small island of superconducting material, which gave the system its name - Cooper-Pair Boxes (CPB). Charge qubits have $\frac{E_j}{E_c} < 1$. Flux qubits exploit the direction of magnetic flux induced by supercurrent for encoding their states. Flux qubits have $\frac{E_j}{E_c} \cong 10$. Finally, the phase qubits are based on S-I-S junctions, which make their ratio as big as $\frac{E_j}{E_c} \cong 10^6$.

In addition to these basic circuits many improved schemes were proposed including quantronium [53, 54] or π-junction [55], transmon [56] and fluxonium [57]. Transmon [56, 58] was proposed in 2007 by scientists at Yale University and became the most popular solution for a superconducting qubit. This scheme is much less susceptible to charge noise than CPB due to the large shunt capacitance and the predominance of Josephson energy over the charge energy. The next step was a 3D-transmon [59], where the capacitor has been redesigned to avoid high electric field amplitude. Due to the optimized design, the coherence time reached 40-50 μs [60]. Another popular scheme was proposed by Vladimir Manucharyan and his collaborators from Yale and called

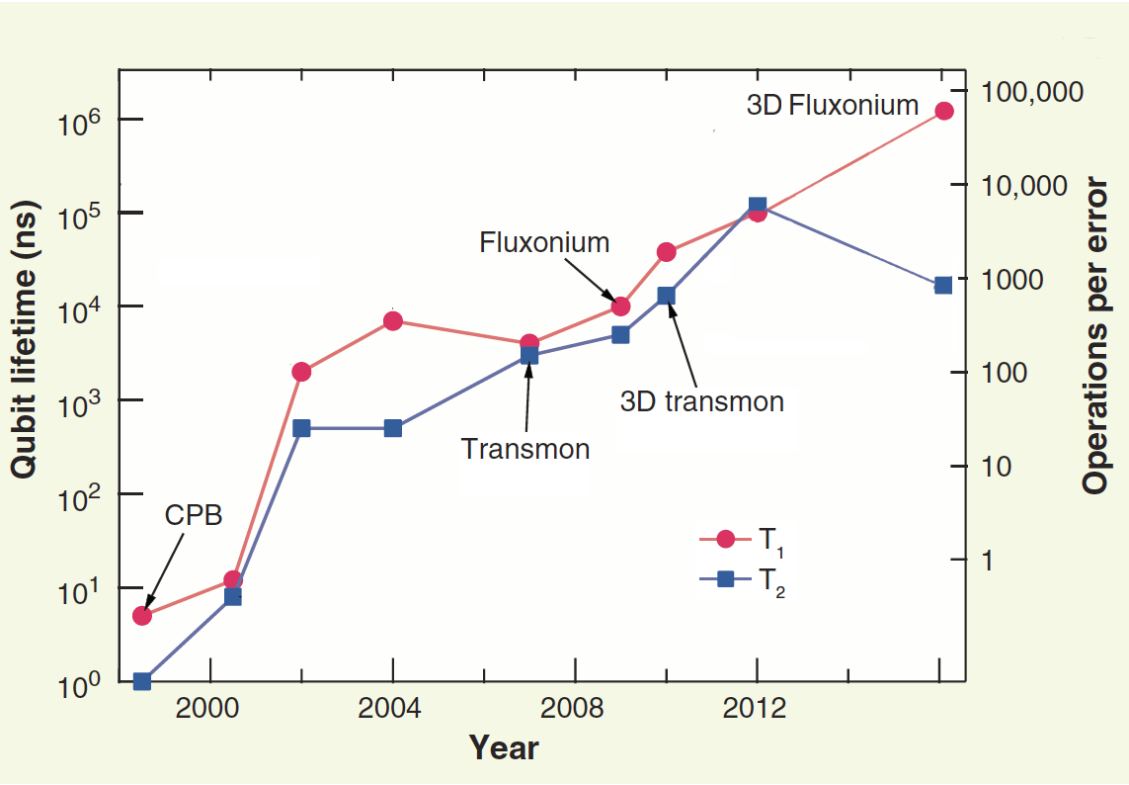

Figure 1.1: Advances in coherence times in superconducting qubits. X-axis corresponds to the year of publication for the given result. The left Y-axis shows the qubit coherence time, and the right Y-axis shows the estimated number of gates that can be applied during this time. Both Y-axes are logarithmic. The data points of red color show the relaxation time T_1, and the points of blue color correspond to decoherence time T_2. Source:

"fluxonium" qubit [57, 61, 33, 62], which has recently shown a millisecond coherence time [63].

New superconducting qubit circuits that could potentially achieve even higher coherence times are still under development. For an update on new advanced developments in superconducting qubit, one can read the following reviews: [64, 65, 66].

1.1.3. Qubit readout

Dispersive readout

Dispersive readout [67] is the most common technique of a projective measurement in the field of superconducting qubits. It relies on transverse coupling in the dispersive limit between the qubit and the cavity. The transverse coupling is based on light-matter interaction between qubit dipole moment and electric field of cavity mode. This system can be described by Jaynes-Cummings model [68] with a Hamiltonian consisting of field, qubit and their interaction terms. In this model, a qubit is presented as a two-level system, and cavity - as a harmonic oscillator.

$$\hat{H} = \hat{H}_{field} + \hat{H}_{qubit} + \hat{H}_{int}. \tag{1.1}$$

For example, the $\hat{H}_{qubit}$ for a widely used transmon qubit will have this form of a slightly anharmonic oscillator with frequency ω_q, anharmonicity α_q and ladder operator $\hat{q}$:

$$\hat{H}_{qubit} \cong \hbar\omega_q \hat{q}^\dagger \hat{q} + \hbar\frac{\alpha_q}{2}\hat{q}^{\dagger 2}\hat{q}^2 \cong \frac{1}{2}\hbar\omega_q\hat{\sigma}_z. \tag{1.2}$$

A *transverse* coupling will provide a *field-field* interaction between a qubit dipole $\hat{q} + \hat{q}^\dagger$ and field of cavity $\hat{c} + \hat{c}^\dagger$ with a coupling term $\hat{H}_{int}$ given by:

$$\hat{H}_{int}^{transverse} \cong g_x(\hat{q} + \hat{q}^\dagger)(\hat{c} + \hat{c}^\dagger). \tag{1.3}$$

In the dispersive limit [56], when detuning between qubit and cavity $\Delta = |\omega_q - \omega_c|$ significantly exceeds coupling strength, $|g_x| \ll \Delta$, the cavity experiences an effective *energy-energy* interaction $\cong \chi_d\hat{\sigma}_z\hat{c}^\dagger\hat{c}$ with $\chi_d = \frac{\alpha_q g_x^2}{\Delta(\Delta+\alpha_q)}$ [69], known as the dispersive or perturbative cross-Kerr interaction. It leads to qubit-dependent frequency shift of the cavity, which allows a projective readout of the qubit state by measuring the amplitude or phase of the probing signal [69].

The readout based on the *transverse* coupling has been widely applied in experiments conducted with superconducting qubits. The results have demonstrated a high fidelity and QND projective readout. However, Purcell effect and unwanted transitions induced by readout photons in the cavity limited the readout creating the trade-off between speed and accuracy. These undesirable effects constitute a fundamental limit for fidelity and QNDness, since they are caused by inevitable higher-order corrections of perturbation theory, which distort the dynamics of the qubit [70, 71, 72] and create additional decay channels [39].

To overcome the Purcell effect limitation for dispersive readout, Purcell filters [73, 74] present one of the possible solutions. Currently, this approach is a standard option, widely used to improve the readout performance. However, it also has limitations. First, it only reduces the Purcell effect, without eliminating it completely; and second, the filter itself is a big bulky structure, which takes a lot of space on the chip. The latter problem is very acute for scaling up number of qubits on the quantum processors

[75]. In a recent paper [76] authors proposes a resonator with intrinsic Purcell filter, which can also help to overcome the last problem.

Alternative readout methods based on different couplings

Recently, a few research groups focus on introducing another circuit architecture to overcome the limits of dispersive readout. A promising approach is based on implementing a coupling scheme that originally involves the energy of the qubit instead of effective energy interaction. In the paper of Didier at all. [77] the *longitudinal* coupling $\cong g_z\hat{q}^\dagger\hat{q}(\hat{c}+\hat{c}^\dagger)$ was proposed as an alternative to the *transverse* coupling $\cong g_x(\hat{q}+\hat{q}^\dagger)(\hat{c}+\hat{c}^\dagger)$. This approach provides a good separation of the states in a quantum non-demolition way. Touzard et al [78] has experimentally proven the high-fidelity readout using this readout scheme. Another work devoted to the *longitudinal* coupling which has shown a high-fidelity readout is a Royer's paper [79].

At the same time, an alternative approach was proposed in our group based on cross-Kerr coupling using a transmon molecule [80, 81, 82, 83]. Indeed, we expect that *cross-Kerr* coupling $\cong g_{zz}(\hat{q}+\hat{q}^\dagger)^2(\hat{c}+\hat{c}^\dagger)^2$ will be a better option to replace *transverse* coupling. This coupling provides a readout shift of $2g_{zz}$ which is independent on detuning between qubit and cavity and can be made as large as few hundreds MHz. It allows to achieve high fidelity and Quantum Non Demolition (QND) readout surpassing limitations on readout power.

The detailed theoretical explanations of the *cross-Kerr* coupling implementation and benefits in comparison to *transverse* coupling can be found in following works [81, 84, 85]. The benefits of using a cross-Kerr coupling to provide a QND readout was also theoretically investigated in a Wang's paper [86] for the flux qubit as an example and for the circuit similar to the transmon molecule in a You's paper [87]. The scheme, similar to the transmon molecule, is also theoretically analyzed in the following paper [88].

1.1.4. Description of the transmon molecule device

A 2D transmon molecule device was first implemented by Dumur [89, 82, 83]. At that time the circuit was consisting only of two transmons with an inductance between them. After, this "transmon molecule" project was taken by Dassonneville [84, 85], who have shown a high-fidelity QND readout in a 3D structure, despite a low coherence time.

Electrical circuit

Nowadays, our 3D transmon molecule is a superconducting circuit whose electrical scheme is presented in Fig. 1.2. The circuit consists of two identical transmons with Josephson energy E_j and capacitance C_s, coupled by a parallel LC-oscillator with inductance L_a and capacitor C_t. This capacitance was added to our circuit later during the PhD project of R. Dassonneville [84]. In our case, the inductor L_a is presented by a chain of 10 small SQUIDs. The circuit has three electrical nodes, connected to each other by three nonlinear LC-oscillators (if we consider Josephson junctions as nonlinear inductors). Thus, there are two degrees of freedom in this circuit, providing two orthogonal modes. As a qubit we use the mode relating to the in-phase oscillations of current through the Josephson junctions. The second mode (ancilla) which relates

to antiphase oscillations of current passing through the inductor L_a will be used for the readout.

In the circuit, the loop made by the two Josephson junctions and the inductance realized a large SQUID. As a result, we are able to tune the qubit frequency by applying external magnetic flux Φ_q through this large SQUID. Since our inductor consists of small SQUIDs, we can also tune the value of inductance L_a. The system was developed in a way that the area of the qubit SQUID is approximately $r = 26$ times larger than the area of the small SQUIDs related to the inductor.

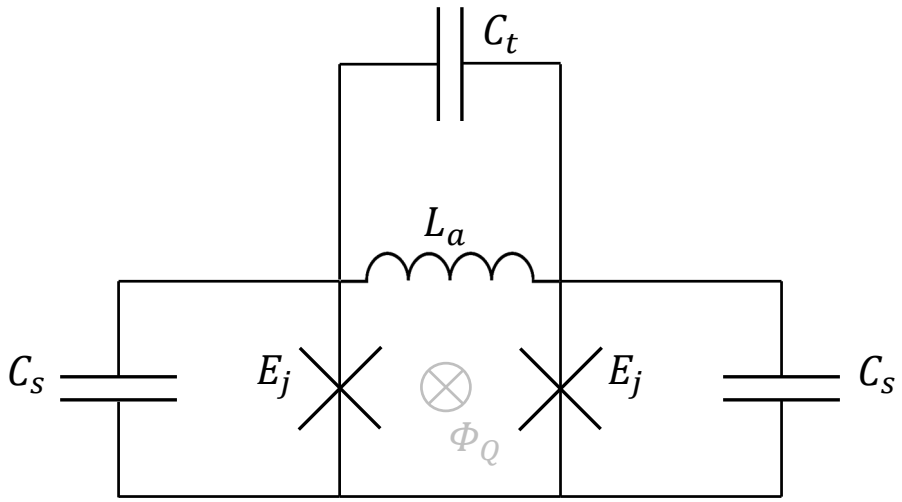

Figure 1.2: The electrical scheme of a "transmon molecule" is a cross-Kerr based quantum circuit. It can be presented as two transmons coupled by a parallel LC-oscillator. E_j, C_s represent Josephson energy and capacitance of each transmon. L_a, C_t represent inductance and capacitance of a parallel LC-oscillator. L_a is created by a chain of 10 small SQUIDs which are not represented here.

This superconducting quantum circuit behaves similarly to a single transmon qubit coupled to an anharmonic ancilla mode by a cross-Kerr coupling. It is described at the integer number of magnetic flux in the large SQUID loop by the Hamiltonian [85]:

$$\hat{H}_{mol} = 4E_{C_q}\hat{n}_Q^2 - 2E_j\cos\hat{\phi}_q + 4E_{C_a}\hat{n}_A^2 - 2E_j\left(\cos\hat{\phi}_a - \frac{L_j}{L_a(n)}\hat{\phi}_a^2\right) - 2E_j\left[\cos\hat{\phi}_q - 1\right]\left[\cos\hat{\phi}_a - 1\right] \tag{1.4}$$

Here, the $\hat{\phi}_q$ and $\hat{\phi}_a$ are phase average and phase difference between the two Josephson junctions, respectively. They correspond to qubit and ancilla modes. The $\hat{n}_Q$ and $\hat{n}_A$ represent their conjugate charge number operators. For qubit mode, the charging energy and effective capacitance will be given by:

$$\begin{cases} E_{C_q} = \frac{e^2}{2C_q} \\ C_q = 2C_s \end{cases}, \tag{1.5}$$

and for ancilla mode

$$\begin{cases} E_{C_a} = \frac{e^2}{2C_a} \\ C_a = 2(C_s + 2C_t) \end{cases} . \tag{1.6}$$

The $L_a(n)$ describes the inductance for given magnetic flux $\Phi_S = \frac{n}{r}\Phi_0$, where r is the ration of surface between the large and small SQUID and n is the integer of flux quanta applied to the large SQUID. Josephson inductance of each junction is given by:

$$L_j = \left(\frac{\Phi_0}{2\pi}\right)^2 \frac{1}{E_j}. \tag{1.7}$$

The last term in Eq.(1.4) describes the coupling term, which can be reduced to fourth order to nonlinear cross-Kerr coupling between ancilla and qubit modes, $-\frac{E_j}{2}\hat{\phi_q}^2\hat{\phi_a}^2$

Spectral characteristics

To analyze the system from a quantum optics point of view, it is convenient to represent the Hamiltonian of transmon molecule Eq.(1.4) through ladder operators as following [85]:

$$\frac{\hat{H}_{mol}}{\hbar} = \omega_q \hat{q}^\dagger \hat{q} + \frac{\alpha_q}{2}\hat{q}^\dagger\hat{q}^\dagger\hat{q}\hat{q} + \omega_a \hat{a}^\dagger\hat{a} + \frac{U_a}{2}\hat{a}^\dagger\hat{a}^\dagger\hat{a}\hat{a} - \frac{g_{zz}}{2}(\hat{a}+\hat{a}^\dagger)^2(\hat{q}+\hat{q}^\dagger)^2 + \mathcal{O}^6 \tag{1.8}$$

The first two terms correspond to the Hamiltonian of a normal transmon with ladder operators $\hat{q}$ and $\hat{q}^\dagger$, frequency $\omega_q = 4\sqrt{E_{C_q}Ej}/\hbar + \alpha_q$ and anharmonicity $\alpha_q = -E_{C_q}/\hbar$. The value of anharmonicity α_q was designed large enough to allow us to use this mode as a qubit. The third and fourth terms in Eq.(1.8) correspond to the ancilla mode with frequency $\omega_a = 4\sqrt{E_J E_{C_a}(1 + 2\frac{L_J}{L_a(n)})}/\hbar + U_a$, anharmonicity $U_a = -(E_{C_a}/\hbar)(1 + 2\frac{L_J}{L_a(n)})^{-1}$, and ladder operators $\hat{a}$ and $\hat{a}^\dagger$. Both ancilla frequency and anharmonicity depend on external magnetic flux. Since in our case the system operates in transmon regime ($E_j \gg E_{C_q}, E_{C_a}$) [56], the values of the qubit and the ancilla anharmonicities mainly depend on capacitance energy. The last term in Eq.(1.8) represents an *energy-energy* cross-Kerr coupling between qubit and ancilla with a strength $g_{zz} = \sqrt{\alpha_q U_a}$. It is based on Josephson junctions non-linearity, and it is non perturbative [90].

Since qubit and ancilla modes are orthogonal, we are able to couple one of them to the electric field of the 3D cavity without coupling the other one. To avoid any coupling of the qubit to the cavity, we align the sample in a way, that dipole moments of the two modes are perpendicular (see Fig. 1.3). This way, the ancilla dipole moment will be oriented in parallel with 3D cavity field, which leads to a strong *transverse* coupling between ancilla and cavity. The correct orientation of sample in the cavity is critical to avoid the unwanted *transverse* and *longitudinal* coupling between qubit and cavity.

Thus, we create a system in which the qubit mode is coupled to ancilla mode by a cross-Kerr coupling, while the ancilla is coupled to the cavity by a usual transverse coupling. Because of this *transverse* coupling, a hybridization occurs between the ancilla and the cavity mode, leading to two hybridized modes called polaritons. These new modes inherit form the specific properties of the ancilla and cavity modes. Consequently, they are coupled with a qubit by a cross-Kerr coupling and can be probed as a 3D cavity by external field. As a result, we can read out the qubit state by probing the polariton frequency and observing a shift.

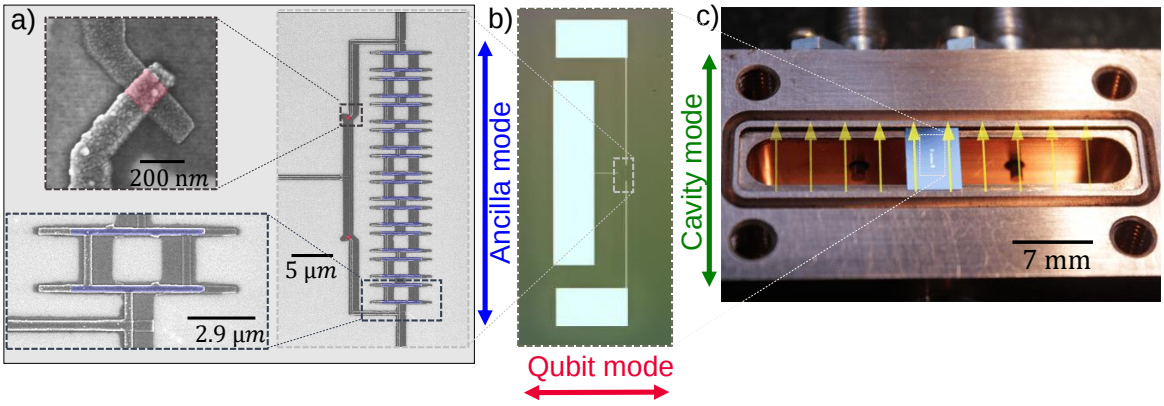

Figure 1.3: a) - electrical circuit of transmon molecule with shown directions of qubit and ancilla oscillation directions; b) - core of transmon molecule consisting of Josephson junctions and SQUID-chain inductor (SEM picture); c) - Single Josephson junction E_j (SEM picture); d) - Single SQUID of L_a (SEM picture); e) - transmon molecule structure Sample-A *(optical microscopy); f) - chip of* Sample-A *placed in copper 3D-cavity with direction of electric field displayed by yellow arrows; g) - table with directions of dipole moments of qubit, ancilla and cavity modes in case of given orientation of sample in the cavity. False colors on SEM pictures shows the positions of Josephson junctions (red for E_j and blue for SQUIDs of L_a).*

1.2. Summary

1.2.1. Main results

The results presented in this thesis can be divided into three topics. First is related to the performance of our single-shot qubit readout, which has demonstrated readout fidelity as high as 99.4% and QNDness above 99%, resilient to high readout power. This is an important result because it highlights the promise of the developing a readout based on cross-Kerr coupling. Second topic is linked to the improvements of qubit relaxation time of transmon molecule due to changes of its parameters and design. Third is related to the setting up an improved process of nanofabrication which lead to increased quality and reproducibility of the samples.

The best results of single-shot readout are shown in Fig. 1.4. For *Sample-A*, which was developed before my PhD, the readout- and π- pulses were optimized as well as phase-sensitive parametric amplifier parameters to find an optimal point. The best fidelity for this sample was measured to be around 98% and was limited by a short $3.3\mu s$ relaxation time of the qubit and state transitions induced by readout power. For *Sample-B*, which was designed and fabricated during my work, we have measured 99.4% of readout fidelity and observed a drastic reduction of the state transitions induced by readout pulse (see Fig. 1.5).

To increase the qubit relaxation time as well as the reproducibility of Josephson junctions, several improvements have been made to the standard nanofabrication recipe. As a result, we obtain the reproducible process of fabrication samples with better aluminum quality (see Fig. 1.7), less amount of surface contamination (see Fig. 1.8) and better symmetry and reproducibility of the Josephson junctions with precise control on its critical current.

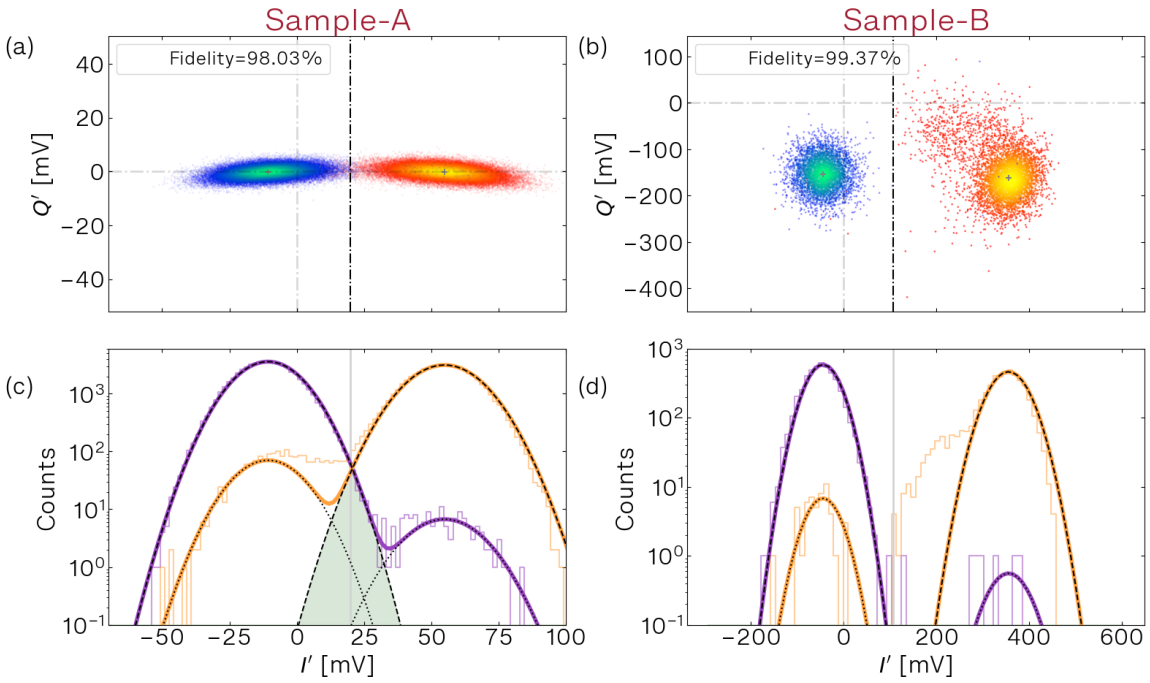

Figure 1.4: The best results of single-shot readout with postselection obtained on Sample-A *(a), (c) and* Sample-B *(b), (d). The bottom and left axis correspond to the new values I' and Q' so that all information about the qubit state is contained in I'. plots a), b) - scattering diagrams with progressive color - more brightness means more dot density. Blue color corresponds to the readout of prepared $|g\rangle$-state and orange color is for prepared $|e\rangle$-state. Dashed black line shows a threshold value. Legend of plots shows the fidelity of readout. Plots c), d) shows histograms, plotted along I'-axis. The left axis is logarithmic and corresponds to the number of counts. The orange and purple step-like line shows the distribution of counts along I'-axis for prepared $|e\rangle$ and $|g\rangle$-states, respectively. A solid line of the same color shows the fit of these distributions by a double Gaussian function. A discrepancy between these two lines explained by the measurements, where qubit state was changed during the measurement time. Dashed and dotted black lines show fit of counts distribution by single Gaussian functions corresponded to expected and unexpected states, respectively. The gray-green area marks an overlap between two Gaussian fits, which lead to error due to limited SNR.*

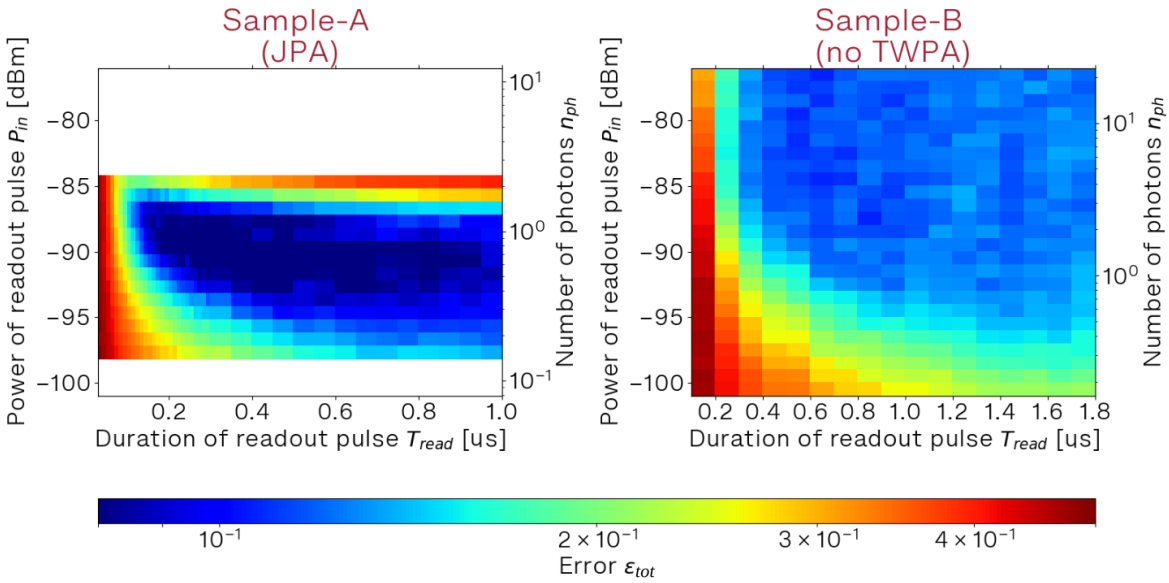

Figure 1.5: Total error ϵ_{tot} as a function of power (left vertical axes) and duration (horizontal axes) of readout pulse for sample-A *(on the left) and* Sample-B *(on the right). The right vertical axis corresponds to the number of excitations in polariton related to given readout power. Blue regions corresponds to small error of readout ϵ_{tot}.* Sample-A *was measured using JPA, when* Sample-B *was measured with no parametric amplifier, this time. On a right plot, the minimal error is bigger because of lack of parametric amplifier. However, the fact that we can have stable fidelity of readout even with high power of readout pulse is interesting by itself. We stopped at -76 dBm in this experiment because higher power started to heat the dilution fridge.*

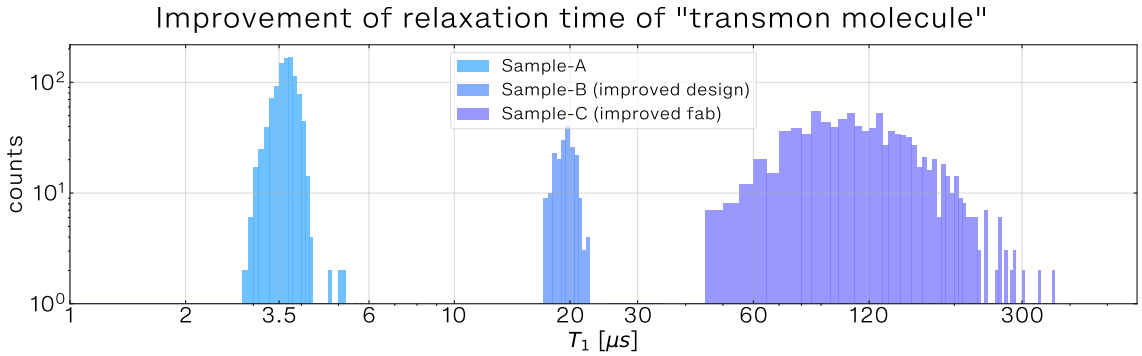

Figure 1.6: Comparison of relaxation time T_1 over three samples. The plot corresponds to histograms along T_1 in a log-scale.

The relaxation time T_1 was significantly improved by optimizing the transmon molecule characteristics and design, as well as the nanofabrication recipe improvements (see Fig. 1.6). In the *Sample-B* the design was changed compare to *Sample-A* and the nanofabrication recipe was adjusted. Then for *Sample-C* a new nanofabrication recipe was developed and tested. However, the results for *Sample-C* are preliminary and need to be confirmed. We observed a possible signature of residual Purcell effect in case of *Sample-A*, which we assume to be caused by residual *transverse* coupling. In case of *Sample-B* we did not observe any Purcell effect.

In conclusion, the new and improved transmon molecule that I have developed during my PhD allows performing high-fidelity qubit readout. Thanks to the direct *cross-Kerr* coupling, the readout does not produce Purcell effect and presents a promising resilience to large readout power.

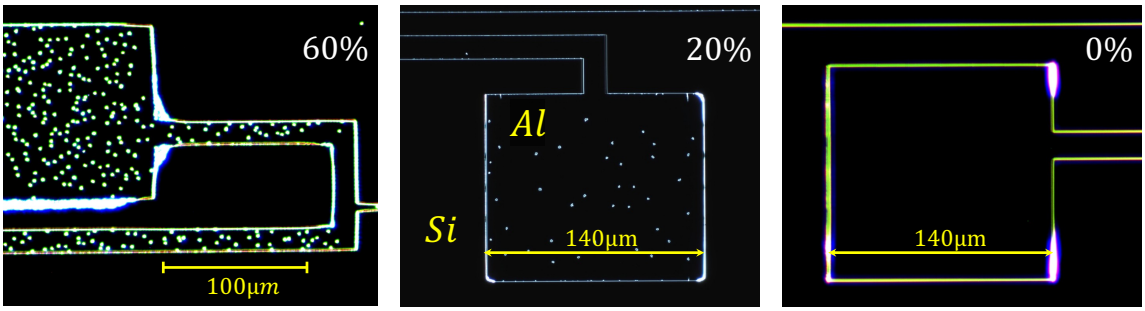

Figure 1.7: Comparison of aluminum quality after changing the power of ultrasonication from 60% *to* 20% *and* 0% *during liftoff step. Pictures obtained by dark field optical microscopy.*

1.2.2. Thesis overview

The Chapter 2 starts with deciding on the spectral parameters for the new transmon molecule in order to increase the relaxation time. We choose the electric circuit parameters according to these decisions, using an optimization algorithm. Then the improved geometrical shape of the pads is described. This shape provides a zero dipole moment of the qubit mode to reduce the unwanted *transverse* coupling, smoother electrical field distribution and exact values of capacitance C_s and C_t. In the end of Chapter 2 we discuss the vortex traps and design automation.

In the next Chapter 3 we give a brief description of the main nanofabrication steps and the usual approaches for implementing Josephson junctions. Then the detailed description of standard nanofabrication process is given. After we list the observed issues related to this process and give the explanations to their presence as well as the ways to avoid them. A new, improved nanofabrication recipe is given right after this, which solves most of the listed issues. In the end of the Chapter 3 we present the results of DC-measurements of the Josephson junctions to analyze their symmetry as well as their critical currents I_c and critical current densities J_c as a function of junction area and fabrication run.

The measurement setup is described in Chapter 4. We start from a small introduction into the field of the dilution refrigerators and continue with a discussion on the

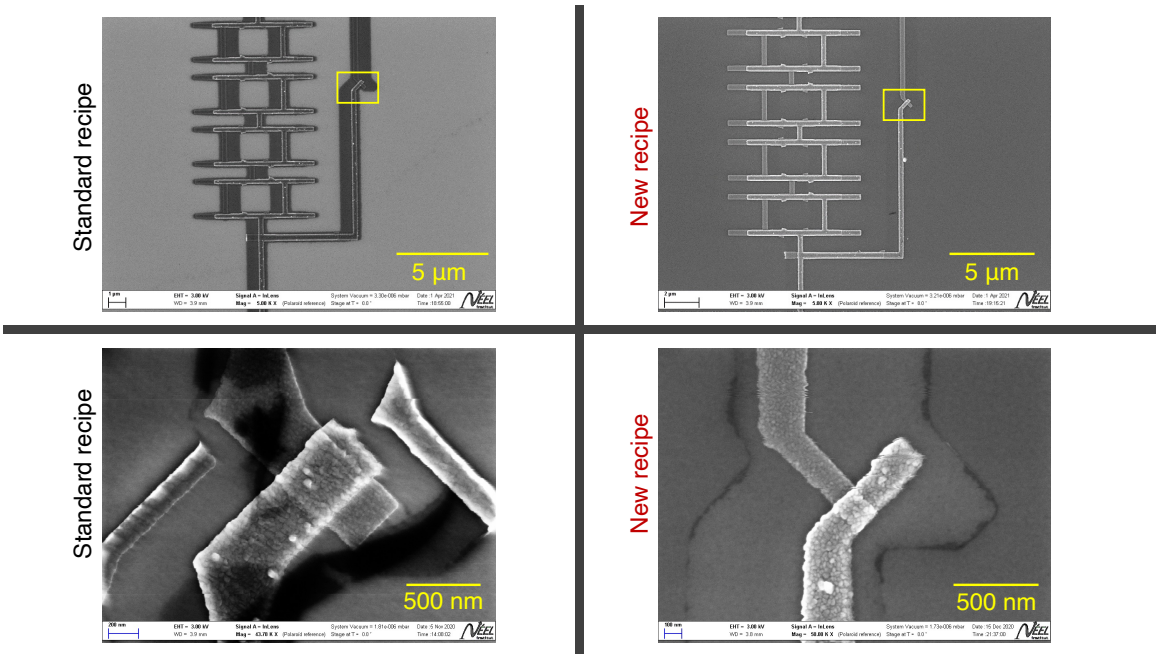

Figure 1.8: Scanning electron microscopy of different samples made by standard nanofabrication recipe (on the left) and the new improved recipe (on the right). The amount of surface contamination (dark zone in the images) around the Josephson junction is drastically reduced in the new recipe.

isolating of the chip from the external noise. Then we present the microwave setup, which includes the cryogenic and room-temperature parts. In the end of the Chapter 4 the software part of the setup is presented.

The main result of this work is presented in Chapter 5. The chapter begins with an introduction of the three measured samples. *Sample-A* is a transmon molecule fabricated and preliminary studied by a previous PhD student Remy Dassonneville and extensively measured analyzed by me; *Sample-B* has a transmon molecule with improved design and parameters developed during my work; and *Sample-C* - the first sample fabricated using a new improved fabrication recipe with almost same design as *Sample-B*. All the measurements of *Sample-A* and *Sample-B* are presented in parallel in order to compare them. We start with single-tone and two-tone continuous microwave spectroscopy results. The two polaritons and their behavior as a function of external magnetic flux and signal power are presented, as well as the qubit frequency and anharmonicity. The parameters of the transmon molecules are extracted from the spectroscopy to be compared between each other and with target values. Then we present the results of coherence times measurements T_1, T_2 and T_{Rabi} of these samples as well as photon-number calibration. In the next section, we present and compare the best results of single-shot qubit readout and its dependence on duration and power of readout pulse. Finally, we present the serial readout and the quantum trajectory experiments. From these experiments we extract the Quantum-non-demolitioness of the readout as well as decay and excitation rates as a function of readout power.

The last Chapter 6 is devoted to conclusions of this work and future prospects of the Transmon Molecule project.

Chapter 2.

Engineering of transmon molecule

This chapter is dedicated to the process of development of the transmon molecule. It begins with setting a goal of increasing the relaxation time of the transmon molecule to further improve the readout fidelity. To achieve this goal, we discuss several optimization strategies based on change of spectroscopic parameters and minimization of qubit's dipole moment and electric field amplitude.

Analyzing the results of the *Sample-A* measurements, I develop a new design for the *Sample-B* and *Sample-C*.

First, we choose the target values of spectroscopic characteristics for *Sample-B*. After we discuss how to achieve them by tuning the electrical parameters: C_s, C_t, E_j and L_a. To satisfy all the conditions, I have used a method of minimization of scalar function of many variables, applying a special Python script.

Second, I will draw the elements of electrical scheme (inductance L_a and Josephson junctions E_j) in an actual layout. The resulting design will be the 'core' of transmon molecule.

Third, I will add large pads to the layout to reflect the remaining electrical capacitance C_s and C_t. We introduce a new geometrical shape which allows us to make a design more sustainable to misalignment in the 3D-cavity. We also optimize the design to decrease the amplitude of electric field to reduce the effect of coupling to Two-Level-Systems (TLS). We calculate the exact size of the pads by conducting finite elements simulations by using software package HFSS$^{\text{TM}}$ [91].

Finally, when all the geometrical parameters were chosen, I have created a fully-automated Python-script to build the actual .gds design. Due to automation, I was able to quickly variate all parameters of the design for each new generation of samples and eliminate the human factor in design errors.

2.1. Choice of electrical parameters

The transmon molecule of previous generation (*Sample-A*) has shown low relaxation time (T_1). It can be improved by optimization of transmon molecule parameters such as the frequency and anharmonicity of qubit and ancilla, as well as the E_j/E_c-ratio and coupling to cavity mode. We have chosen the following objectives. First, since we have observed a residual Purcell effect in *Sample-A*, we would like to reduce it by increasing the detuning between the qubit and readout frequencies. It will not affect the possibility of readout in our case, due to using of the cross-Kerr coupling $\alpha_q g_x^2/(\Delta(\Delta+\alpha_q))$.

Parameter	Value	Change
$\omega_Q/2\pi[GHz]$	6.284	$\uparrow$
$\omega_A/2\pi[GHz]$	7.78	$\rightarrow \omega_c$
$g_{ac}/2\pi[MHz]$	295	$\approx$
$\alpha_q/2\pi[MHz]$	-88	$\approx$
$U_A/2\pi[MHz]$	-13.5	$\downarrow$
$g_{zz}/2\pi[MHz]$	34.5	$\approx$

Table 2.1: The change we would like to apply to Sample-A *parameters. Symbol's meaning is following:* $\uparrow$ / $\downarrow$ *- increase/reduce the value,* $\approx$ *- keep the same value,* $\rightarrow x$ *- make the value close to* x*.*

Second, we have decided to extremely reduce the ancilla anharmonicity U_A to avoid the undesirable nonlinear effects that arise when the readout power increases. However, the reduction is limited by the desired value of cross-Kerr coupling g_{zz}. Third, we would like to place the ancilla frequency ω_A close to the bare resonator frequency ω_c. As a result, the ancilla and cavity are strongly coupled leading high transmission of readout signal, which simplifies the readout of qubit state. Finally, we would like to keep other parameters of previous sample: E_j/E_c-ratio in transmon regime, the large cross-Kerr coupling level, avoid resonance of doubled qubit frequency $2\omega_Q$ with both ancilla and cavity frequency. These parameters are reflected in Fig. 2.2.

In this chapter, we will call all spectroscopic parameters *an output*, and all electrical circuit parameters *an input*. In this way we have four parameters of electrical scheme *input*: E_j, L_a, C_s and C_t; and expected spectroscopic parameters *output*: ω_Q, ω_A, α_Q, U_A, E_j/E_c. The electrical circuit of transmon molecule is shown in Fig. 1.2.

According to the equations presented after Eq. 1.8, we can calculate the output parameters from the input ones. However, the current problem to be solved here is inverse. Since the set of input parameters exist not for any set of output parameters, the formulas can not be reversed. This problem can not be solved analytically, and we have decided to use computer optimization algorithms instead of symbolic calculations.

In a simple case of 3D-transmon [59] we would only need to choose two parameters E_j and E_c - Josephson and capacitance energy, respectively - to satisfy conditions for qubit frequency, anharmonicity and $E_j/E_c > 50$. Since the transmon anharmonicity depends only on E_c, it can be controlled separately. And the frequency of transmon can be chosen by tuning E_j in a range where the condition on E_j/E_c is satisfied.

In our case, however, the complex relationship of several existing variables is difficult to optimize. The anharmonicity of ancilla U_A is a function of two capacitances: C_s and C_t. In addition, the ancilla frequency ω_A depends on both L_a and E_j

We can not simply choose any set of *output* spectroscopic values since it is likely that no suitable set of *input* values exists. To solve this problem, I defined a function related to every *output* parameter, which takes the value of the parameter as an argument and ranks it. The ranking function will return 'good' rank if the actual value of the parameter is close to the target one, and 'bad' in the opposite case. Each rank-function can return any value from 0 to 1, where 1 is 'good' and 0 is 'bad'. By multiplying individual ranks, we are able to evaluate a set of *output* parameters as a total rank. Varying a set of input parameters in an optimization algorithm, we would like to maximize the total rank.

It is important to define the rank-functions correctly. First, they must reflect

Figure 2.1: Process of ranking the set of input parameters. First, we calculate a set of output *parameters related to the* input *parameters, based on equations 1.1.4. After ranking each of the* output *parameters (spectroscopic values) individually, we multiply them to calculate a total rank. Our goal is to maximize the product in the optimization algorithm.*

our objectives for each of the parameter. Second, the range of allowed values for each parameter must be wide enough and the smoothness of each function should be sufficient for the optimization algorithm to find a solution.

The plots of the functions for different values are presented in Fig. 2.2. We build them as sums or products of three basic functions to keep the smoothness of the resulting function: Exponential, Sigmoid and Gaussian

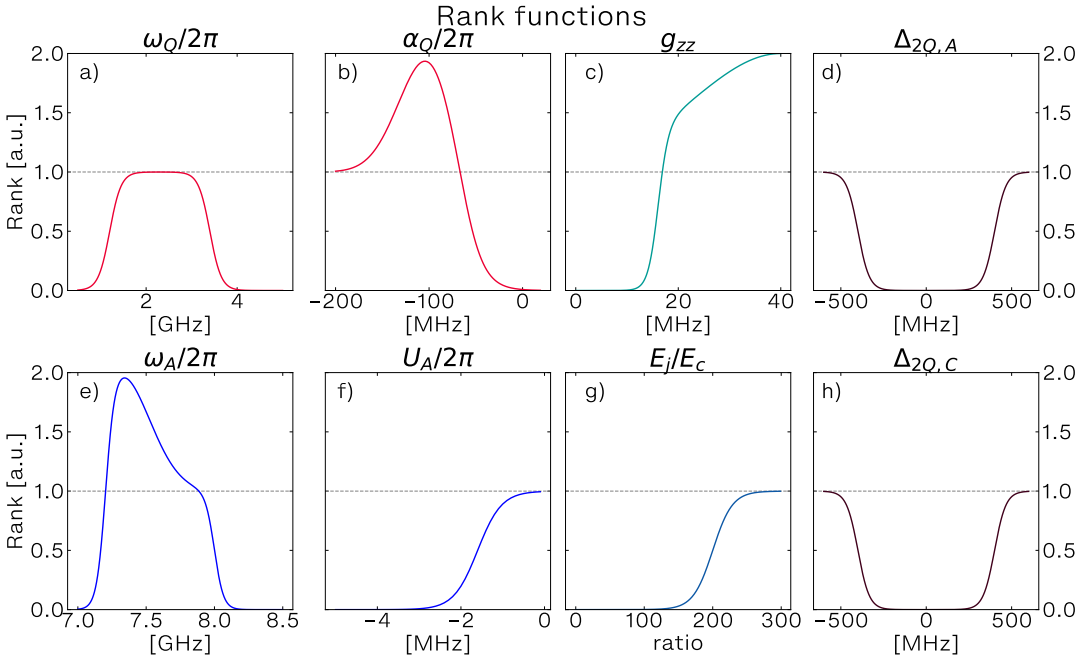

Figure 2.2: Examples of ranking functions which I have used in the optimization algorithm. Plots reflect the rank of a parameter as a function of its value for a) - qubit frequency ω_Q; b) - qubit anharmonicity α_Q; c) - cross-Kerr coupling g_{zz}; d) - detuning between doubled frequency of qubit transition $|g\rangle \rightarrow |e\rangle$ and ancilla frequency; e) - ancilla frequency ω_A; f) - ancilla anharmonicity U_A; g) - E_j/E_c-ratio; h) - detuning between doubled frequency of qubit transition $|g\rangle \rightarrow |e\rangle$ and cavity frequency;

Thus, by defining the ranking functions, we have achieved a representation of objectives in a concrete form suitable for the computer processing. By running a standard optimizer of scipy library, I got a set of *input* parameters with the best rank. If the set of parameters did not satisfy me, I have adjusted the rank-functions accordingly.

Value	*Sample-A*	Target
C_s $[fF]$	110	125
C_t $[fF]$	59.6	87
$E_j/2\pi\hbar$ $[GHz]$	29.2	7.3
L_A $[nH]$	5.32	2.66
$\omega_Q/2\pi$ $[GHz]$	6.284	2.78
$\omega_A/2\pi$ $[GHz]$	7.78	7.35
$g_{ac}/2\pi$ $[MHz]$	295	> 100
$\alpha_q/2\pi$ $[MHz]$	-88	-77
$U_A/2\pi$ $[MHz]$	-13.5	-1.3
$g_{zz}/2\pi$ $[MHz]$	34.5	10.1

Table 2.2: Comparison of electrical and spectroscopic parameters extracted for Sample-A *and target parameters, respectively.*

As a result, I have chosen a number of configurations suitable for engineering and particularly the one described in a Table 2.2.

As reflected in a Table 2.2, I aim to reduce the qubit frequency $\omega_Q/2\pi$ from $6.3GHz$ to $2.8GHz$ keeping the qubit anharmonicity at the same level of $-80MHz$. I have also decided to reduce anharmonicity of ancilla by a factor of 10 in comparison to the sample *Sample-A*. The cross-Kerr coupling g_{zz} was also reduced (now it is 3 times less than in *Sample-A*). However, this should not limit the readout due to the quantum limited amplifiers and the ancilla in resonance with the cavity

All the scripts with different rank functions and *input* and *output* parameters can be found in my GitHub repository [92].

2.2. Core of the circuit

To implement the electrical circuit, we use the chain of ten SQUIDs as an inductance L_a, and two separate Josephson junctions as E_j. We use SQUIDs in the inductance to be able to tune the inductance value *in-situ* by applying an external magnetic flux. The Josephson junctions which compose the SQUID chain are all made to be identical. We make a SQUID chain instead of single SQUID to build an inductance with small non-linearity. With the same total inductance, the nonlinearity of SQUID chain is less than the nonlinearity of single SQUID due to reduction of phase difference on sides of each junction. Capacitors C_s and C_t are formed by large aluminum pads.

In general, I have chosen to keep the geometry of the core fixed, changing only the areas of Josephson junctions. This was done in order to better understand the effect of design modifications.

2.3. Geometry of superconducting pads

It is necessary to carefully choose the shape and size of pads for the qubit, since it will define the capacitances C_s and C_t of our circuit. In case of the transmon molecule, we have three pads corresponding to the three nodes in the electrical scheme. We do not have a grounded pad as we are using 3D-transmon approach. Since the distance to grounded surfaces is relatively large, capacitance to ground can be neglected. The

resulting number of capacitances in this system is three, and two of them must be identical.

The dipole moment is another important characteristic that we need to take into account when designing the shapes of the pads. It is necessary to minimize qubit dipole moment and orient it orthogonally to the electric field of a cavity to suppress the unwanted transverse coupling between qubit and cavity. At the same time, the dipole moment of ancilla must be large enough and oriented in parallel with the electrical field of the cavity to achieve a strong coupling between ancilla and cavity.

Finally, the reduction of the amplitude of the electric field associated with qubit mode is also desirable since it can lead to unwanted coupling of qubit to TLS (two-level systems). The TLS results from the possibility of tunneling of atoms between two energetically similar states in the disordered lattice [32]. These systems can be in resonance with qubit and couple to the qubit by electric field, which can lead to decoherence of superconducting qubits [93, 31]. Nevertheless, the general solution is to avoid the undesirable effects by redistributing the electric field of qubit. This approach allows 3D-transmon [94] to show a high decoherence time [95, 96, 97]. This is a motivation to use a flip-chip technology to separate transmon capacitor pads [98].

This way, by reducing the amplitude of electric field we reduce not only the radiative losses, but also the coupling strength to the TLS ensemble. As a result, we expect the qubit relaxation time to increase.

2.3.1. Overview of *Sample-A*

In the case of *Sample-A*, all three pads have a rectangular shape. The design of the pads is depicted in Fig. 2.3. A pad of size $200\mu m \times 1210\mu m$ was placed in the center, and two identical pads of size $350\mu m \times 250\mu m$ were placed on the two sides. The gap between central and side pads equals to $150\mu m$. The core of the circuit consisting of Josephson junctions and submicron wires was positioned near the central pad. To increase the dipole moment of ancilla, the side pads related to C_t capacitance were placed at a distance from each other. The wires connecting the core and the side pads lie along the edge of the central pad.

In this configuration, it is easy to achieve required capacitance values due to many variable geometrical parameters of the system. Nevertheless, there are few weak points related to this geometry which I would like to describe below.

First, the central pad is offset from the center axis of the side pads. This offset leads to a significant dipole moment of qubit (See Fig. 2.4). In addition, the electric field between the wires and central pad increases the qubit dipole moment even more. This should not present a problem in the ideal case when the sample is oriented orthogonally to the electric field of the cavity. However, in case of any misalignment of sample in the cavity, the dipole moment will lead to direct transverse coupling of qubit mode to the cavity field.

Second, in this configuration, we expect the amplitude of electric field to be large and couple to many TLS. The maxima of this field will be present on a sharp corners of the central pad and small wires, due to its location close to the pads of different potential. This was confirmed by finite element simulations made in HFSS (see the Fig. 2.5).

These two factors lead to the appearance of unwanted transverse coupling and stimulate coupling of qubit to the TLS, which induces a decoherence of qubit. We

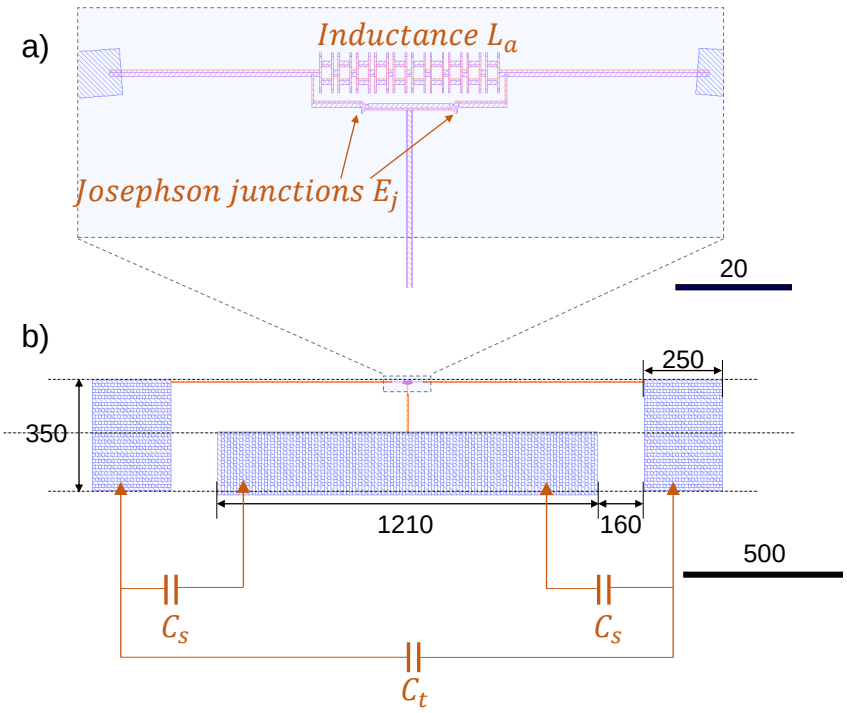

Figure 2.3: The design of a transmon molecule of Sample-A. *All sizes are given in micrometers ([μm]). a) - core of the sample consisting of Josephson junctions; b) - aluminum pads, which forms the capacitances C_s and C_t.*

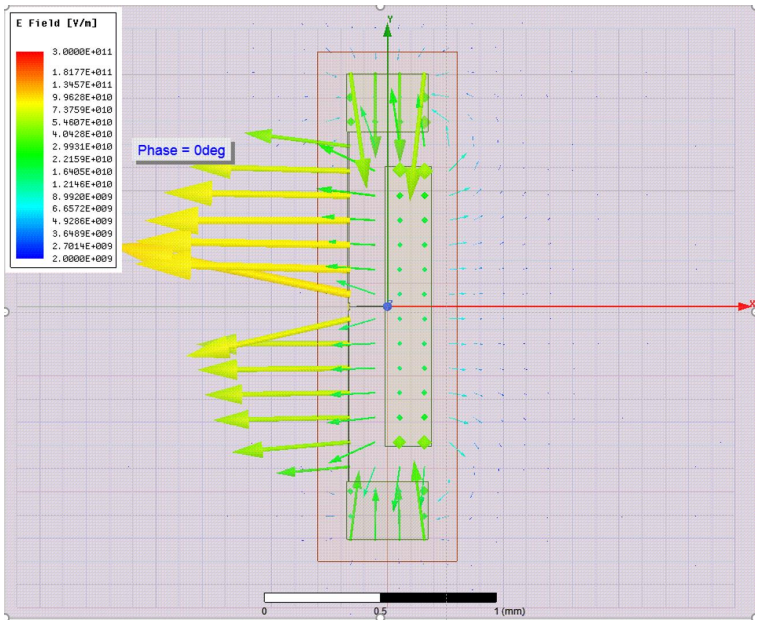

Figure 2.4: HFSS simulation of electric field produced by qubit mode of Sample-A.

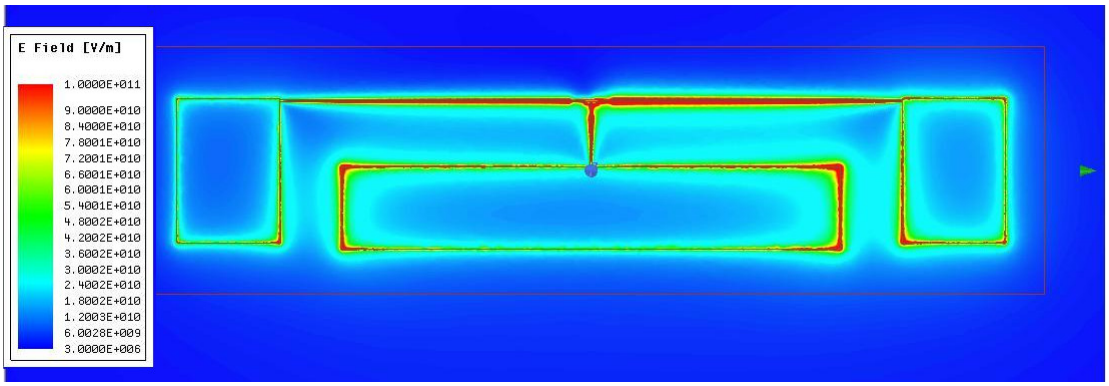

*Figure 2.5: Shape of the pads in previous generation transmon molecule: (*Sample-A*). Color reflects the intensity of electric field in the surface plane achieved by finite element simulation.*

assume that the low T_1 we have measured in case of *Sample-A* ($T_1 \approx 3.3\mu s$) can be at least partially explained by the non-optimized pads geometry.

2.3.2. Circular geometry for the transmon molecule

To avoid the transverse coupling between qubit and cavity, we use circular geometry of concentric transmon [99, 100]. Concentric transmon is a qubit consisting of a Josephson junction (or SQUID) and two pads, forming the capacitor. The main difference from standard transmon is a shape of the pads: the inner circle circumscribed by the outer ring with the same center. It has a very low dipole moment due to the central symmetry of this configuration.

To adjust the concept of concentric transmon to our transmon molecule structure, we modify it by adding the third node and by connecting the three nodes with inductance and two Josephson junctions.

The detailed design is presented in Fig. 2.6. The central circle is surrounded by two ring sectors. The qubit mode is associated with oscillations of current between the circle and ring sectors. And the ancilla mode is associated with oscillations of current between the two ring sectors. In the next subsection, this will be proven by HFSS simulations.

The proposed configuration allows us to minimize the dipole moment of a qubit, at the same time keeping the dipole moment of ancilla large enough to provide strong coupling between ancilla and cavity. It reduces transverse coupling between qubit and cavity, even in case of misalignment of the sample. Other advantages of this configuration include low radiative losses due to small dipole moment of qubit mode; and less coupling to TLS due to more smooth electric field distribution. We also aimed to minimize the amplitude of an electric field using Ansys HFSS$^{\text{TM}}$ simulations.

2.3.3. HFSS simulations

Finite element simulations

It is necessary for us to simulate the capacitances of our circuit C_s and C_t and reach the target values by varying geometrical parameters. Other targets of simulations are

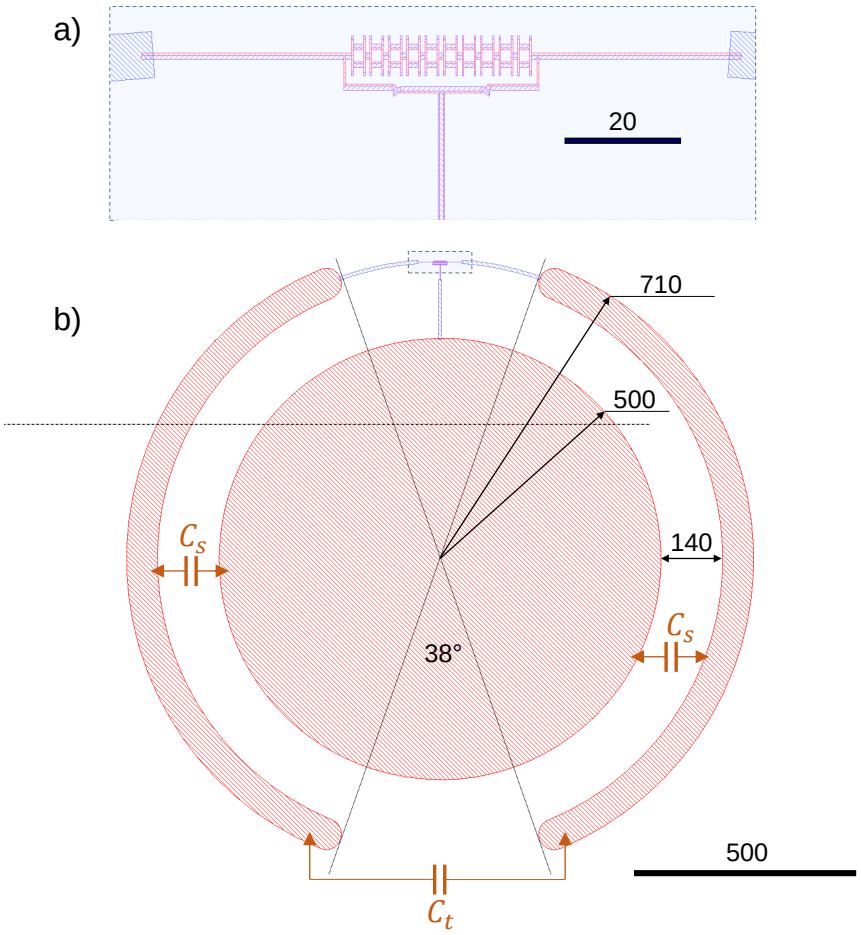

Figure 2.6: The design of transmon molecule with circular geometry. All sizes are given in micrometers ([μm]) This geometry minimizes the dipole moment of qubit mode and reduces the amplitude of electric field.

to minimize the amplitude of electric field, and to prove the significant decrease in dipole moment of qubit mode.

Building model for HFSS simulations

We model the 3D-cavity by a cuboid box made of infinite conducting material. The sizes $35mm \times 5mm \times 24.5mm$ were chosen to be similar to sizes of the 3D cavity. A chip substrate is modeled by a cuboid placed in the center of cavity (sizes $5mm \times 5mm \times 0.3mm$). The relative permittivity of the chip-box is chosen to be $\epsilon = 11.45$ which is equal to the permittivity of silicon at cryogenic temperatures. A superconducting circuit is modeled by a combination of infinite conducting 2D planes and inductive lumped elements corresponding to aluminum pads and Josephson junctions, respectively.

Extraction of capacitance values

To be able to extract the capacitances C_s and C_t, we simulated the eigenmodes of the model described above. As a result of simulation, we are able to see three eigenfrequencies associated with bare cavity, ancilla and qubit. We have simulated the eigenmodes when varied the lumped inductances to evaluate the coupling between these modes.

We extract the capacitances from the two eigenfrequencies obtained by HFSS simulations related to qubit and ancilla modes ω_Q, ω_A and the lumped inductances L_j and L_a using next equations:

$$C_s = \frac{1}{2L_j\omega_Q^2} \tag{2.1}$$

$$L = \frac{L_j L_a}{2L_j + L_a} \tag{2.2}$$

$$C_t = \frac{1}{L_a\omega_A^2} - \frac{1}{C_s} \tag{2.3}$$

To verify the method, I have first simulated a *Sample-A* and compared it to the experimental data. The initial goal was to compare the simulated eigenfrequency with the result obtained in spectroscopic experiment (see Chapter 5.2). The first results were not successful. To overcome this problem, I have modified the model of *Sample-A* by adding models of wires and improved the initial mesh. As a result, the simulated capacitances became close enough to the values measured in experiment. Moreover, I have applied this level of detalization in my further works.

Josephson junction self-capacitance

The self-capacitance C_j of a junction can be estimated through a simple model of a parallel plate capacitance $C_j = \epsilon_0\epsilon_r S/d$, where $\epsilon_r = 10.5$ the relative permittivity of aluminum oxide, S the area of the junction and $d \approx 2nm$ is the thickness of oxide layer. This results in a capacitance per area unit of $C_j/S \approx 45fF/\mu m^2$. [84].

This self-capacitance was not added to the simulation model of HFSS, since its value of around $\approx 2 - 4fF$ is negligible compared to the target C_s and C_t.

Simulation of circular transmon molecule - *Sample-B*

The HFSS-model of circular transmon molecule has been fully parameterized. The main independent geometrical parameters are: radius of inner circle R_{circle}; gap between inner circle and ring sectors Gap; width of ring sectors $Width_{RingSec}$; and the angle of the sector Θ_{sector}. Then, I have conducted more than one hundred HFSS simulations with many variations of these geometrical parameters. The full list of obtained results can be found in my dedicated GitHub repository [101]. We have found that to reach the target values of $C_s = 125fF$ and $C_t = 87fF$ we would need the geometrical parameters equal to: $R_{circle} = 500\mu m$, $Gap = 140\mu m$, $Width_{ringsec} = 70\mu m$, $\Theta_{sector} = 142°$.

Decreasing an amplitude of the electric field

When engineering a superconducting qubit, it is important to take into account the electric field amplitude produced by its mode. The importance of this parameter is explained by the presence of tunneling TLS in a substrate. It has been shown that in case of simple 3D-transmon, the gap between pads affects crucially its relaxation time due to change of the electric field distribution.

In our case, the electric field imposes an additional restriction on Gap. It also limits Θ_{sector}. Indeed, if the two ring sectors are too close to each other, the field density will be enormous.

The examples of electric field distributions of qubit mode for different geometrical parameters are shown in Fig. 2.7.

During minimization of electric field, we aim to fix the target values of capacitances C_s and C_t. The easiest way is to increase the gap between pads as well as the size of the pads themselves. However, this solution is limited by the size of the qubit (less than wavelength of photon with qubit frequency). As a result, we would need to make the electric field as smooth as possible to reach the given capacitance value on a given space. This way, our target is to minimize the amplitude of electric field in locations where it reaches its maximum values.

For this purpose, the circular shape is much better than previous design, since the gap between the inner circle and the ring is fixed, and electrical field is smoothly distributed along the arcs. The length of thin wires is also significantly reduced, preventing the electric field from focusing on these areas. In addition, the ends of the ring sectors have been rounded to avoid focusing the electric field on sharp corners.

Summary of HFSS simulations

We have proposed the circular design of transmon molecule to overcome the problem of qubit dipole moment. We have described the model we used for finite element simulations in HFSS and presented the method of extraction values of capacitances C_s and C_t. Finally, we have discussed the strategies to minimize the amplitude of electric field. As a result, we have proven the benefits of the circular geometry and defined the exact sizes used for further work.

2.4. Computer-aided design (CAD) of layout

In the previous section, the exact shape of transmon molecule was defined. This section is devoted to the process of drawing a sample for nanofabrication using a

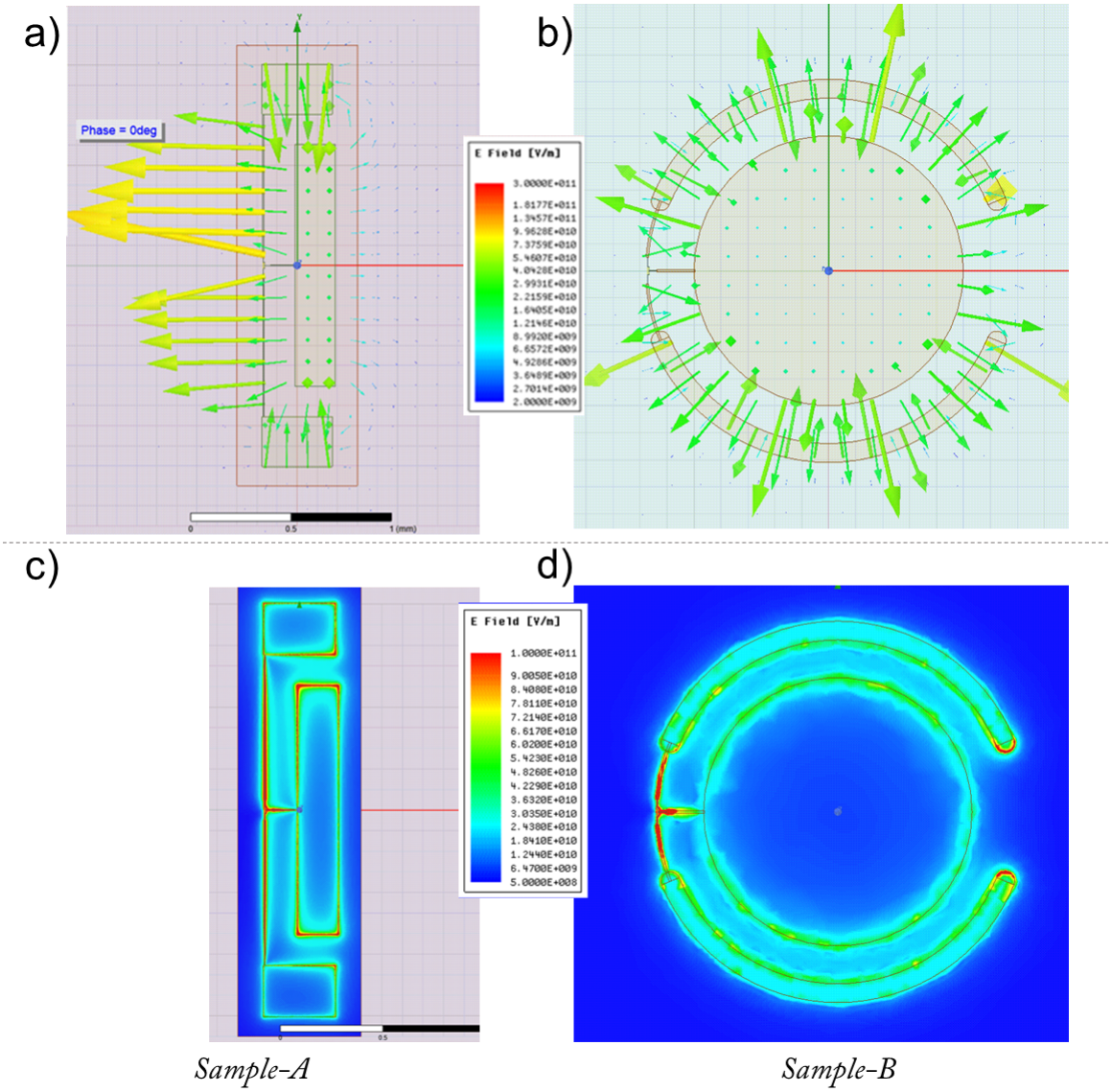

Figure 2.7: Result of HFSS simulations of electric field produced by qubit mode. The amount of energy stored in this mode is set as constant in both cases of Sample-A *and* Sample-B*. a) - vector electric field of* Sample-A*; b) - vector electric field of* Sample-B*; c) - magnitude of electric field of* Sample-A*; d) - magnitude of electric field of* Sample-B*.*

Computer-Aided Design program.

Design objectives

Our main objective is to create a drawing of future sample *Sample-B* in .gds format.

The drawing must consist of several layouts which correspond either to different steps of nanofabrication, or to different radiation doses for lithography (see more details about lithography process in section 3.2.2 of Chapter 3). We use 2-inch silicon wafers suitable for at least 30 copies of a chip with size equal to $5mm \times 6.8mm$. The maximum number of chips ensures a success yield of nanofabrication run. We vary the parameters of the chips due to some uncertainty of nanofabrication process. However, it is a challenging task to vary some given parameters of each chip without any mistake, when the number of chips is big.

We also pattern test-structures consisting of copies of the core for each sample to measure a critical current of each junction. The final step includes adding markers on a separate layout, as well as creating the instruction files for the lithography.

Design by Python script

In this work, I have decided not to use graphical instruments for creating the drawings. Instead of it my approach was based on Python script which I developed for this purpose. This script takes lists of variable parameters and creates a set of .gds files, including the drawings of the chips and instruction files. It allows us to ensure the reproducibility of the design and simple process of varying the parameters reducing the chance of error. It also guarantees the exact correspondence between the core of transmon molecule and test structure of each chip. One of the main benefits is that automated design process allows to quickly integrate adjustments based on nanofabrication results into a new .gds-file.

I have decided to use a gdsCAD python library working on Python 2.7 for developing the script. If necessary, it can be adapted to any Python 3 CAD package by changing few methods which are used to build the gds cell. At the time when I have started developing this script, the relevant products of IQM (KQCircuits [102]) and IBM (Qiskit Metal) were not yet released.

The CAD scripts, that I have developed can be found in my GitHub repository [103]

The repository includes ready .gds-files for each wafer, as well as the code which was used to build them.

2.4.1. Vortex pinning

Since we use an external magnetic coil to tune the frequencies of ancilla and qubit, we have expected the appearance of the Abrikosov vortices [104, 105], in superconducting structures. The Abrikosov vortex is a vortex of current in superconducting material, creating a magnetic flux equal to one quantum of magnetic flux Φ_0. Since these vortices can freely move along the surface of the superconducting film, it will lead to several problems: it can produce energy dissipation when oscillating in resonance with microwave field; and if it is moving close to the SQUID, it can randomly change the amount of magnetic flux passing through the SQUIDS, changing the actual qubit frequency and inducing decoherence.

To avoid these unwanted effects, the standard technique is to create many small holes in the superconducting films, which will trap the vortices at a local position. This method is called "vortex pinning". In addition, if the wire is thin enough, this will also decrease the probability of appearance of vortices. We have applied both of these methods in our design.

Limiting magnetic field

We would like to calculate the expected maximum of magnetic flux which can be introduced into a small SQUID loop without introducing ant Φ_0 inside the wire of width w. A magnetic field that is necessary to apply to make one flux quanta to pass through the SQUID can be calculated by $B = \Phi_0/S$. A vortex can enter inside a wire of width w in presence of magnetic field equal to $B_{lim} = \Phi_0/w^2$ [84]. This means that the number of flux quanta which can be introduced into the SQUID before reaching the B_{lim} can be calculated by:

$$n_{\Phi_0} = \frac{S}{w^2}. \tag{2.4}$$

In case of *Sample-A* the width of wire was $4\mu m$ and the area of SQUID of qubit was $S = 6 \times 30\mu m$. By applying the equation 2.4 we calculate the number of flux equal to $n_{\Phi_0} = 11.25$. The value of limiting magnetic field in this case is expected to be $B_{lim} = 0.13mT$

Nevertheless, according to the experimental data, we have registered vortex appearance at $n_{\Phi_0} = 6$ which is two times lower than expected. This can be explained by redistribution of actual magnetic field due to Meissner effect. The instabilities of spectrum provoked by vortices can be found in Fig. 5.6 a) of Chapter 5.

Parasitic inductance

The minimal width of the wire will be limited by parasitic inductances. We need to keep them small enough in comparison to the inductances of Josephson junctions. Small wires of width $0.2\mu m$, thickness $20nm$ and length $40\mu m$ give a parasitic kinetic inductance of approximately $0.4nH$. Meanwhile, the large wires of width $4\mu m$, thickness $70nm$ and length $700\mu m$ give a parasitic kinetic inductance of $0.1nH$ [84]. A standard solution is to make wires of changing width. Thin sections would be placed near the SQUIDs to prevent appearance of vortices, and thick sections are at greater distance to reduce the total parasitic inductance.

In a design of *Sample-B* in addition to the method described above, we were also able to decrease the length of the wires to minimize its parasitic inductance.

Density of holes

To prevent vortex appearance, the distance between the holes should approximately equal to the width of the wire, w which we have calculated above. For *Sample-A* the square holes were designed in the square grid nodes. The side of each square hole and the gap between them was equal to $10\mu m$. However, during the fabrication process, the lithography has failed to print the holes due to the proximity effect.

I have decided to enlarge the size of the holes and the distance between them to prevent this error. At the same time, I have chosen to use a hexagonal lattice instead

of the square one and change its shape to the circular one to increase the density of holes.

For *Sample-B* the hexagonal lattice consisted of round holes with radius $10\mu m$ and distance between edges of the neighboring holes $20\mu m$.

For *Sample-C* the radius of the holes was decreased to $7\mu m$ and distance between edges of the neighboring holes was $16\mu m$ due to improved fabrication process.

Holes effect on the capacitance

We have not included the holes in the model during the HFSS modeling, since it would require more computer memory than we had available. However, we have considered the expected difference to be negligible as the size of the holes is much smaller than the distance between pads and the holes will not significantly affect the electric field distribution.

2.5. Chapter key points

The motivation of this chapter was to develop the design for a new generation of transmon molecule *Sample-B* based on the results of the previous one (*Sample-A*). The main objective was to improve the relaxation time T_1 of the qubit.

We have discussed the target spectroscopic characteristics for a new transmon molecule. The values of electrical parameters C_s, C_t, E_j and L_a were determined through an optimization algorithm based on ranking functions.

We have described the geometrical configuration of the design, including the core of the sample, capacitance of the pads, dipole moments related to qubit and ancilla modes and electric field distribution.

We have conducted HFSS simulations of pads capacitances and electric fields to prove the benefits of circular shape and defined the exact sizes of pads.

Several solutions for problems associated with Abrikosov vortices and parasitic parameters were discussed: the vortex pinning by holes and the wire width control. We discussed the limiting magnetic field for a given width of the wire and calculated the number of flux quanta which can be applied. The changes in configuration of pinning holes were described as well.

The practical result of this chapter is the .gds file of the design, which can be used in the nanofabrication process.

Chapter 3.

Nanofabrication of superconducting circuits

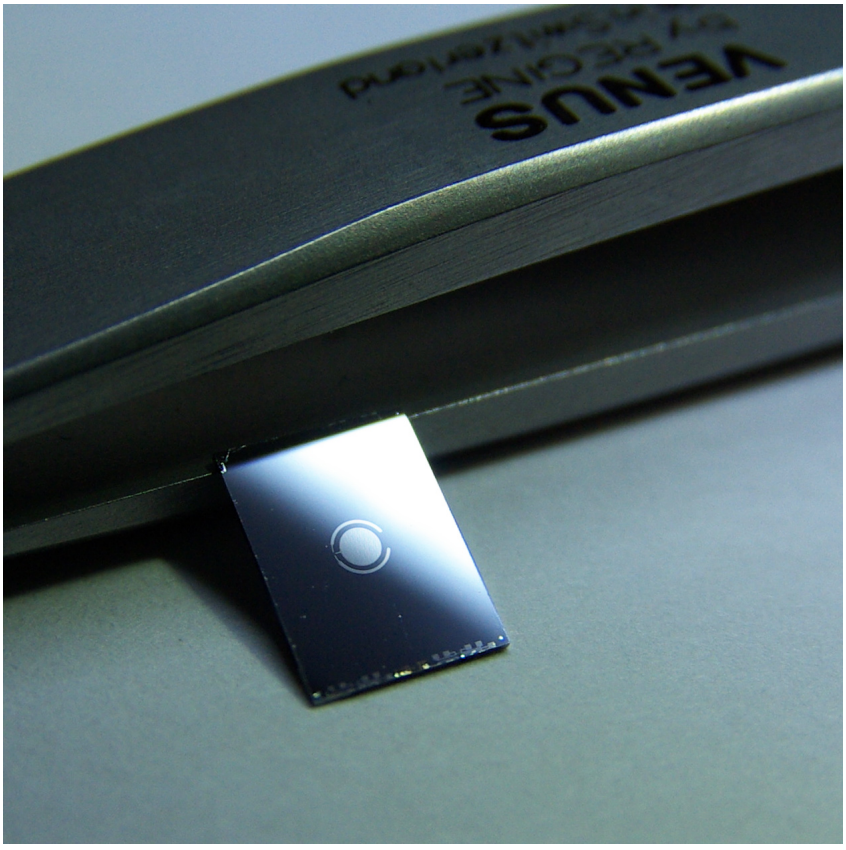

Figure 3.1: Photography of ready sample. Size of chip: 6.8 mm x 5.0 mm.

This chapter describes two fabrication process I have used to make a new generation of transmon molecules - one process which was conventional in our lab, and the new one I've implemented during my PhD work. It includes the description of the basics of nanofabrication, as well as different techniques of making Josephson junctions with precise modeling to predict their size. Detailed examples illustrate each stage of the recipe. In addition, I describe several fabrication problems which one can face and their solutions. At the end of this chapter, a precise recipe is provided.

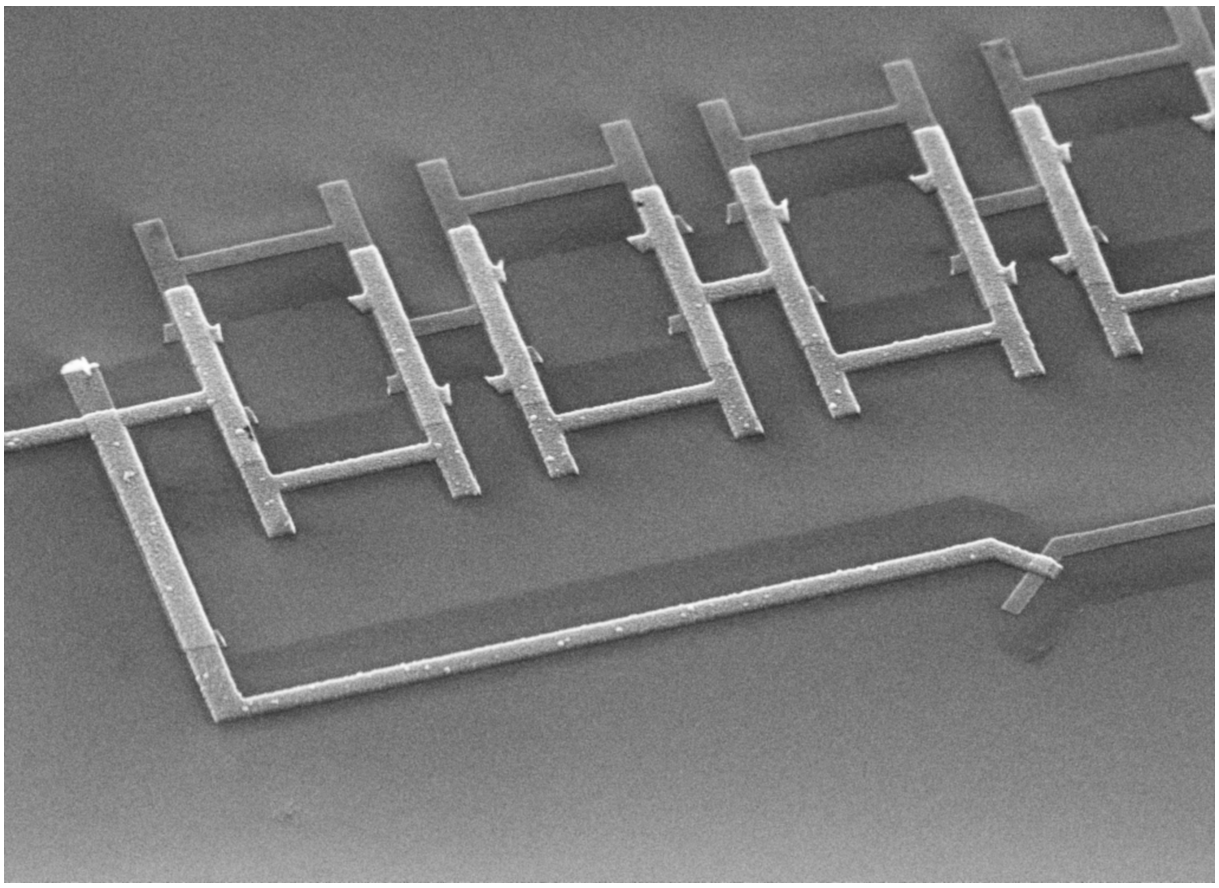

Figure 3.2: SEM picture the core of Sample-C *clone from wafer14.*

3.1. Description of the desired result

This section will describe exactly what we want to obtain as a result of nanofabrication as well as describing the process chain. The resulting sample of nanofabrication process is shown in Fig. 3.1 as an example. Fig. 3.2 shows a scanning electron microscopy of Josephson junction and SQUIDs of the resulting sample.

3.1.1. The target of the superconducting structures

The goal of fabrication is to create superconducting structures of a given shape on the surface of the substrate, but also to minimize the decoherence sources that can appear during the fabrication. Different research groups use different methods to achieve this goal. Here I will focus on our technical process. But first, let's define the end result we are aiming for.

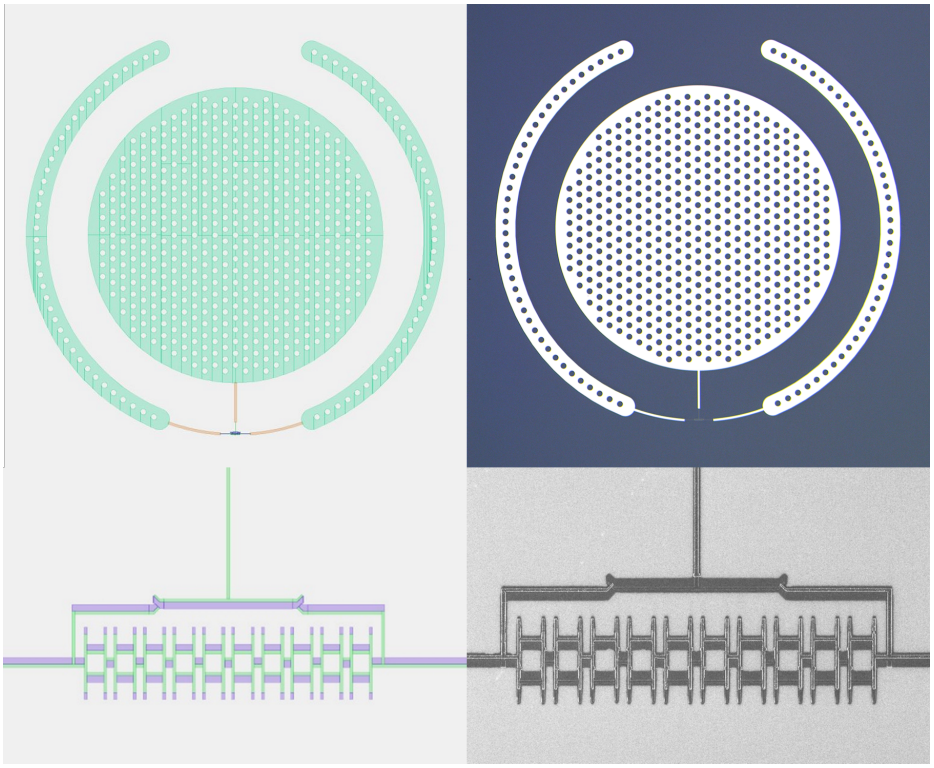

Figure 3.3: (a) Drawing of the structure's design in .gds format for lithography. (b) Aluminum structures resulting from nanofabrication.

In the Fig. 3.3 you can see an example of the structures I have made for this project. It includes aluminum hole plates, wires and Josephson junctions of different sizes. This was achieved as the result of two fabrication processes described below. This is a circular transmon molecule consisting of three large aluminum pads with holes to catch the magnetic flux vortices. More detailed explanation is given in section 2.4.1 of Chapter 2. The radius of the inner circle is $R_{circ} = 500\mu m$. The gap between the inner circle and the ring sectors is $Gap = 140\mu m$ The width of the ring sectors is $Width_{ring_{sec}} = 70\mu m$. From each pad, $Width_{wire} = 8\mu m$ thick wires depart, connecting the pads to each other through microscopic elements at no Josephson junctions, a photo and drawing of which is in the enlarged image.

3.1.2. The choice of materials

All samples described in this manuscript were made by deposition aluminum circuits on a silicon substrate. In the following part, I will explain why.

Silicon is a conventional substrate to support superconducting circuits. Differently from microelectronics, silicon participate very little to the qubit properties, only through its dielectric constant, and it's possible. But it is not a single possible solution: in many groups, people are using sapphire [106]. This dielectric material is very chemically stable. This prevents losses due to the formation of surface oxide. Nevertheless, qubits on high-resistivity silicon substrates dominate. Silicon is a very chemically pure, well-studied and easy-to-use material. At the same time, silicon is cheaper and at the same time, qubits on these substrates showed good coherence. In all fabrication cycles, I used 2-inch wafers made of silicon with resistance $10kOhm - cm$.

There are also different possible options of superconducting materials to use for circuits themselves, but the most common are aluminum, niobium. Aluminum is essentially useful mostly because it can form oxide films of high quality to make SIS Josephson junctions, and due to its affinity to the silicon substrate. Nevertheless, there are many studies on the possibility of increasing the coherence times of the qubit by using other materials such as: titanium nitride [107, 108], tantalum [109]

3.1.3. A short introduction to the nanofabrication process

A process that we use here can be roughly described by the following steps: On a 2-inch high-resistive silicon wafer, we deposit golden markers. Then the wafer is cleaned in oxygen plasma with reactive ion beam etching and baked to remove water from it. After that, two layers of positive electron resist are deposited in a way that the more sensitive resist is below the less sensitive one. This technique is used to create undercuts by exposing the bilayer resist to a certain dose of electrons. After the lithography is complete, the mask must be developed by immersing the sample in a solvent. After that, the mask should be cleaned of residual resist by oxygen plasma etching. The next step is a double angle deposition of two layers of aluminum using double angle evaporation technology with static oxidation of the first layer before deposition of the second one. After lift-off step is applied to remove all the resist and metal from everywhere except the places where metal was touching the substrate. The final step is dicing the wafer to samples and additional cleaning if necessary.

3.2. Introduction to Lithography

In this section, we will try to introduce the reader to the basics of lithography in general and electronic lithography in particular. We will also give an introduction to the proximity effect and to the application of lithography for double-angle evaporation - the use of a controlled undercut technique. At the end of the section, the simplest case of using electron lithography to create gold markers is demonstrated.

3.2.1. Definition of Lithography. Uses in microelectronics

The lithography process is widely used in all kinds of microelectronics and nanofabrication to shape structures on a substrate surface [110].

The idea of any lithography is to create a mask. A mask is a layer of a special substance, a resist, on which a pattern is engraved by selective exposure to light. After developing it in a special solvent, the resist will have holes in selected locations. The mask can then be used to etch the surface of the substrate or to apply a substance on top of the substrate through the holes of the mask.

As illustrated in the Fig. 3.4, if one etches the substrate with a mask on top of it, the substrate will be etched in places where the mask has a hole. After that, the mask can be removed by the dissolution process. As a result, the final substrate will be edged well. Another scenario is to deposit material on top of this mask and then do the so-called lift-off to remove the mask and material on top of it. However, it will stay in a place where material touches the substrate.

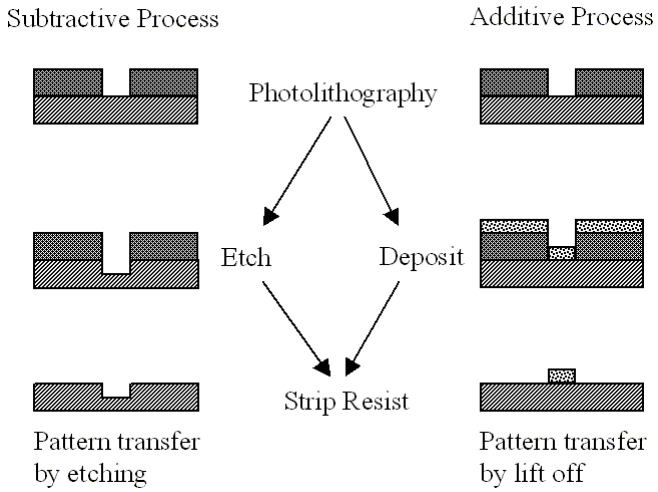

Figure 3.4: Examples of use of ready mask for etching substrate or deposition of new material

3.2.2. Different types of lithography

Positive and negative resists

Lithography can be performed with a positive or negative resist type by exposing it to photons or electrons. We deposit one layer of resist on a bare substrate to create a mask. Two types are possible – negative or positive. The two types of resist react differently to exposure: for the positive resist, exposure stimulates depolymerization, whereas for the negative resist, exposure causes the polymerization. And it turns out that the developer removes the exposed positive resist or the unexposed negative resist. [111].

As you can see in the Fig. above, to prepare the mask of a given shape, you can use either a positive resist exposing it in places for removal during the development stage or a negative resist exposing it everywhere except places you want to remove during the development stage.

Static mask lithography and Maskless lithography

There are two ways to make photolithography: to scan the resist with a laser beam and expose it on a pixel-by-pixel basis (so-called maskless photolithography [112]) or

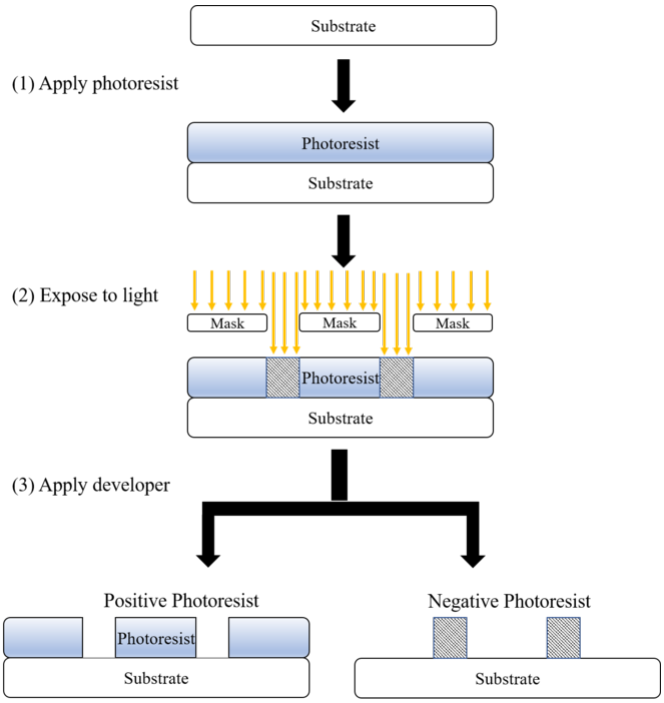

Figure 3.5: Examples of preparing the mask as a result of lithography process with using positive and negative photoresist (Picture from www.wikipedia.org)

to use a static mask. In the case of a static mask, the mask is first prepared as a stencil with holes for light to go through. This mask is placed in between the substrate with resist and source of light to quickly expose all necessary places to a flash of light. For its simplicity and its high speed, it is widely used in microelectronics. In addition, the same mask can be reused to make many of the same devices as shown in the Fig. 3.5 for example.

Photolithography and electron-beam lithography

There are also different types of lithography, distinguished by the way resist is exposed. The most popular is optical lithography, where the resist is exposed to photons of a given wavelength. The second one is the electron beam lithography, where the resist exposed by electron beam [113].

In microelectronics, photolithography is much more widely used than the electron-beam lithography since it is cheaper and a static photomask is used, making a high-volume production possible. Although with optical lithography, it is difficult to have a resolution less than a photon wavelength of a few hundred nanometers because of the Rayleigh diffraction limit. Actually, it is possible to overcome it by creating more complex static masks and using specific resists and doses which allows achieving 14 nanometers tech process for microprocessor manufacturing [114, 115].

The primary advantage of electron-beam lithography is that it can draw custom patterns by direct-write with sub-10 nm resolution because the Debroglie wavelength of accelerated electrons is much less. However, as it is impossible to use a mask with electron lithography it has a low throughput which limits its usage to photomask fabrication and experimental prototyping. An important difference is also that while photons are absorbed depositing all their energy at once, electrons deposit their energy

gradually and scatter within the resist during this process. This can, among other things, lead to a proximity effect (see more in subsection 3.2.4).

3.2.3. A simple example of lithography: Making gold markers

A good simple example of the e-beam lithography we use in this work is the preparation of markers. The explanation of why we need markers, see in subsection 3.4.5 about electron beam lithographer focus. Here we focus on a fabrication process.

In the Fig. 3.6 all steps of fabrication of golden markers are shown.

After the preparation of a two-inch bare silicon wafer, we deposit a single layer of electron resist PMMA 3% by spin coating. This resist is baked on a hot plate to harden it. After baking, we measure the thickness of the resulting resist by an interferometric machine to control the process. Then we write a pattern by electron beam using NANOBEAM lithographer to expose the place where we want to remove the positive resist. After we develop it in MIBK:IPA (Methyl isobutyl ketone : Isopropyl alcohol 1:3)

In the Fig. 3.7 you can see the microscopical pictures of resist at different stages of described process: a) right after the exposure to the electron beam, b) after the development stage (ready mask), c) after gold deposition through the mask d) after lift-off in NMP with $80°C$ (markers are ready)

3.2.4. Bilayer mask lithography with undercut

In this subsection, we describe a two-layer mask for double-angle evaporation, using controlled undercut. Also in this subsection, we discuss the so-called proximity effect, which complicates lithography.

Bilayer mask and Undercut

For more complex structures, one layer of resist might be not enough. For example, to make Josephson junctions, a bilayer resist is usually required. [116] In our work, the bilayer mask consist of two layers of positive electron resist. For the first layer we use the copolymer PMMA-MAA mixture and for the second we use PMMA. The copolymer is more sensitive to e-beam exposure compared to PMMA. (See Fig. 3.8). This allows us to expose the lower resist layer right through the top one without affecting it, using a certain electron dose. Then during development, we can make a bridge: to remove the lower resist by keeping the top one hanging over the substrate. This is a so-called controlled undercut [117, 118]. In my work in most cases I was using a controlled undercut of $700nm$. Of course, in order to get a satisfactory result, it is important to choose the right dose that is sufficient to illuminate the lower layer of resist without destroying the upper layer.

Proximity effect

One of the difficulties arising from the use of electron lithography is related to the so-called proximity effect [119]. As the electron beam passes through the resist layer(s) and penetrates the substrate, the electrons scatter on the substrate atoms and may expose the resist by back scattering in ax extended adjacent regions. This effect is highly dependent on the speed/energy of the electrons. To reduce the effect,

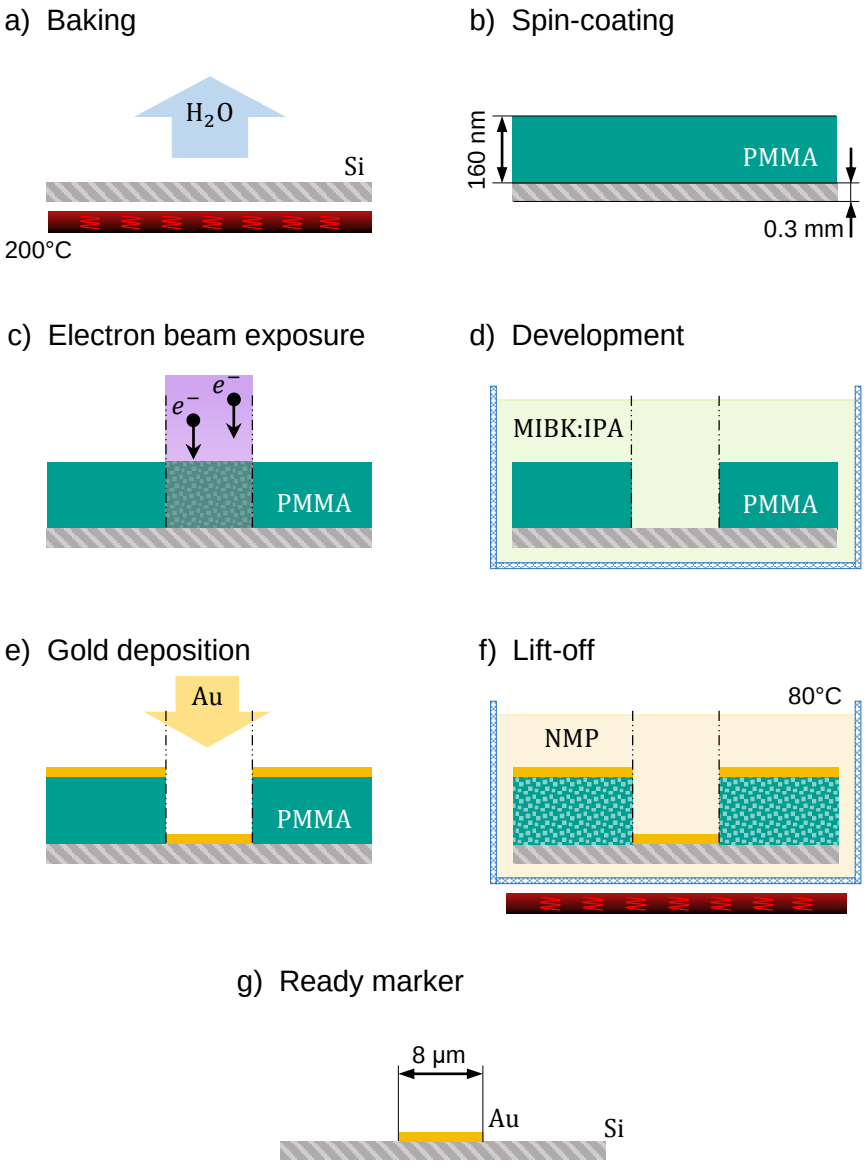

Figure 3.6: Steps of preparation of the golden markers

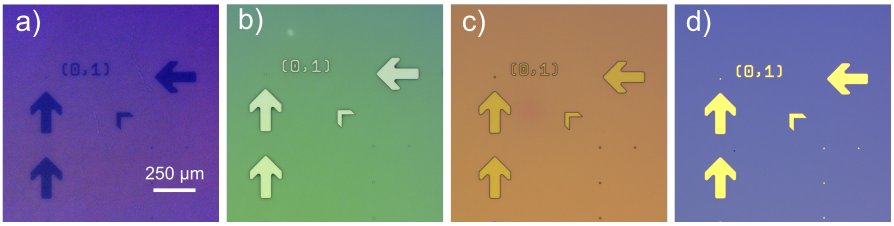

Figure 3.7: Four steps of markers preparation: (a)-exposed resist, (b)-developed mask, (c)-gold deposited, (d)-lift-off done. Optical microscopy. Here and below we use ZEISS "Axioscope 5" Microscope with camera ZEISS "Axiocam 105 color" to make microscopical pictures in clean room.

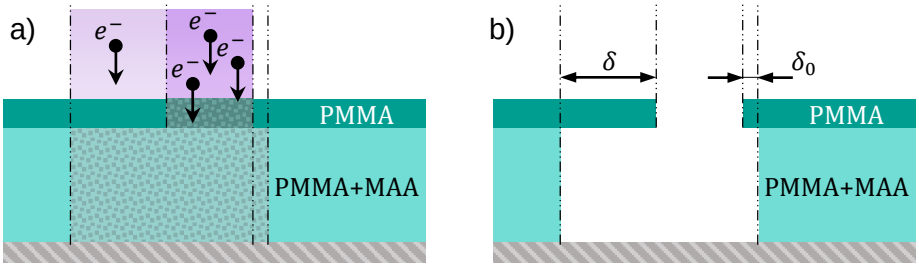

Figure 3.8: Undercut appearance. a) During electron-beam lithography the weaker electron dose expose the lower layer of resist through the top layer, when stronger dose exposes both layers. b) After development process in place where the dose were weaker we observe an undercut.

one usually tries to use higher energy electrons, since their high momentum makes them less likely to scatter back into the resist.[120] The effect is well illustrated by Fig. 3.9. As the kinetic energy of the electrons increases, they penetrate deeper into the substrate and have less chance of reaching the surface due to random scattering.

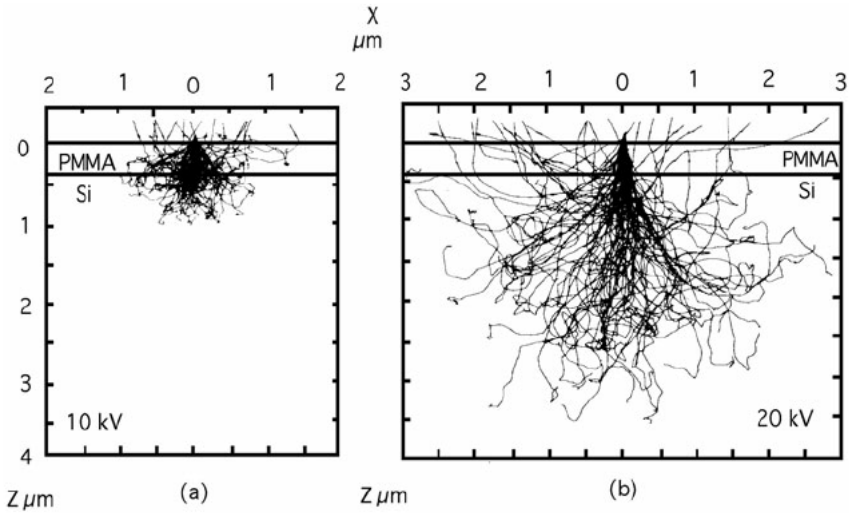

Figure 3.9: Monte Carlo simulation of spatially distributed beams in electron beam lithography. Picture from article [120]

In our case we are using an electron beam with $80keV$ energy and backscattered electrons can affect surroundings around tens of micrometers.

To avoid detrimental proximity effect, doses of electron exposure must be adjusted. This optimization is suitable because long range proximity effect must be evaluated.

Of course, proximity effect also leads to creation of unwanted undercut, called also "native undercut". According to the book of Levinson [121] and article of Lecocq [118] in our case we expect the natural undercut to be around $40nm$. The proximity effect can not only affect the undercut depth by affecting the bottom layer of the copolymer, but can also obscure the top layer of PMMA, which leads to changes in the dimensions of the resulting structures. Especially vulnerable to proximity effect are those structures that are packed close to each other. As examples, such structures are small elements located close to large shapes, integrated capacitors, chains of Josephson junctions and SQUIDs. Scanning electron microscopy. The width of junction slit is $200nm$. The width of wire slits is $350nm$. You can see the decrease in the height of the resist surface where the undercut was made. This is a consequence of the fact that in these places the resist has been exposed to a low dose of electrons.

Dose calibration

One way to combat this is to divide the structure into more forms with different corrected doses. Usually a higher dose is required at the edges of the structure, since that is where the effect of backscattering electrons is significantly lower. The electron dose can be reduced closer to the center of structures, especially large ones, since this will be compensated by backscattering electrons.

As already mentioned in this chapter, dose calibration is critical to successful lithography. We have used several different doses for different classes of structures. For large elements, the proximity effect plays a significant role, so we reduce the

dose to account for the additional dose from backscattering electrons. Separate dose calibration is required for areas where the undercut should be. Dose calibration is performed to optimize all these conditions. In the first fabrication run, a design with elements of different sizes is prepared, and this design is repeated with different doses. Then, after exposure, it can be clearly seen for which elements which doses are best suited. On Fig. 3.19 there are examples of photography of optical microscope at high, low, and normal doses. To learn more about dose calibration, go to section 3.4.5

3.3. Different ways of implementing Josephson junctions

The core of any superconducting qubit is the Josephson junctions [44, 122]. It is the most complicated part that requires the highest precision of fabrication. Actually, a Josephson junction is built of two superconductors coupled by a weak link. To make it, it is possible to include a piece of an insulator or a non-superconducting metal in between. In our case, we focus on a simple case of superconductor–insulator–superconductor junction, (or S-I-S). To make it we need to create two overlapped layers of aluminum, with aluminum oxide between them as an insulator, with a connection of these two layers to different poles.

It is possible to make this junction by using two steps of fabrication: during the first process, we create the first layer of aluminum by etching through the first mask. Then we oxidize it and evaporate the second layer. This approach is applied in industry and described by some scientific groups as well: [123, 124]. Despite some advantages, they do not use it widely because of the reasons below.

Josephson energy exponentially depends on the thickness of the oxide layer and because of this, the oxidation process is a bottleneck in the precision and reproducibility of Josephson junction fabrication. In order to achieve sufficient control over the accuracy of the obtained junctions, it is necessary to create alumina oxide under controllable conditions. It requires stable, repeatable and controlled conditions of oxidation. Thus, if one decides to make Josephson junctions using the approach of two steps fabrication, he or she will be required to get rid of the natural oxide formed on the first layer of metal. In addition, the two processes of fabrication add more complexity because of the good alignment localization of the first mask.

Therefore, the most convenient way to create a Josephson junction is to apply two layers of metal with oxidation between them in a single vacuum process. By this way, the sample is not removed from the vacuum chamber between the two evaporation, thus avoiding contamination or natural oxidation. I will introduce their different techniques to do this. Two of them were used for the sample fabrication in my project.

3.3.1. Bridge-free technique

I will start the explanation from the Bridge free technique. I decided this order because I have found it easier for understanding. This technique was invented in Grenoble by Lecocq and others [117, 118], as an alternative to the more common Dolan-Bridge technique (which we will also describe later in the subsection: 3.3.2). The Bridge-free technique is particularly useful for making larger Josephson junctions and for making parts of the substrate surface to which aluminum will be applied more

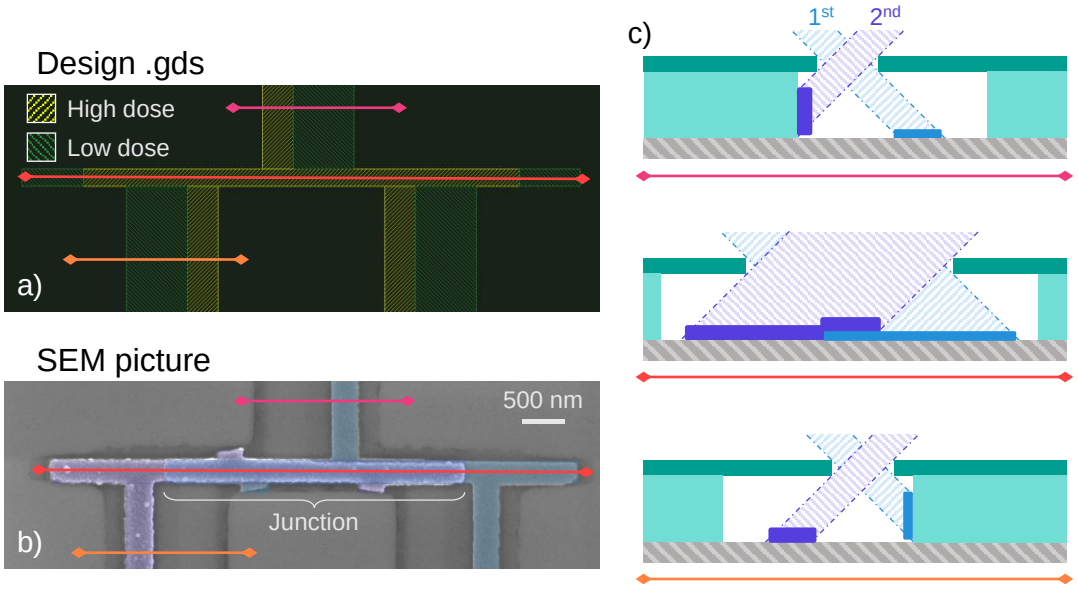

Figure 3.10: Bridge Free Fabrication technique to perform Josephson junctions. (a) A top-down view of the mask in the design. In areas marked in dark green, we have a reduced dose of electrons. Thus, a controlled undercut is formed in these areas. In areas colored yellow, the electron dose is high enough to remove both layers of resist. (b) Scanning electron microscopy image of the ready Josephson junction made with BFF technique. The light blue false color corresponds to the first aluminum evaporation, while the magenta blue refers to the second evaporation. (c) Schematic cross-sectional diagram of the controlled undercut.

accessible for cleaning and etching.

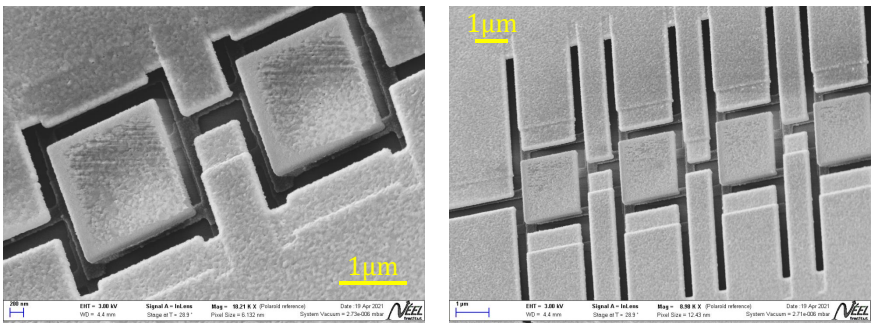

Figure 3.11: Aluminum evaporated onto a bilayer mask to make Josephson junctions by bridge free technique. Chains of Josephson junctions of different sizes are shown.

Brief description

Bridge-free fabrication (BFF) technique actively uses controlled undercut. The main idea of the bridge-free technique is to make it possible to apply metal to the substrate in only one of the two angle of evaporation in certain places, using an asymmetrical undercut. Whenever we want to create a wire, we use undercut from a single side.

As shown in the Fig. 3.10 a) we have prepared a mask with undercuts on different sides for the bottom and the top vertical wires. And between these vertical wires we made a horizontal section with undercuts on both sides. It is this section that will form the junction, because in this area the metal will be applied twice, at both angles. The vertical wires will be applied only once in the first or second sputtering, depending on the orientation of the undercut. On a Fig. 3.10 c)

On a Fig. 3.10 you can see the vertical crossection of the mask in three places: the first place shows the wire applied in the first evaporation, the second one shows the formation of Josephson junction between layers of aluminum applied at two angles, and the third one shows the next wire applied in the second evaporation. The metal that was deposited on the resist wall will be washed off during the lift-off. Thus, we get a Josephson junction, to the banks of which the wires are not connected galvanically. The SEM picture of the finished Josephson junction, made by Bridge free technique, is shown in Fig. 3.10 (b). Comparing the design drawing with the final result, you can see additional very short branches of wires that have no continuation. Their presence is explained by the proximity effect.

Precise description

By varying the manufacturing process, we can, within certain limits, control all the geometric dimensions of our mask: the thickness of the resist layers, the width of the gap, the depth of the undercut and the thickness of the aluminum applied. The area (and therefore the critical current) and the quality of the resulting Josephson junction depend entirely on the choice of these parameters. Hereafter, a geometric model is described to calculate the size of Josephson junctions produced by BFF technology,

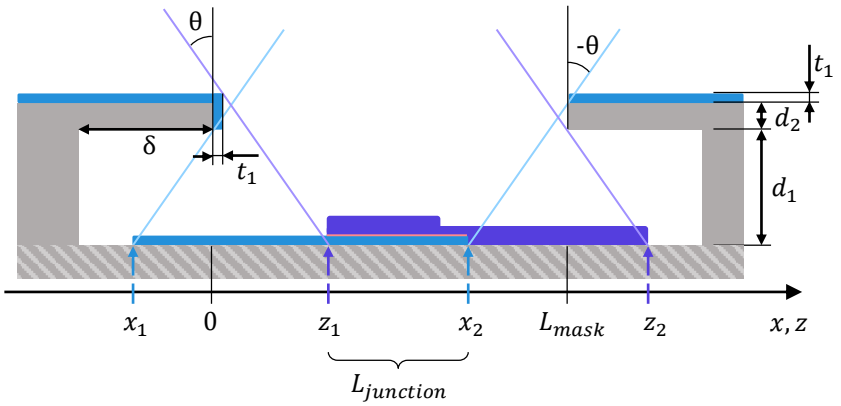

Figure 3.12: Exact model for calculating the Josephson junction area obtained by BFF application. The light blue color indicates aluminum deposited in first evaporation. Purple-blue indicates the second layer of aluminum. X and z coordinates have the same axis, just shows coordinates of different layers of aluminum.

depending on the size of the mask. This model is also used to calculate the size of the mask when you want to get a Josephson junction of a given size.

It is important to note that when applying the second aluminum layer of thickness t_2, it is significant to make it noticeably thicker than the thickness of the first layer $t_2 > t_1$, as otherwise the second layer of aluminum will be separated due to the shadow produced by the first layer. (see Fig. 3.12) In our case we use $t_1 = 20nm$ and $t_2 = 50nm$ (see Fig.: 3.13)

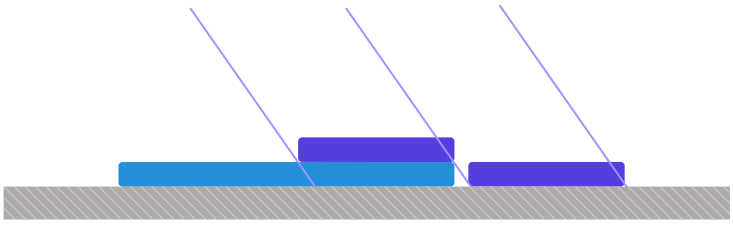

Figure 3.13: This schematic illustrates why it is necessary to make a second layer of aluminum significantly thicker than the first. Otherwise, an unwanted gap can appear.

Consider now Fig. 3.12 . It shows in more detail a schematic cross-sectional diagram of the mask with two subsequent applications of aluminum - that is, the analog of the middle panel of Fig. 3.10 (c) . In the above diagram, d_1 and d_2 denote the thicknesses of the lower and upper resist layers, respectively. θ is the evaporation angle. δ is the depth of the controlled undercut. By L_{mask} we denote the width of the slit in the mask, which we directly control in the lithography process and which is formed in areas of high exposure dose. Now let us calculate the positions that the aluminum will occupy after evaporation. For the first layer of aluminum we denote the edges by x_1 and x_2, and, for the second layer we denote z_1 and z_2.

After the first evaporation, the first layer of aluminum (designated as light blue) will be located according to trigonometric calculations between the following coordinates:

$$x_1 = -d_1 \tan\theta \tag{3.1}$$

$$x_2 = -(d_1 + d_2)\tan\theta + L_{mask} \tag{3.2}$$

which gives us the extent of the first evaporation:

$$L_1 = x_2 - x_1 = L_{mask} - d_2 \tan\theta \tag{3.3}$$

Note that the resulting length of the aluminum differs from the width of the gap in the mask. It is indeed smaller. This effect is explained by the non-zero thickness of the second resist layer.

Performing the same procedure for the second evaporation, and taking into account the presence of a layer of aluminum of thickness t_1 on the surface of the bilayer mask resulting from the first evaporation, we obtain:

$$z_1 = t_1 + (d_1 + d_2 + t_1)\tan\theta \tag{3.4}$$

$$z_2 = d_1 \tan\theta + L_{mask} \tag{3.5}$$

which lead to:

$$L_2 = z_2 - z_1 = L_{mask} - t_1 - (d_2 + t_1)\tan\theta \tag{3.6}$$

Again, the extent of the second aluminum layer L_2 is less than the first, which can be explained by the presence of an aluminum layer already deposited, which both reduces the width of the mask slot and increases the total thickness of the mask.

For us the most interesting value is the size of the junction:

$$L_{junction} = x_2 - z_1 = L_{mask} - t_1 - (2d_1 + 2d_2 + t_1)\tan\theta \tag{3.7}$$

Which means that, we must select the slit size of the mask in the lithography with respect to the mask parameters to make a Josephson junction of a given size:

$$L_{mask} = L_{junction} + t_1 + (2d_1 + 2d_2 + t_1)\tan\theta \tag{3.8}$$

The area of given junction then we can write:

$$S_{junction} = L_{junction} W_{junction} \tag{3.9}$$

where $W_{junction}$ is a width of junction. And we are assuming that $W_{junction}$ is not modified by the angle of evaporation from the designed width of W_{mask}, which is the case if there is no overdose during exposure.

It is also necessary to choose the depth of undercut correctly, taking into account the thickness of the resists d_1 and d_2. If it is too small, some metal intended for the junction will lie on the resist wall and will be washed away by the lift-off. If the depth of the undercut is too deep, then in places where we wanted one of the coatings to be on the resist wall (for example in the case of wires) there may be areas of metal that touches the substrate. Thus, for the minimum-necessary value of undercut in junction area in the case of BFF is given by:

$$\delta > d_1 \tan\theta \tag{3.10}$$

In the case of wires, it is necessary to consider the native undercut δ_0. The width of wire L_{mask} must satisfy the following condition:

$$L_{mask} < (d_1 + d_2)\tan\theta - \delta_0 \tag{3.11}$$

3.3.2. Dolan-Niemeyer bridge technique

In our work, we use two types of Josephson junctions. We use the BFF technique described above to make large junctions that make up the chain of SQUIDs for inductance. And the small junctions are made using standard Dolan bridge technique [125, 116], which you can read about in subsection 3.3.2. The Dolan bridge technique is justified if it is necessary to obtain identical small Josephson junctions.

Brief description

This technology creates a suspended bridge based on a double-layer mask. The substrate under the bridge is coated with metal by evaporating it at different angles. (See Fig. 3.14) The junction area of Dolan bridge technology does not depend on the thickness of the underlying resist layer, in contrast to the situation with BFF. And because of this it is more accurately controlled, especially in the case of small junctions (less than $0.1\mu m^2$).

Precise description

Note a common design flaw with this type of junctions: if the bridge is too wide, the wires will not cross completely. In this case, the crossing area will not be reproducible. It is necessary to take into account the thicknesses of resists and evaporation angles to correctly calculate the width of the bridge.

Now we want to calculate what will be the area of the resulting junction, with the known width of the design.

If the Josephson junction is done correctly, its area is determined solely by the width of the two resulting wires. We can calculate them using the formulas of the BFF technique (Formula 3.7 and Formula 3.8) already known to us. Only now, take into account that the width of the wire will be $\sqrt{2}$ times different from its horizontal cross-section (since the wire is rotated by 45°). That is, the cross-section of the wire along the direction of the change in the angle of vaporization is greater than the width of the wire by the root of two $L_{wire} = \sqrt{2}W_{wire}$

As mentioned, the area will be obtained by multiplying the width of the wires, which, given the square root, will give:

$$S_{junction} = W_1 W_2 = \frac{L_1 L_2}{2} \tag{3.12}$$

where $W_{1,2}$ is widths of resulting wires. Taking into account formulas for resulting size of aluminum after first and second evaporation L_1, L_2, we can calculate the widths of both wires.

Substituting the values for $L_{1,2}$ from equations 3.3, 3.6 we obtain:

$$L_1 = \sqrt{2}W_{mask} - d_2 \tan\theta \tag{3.13}$$

$$L_2 = \sqrt{2}W_{mask} - t_1 - (d_2 + t_1)\tan\theta \tag{3.14}$$

After multiplication we have double area as:

$$2S_{junction} = L_{mask}^2 - (t_1 + (2d_2 + t_1)\tan\theta)L_{mask} + (t_1 + d_2\tan\theta + t_1\tan\theta)d_2\tan\theta \tag{3.15}$$

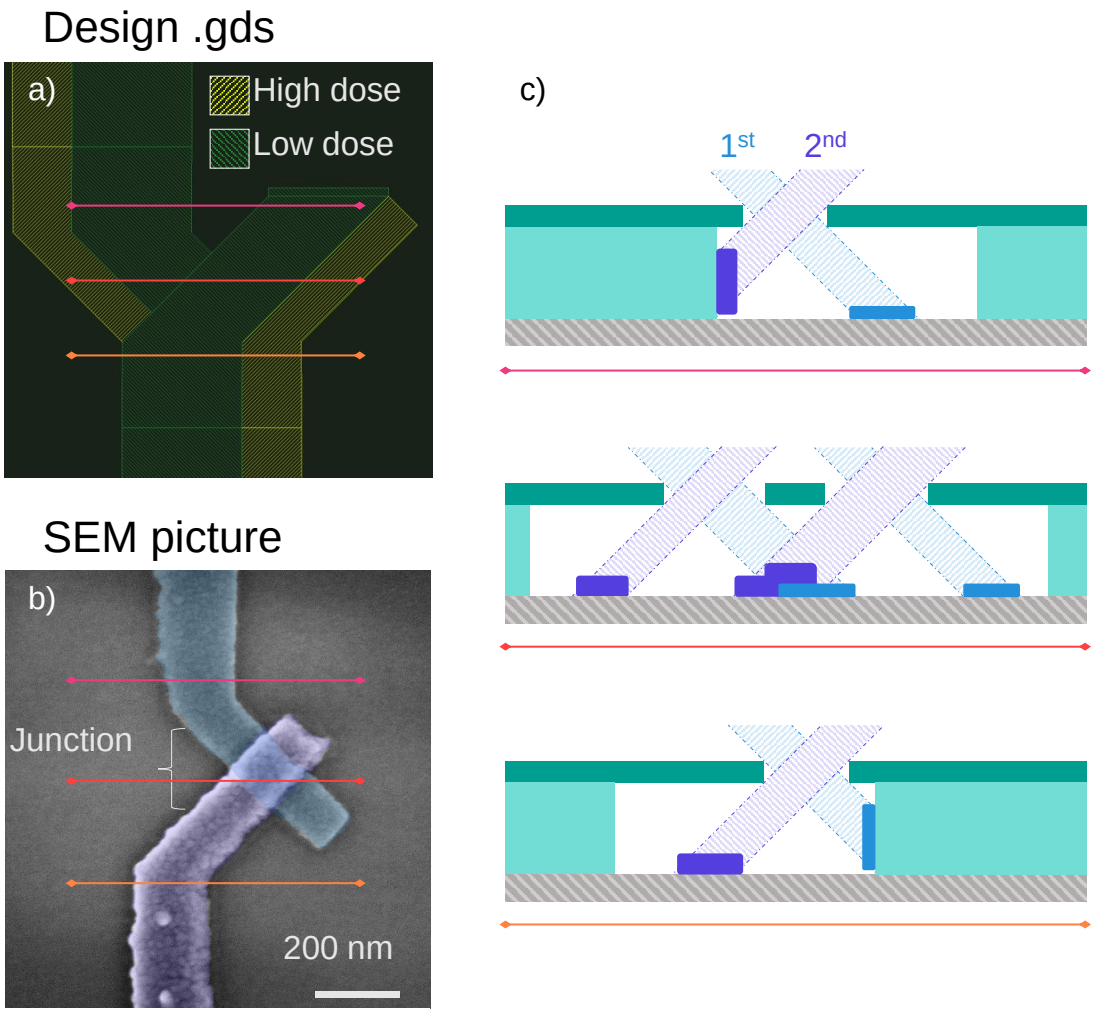

Figure 3.14: Example of Josephson junction made using Dolan bridge technique. The .npf file instruction for electron beam lithography with two different doses are shown on the top figure. The scheme of the bilayer mask and double angle evaporation of aluminum is shown in the bottom figure.

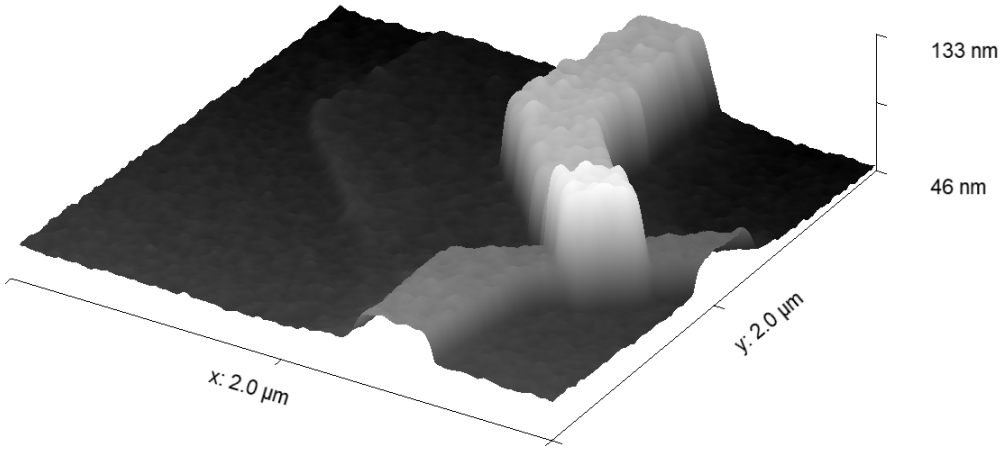

Figure 3.15: Illustration of resulting Josephson junction as a crossection of two aluminum wires. Atomic force microscopy.

or

$$2S_{junction} = 2W_{mask}^2 - (t_1 + (2d_2 + t_1)\tan\theta)\sqrt{2}W_{mask} + (t_1 + d_2\tan\theta + t_1\tan\theta)d_2\tan\theta \tag{3.16}$$

We can solve this expression as a quadratic equation with respect to W in order to obtain the value of the mask width needed to obtain a junction with a given area.

3.3.3. Manhattan pattern

Another remarkable way to realize Josephson junctions is the so-called "Manhattan pattern". With this method, outstanding repeatability of junctions has been demonstrated [126, 127, 128, 129].

In this case, the double-angle evaporation is not made in one vertical plane, but in two vertical planes, with an angle of 90° between them. The idea is to put the metal on the "avenues" in the first vaporization and on the "streets" in the second.

One advantage of this method is that there is no need for a double layer mask.

The condition for successful application in this case is that the metal does not get on the substrate "avenue" in the case of applying metal to "street". This is verified by the condition:

$$x_2 < -\delta_0 \tag{3.17}$$

Which imposes a limit on the width of the wire:

$$L_{mask} < (d_1 + d_2)\tan\theta - \delta_0 \tag{3.18}$$

3.4. Detailed description of standard fabrication process

This section will describe all the specific details of the fabrication recipe used at the Neel Institute. All steps of fabrication will be described here, from the preparation

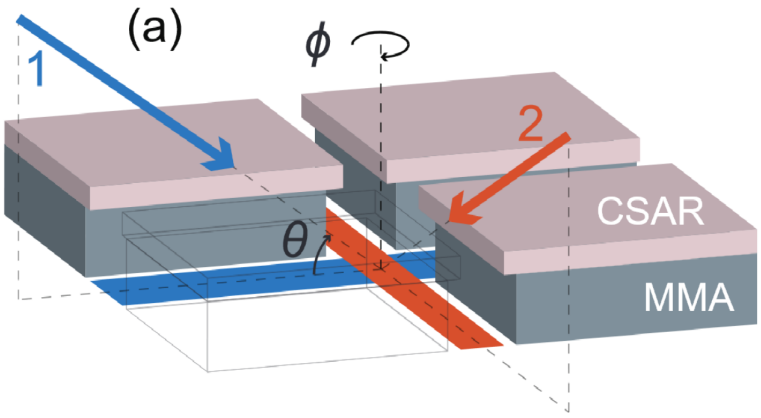

Figure 3.16: Manhattan pattern of Josephson junction fabrication. [126]

of a new wafer to the preparation of the sample up to the loading into the dilution fridge. We have tried to make the description as complete and detailed as possible, so that all the processes described can be replicated exactly. Thus, some of the readers who are not involved in nanofabrication may find the section boring. In this case, it can be safely skipped.

All the actions described below are performed in the clean room of the Neel Institute ISO7 (FED STD 209E equivalent is "Class 10,000 "). In fact, this means that the number of dust particles in that room does not exceed a certain concentration. In this case, in one cubic meter of air there are no more than 352,000 particles larger than 500 nm, no more than 83,200 particles larger than one micron, and no more than 2,930 particles larger than 5 micrometers.

3.4.1. Characteristics of the silicon substrate

For all the samples described, we used single side polished intrinsic silicon wafers, 2 inches ($50.8mm$) in diameter, $0.25 - 0.30mm$ thick. The wafers were manufactured by Siltronic ^{TM} using FZ (Float-zone) growth technology with a crystal orientation of 100 and an internal resistance of $> 10\ k\Omega cm$.

We use 2-inch wafers for two reasons: *(i)* the thickness of the resist after the spin coating has a sufficiently uniform distribution compared to a smaller sample, *(ii)* the probability of obtaining a sample with successful parameters is higher if you make more samples with small variations in the size of junctions in a single fabrication run.

3.4.2. Standard recipe - golden markers

Here is a recipe for the fabrication of the gold markers needed for the further orientation and focusing of the electron lithograph. For the gold to stick firmly to the surface of the silicon, we deposit a thin layer of titanium between them. The markers are square with a size of $8\mu m$

1) Wafer preparation,

   Prebaking the wafer $2min$ at $180°C$ on a hot plate to dry it completely. For better contact with the hot plate, we also pump wafer to it through a small hole.

The hot plate model is "UniTemp ™ GmbH HP-155"

2) Electron resist PMMA 3% applying

- Spin-coating of resist

  Spin-coating a 3% solution of PMMA 950K AR-P 679.03 in Ethyl lactate using a centrifuge at $4000rpm$ with $4000rpm^2$ acceleration for $30s$.

  Here and everywhere else we use a centrifuge POLOS™ "SPIN150i"

  To reduce the resist contamination, we blow on the wafer with filtered nitrogen right before applying the polymer. The pipette we use to apply the resist is also blown with compressed nitrogen to avoid contamination.

- Baking the resist

  We bake the wafer with resist on the same hot plate for $5min$ at $180°C$. During the baking process, the solvent evaporates and the resist hardens.

  All these procedures (spin-coating and baking) are carried out inside a fume hood "ADS ™ Air Laminare Optimale 12" with additional filtration to avoid possible contamination of the mask.

- Measuring thickness

  Then a bilayer resist is ready and thickness of resist is measured using interferometer Mikropack™ Nanocalc 2000

  We select the refractive index "PMMA 950" from the database. Expected thickness is around $150nm$. The rotation speed of the centrifuge can be adjusted to achieve a more accurate resist thickness.

  As a reference for additional information about spin-coating, I would recommend a relevant chapter of Jan Goetz PhD thesis [130].

3) E-beam writing markers

For writing a pattern of markers, we use an $10C/m^2$ electron dose, and a large e-beam current of about $30nA$.

For all e-beam lithography processes in Neel the masker is used "NanoBeam LTD nB5" electron lithographer.

For markers lithography, a large current $30nA \pm 5nA$ is applied for exposure because we don't really care about high resolution. The marker orientation on the wafer is performed by locating the wafer angles manually, using a built-in, scanning electron microscope in the masker.

4) Development of the mask

To develop the mask we use MIBK-IPA (Methyl Isobutyl Ketone - Isopropyl alcohol) as developer in proportion (1:3) respectively. The sample is developed for 60 seconds in MIBK-IPA and then in IPA for 30 seconds more. Finally, we dry the wafer using a compressed nitrogen gun with a filter.

All beakers were thoroughly washed with hot water, Neutral detergent (RBS® T 230), and rinsed with deionized water before use.

For all operations with sample immersion in chemicals (except hydrofluoric acid), we used Duran® glass beakers. All manipulations are also carried out in a special fume hood.

When drying with compressed nitrogen, it is important to direct the jet strictly perpendicular to the wafer surface to avoid possible blowback. It is also recommended to cover the possible escape paths of the wafer with the palm of your hand.

5) Metal evaporation

A $5nm$ titanium at rate $0.1nm/s$ is deposited on the wafer, followed by a $50nm$ gold at $0.1nm/s$. The PLASSYS^{TM} MEB550S electron-beam evaporation unit is employed for this purpose. Since a single layer mask is applied, we use tilting equal to zero. Metal evaporation starts after pre-pumping with a turbopump to vacuum of $P_{CH} = 5 \cdot 10^{-7} mbar$ and $P_{LL} = 2 \cdot 10^{-6} mbar$ in the chamber and in the loadlock, respectively.

6) Lift-off

The liftoff, is performed by soaking the wafer in a beaker with NMP (N-Methyl-2-pyrrolidone) at $80°C$ for 5 to 20 hours. To heat up the NMP, we use a "Stuart^{TM} SD300" digital hotplate.

Then blisters are observed in places where the metal began to peel from the plate. Then, using a pipette and taking liquid from the same vessel, we carefully deflate the metal. After that, we move the wafer to a new beaker with NMP and expose it to ultrasound for 1 minute at 60% power.

For ultrasonication here and after, we use Elma® "T490DH Transonic Digital" Ultrasonic Cleaner, with working frequency of $40kHz$ and ultrasonic power of $110W$ at 100% power. (It is worth noting that the power declared by the manufacturer corresponds to reality only when two-thirds of the vessel is filled with liquid. However, in our case, the vessel is always filled only by 10-20% of the volume due to the lack of a dip cell.)

Finally, we rinse the wafer in acetone, ethanol and IPA and then dry it with compressed nitrogen.

Acetone, ethanol and IPA which we use are produced by these suppliers: Acetone - Honeywell, Ethanol - Honeywell, IPA - CarlRoth.

As a result of the above operations, we have a wafer with gold markers on it, which will be useful to us in the future.

3.4.3. Standard recipe - aluminum structures

1) Wafer preparation

- Reactive Ion Etching
  First, we want to make sure that there is no residual resist or any other organic material on the surface of the wafer. To do this, the wafer is etched in oxygen plasma in PLASSYS ^{TM} for 5 minutes at a power of $20W$ at pressure $0.07mbar$.
- Prebaking
  The wafer is prebaked on a hot plate to dry it during $2min$ at $200°C$.

2) Bilayer resist deposition

- First layer of resist PMMA-MAA

  Spin-coating a PMMA-MAA 9% (9% solution of mixture ARP 617.14 and AR 600.07 (9:5) in 1-Methoxy-2-Propanol) using a centrifuge at speed 4000rpm with $4000rpm^2$ acceleration for $30s$.

  To reduce the probability of resist contamination, we blow again on the wafer with filtered nitrogen right before applying the polymer. The pipette we use to apply the resist is also blown with compressed nitrogen to avoid contamination.

  The choice of resist solution concentration and rotation speed is determined by the selected thickness of the mask. The more resist is diluted, the thinner the mask becomes. And this, in turn, leads to an improvement in lithographic resolution, but at the same time to a decrease in mechanical strength.

  The choice of resist PMMA can be explained by its high resolution [131]

- Baking resist

  The wafer is heated on hot plate for $10min$ at $200°C$. During the baking process, the solvent evaporates and the resist hardens, which allows us to apply a second coat after that without mixture between them.

- Measure of thickness d_1

  It's important at this stage to know the thickness of resist d_1. We measure it with same interferometer Mikropack^{TM} Nanocalc 2000 We select the refractive index "PMMA" from the database. Expected thickness should be around $690nm \pm 10nm$ and should not have a high spread. This is important to get good homogeneity in junction sizes. The rotation speed of the centrifuge can be adjusted to achieve a more accurate resist thickness. A small variation in resist thickness from one wafer to another can be compensated when creating the .gds file by taking into account Formula 3.8. Even if the thickness of resist is not precisely the same as projected, .gds file can be adjusted to take it into account.

- Second layer of resist PMMA

  Apply a 4% solution of PMMA 950K AR-P 679.04 to the substrate by spin-coating using a centrifuge at $5000rpm$ with $5000rpm^2$ acceleration for $30s$.

- Baking resist

  We bake a wafer with two layers of resist for $5min$ at $180°C$.

- Measure of thickness d_2

  To measure thickness, d_2 we use a model of two layers of resist on top of a silicon substrate. For first layer we set refractive index from database "PMMA" and thickness equal to what we have measured for d_1, and for second layer we set refractive index "PMMA950" to extract its thickness. We expect it to be around $230nm \pm 5nm$, if it is not the case .gds file can be adjusted.

  All spin-coating and baking procedures are carried out inside a fume hood "ADS ^{TM} Air Laminare Optimale 12" with additional filtration to avoid possible contamination of the mask.

3) E-beam writing structures

For writing pattern of aluminum structures, two different current intensity are applied. Relatively big structures (more than $1\mu m$ of any dimension) the current is set at $26nA$. For small structures with dimension less than $1\mu m$ such as Josephson junctions and it's wiring, the current is set at $1.3nA$ to achieve the highest resolution.

Electron dose strongly depends on size of given structure and its surroundings:

- $11C/m^2$ for small wires and junctions
- $3C/m^2$ for the undercuts
- $10C/m^2$ for big pads
- $11C/m^2$ for wires with a width of 5 - 20 μm

For more details about e-beam lithography procedure and choice of dose, current and other parameters have look on section 3.4.5.

4) Developing mask

This step is similar to the development of markers described above. We use MIBK-IPA - Methyl isobutyl ketone : Isopropyl alcohol (1:3) developer for 60 seconds and IPA for 30 seconds. Finally, we dry the wafer using a compressed nitrogen gun with a filter.

5) Edges cleaning

To do this, the wafer is etched in oxygen plasma in PLASSYS ™ for 15 seconds at a power of $10W$ at pressure $0.07mbar$.

This step is necessary for two reasons: *(i)* - to make sure that the surface of the substrate under the mask is clean and not contaminated by resist residue; *(ii)* - to polish the edges of the mask. According to [132] cleaning the surface helps to prevent aging effect of resulting Josephson junctions.

The oxygen plasma is generated by a capacitive coupled parallel plate source, and this means that the plasma etching is directional, preferentially etching vertically.

6) Aluminum double angle evaporation

- Pre-pumping

  We load the wafer in another PLASSYS™ evaporator. It is used only for non-magnetic metals, which is very important to make sure when creating superconducting circuits. It also has a cryogenic pump to pump out the chamber, which is important to use when creating a Josephson junction, to remove any residual water vapor. This is important to remove all water from the environment, as it is a critical condition for obtaining aluminum oxide of good quality and high reproducibility. Usually, after loading the sample, we keep pumping at least for one night, or preferable during weekends. The critical current density of the resulting Josephson junctions depends strongly on this step.

- First evaporation of aluminum

  Once the chamber has been evacuated long enough, we proceed to the first evaporation of aluminum. We perform it with a tilting of $+35°C$ relative to the vertical axis. We deposit $20nm$ aluminum, automatically controlling the thickness and evaporation rate at $0.1nm/s$ with the quartz oscillator built into the chamber.

- Oxide layer formation

  After that, we set table to the position when wafer surface looks up and let oxygen go to the loadlock of PLASSYS. When pressure of oxygen stabilize around $5.00mbar \pm 0.05mbar$ (usually it happens in 50-70 seconds) we wait for $5min$ of static oxidation.

- Second evaporation of aluminum

  Right after this process is finish, we pump oxygen out of loadlock up to the pressure around $1e-5mbar$ and start a second evaporation of aluminum with another tilting angle of $-35°C$. This time, we evaporate a thicker layer of aluminum (reason is illustrated on Fig. 3.13).

  As soon as thickness of second layer reaches 50 nm, we stop the evaporation and finish the process by letting the atmospheric pressure into a loadlock, opening it and taking out the wafer.

As a result of evaporation we have all the mask covered by aluminum as on the Fig. 3.11 for example.

7) Lift-off NMP $80°C$

To remove the mask with aluminum on top, we proceed exactly as for markers preparation. We immerse the wafer in NMP at $80°C$ and keep in the beaker for 5 to 24 hours. Then we finish the process with a stream of NMP from a syringe or pipette, followed by an ultrasonication during 1 minute at 60% power. Then we rinse off the residue by successive rinses in acetone, ethanol, isopropyl alcohol.

After this, the wafer is ready and can be removed from cleanroom to provide quality control tests (look in section 3.7 for more details about it).

3.4.4. Dicing the wafer

If the quality tests show promising parameters, then we saw the wafer to get 5 x $6.8mm$ chips that are compatible for insertion inside our 3D cavity. This step is realized in CIME-Nanotech in Grenoble.

First we need to protect the structures from damage by a layer of polymer, then saw it with a special machine Disco^{TM} DAD 321 Automatic Dicer and after wash the polymer away.

1) Applying polymer shell

For protection, we apply two layers of resist: first we apply the electronic PMMA that we already used before, and then we use the optical one. S1818. The reason of this choice is that the optical resist is more viscous and creates a thicker protective layer, but at the same time it is more sticky, and it can be difficult to wash off. For that purpose, it helps us to have the first PMMA layer.

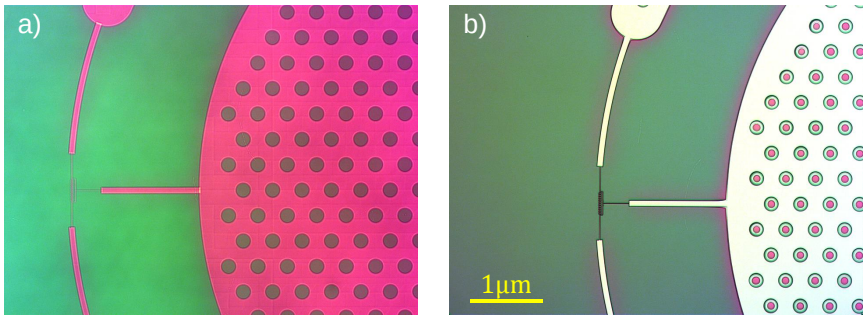

Figure 3.17: Optical microscopy a) - bilayer resist, just exposed by electron-beam. In those places where the resist was exposed, you can see the color change to pink, meaning the change of thickness. b) - Same bilayer resist after development in MIBK:IPA. It's gone where the resist was exposed, baring the substrate. In the places where we want to have holes in the aluminum, we left the resist columns.

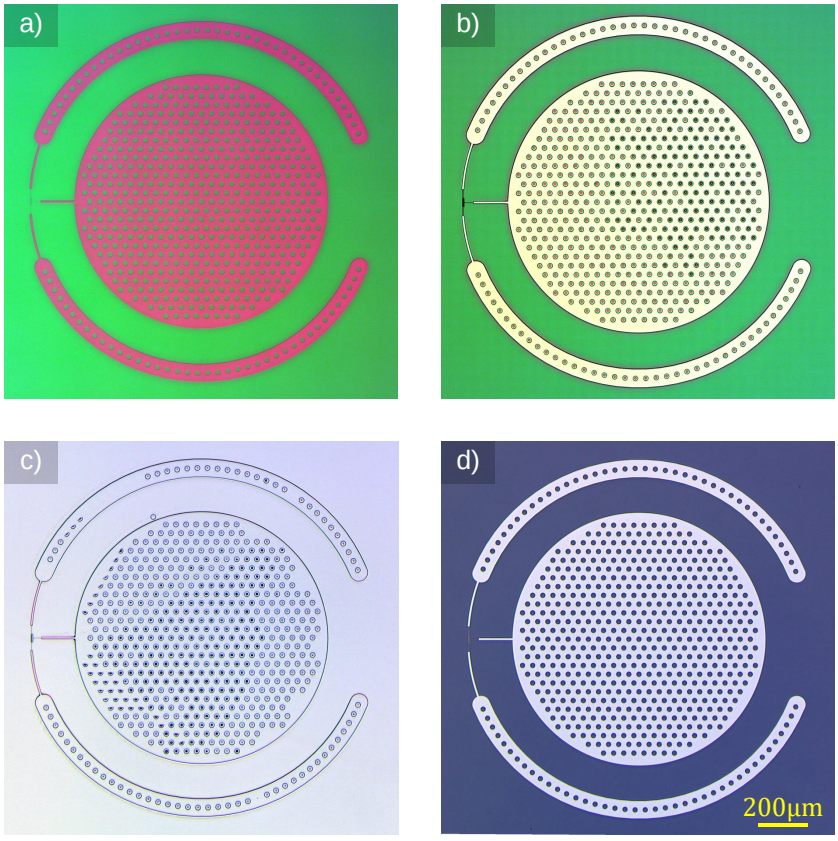

*Figure 3.18: Four optical microscopy pictures with four different steps of fabrication. a) - after e-beam exposition; b) - after development; c) - after metal evaporation; d) - after the liftoff. *Samples can be different. Pictures are given as an example.*

2) Dicing

We also cover the wafer with plastic wrap from both sides in addition to protection by polymer resist. The cut is made along lines oriented along special gold markers. When sawing, the machine cuts a gap in the plate about more than a hundred microns thick, so important structures should not be placed close to the edge of the sample.

3) Cleaning

After dicing, we have a stack of samples with the resist on top and the plastic film glued on. To clean them, we consistently rinse them in three containers of acetone. Finally, we wash each sample in a stream of ethanol and IPA followed by ultrasonication at 20% power for $1min$

3.4.5. Other details about E-beam lithography

This subsection describes the details of electron lithography that must be considered to obtain a satisfactory lithographic result. It includes a description of stitching, start focusing, and electron dose calibration.

Stitching

During electron beam writing, the electron beam is deflected by a system of magnetic lenses to hit a certain point. However, there is a limit to the magnitude of this deflection. In case the structure we draw is larger than these limits, it might be necessary to move the stage where the substrate lies. Thus, it becomes necessary to stitch the two writing regions together. This divides the entire recording area into squares called Mainfields ($300\mu m$ x $300\mu m$ in our case) and Subfields ($20\mu m$ x $20\mu m$). The transition from one main field to the other involves a mechanical movement of the stage. In the transition from one subfield to another, the electron beam is moved by means of coarse deflection coils. The choice of main field size is determined by a compromise between the desire to make it smaller to improve lithographic quality and the desire to make it larger to avoid unnecessary mechanical shifts of the head, thereby extending its life. Reducing the main field helps to minimize aberrations and avoid ruptured structures. Indeed, aberrations are stronger when the point is farther from the center of the field.

Focusing

To avoid errors when stitching the edges of the main fields, it is important that the electron beam is well focused. We need the electron beam to be in focus at each point where we are going to do the lithography. We can't neglect the possibility of surface irregularities. This can be a general bend, a general slope, or local thickness variations. Note that according to the manufacturer's statement, the thickness of our wafer has an error of up to 25 micrometers. That's why we created special gold markers on each chip that the lithographer can focus on. In addition, using these markers we can precisely calibrate the positions of the corners of the chip, which is necessary for accurate orientation during lithography. This not only helps to avoid stitching problems, but is also necessary to obtain a high resolution mask.

Also, to have initially good focus, it's important to set the right attitude of the gun taking into account the substrate thickness. In our case, the right attitude is already calibrated and stored in database under the name "datum8". According to Nanobeam instruction: "the XY stage assembly has a metal block, which has 11 steps with a height difference of 0.11 mm per step. Each step has a focus chip fitted. A datumstep is chosen to match the height of the chuck in use."

We also use a pair of global markers to set a common grid of global coordinates on the wafer. These coordinates are used to find the local markers of each pattern.

Doses

As already mentioned, it is necessary to use the right dose of electrons for writing each given structure. However, we have not yet talked about how exactly this dose should be chosen. For this purpose we usually use a variation of the dose for structures of different sizes, with the subsequent study of the resulting masks. On Fig. 3.19 images from optical and electron microscopes are presented to illustrate the effects of too high and too low dose with explanations. Another example of dose variation when structures are smaller than the micron scale is shown on Fig. 3.20.

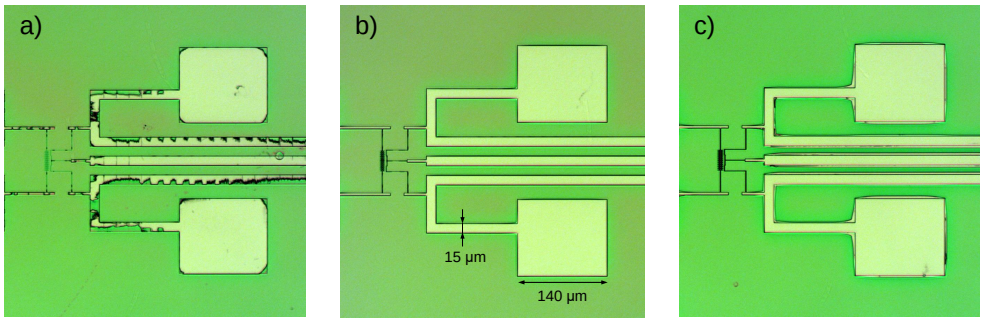

Figure 3.19: Example of same pattern written with different dose. From left to right, we increase the dose. (a) correspond to $10C/m^2$*; (b) correspond to* $13C/m^2$*; and (c) correspond to* $21C/m^2$*. As you can see, if the dose is too low, the structure is not fully written. Especially those areas suffer that experience less proximity effect - corners and edges. If the dose is too high, the size of the illuminated area increases due to the same proximity effect. *This particular pictures are made after cold development as a part of new recipe (see section 3.6). So optimal dose is not the same as in standard recipe*

Current of Nanobeam

Regarding the current we use for writing, it is simply that the greater the current, the faster the writing on the one hand and the less accurate the resulting structures on the other. So we apply current of $1.3nA$ for Josephson junctions and $26nA$ for large pads. Also, it should be taken into account that using the electron gun in the high current mode leads to its heating. Due to that, a waiting time of about $10min$ to $60min$ is needed to cool down the e-gun and recover a stable current. So we always start with small structures at a small current. And when writing is finished, we always switch back the electron gun to low current mode.

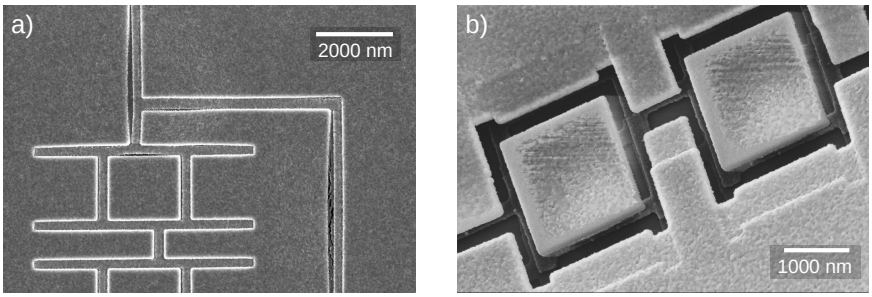

Figure 3.20: Another example of different electron doses applied for small structures. Both images are scanning electron microscopy after aluminum evaporation and before liftoff. On figure (a) dose was $12.1C/m^2$*, on (b) it was* $18.5C/m^2$*. In the left picture, you can clearly see that the gap in the mask was not formed and aluminum covers the entire surface. It means that the mask did not show up completely - obviously the dose was insufficient. The picture on the right is a great example of what a mask with aluminum applied to it should look like. Through the slits in the mask, you can see the surface of the substrate with the Josephson junction applied to it. In the areas around the slits, you can see the surface subsidence due to the undercut. *This particular pictures are made after cold development as a part of new recipe (See the recipe in section 3.6). So optimal dose is not the same as in standard recipe*

Nanobeam file system

The resulting qubit design results in a file with a .gds (Graphic Database System) extension. In the microelectronics industry, .gds files are typically the end product of the integrated circuit design cycle, and they are sent to factories to make masks and then chips. This type of file contains layers and nested cells. In the design, we used different layers to denote different doses during lithography and cells to divide the design into logically separate elements. All shapes in this format are specified as a chain of dots. You can use the free KLayout editor to view this format.

But since the electronic lithographer does not recognize the .gds format, the files of this format must be converted to a special format understandable to the lithographer - so-called .npf. For this purpose, a small utility written in Java is used.

Also, a lithograph instruction file with the extension .njf is needed for writing. It can be edited as a text file. This file specifies the global focus, position of the global and local marks, the path to the various .npf files and a list of doses associated with each layer used. We use separate .njf instruction files for two current modes we use. While working on my PhD, I generated .njf files automatically along with the design files.

The Nanobeam Batch File (.nbf) is used to execute multiple .njf files one after the other. The desired write parameters, such as acceleration voltage and write current, are set in this file. Instructions for autofocus, beam calibration and even loading/unloading chunks can also be set in it, which can be useful if writing on multiple wafer is performed. The batch file can be set separately for each .njf file, or it can be the only file in a series.

3.5. Issues of nanofabrication

In this section, we will describe the unwanted effects that we found as a result of fabrication. We will consider each of them in terms of probable harm to our superconducting structures. Then we will find out which of these effects can be avoided, and what needs to be changed in the fabrication recipe to do so. The effects described in this section are not unique in themselves. This has been repeatedly observed both by my colleagues at the Neel Institute and by researchers in other laboratories. This is why we find it an interesting topic to discuss here.

3.5.1. Veil of Death

In each case of fabrication according to the standard recipe, studying the sample in the scanning electron microscope, we invariably found dark areas around the aluminum structures in those places where the undercut was made.

The effect of this subsection is well represented in Fig. 3.21. This darkening has been repeatedly described in the literature and has the pathos-like name "Black Veil of Death [133, 132, 134, 135].

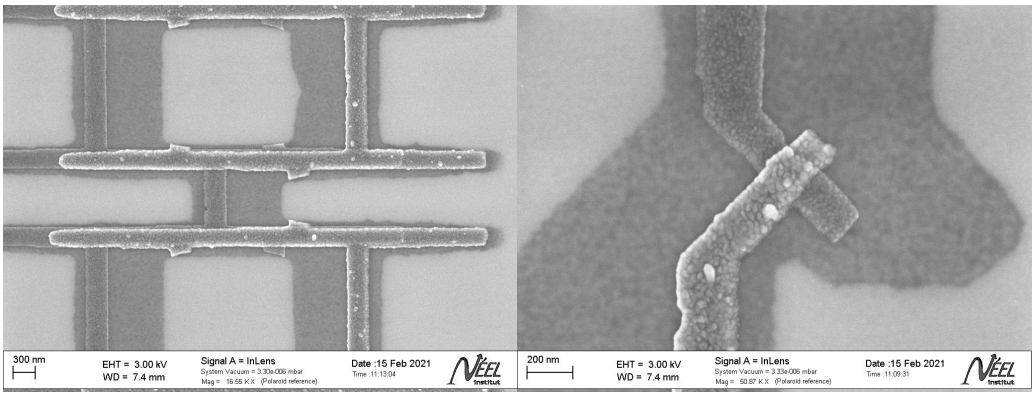

Figure 3.21: A prime example of the Veil of Death effect found in areas where undercut took place. Picture obtained with scanning electron microscopy of wafer8

In the first mentioned paper [133] this darkening was described as an extremely thin film (about $1nm$ thick) and two assumptions were made about the nature of this film: either it is fully oxidase aluminum scattered by residual pressure due to out gassing of the resist; or it is some sort of organic residue from the development process. As reported in the same paper, this phenomenon does not cause the qubit to malfunction, but it has been suggested that it could spoil the decoherence time.

The second paper [132] reports the successful use of oxygen plasma to remove this film from the surface. It also assumes that it is a film of aluminum or aluminum oxide that falls from the side walls of the resist to the device and can be a source of dielectric losses.

The third paper [134] offers a different explanation for the appearance of the Black Veil of Death. The authors of this paper insist that this film is a carbon contamination formed either by a chemical reaction of the resist wall during aluminum evaporation or by the collapse of the resist wall during liftoff. It also confirms the successful use of oxygen plasma for the removal of these contaminants.

The fourth article [135] is devoted to improve the quality and reproducibility of Josephson junctions fabrication. This paper also describes a similar phenomenon - residual resist contaminating areas around aluminum structures. This work convincingly shows that this contamination is formed before evaporation. The contamination was eliminated by using oxygen plasma etching or chemical washing of the mask. This brings us to the important question regarding the Veil of Death - is this film on the surface of the applied metal, or does it lie between the substrate and the aluminum? In the first case, it can simply be scraped off with oxygen plasma, as it has already been shown in the aforementioned works. In the second case, however, cleaning with oxygen plasma will only remove the visible areas, leaving the organic compounds lying directly beneath the aluminum, which is bad for the coherence time.

During my PhD, after observing this phenomenon of Veil of Death, we decided to study it in more detail.

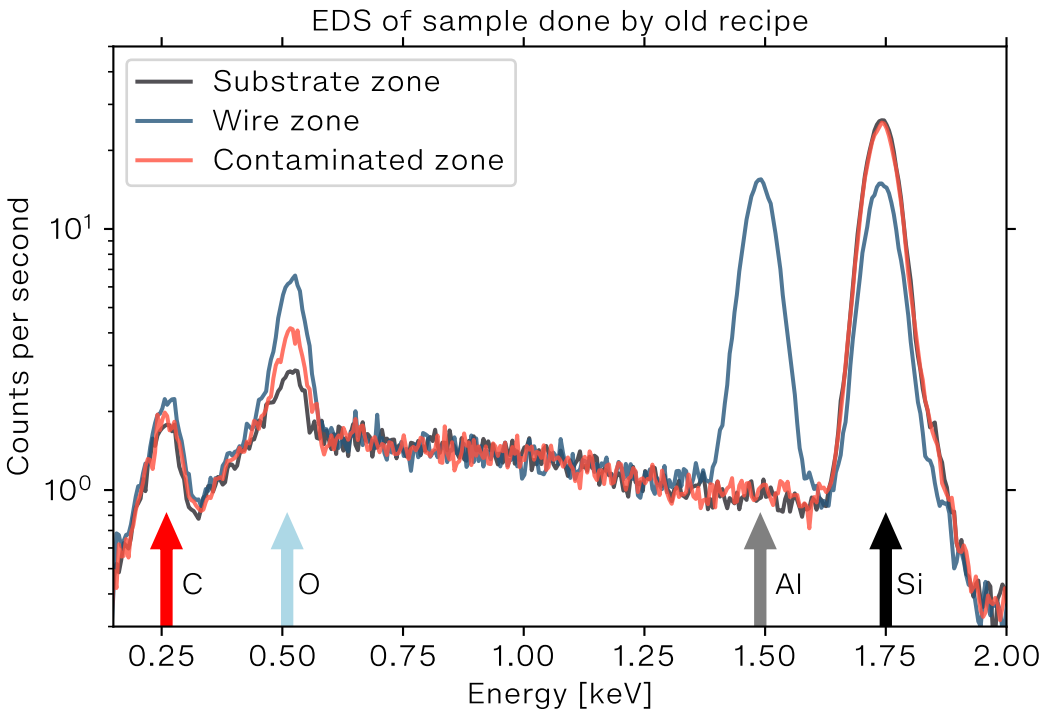

Figure 3.22: Energy-dispersive X-ray spectroscopy made in three areas of the chip: on a substrate, on aluminum layer and on a Death Veil made on a sample fabricated by old recipe. What is worth noting, an increase in the signal is in the place where the Veil of Death is visually observed in the $150keV$ *energy region corresponding to carbon and* $200keV$ *energy corresponding to oxygen.*

First, an Energy-dispersive X-ray spectroscopy (EDS) of this film was performed using a scanning electron microscope (see subsection for more details on this device). From the results of the analysis, we can conclude that the composition of this film contains mostly carbon and oxygen, but there are no distinguishable traces of aluminum or nitrogen. We can conclude that the Veil of Death is a residual electron resist. The results of the analysis are shown on Figure 3.22 and on Fig. 3.23

It is unclear to me how exactly this film is formed. However, ways have been found to get rid of this. First, the method of etching in oxygen plasma proved to be excellent

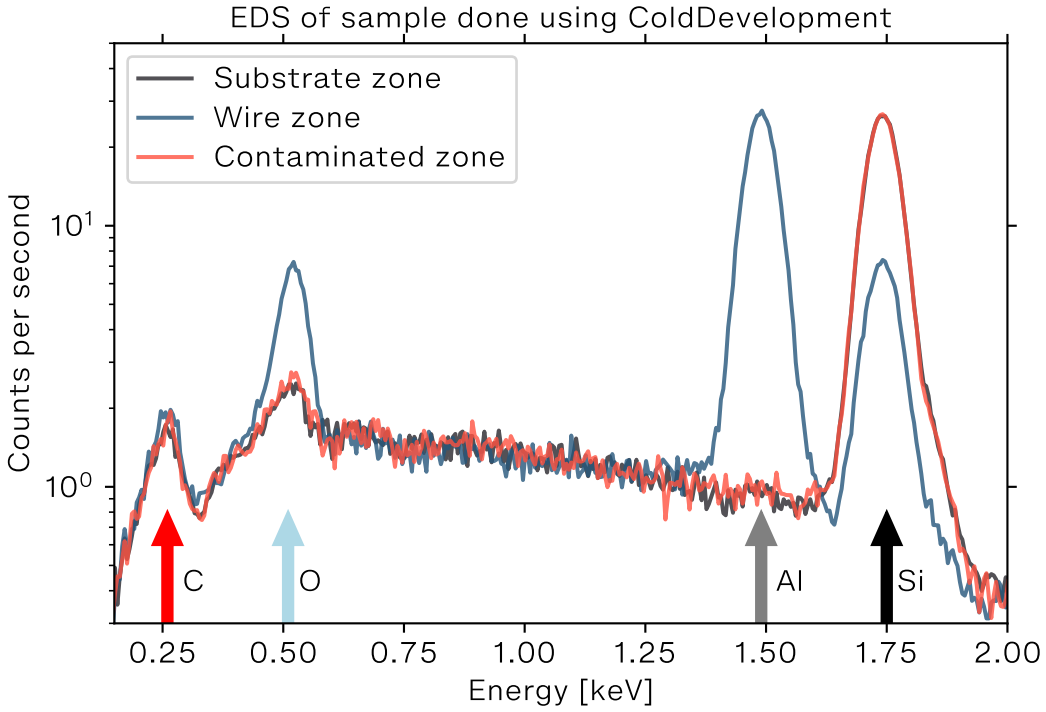

Figure 3.23: Energy-dispersive X-ray spectroscopy made in three areas of the chip: on a substrate, on aluminum layer and on a Death Veil made on a sample fabricated using cold development in IPA-DI mixture.

in our case: three minutes at $10W$ power was enough to completely eliminate the Veil of Death. The results of scanning electron microscopy before and after cleaning are shown on Fig. 3.24.

Secondly, more importantly, the application of the cold development in IPA-DI mixture process does not seem to cause this Veil of Death to appear and SEM observation no longer detects the veil. On Fig. 3.25 you can see the difference between the resulting structures after the standard fabrication recipe and the recipe involving a cold development process

It was found that holding the liftoff with the wafer upside down sometimes reduces the effect.

I do not have an exact answer as to how this film is formatted. I can only list the facts that I know:

1) Veil of Death always fills the resist cavities under the undercuts

2) The appearance of this film occurs with both Bridge free technique and Dolan bridges.

3) Especially stable is the edge of this film in those places where it is close to the resist wall. This is also visible on Fig. 3.26 c) and d).

4) Several times I observed a partial separation of this film from the surface of the substrate. Even then, however, it did not wash off completely, continuing to cling by its edges to the structures. See few examples on Fig. 3.26 a) and b). This behavior is also visible in this work [132] (Figure 4.5).

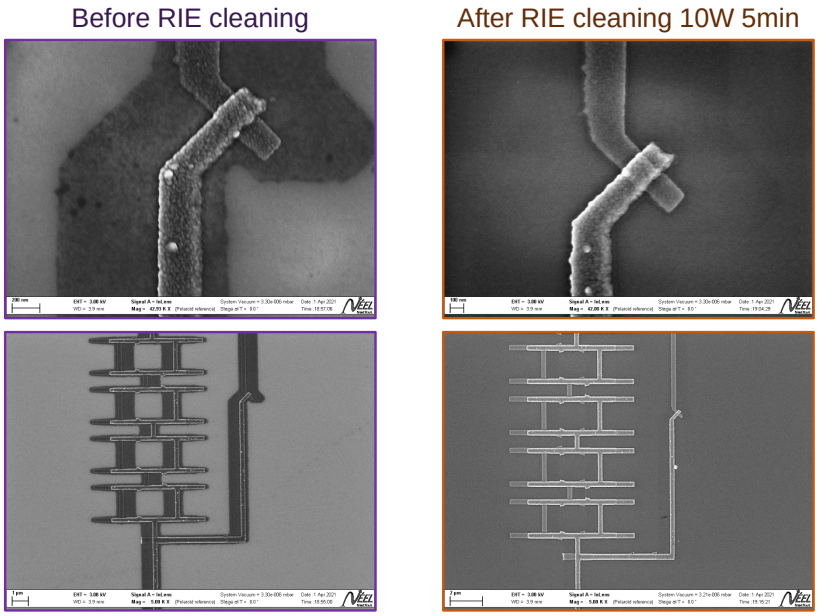

Figure 3.24: Two samples from same wafer8, observed by scanning electron microscopy. One on the left was not cleaned, and the one on the right was cleaned with $10W$ *oxygen plasma for* $5min$*.*

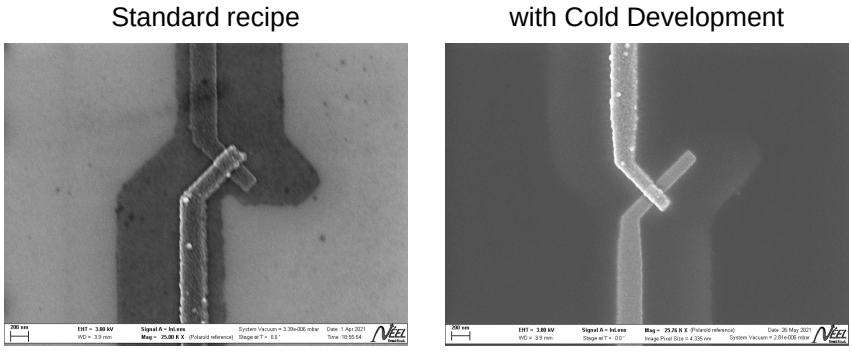

Figure 3.25: The SEM image of a Josephson junction made according to the standard recipe is on the left. A similar Josephson junction made using cold development is made on the right. In both cases, no additional cleaning techniques were used. However, the Veil of Death was not detected in the image on the right.

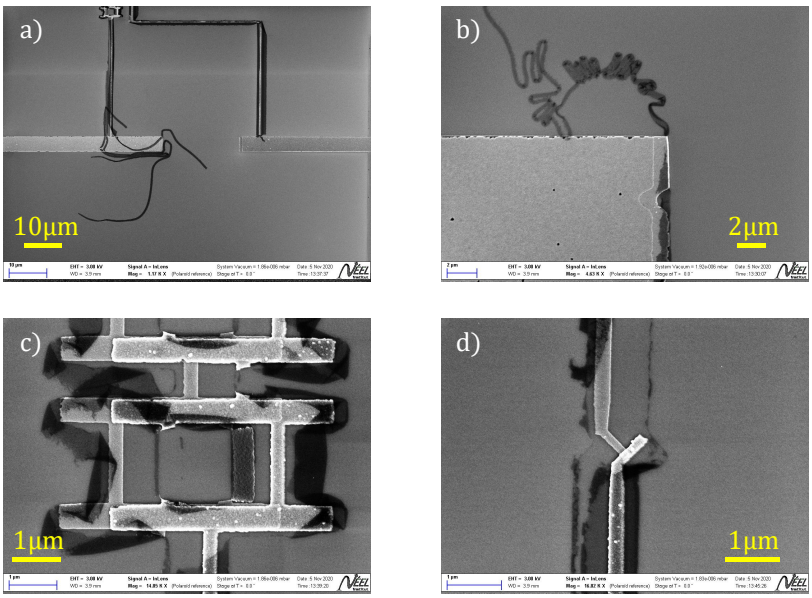

Figure 3.26: An example of Death Veil accidentally found in violation of the standard prescription (ultrasonication was skipped, and the wafer had time to dry after liftoff. Then it was placed again in NMP for 15 hours followed by standard ultrasonication and rinsing). It is remarkable that here we see the film similar to Veil of Death has peeled off and is hanging on the corners of the aluminum structures. Such behavior may support a version of Veil of Death formation in the process of liftoff.

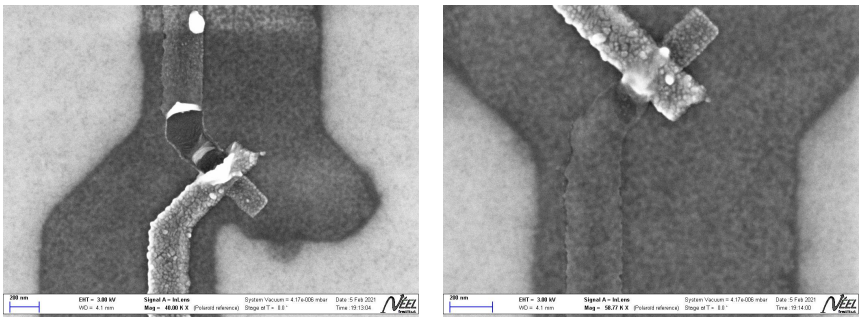

Figure 3.27: Scanning Electron Microscopy of wafer7 after DC-measurements. Several junctions were exploded with high voltage, and the aluminum was vaporized. The surface of the substrate was exposed and the Veil of death was found on it.

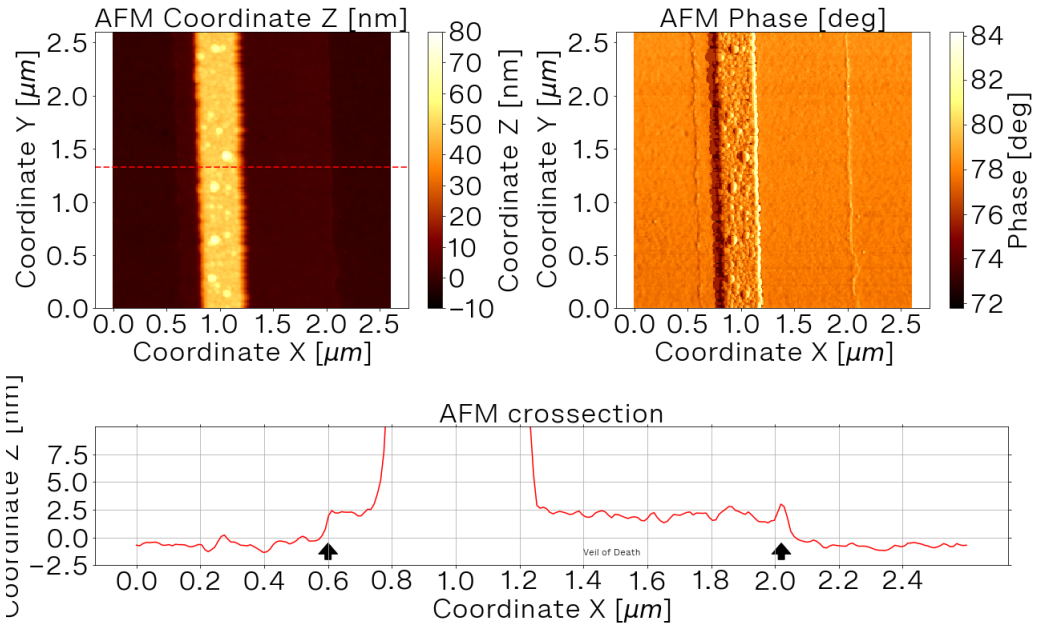

Figure 3.28: Measurement of the thickness of the death veil using atomic force microscopy. Sample w8ch29 (old recipe, no cleaning).

5) The Josephson junction exploded during DC measurements was examined once. In the place where the aluminum had evaporated, exposing the substrate, the Death Veil film was also present. It could be evidence of the formation of this film during development and not during liftoff. The result of Scanning Electron Microscopy after explosion if presented on Figure 3.27

6) This version of the formation of Death Veil is also supported by the fact that the film disappeared when the process of developing was changed.

7) It has been proven that the film is composed of carbon and oxygen.

8) It does not wash off with alcohol or acetone or NMP, even with a long exposure (more than an hour).

9) The thickness of the death veil measured by AFM was around $2nm$. See plot on Fig. 3.28

3.5.2. Black specks

Examining the finished aluminum structures under an optical microscope, we repeatedly found black dots uniformly covering the large aluminum elements. These dots were particularly well distinguished under a dark-field microscope. Examples of obtained images are shown in Fig. 3.29. The version that it was dust was quickly rejected, as these dots were never observed on the surface of the substrate, nor they were removed by either chemical or mechanical methods.

This effect were constantly observing for all wafers prepared by standard recipe. Moreover, many other colleagues working with me in cleanroom told me that they have the same trouble. For example, you can see a similar problem in Figure 4.10 in the thesis of Luca Planat [136], who uses a similar recipe in the same clean area.

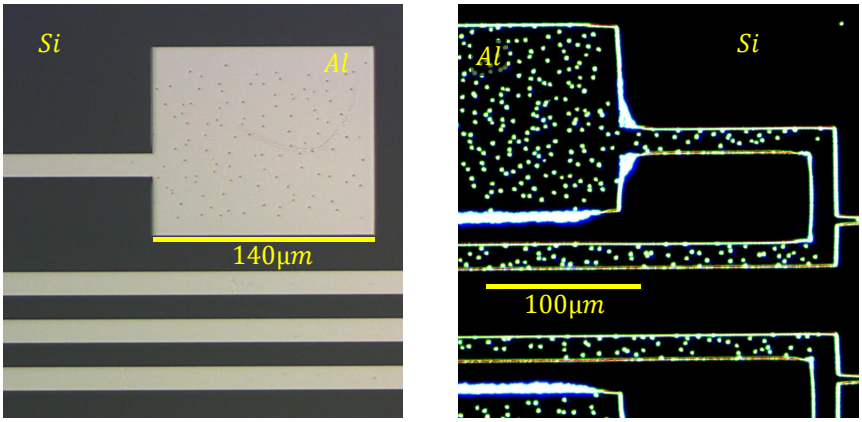

Figure 3.29: Optical microscopy of aluminum pad with Light Field on the left and Dark Field on the right.

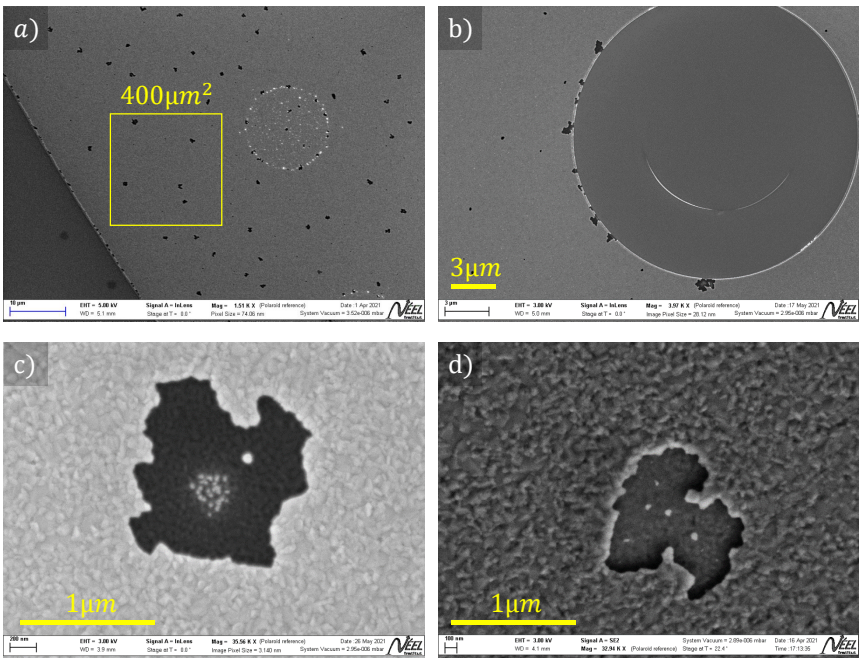

Figure 3.30: A few examples of detected "specks" on aluminum. Scanning electron microscope images. From picture a) we can conclude about the approximate density of the spots. Figure b) illustrates the tendency of these spots to form more often on the edges of structures. Pictures c) and d) show an enlarged image of the spot. All except d) are made with the detector located quite far away from the sample, while d) shows an image of the detector located closer. This gives more information about the geometric shape of the sample under study.

Studies with a scanning electron microscope allowed us to look at these points in more detail. See Fig. 3.30. The size of such specks varies from $100nm$ to $1\mu m$. The unusual shape of the edges is also noteworthy. Speck density varies from sample to sample, but is approximately 0.01 to 0.05 pieces per square micron.

From the beginning trying to understand the nature of the observed spots we assumed two versions: (i) contamination, perhaps on the surface of the aluminum or in the material itself, (ii) a hole in the aluminum - something like a fallen out grain. The second version is supported by the jagged shape of the edges. The comparison of pictures c) and d) on Fig. refsem$_p$*owder*$_1$*isalsoagoodindicatorinfavorofthesecondversioncomparedtothefirst.Whileth*
dimensionalshapeoftheobjects, andintheimageobtainedfromthisdetectorthespecknolongerlookslikeas

Another indication that this is a pit and not contamination is that sometimes bright areas are noticeable in the center of the spot. This we can clearly see on picture c) in Fig. 3.30. Probably in these places the hole is less deep and the electrons reach the detector.

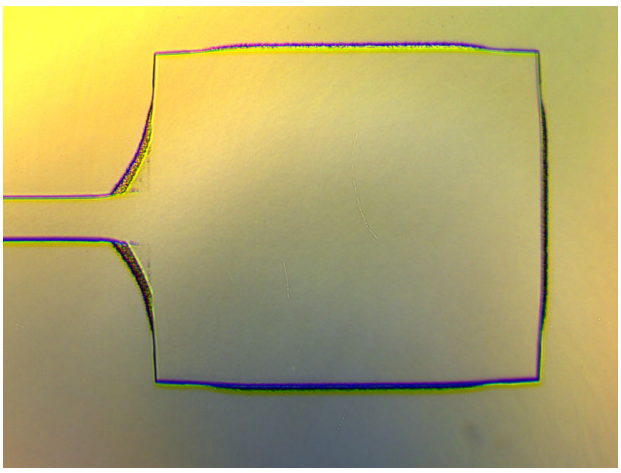

Figure 3.31: Light-field optical microscopy image obtained before the liftoff. The mask is completely covered with aluminum. No dark spots are observed. Color aberrations are caused by the very narrow aperture we used to reliably detect any possible defects on the surface.

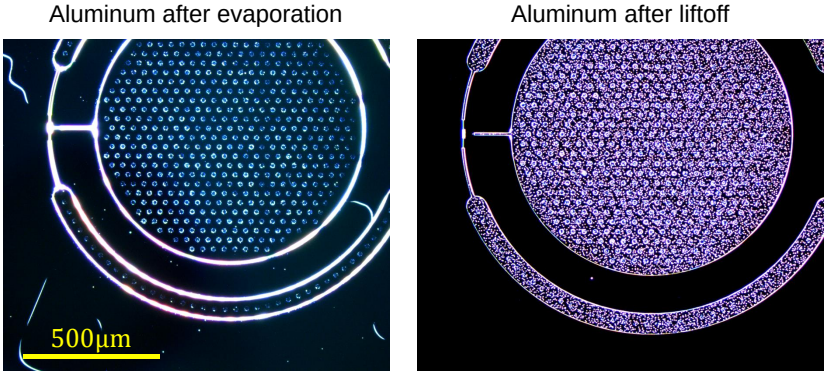

Figure 3.32: Comparison of optical dark-field microscopy images obtained before and after the liftoff. In the first case, only insignificant glare is noticeable, mainly on the edges of the patterns. In the second case, the aluminum is covered with spots.

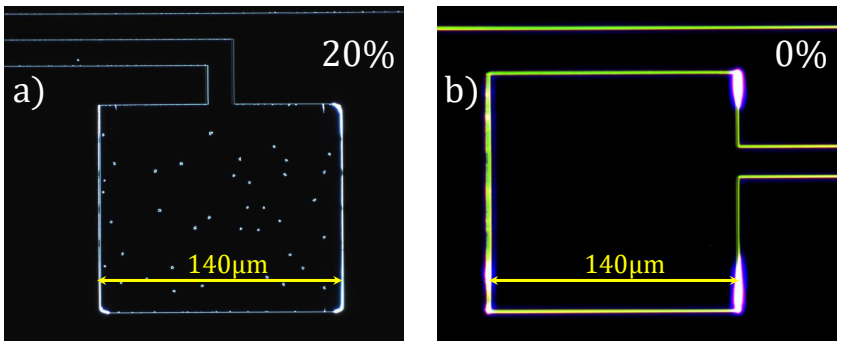

Figure 3.33: Comparison of aluminum pads obtained by fabrication a) - with the use of ultrasonication with reduced power (from 60% to 20%); and b) - without the use of ultrasonication at all. Dark-field optical microscopy. When the ultrasound power is reduced, a decrease in spot density to about 0.002 spots per square micron is noticed. When canceling ultrasonication completely, no specks were found.

Regarding the formation of these specks, we know that before the liftoff, the aluminum looks perfectly clean. (See Fig. 3.31). However, after the liftoff, in places where the aluminum had just been smooth and clean, we see these indentations. (See Fig. 3.32) This led us to suspect that the depressions are the result of the application of ultrasound during the liftoff. As a result of poor local adhesion, pieces of the top aluminum layer separate under the action of ultrasound.

To combat this effect, we tried reducing the power of the ultrasound, trying to leave it sufficient for a successful elevator. As a result, a marked improvement was noted (see Fig. 3.33. On this figure, there are two microscopic pictures of the same aluminum element of two different wafers are shown. The left image corresponds to the wafer that we subjected to ultrasonication with three times less power than in the standard recipe during liftoff. The right image corresponds to the wafer, for which we did not do ultrasonication at all during the liftoff. The two wafers were made simultaneously with an identical design and identical recipe, except that the first was also etched in hydrofluoric acid before sputtering. However, this difference should have no effect in our opinion.

3.5.3. Metallic islands around junction

Occasionally, as a result of fabricating a Josephson junction using Dolan bridge, we found small aluminum islands or as we call them within the group - the mustache, next to the junction. (See example on Fig. 3.35) There is no doubt about their origin: this is the result of the fact that the metal, which was supposed to lie completely on the resist wall, was partially on the surface of the substrate. The appearance of these islets can be predicted using the Formula 3.11.

We believe that these metal islands may contribute to decoherence because they are in the vicinity of Josephson junctions - where electric fields are very strong. In any case, we don't want unnecessary elements around junctions, so we prefer to avoid these islands.

As you can see from the Formula 3.11, there are three ways to get rid of this undesirable effect. We can decrease the width of the wire, but this will also change the

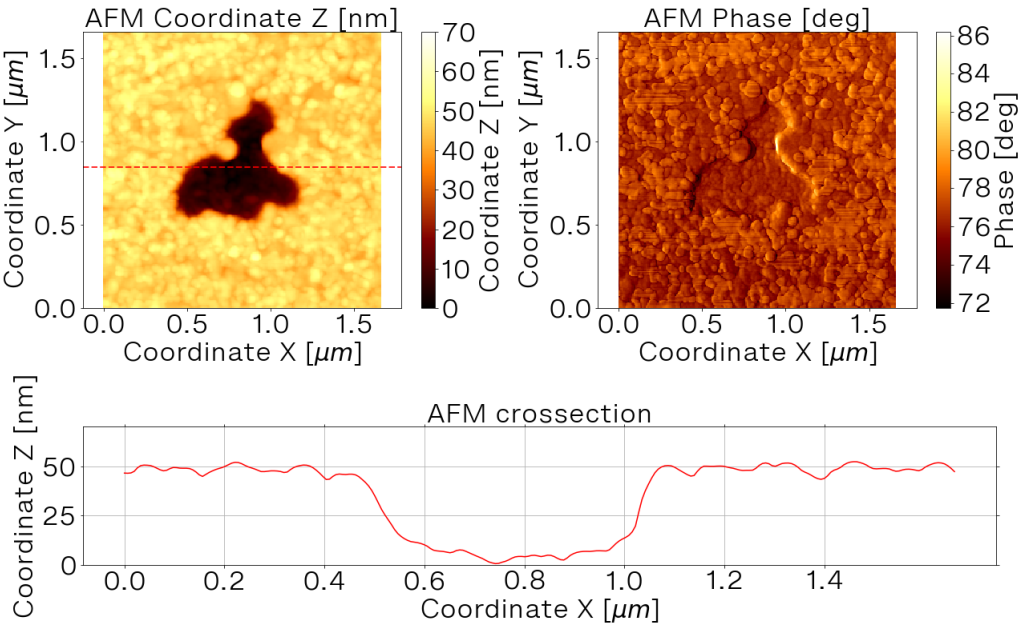

Figure 3.34: AFM picture

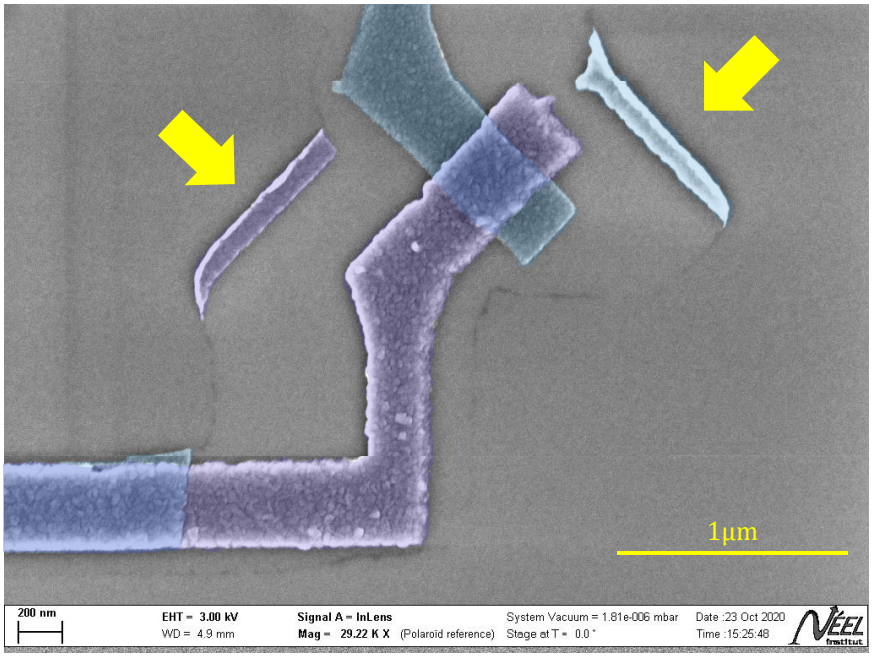

Figure 3.35: Example of aluminum islands around junction (marked by yellow arrows). The blue false color indicates the result of the first evaporation. The purple one is for the second. Scanning electron microscopy image.

value of the junction critical current. We can also reduce the spray angle or increase the thickness of the resist. We chose the latter option. To increase the thickness of the resist, simply reduce the centrifuge speed during spin-coating. Thus, the centrifuge speed is reduced in the new recipe.

3.5.4. Unexpected area of small junctions

One of the challenges on the way to obtaining the target parameters of the qubit was controlling the area of small junctions. A discrepancy was found between the real dimensions of the junctions and the value predicted by the Formula 3.15.

On the graph on Fig. 3.36, each point corresponds to a junction, the area of which was measured using SEM. Different colors indicate different fabrication runs. Each time we fabricate a new wafer, we measured area of junctions using SEM. You can see that all the points are far from the dashed line, indicating compliance with expectations. However, all the points still lie on the same line, which we fitted with a linear dependence. This empirical dependence was found to be $y = 1.34x + 0.015$, where x, y are in $[\mu m^2]$ units. Remarkably, this law is satisfied over a wide range of junction areas. And it also remained unchanged for different runs of the fabrication (including the variation of the mask thickness). It means that the area of such junctions is still predictable even when using different mask thicknesses.

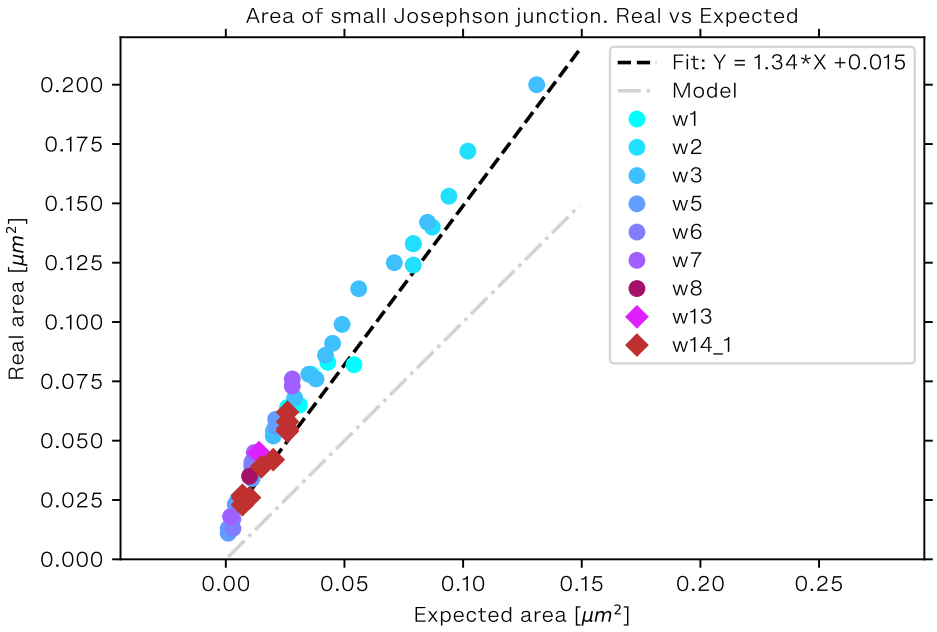

Figure 3.36: Dependence of the real area of the Josephson junction made by Dolan bridge technique on the expected area, according to the model. Each point represents one junction. The different colors indicate the different runs of the nanofabrication. Real area is measured using scanning electron microscopy. The round shape of the dot means a standard recipe. A diamond-shaped dot means using a new recipe of nanofabrication.

Discrepancies were also found for the lengths of large crossings made using the bridge free technique. However, due to their large size, resist thickness-related effects

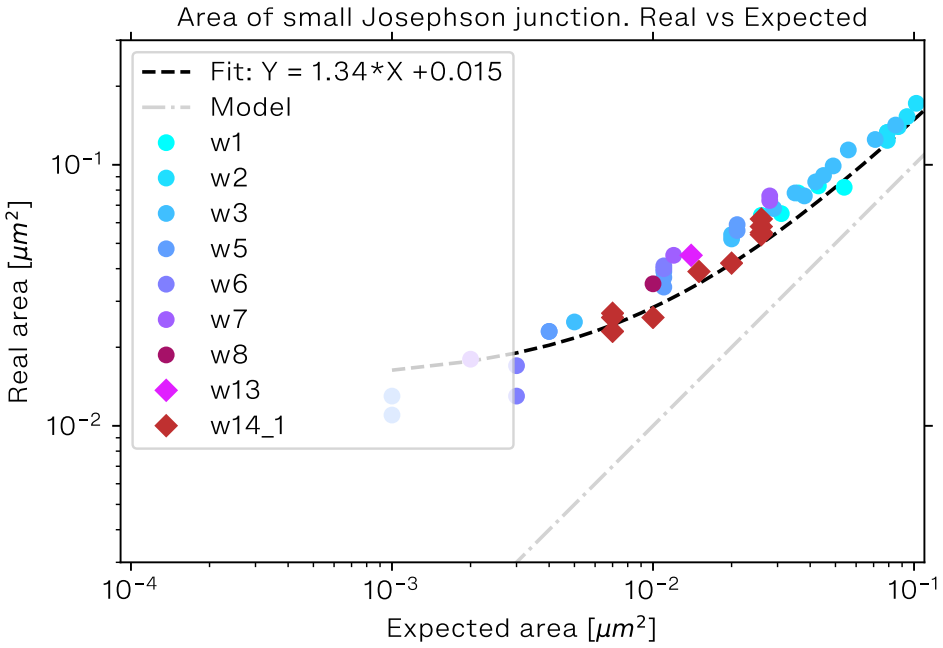

Figure 3.37: Same plot as on Fig. 3.36, but in double logarithmic scale.

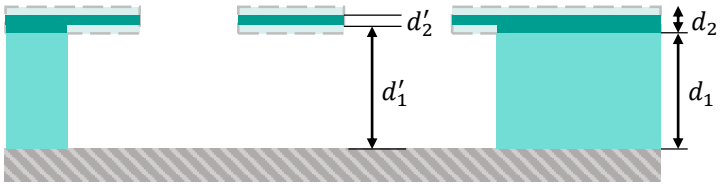

Figure 3.38: Illustration of the idea of thinning the top layer of resist during development or oxygen-plasma etching.

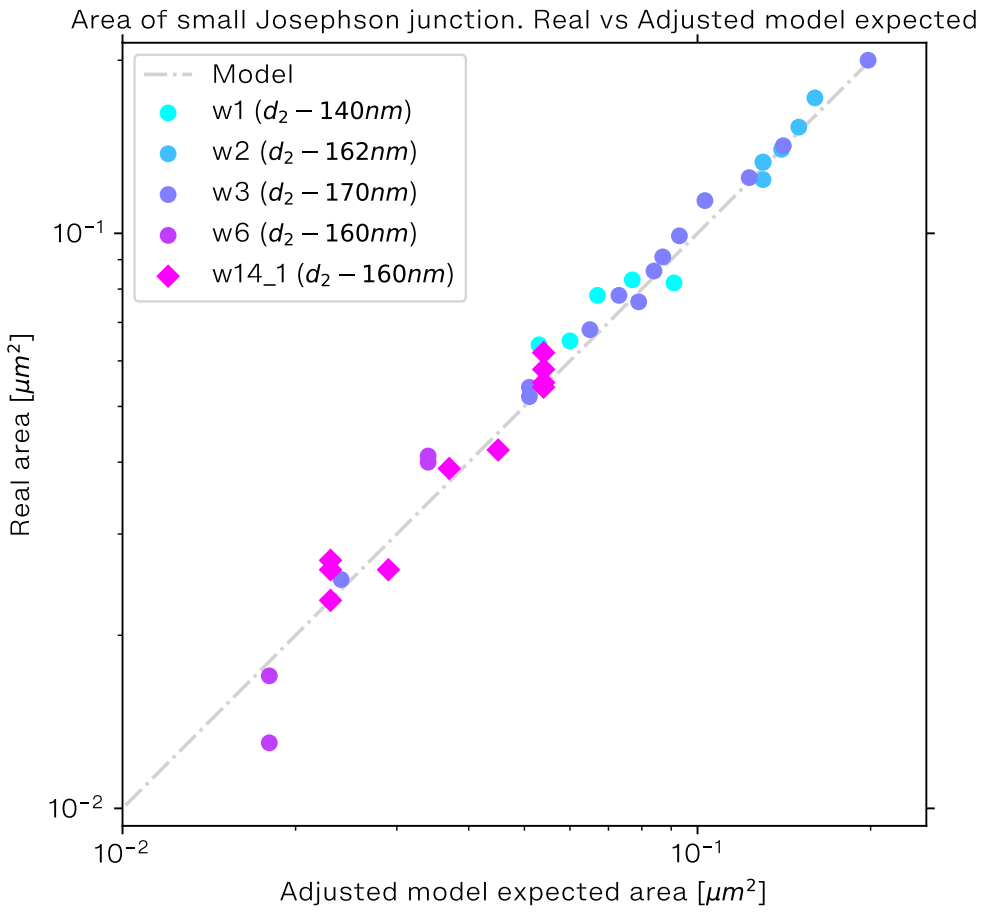

Figure 3.39: Adjusting the thickness of the upper resist layer when calculating the junction area. A good match with the real area of junction is achieved if the thickness of the upper layer of the resist is reduced by $140 - 170nm$.

play a much smaller role (usually a few percent), while for small Dolan bridge nodes, the difference can be more than 100

As for the source of this error, it has not yet been accurately determined. There were different versions, including: *(i)* sagging of the Dolan bridge; *(ii)* thinning of the resist top layer during the development process (and/or oxygen etching); *(iii)* an error in the resist thickness measurement. The first hypothesis was rejected after examining the mask with aluminum applied to it using SEM. As for the last two hypotheses, which is shown in Fig. 3.38, it was found that if the thickness of the upper resist was $140 - 160nm$ less, we would get a pretty good agreement with the theory.

Nevertheless, additional measurements of the mask thickness after developing and after etching showed no change in thickness. In addition, according to the simulations, thickness of top layer must be reduced by around 60% - 70% to achieve consistency with the model, which is very significant.

3.5.5. Aluminum grains

Another interesting effect we observed in EMS is shown in the following Fig. 3.40.

Whenever we look at a Josephson junction, we can easily distinguish the thin lower layer of aluminum from the thicker upper layer by the characteristic grains on the surface of the second layer.

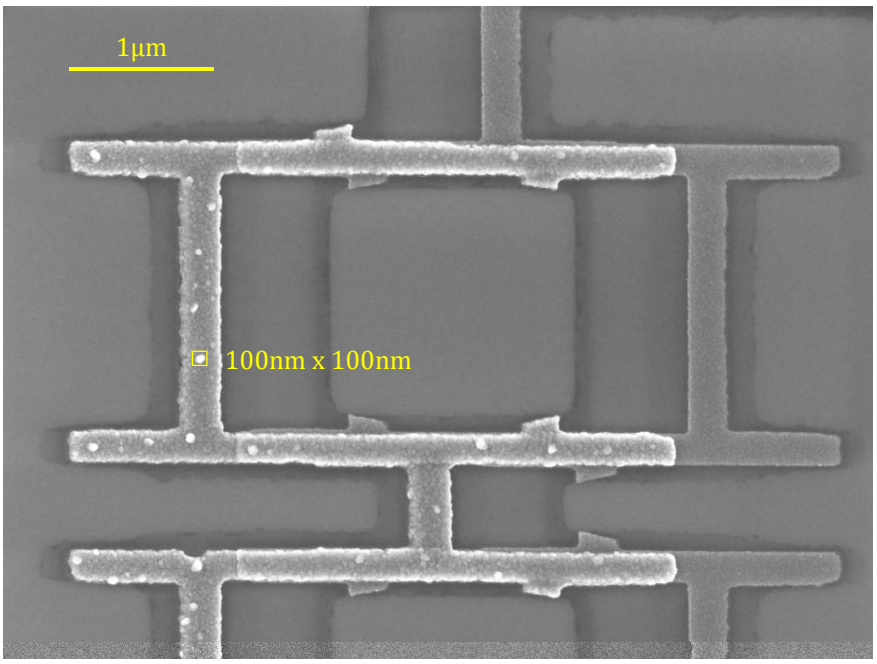

Figure 3.40: Comparison of the first (20 nm) and second (50 nm) aluminum layers. The first layer looks clean and smooth, while the second one has individual, coarse grains smaller than 100 nm. Scanning electron microscopy of sample from wafer1.

Perhaps it is the aluminum grains that are more likely to appear when the aluminum is thicker. In addition to thickness, two other factors can distinguish these two layers of aluminum and can cause this apparent difference. *(i)* Initially, the first layer was oxidized in pure oxygen under controlled pressure in the chamber, and the second layer was removed from the chamber immediately after sputtering and received its oxide under atmospheric conditions. *(ii)* Secondly, the chamber was pre-vacuumed to

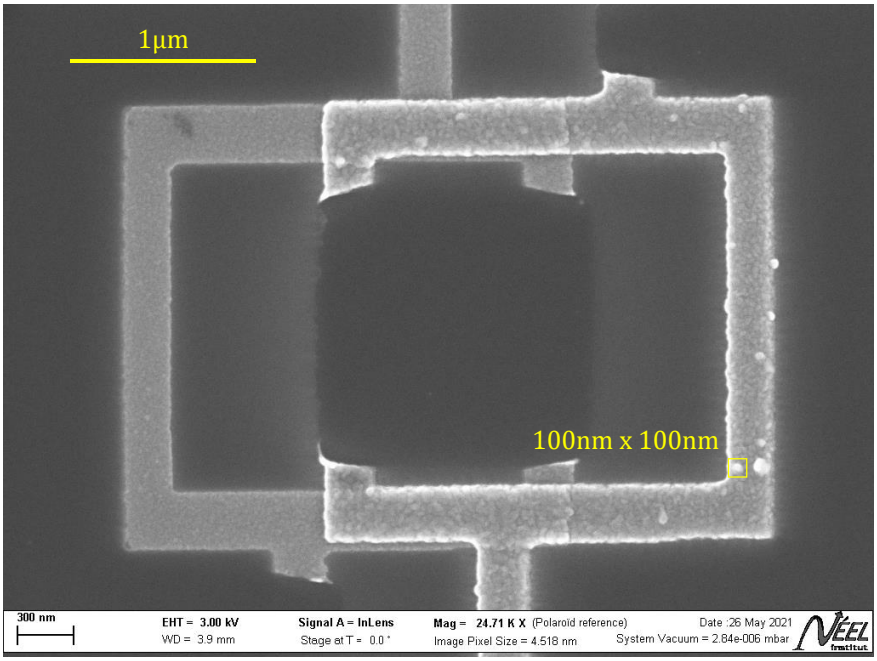

Figure 3.41: The same effect was observed after using a new recipe that included an additional pumping of the chamber after oxidation of the first layer in order to apply the second layer under cleaner conditions, as well as oxidizing both layers of aluminum under the same conditions. Scanning electron microscopy of sample from wafer14.

a deep vacuum for more than eight hours before the evaporation of the first aluminum layer. The second layer, on the other hand, was applied after oxygen was pumped into the chamber and then roughly evacuated with a turbopump in a few minutes.

To test these two hypotheses in the new recipe for aluminum deposition, we use *(i)* an additional evacuation of the chamber after the oxidation of the first layer, and *(ii)* an additional oxidation step for the second layer. Nevertheless, even with the new prescription, this effect was still observed.

3.6. New recipe of nanofabrication

3.6.1. Changes in recipe

Markers by optical mask

Since the size of gold markers for the orientation of the electron lithograph does not exceed 8 µm, nothing prevents them from being produced using optical lithography. This saves a lot of time, especially if mask lithography is used. In our case, the production time of one wafer with markers is reduced from about 30 hours to 5 hours. Such a long time is due to the fact that in our institute the electronic lithographer is loaded and unloaded once a day. Of course, this reduces the resolution of the resulting markers, but as experiments have shown, this does not affect the final quality of the lithography as long as the lithographer is able to recognize the markers.

Silicon oxide removal with HF

We added this stage in order to reduce the number of TLS (two-level systems) coupled to the qubit, to improve its coherence. It is known that many TLSs are stored in silicon oxide layer. This technique is widely used in the field to achieve this goal [126].

We etch with HF twice: first we etch the bare wafer before starting work, and then we etch the silicon under the mask just before applying the metal. The mask is practically unaffected by this etching. Hydrofluoric acid reacts strongly with silicon oxide and very weakly with polymers due to its chemical properties.

After etching, it is critical to load the wafer into the vacuum chamber of the evaporator as quickly as possible. In my work, I stored a wafer into the vacuum exicator for one hour between the etching and loading. I estimate that the wafer spent no more than 2 minutes in atmospheric conditions before evaporating.

Cold development of the mask

It is known that the use of cold development allows you to achieve greater resolution in lithography [137, 138, 139, 140]. Since it is important for us to make small junctions as uniform as possible, we decided to try this method. Comparing the results of the resulting structures, we, in turn, also confirm this observation. Compare, for example, Figures 3.40 and 3.41. In the first case, an old recipe was used, in the second case, a new recipe with a cold developer (a cold mixture of IPA and DI-water). You can see that the edges of the structures are smoother, and the corners are sharper.

An unexpected bonus was that, according to our observations, the Veil of Death 3.5.1 effect almost never occurs when cold development is used.

Increased thickness of first layer of resist

We decided to increase the thickness of the bottom resist layer to get rid of the metallic islands described here 3.5.3. To do this, we slightly reduced the rotation speed of the centrifuge (from $4000rpm$ to $3800rpm$).

Evaporation changes

As discussed above, the cleanliness of the chamber, and especially the absence of traces of water in it, is extremely important when making Josephson junctions. Therefore, it was decided to include an additional pumping step in the evaporation recipe by evaporating titanium onto the chamber walls before the first and second application of aluminum. This method is widely used by many groups for the final increase in vacuum depth [126].

It was also decided to oxidize the second layer of aluminum, too, by pumping oxygen into the chamber at the end of the process. This decision was made out of general considerations. It seems better to let pure oxide form under controlled conditions than natural oxide under atmospheric conditions.

Advanced liftoff

After we found out the nature and cause of the hole formation described in the subsection 3.5.2, we decided to reduce the power of ultrasonication during liftoff from

60% to 20%. Unfortunately, the complete abandonment of this procedure leads to small pieces of aluminum getting permanently stuck around critical structures. Also, without ultrasonication it is extremely difficult to tear off the resist columns where the holes for vortex trapping are designed.

To keep the liftoff process reliable in spite of the decreasing power of the ultrasound, we do it longer (usually all night). If necessary, we also change the solvent to a new, clean one after a few hours.

We also began to make a liftoff by putting the wafer face down with the edges against the spherical glass. The idea behind this method is that anything that peels off the wafer tends to fall down, away from the surface of the sample, under the action of gravity. It's hard to characterize how much it really improves the quality of the liftoff. In any case, it costs nothing to apply it.

Final oxygen plasma cleaning

As it was found out, the final cleaning with oxygen plasma can effectively remove the Veil of Death film from the sample surface (except where it is sealed with aluminum on top). See the details of cleaning by oxygen plasma in section 3.5.1. In any case, it seems like a good idea to be guaranteed to remove the residual resist after sawing the wafer.

3.6.2. New recipe description - golden markers

1) Wafer preparation

   Prebaking the wafer $2min$ at $180°C$ on a hot plate.

2) Optical resist S1805 applying

   Spin-coating of S1805 optical resist using a centrifuge at $4000rpm$ with $4000rpm^2$ acceleration for $30s$.

3) Baking the resist

   We bake the wafer with resist on the same hot plate for $1min$ at $115°C$. The measured thickness of resist layer was approximately $2\mu m$.

4) Ultraviolet exposure

   We expose the optical resist through the static optical mask (see subsection 3.2.2) using the Mask Aligner UV KUB 3. For exposition, we use power of 25% during 25 *sec*.

   The static optical mask is a glass plate with a layer of chromium etched by lithography. It was prepared for this project using laser lithographer Heidelberg instruments "DWL 66fs".

5) Development of the mask

   To develop optical resist, we use Megaposit MF-26 A Developer. We plunge the wafer with exposed resist into a beaker with developer for 60 *sec*, and then stop the development by plunging the sample into deionized water for 30 *sec*. Then we dry it by filtered nitrogen.

6) Metal evaporation

This step is the same as we did for markers prepared using e-beam lithography.

A $5nm$ titanium at rate $0.1nm/s$ is deposited on the wafer, followed by a $50nm$ gold at $0.1nm/s$. The PLASSYS™ MEB550S electron-beam evaporation unit is employed for this purpose. Since a single layer mask is applied, we use tilting equal to zero. Metal evaporation starts after pre-pumping with a turbopump to vacuum of $P_{CH} = 5 \cdot 10^{-7} mbar$ and $P_{LL} = 2 \cdot 10^{-6} mbar$ in the chamber and in the loadlock, respectively.

7) Lift-off

The liftoff, is performed by soaking the wafer in a beaker with NMP (N-Methyl-2-pyrrolidone) at $80°C$ for 5 to 20 hours. To heat up the NMP we use a "Stuart™ SD300" digital hotplate

Then blisters are observed in places where the metal began to peel from the plate. Then, using a pipette and taking liquid from the same vessel, we carefully deflate the metal. After that, we move the wafer to a new beaker with NMP and expose it to ultrasound for 1 minute at 60% power.

For ultrasonication here and hereafter, we use Elma® "T490DH Transonic Digital" Ultrasonic Cleaner, with working frequency of $40kHz$ and ultrasonic power of $110W$ at 100% power. (It is worth noting that the power declared by the manufacturer corresponds to reality only when two-thirds of the vessel is filled with liquid. However, due to the lack of a dip cell, in our case, the vessel is always filled only by 10-20% of the volume.)

Finally, we rinse the wafer in acetone, ethanol and IPA and then dry it with compressed nitrogen.

Acetone, ethanol and IPA which we use are produced by these suppliers: Acetone - Honeywell, Ethanol - Honeywell, IPA - CarlRoth.

1) Wafer preparation

2) Metal evaporation

A $5nm$ titanium at rate $0.1nm/s$ is deposited on the wafer, followed by a $50nm$ gold at $0.1nm/s$. The PLASSYS™ MEB550S electron-beam evaporation unit is employed for this purpose. Since a single layer mask is applied, we use tilting equal to zero. Metal evaporation starts after pre-pumping with a turbopump to vacuum of $P_{CH} = 5 \cdot 10^{-7} mbar$ and $P_{LL} = 2 \cdot 10^{-6} mbar$ in the chamber and in the loadlock, respectively.

3) Lift-off

We immerse the wafer in NMP at $80°C$ and keep in the beaker for 5 to 24 hours.

To improve the liftoff, we place the wafer in the beaker **face down**, resting it against the edges of the spherical glass.

Then we finish the process with a stream of NMP from a syringe or pipette, followed by an ultrasonication during 1 minute at **20%** power. Then we rinse off the residue by successive rinses in acetone, ethanol, isopropyl alcohol.

3.6.3. New recipe description - Aluminum structures

1) Wafer preparation

- Reactive Ion Etching

  Wafer is etched in oxygen plasma in PLASSYS ™ for 5 minutes at a power of $20W$ at pressure $0.07mbar$.

- Prebaking

  This time, the wafer is prebaked on a hot plate to dry it during $2min$ at $200°C$.

- **Removing silicon oxide by BOE**

  Immersion in HF solution in NH_4F (1:7) for 20 seconds. Then consecutive washing in two beakers with deionized water and a beaker with IPA.

- Prebaking

  Since the waffles came into contact with water after the BOE, we need to bake them again.

  This time, the wafer is prebaked on a hot plate to dry it during $1min$ at $100°C$. But the best way would be to bake under vacuum to avoid the formation of new oxide.

- Store under vacuum until ready for further work

2) Bilayer resist deposition

- First layer of resist PMMA-MAA

  Spin-coating a PMMA-MAA 9% (9% solution of mixture ARP 617.14 and AR 600.07 (9:5) in 1-Methoxy-2-Propanol) using a centrifuge at speed $\mathbf{3800}rpm$ with $\mathbf{3800}rpm^2$ acceleration for $30s$.

  To reduce the probability of resist contamination, we blow on the wafer with filtered nitrogen right before applying the polymer. The pipette we use to apply the resist is also blown with compressed nitrogen to avoid contamination.

- Baking resist

  The wafer is heated on a hot plate for $10min$ at $200°C$.

- Measure of thickness d_1

  We measure it with same interferometer Mikropack™ Nanocalc 2000 We select the refractive index "PMMA 950" from the database. Expected thickness should be around $720nm \pm 10nm$.

- Second layer of resist PMMA

  Apply a 4% solution of PMMA 950K AR-P 679.04 to the substrate by spin-coating using a centrifuge at $5000rpm$ with $5000rpm^2$ acceleration for $30s$.

- Baking resist

  We bake a wafer with two layers of resist for $5min$ at $180°C$.

- Measure of thickness d_2

  We measure thickness of second layer with interferometer Mikropack™ Nanocalc 2000 We select the refractive index "PMMA 950" from the database. Expected thickness should be around $230nm \pm 10nm$.

3) E-beam writing structures

   As soon as we will use another development process, all the doses were recalibrated. The list of new doses for each type of element if below:

   - $18.5C/m^2$ for small wires and junctions
   - $2C/m^2$ for the undercuts
   - $15C/m^2$ for wires with a width of 5 - 20 μm
   - $11C/m^2$ for big pads

4) **Cold development of the mask**

   This new step involve other compounds for the development process. We now use a **mixture (3:1) of IPA and deionized water** as developer and pure deionized water as a stopper.

   To perform the development we prepare two beakers, one with developer and another one with stopper. We cool both beakers to $1°C \pm 0.1°C$ until the temperature is stable. We measure the temperature with a thermocouple immersed in a beaker with developer. For this we use a chiller Neslab RTE-111.

   When everything is ready, immerse the wafer in developer for 60 seconds at temperature $1°C \pm 0.1°C$. In my work, I keep the wafer steady in the developer without rinsing it to ensure the reproducibility of the process. Then I move it to the beaker with the stopper for 30 seconds. At the end, I dry it with a stream of filtered nitrogen, pointing the gun perpendicular to the surface of the sample.

   The developer mixture was prepared by me in advance and stored in the fridge in cleanroom, to ensure the same concentration for each fabrication cycle.

5) Edges cleaning

   The wafer is etched in oxygen plasma in PLASSYS ™ for 15 seconds at a power of $10W$ at pressure $0.07mbar$.

6) **Removing silicon oxide by BOE**

   Immersion in HF solution in NH_4F (1:7) for 20 seconds. Then consecutive washing in two beakers with deionized water and a beaker with IPA.

7) Aluminum double angle evaporation

   - Pre-pumping

     We load the wafer in PLASSYS™ evaporator. It is used only for non-magnetic metals, which is very important to make sure when creating superconducting circuits. After loading the sample, we keep pumping it at least for one night, or preferable during weekends, with a cryogenic pump of temperature 13K.

- **Titanium sublimation pumping**

  To improve the depth of the vacuum, we use the sublimation pumping effect. To do this, we evaporate titanium in the chamber with rate $0.1nm/sec$ during 10 min. During this process, the table with the sample is tilted away from the evaporator to avoid deposition of titanium on the sample.

- First evaporation of aluminum

  We perform it with a tilting of $+35°$ relative to the vertical axis. We deposit $20nm$ aluminum, automatically controlling the thickness and evaporation rate at $0.1nm/s$ with the quartz oscillator built into the chamber.

- Oxide layer formation

  We set the table to the position of $+180°$ when wafer surface looks up and let oxygen go to the loadlock of PLASSYS. When pressure of oxygen stabilize around $5.00mbar \pm 0.05mbar$ (usually it happens in 50-70 seconds) we wait for $5min$ of static oxidation.

- **Titanium sublimation pumping**

  To completely remove any residuals of oxygen in the chamber, we add a step with pumping by turbopump until pressure of $1.0e-6$ $mbar$. Then we improve the depth of the vacuum by evaporating titanium in the chamber with rate $0.1nm/sec$ during 15 min. During this process, the table with the sample is tilted away from the evaporator to avoid deposition of titanium on the sample.

- Second evaporation of aluminum

  We start a second evaporation of aluminum with another tilting angle of $-35°$. This time we evaporate a thicker layer of aluminum (reason is illustrated on Fig. 3.13)

- Second oxide layer formation

  We repeat the procedure that we made after first layer of aluminum was evaporated to have same type of oxide on both layers.

  We set the table to the position of $+180°$ when wafer surface looks up and let oxygen go to the loadlock of PLASSYS. When pressure of oxygen stabilize around $5.00mbar \pm 0.05mbar$ (usually it happens in 50-70 seconds) we wait for $5min$ of static oxidation.

As a result of evaporation we have all the mask covered by aluminum as on the Fig. 3.11 for example.

8) Lift-off NMP $80°C$

To remove the mask with aluminum on top, we proceed exactly as for markers preparation. We immerse the wafer in NMP at $80°C$ and keep in the beaker for 5 to 24 hours.

To improve the liftoff, we place the wafer in the beaker **face down**, resting it against the edges of the spherical glass.

After few hours in NMP we change the beaker and solvent to a new clean one. Then we finish the process with a stream of NMP from a syringe or pipette, followed by an ultrasonication during 1 minute at **20%** power. Then we rinse off the residue by successive rinses in acetone, ethanol, isopropyl alcohol.

After this, the wafer is ready and can be removed from cleanroom to provide quality control tests (look in section 3.7 for more details about it).

3.6.4. Dicing the wafer

If the quality tests show promising parameters, then we saw the wafer to get 5 x 6.8mm chips that are compatible for insertion inside our 3D cavity.

First we need to protect the structures from damage by a layer of polymer, then saw it with a special machine Disco^{TM} DAD 321 Automatic Dicer and after wash the polymer away.

1) Applying polymer shell

   For protection, we apply two layers of resist: first the electronic PMMA, and then the optical S1818. The reason of this choice is that the optical resist is more viscous and creates a thicker protective layer, but at the same time it is more sticky, and it can be difficult to wash off. For that purpose, it helps us to have the first PMMA layer.

2) Dicing

   In addition to protection by polymer resist, we also cover the wafer with plastic wrap from both sides. The cut is made along lines oriented along special gold markers. When sawing, the machine cuts a gap in the plate about more than a hundred microns thick, so important structures should not be placed close to the edge of the sample.

3) Cleaning

   After dicing, we have a stack of samples with the resist on top and the plastic film glued on. To clean them, we consistently rinse them in three containers of acetone. Finally, we wash each sample in a stream of ethanol and IPA followed by ultrasonication at 20% power for 1min

3.7. Room temperature Josephson junctions characterisation

This section is devoted to characterizing the resulting samples to see if they are suitable for subsequent measurements at low temperatures. The main tool for characterizing Josephson junctions that we use is DC-measurements at room temperature. They allow us to quickly and accurately estimate the expected critical current.

3.7.1. Estimation of critical current by measuring room temperature resistance of the junction

The key parameter of any Josephson junction is its critical current. To measure it directly, the junction must be cooled down to the critical temperature of superconductivity. But there is a way to estimate this parameter at room temperature based on the resistance of the insulator layer between aluminum pads.

To do this, we use the Ambeokar-Boratov formula [141], which combines the critical current of the junction I_C and its normal state resistance R_N at low temperature:

$$R_N I_C(T) = \frac{\pi}{2}\frac{\Delta}{e}\tanh\frac{\Delta}{2k_B T} \approx \frac{\pi}{2}\frac{\Delta_{Al}}{e} \tag{3.19}$$

where Δ is the superconducting gap and k_B is the Boltzmann constant. Since we use thin films of aluminum for the gap, we can take $\Delta_{Al}/e = 210\mu V$. Due to the fact that the measurements are taken at an ultra-low temperature of about 20 mK, we can use a simplified Formula 3.19.

However, to measure the normal junction resistance, you need to cool it down to a low temperature. The junction resistance measured at room temperature will differ from the normal resistance due to the temperature broadening of the Fermi-Dirac distribution, which encourages more tunneling as more vacant states appear [142]. To account for this factor, we introduce a constant coefficient $r_0 \approx 1.3$ [143]:

$$R_N = r_0 R_{RT} \tag{3.20}$$

Thus, we calculate the critical current of a Josephson junction by knowing its resistance at room temperature using the formula:

$$I_C \approx \frac{2.5374\text{e}-4}{R_{RT}} \tag{3.21}$$

3.7.2. Non-destructive resistance measurements

Thus, room temperature resistance measurement became a reasonable way to control the resulting Josephson junction quality. But providing this type of measurement requires a certain level of accuracy because it is easy to burn the junction by applying too much voltage to it - which, however, may happen just because of the static discharge. The scheme of a setup that was used to measure the resistance of junctions at room temperature is described below.

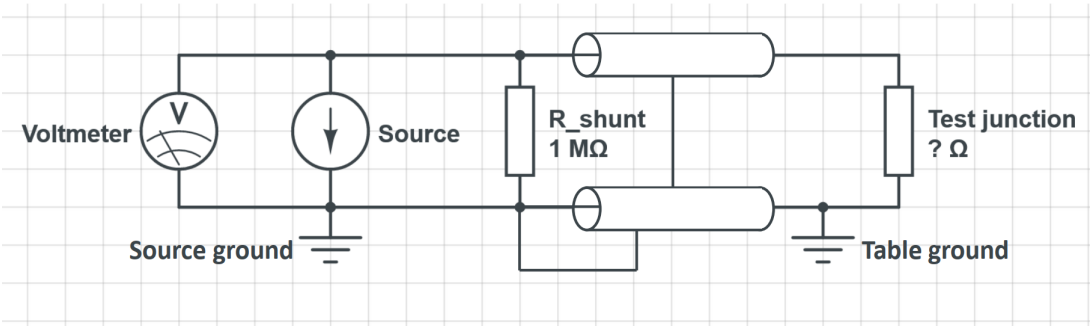

Figure 3.42: Electric scheme of the setup for Josephson junction DC-measurements. R_{shunt} is added to guarantee the equal electric potential of probes at the moment of connection to the junction.

To provide these measurements, we use a special probe-station with 6 or 12 μm probes. The idea of the measurement is to feed a known current through a circuit incorporating a Josephson junction and measure the voltage drop across it. Having plotted the volt-ampere characteristic, we fit the resulting points to a straight line

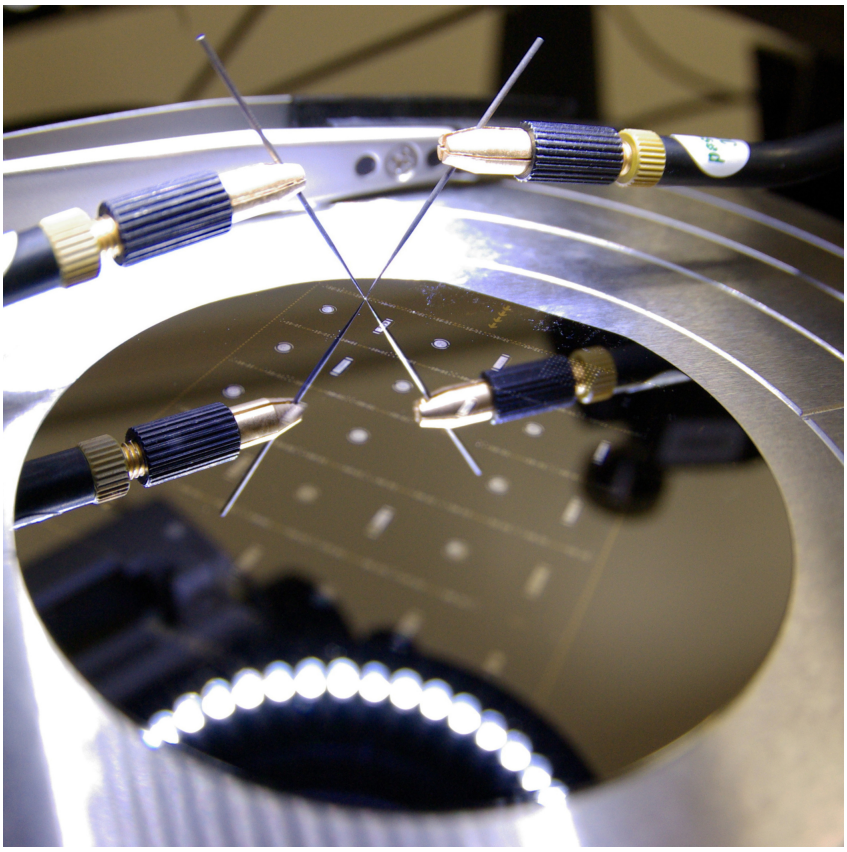

Figure 3.43: Photo of the wafer during DC measurement at the probe station

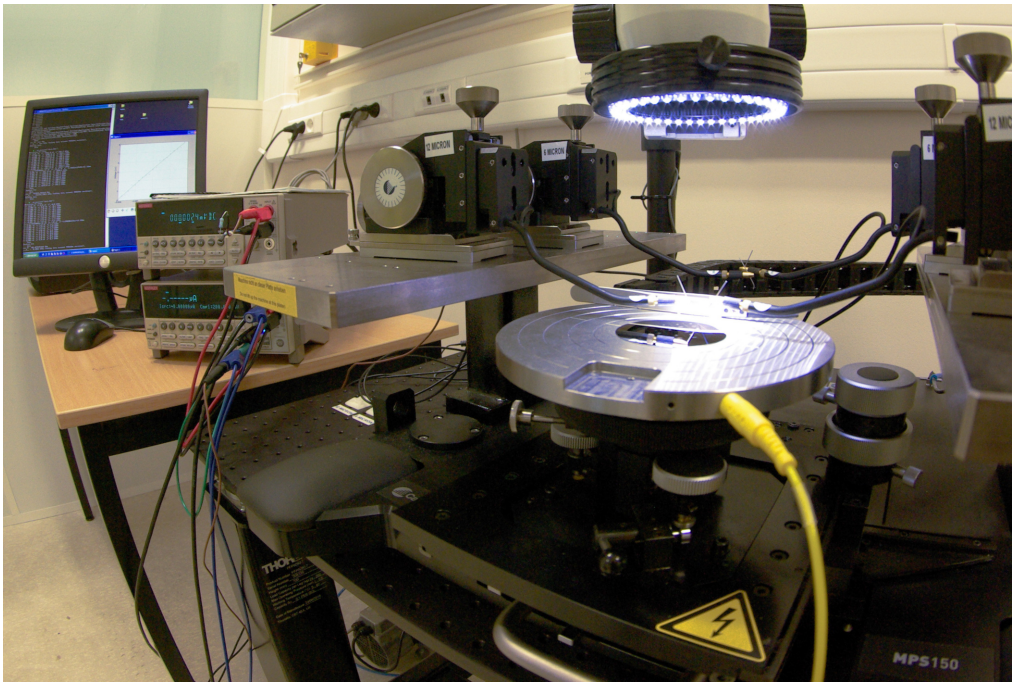

Figure 3.44: Photo of all the probe station setup: probe table, current source, voltmeter and computer.

as it shown on Fig. 3.45. The slope coefficient is the resistance. This method allows getting rid of possible offsets of devices.

Josephson junctions are very fragile structures. And the smaller they are, the easier it is to burn them out. To avoid burning the junction, we limit the currents supplied to $\pm 10 - 100nA$ with step not more than $1nA$. But even this is not enough to protect the junction from combustion during measurement. A great danger to junctions is the static charge built up on the installation or the researcher's body. This charge can pass through the junction at the moment of switching. To avoid this, we use earthing, as shown in the diagram. We do not use institute ground as it is highly noisy, but we do use filtered current source ground. We also connect the banks of the current source with a large $1MOhm$ resistor to avoid static charge build-up. (Of course, this parallel resistor we took into account during data processing). The whole scheme is shown in Fig. 3.42. Another trick we use before we connect the probes to the junction connectors is to switch on the current source by bringing it to zero. This avoids "switching on" the supply when the junction is already connected.

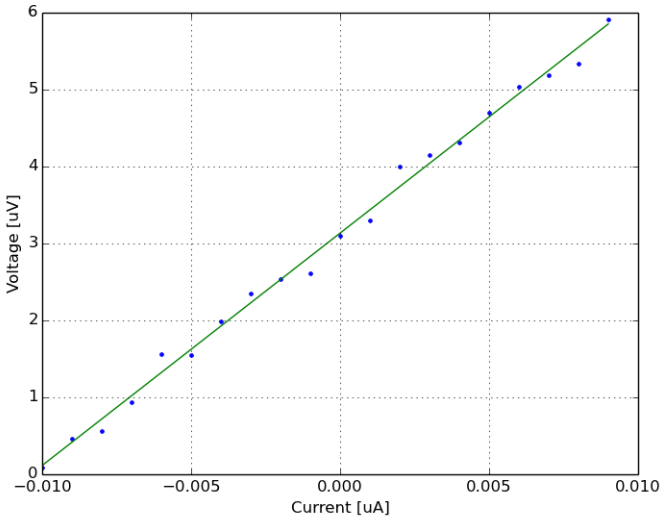

Figure 3.45: Example of the resulting volt-ampere characteristic of Josephson junction.

We carry out these measurements for specially made test junctions as well as for junctions built into qubits.

3.7.3. Discarding parasitic resistances

The characteristic value of the resistances we measure is a few to a few tens of $kOhm$s.

Naturally, when measuring resistance, we are actually measuring not only the resistance of the junction oxide film, but the sum of the resistance of this film with the resistance of the wires on the chip, and the resistance of the parts of the measuring circuit.

It is also worth remembering that the silicon substrate is also a weak conductor. In our case, we use a substrate of high impedance undoped silicon with a resistance of 10,000 Ohms per centimeter.

Before we started measuring, we shorted the samples to each other and measured the resulting resistance. It was about 0.1 ohms, which is 4-5 orders of magnitude lower than the measured resistances and completely negligible.

Linear resistance of aluminum wires

Then there is the resistance of the 70 nm aluminum pads and the wires on the chip, which can be 20 or 50 nm thick, depending on the evaporation layer. In order to assess the resistance value of the wires, special test structures were made with different lengths of wire. The results of dc-measurements of this structures you can see on Fig. 3.48. All measured wires were 350 nm wide and 50 nm thick. After fitting the data, the linear resistance was found to be around 5 ± 1 $Ohm/\mu m$. The variation is mainly due to the different resulting widths for different fabrication runs.

Recall that the tabulated value for bulky aluminum resistivity is supposed to be 0.028 $Ohm \cdot mm^2/m$. But because the thickness of the wire is on the nanometer scale, we expected this reduction in conductivity. Thus, for a wire with a cross-section of 50 $\times$ to 350 nm the resistivity should be 1.6 $Ohm/\mu m$.

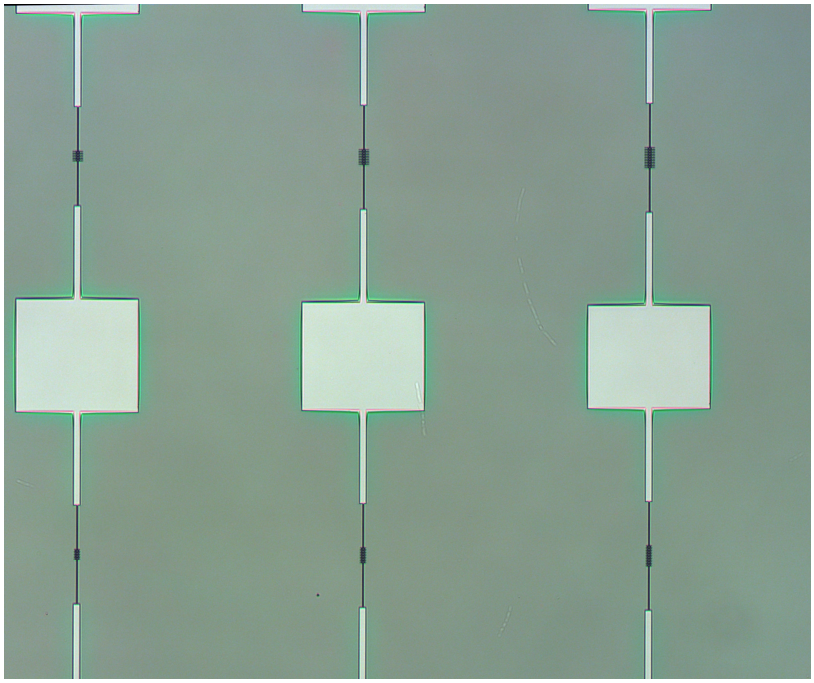

Figure 3.46: Example of test-structures we have done for dc-tests.

Chains of junctions in series

To get rid of parasitic wire resistance in measurements, one approach was to make a series of test structures with different numbers of identical Josephson junctions connected in series, or SQUIDs connected in series as on Fig. 3.46 The total length of all connecting wires is kept constant in this case. The result of resistance measurements of series with different numbers of junctions is shown in Fig. 3.47

There is a nuance, in case the number of single junctions is odd, one of the feeder wires will be 20 nm thick and the other 50 nm thick. If the number of junctions is

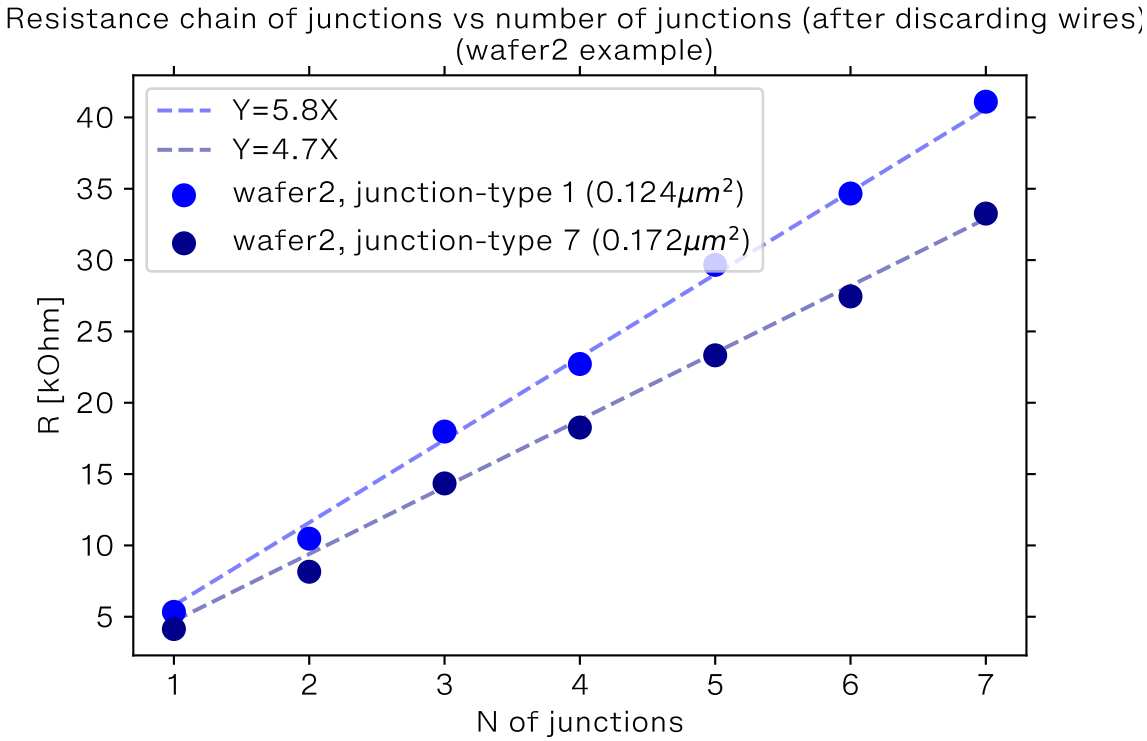

Figure 3.47: Result of resistance measurement of series of junctions. Each color correspond to a given size of junction. By fitting the data by linear equation, we can extract the average resistance of each junction size.

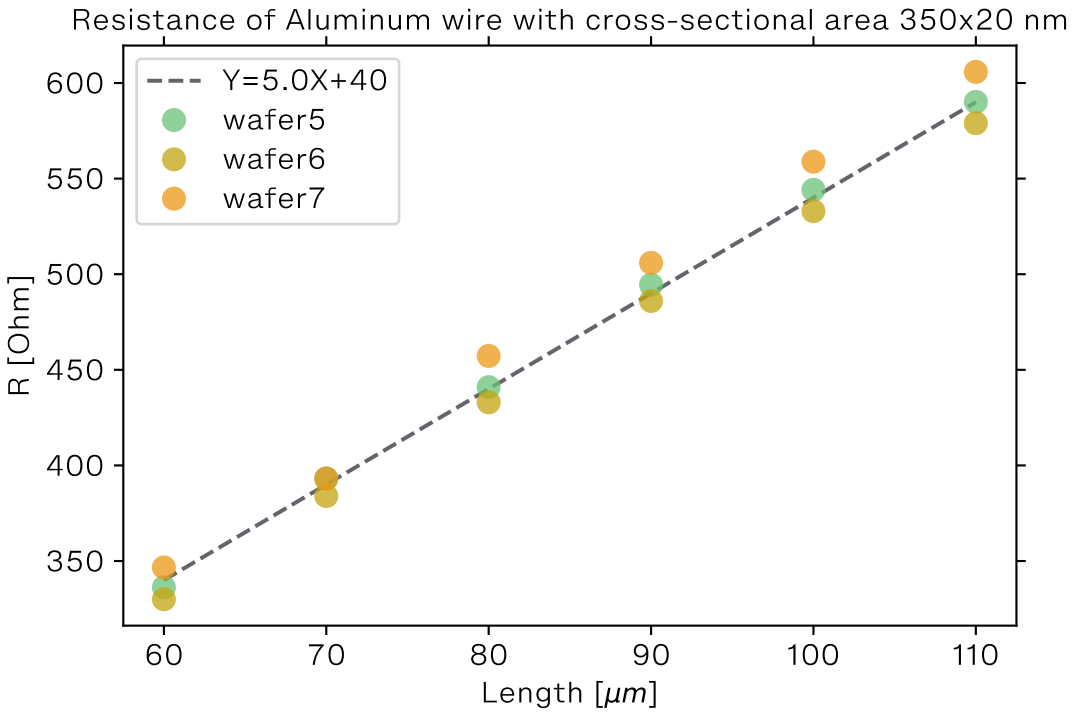

Figure 3.48: Results of resistance measurements for aluminum wires of different length (X-axis) and fabrication run (color). All wires must be 50 nm thick and 350 nm wide. We consider the slope coefficient of the straight line as a linear resistance.

even, then the thicknesses of the feeder wires are equal. However, since in our case the resistance of junctions is much higher, we have neglected this effect.

If this method is used, the accuracy of the average resistance measurement is higher due to the possibility to discard the constant associated with the parasitic resistance. However, this method is poorly suited for characterizing the repeatability of the resulting samples. For this reason, and because of the proximity effect on junctions, we switched completely to measuring the resistances of individual junctions.

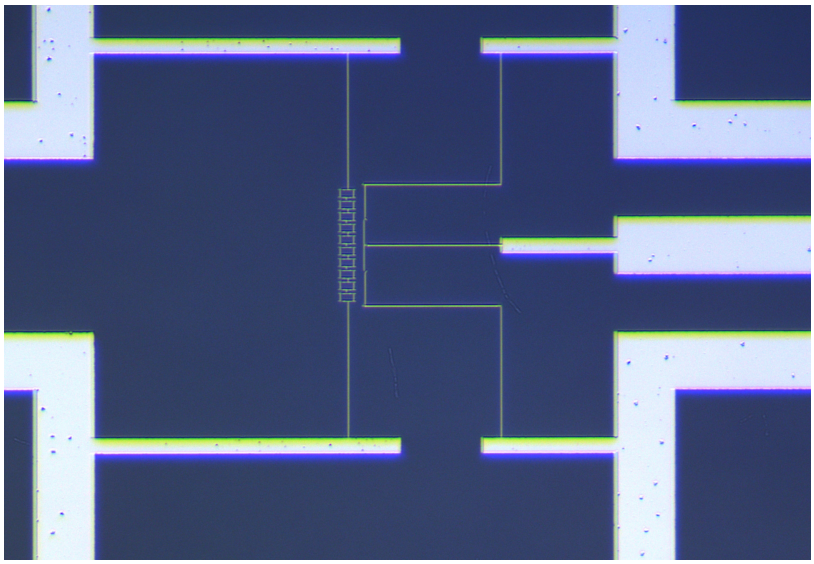

Figure 3.49: Example of test structure for dc-measurements. In this case, all the junctions have exactly the same environment as inside the qubit. The only change is that there are no two wires connecting the left and right side. Thanks to this change, it is possible to measure the resistances of all the junctions separately.

Exact copies of qubit hearts for dc-tests

The important question is to what extent we can transfer the result of a single junction resistance measurement to the situation of our cubit, in which several junctions are close together and experience a Proximity effect. To avoid the possible measurement error associated with proximity effects, we have developed other test structures that replicate the hearts of qubits entirely, but with discontinuities that allow the resistance of each junction to be measured separately as it is shown in Fig. 3.49. Experiments showed that the resistances of individual junctions differed markedly from those of junctions surrounded by other junctions. Therefore, we completely abandoned the test structures with single junctions and switched to copies of the hearts of real qubits with discontinuities.

However, this then raises the question of how to eliminate wire resistances in this situation. We solved this by doing the same test structure, but with shorts instead of junctions. Then, by measuring the resistances with those junctions, we could eliminate all the parasitic resistances. According to these measurements, the sum of the parasitic resistances is no more than $0.5kOhm$. For the inductor, the parasitic resistance is about $0.44 - 0.47kOhm$, which is 10% of its resistance and must be taken into account.

On the other hand, thanks to the measured resistance of wires in special test structures, we can obtain the calculated resistance of wires and extract these values

from the measured values. The calculated wire resistances agree well with the measured parasitic resistances.

We actively used measurements of such test structures to find out whether we were able to obtain Josephson junctions with the desired properties. However, to decide whether to load a particular sample, we also carried out direct dc-measurements on a real qubit.

3.7.4. Extraction of resistance values of exact junctions inside the sample

It is, unfortunately, impossible to produce identical Josephson junctions, that is why measuring of junctions in test structures can give some information, but can not be approximated to the real sample. This means that we need to get information about the junctions that are found directly in the sample to be loaded into the fridge. But there's a problem: we can't measure each junction in a qubit in isolation, as they are connected to other junctions.

Assuming that all parasitic resistances are negligible or eliminated using short-circuit samples, the circuit looks like the one shown in Fig. 3.50. Points A, B and C mark the cubit areas into which we can stick the probes. Let's look at how we can extract the values of each resistor by measuring the resistances between the three pairs of nodes. Since the two circuits in Fig. 3.51 are equivalent, we can imagine that we are measuring the circuit on the right (Y-shape). Then if we represent the results of these three measurements as $X = R_1 + R_2$, $Y = R_2 + R_3$, $Z = R_1 + R_3$ we get the following expressions:

$$\begin{cases} X = R_1 + R_2 \\ Y = R_2 + R_3 \\ Z = R_1 + R_3 \end{cases} \quad \begin{cases} R_1 = 0.5(X - Y + Z) \\ R_2 = 0.5(X + Y - Z) \\ R_3 = 0.5(-X + Y + Z) \end{cases} \tag{3.22}$$

Then to calculate the resistances of real elements we only need to use the conversion from star to delta using $Y - \Delta$ circuit transform (see Fig. 3.51.

Thus, the resistance values of real junctions (inductance) correspond to the values R_A, R_B, R_C:

$$\begin{cases} R_A = R_P/R_1 \\ R_B = R_P/R_2 \\ R_C = R_P/R_3 \end{cases} \tag{3.23}$$

where R_P is the sum of the products of all pairs of impedances.

$$R_P = R_1R_2 + R_2R_3 + R_3R_1 \tag{3.24}$$

3.8. Analysis of the results of DC-measurements at room temperature.

Before I started fabricating new samples, I set the goal specified in the Chapter 2 to fabricate a qubit with junctions with a given critical current value. To determine at what point the goal is achieved, it is useful to formulate it in terms of the resistance of

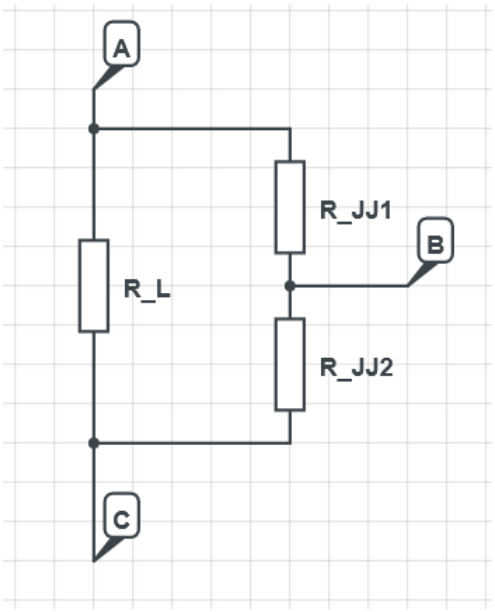

Figure 3.50: electrical scheme of real qubit heart from dc-measurements point of view.

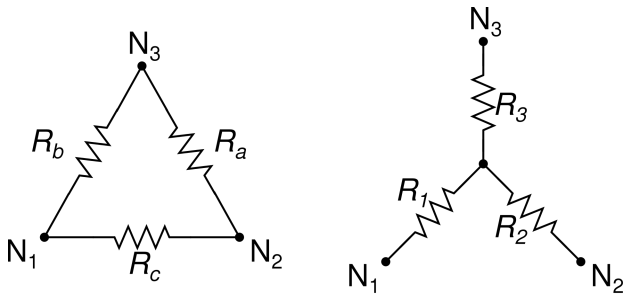

Figure 3.51: $Y - \Delta$ circuit transform example.

Josephson junctions at room temperature, since this value correlates with the critical current and can be easily measured.

In estimating the desired resistance, I started from the values measured for sample-A by a previous student working on this project. So, if I want to get the critical current 4 times less than in *sample-A*, I just aim to get 4 times the resistance.

These values can be different from ones given by Ambeokar-Boratov formula. However, I chose to rely on these values because they are based on a sample made and measured under the same conditions - so we have a good reference point. As soon as we are targeting I_c of paired Josephson junction to be 4 times less than in *sample A* and inductance L_a of SQUID-chain 2 times less, we consider as a target in terms of resistance:

	$R_{JJ}[kOhm]$	$R_{chain}[kOhm]$
sample A	6.7	8.26
Target	26.7	4.13

3.8.1. Critical current I_c of junctions

This chapter will present the main results obtained from the DC-measurements of our fabricated samples. An important characteristic of fabrication of Josephson junctions is their repeatability in terms of critical current. Moreover, it makes sense to speak both about the uniformity of the junctions within one wafer and about their repeatability from one run of fabrication process to another. The value of critical current I_c in turn depends on two quantities: *(i)* the physical size of the junction S_{JJ}, the accuracy of which is determined by the quality of the two-layer mask and *(ii)* the critical current density J_c, which mainly depends on the aluminum oxidation process during the evaporation process.

Critical current versus area of junction

The results of all measurements of junctions made by using the Dolan Bridge and BFF technique are shown in Figures 3.52 and 3.53, respectively. The x-axis shows the junction area measured directly using SEM. On the left y-axis, the value of the inverse resistance is plotted. The right axis corresponds to the critical current calculated using the Ambeokar-Boratov formula 3.21. If the critical current density J_c value is stable, we should expect a linear dependence of the critical current on the area. A deviation from this dependence indicates either a measurement error (resistance or area) or a variation in the J_c. As noted in previous works of our group, when using our recipe, the value of J_c can vary from 20 to 40 A/cm^2 [144, 84, 136, 145].

As can be noted from Figures 3.52 and 3.53, the critical current density remains stable with considerable variation in the junction area.

The magenta points away from the main trend correspond to wafer1, the first fabrication run, during which a mistake were made: the chamber was not continuously pumped by the cryogenic pump during the night. In this case, the calculated value of J_c was around 8 A/cm^2.

Critical current density distribution

Fig. 3.54 allows a more precise estimation of the critical current density J_c and its distribution for each of the wafers. It shows that, on average, the values of most

points do lie between 20 and 40 A/cm^2 as already mentioned. This graph also makes it possible to estimate the scatter of the J_c value within each wafer and the overall drift from one run of fabrication to another.

We explain the low critical current density for wafer1 by the fact that during the evaporation process for this wafer the condition of long-term pumping by the cryogenic pump was not fulfilled, while for all others this step was strictly followed.

As for wafer14, for which there is some exceeding of expectations regarding J_c - in its case, a new recipe was used, which, among other things, includes an additional step of sorption pumping by evaporation of titanium.

Wafer5, which also shows increased critical current density, was made according to the standard recipe, but immediately after the maintenance of PLASSYS evaporator machine. Moreover, we ran a full evaporation cycle at no load by covering the sample with a flap to make sure a good operation of the machine after the maintenance, can also be counted as sorption pumping.

Thus, we have an argument in favor of the hypothesis about the importance of the absence of water vapor in the chamber during the oxidation of aluminum.

Critical current density versus area of junction

Fig. 3.55 shows the dependence of the calculated critical current density on the junction area. In some cases we noticed some dependence of J_c on the junction area. For example, this is noticeable in the cases of wafer3, wafer6, and wafer7. These cases are marked with a brighter color. And in the case of small junctions made by Dolan Bridge technique a positive dependence of J_c on the area is observed, whereas in the case of large junctions J_c on the contrary decreases with the area.

This effect may be related to the fact that in reality the oxide film may be inhomogeneous and edge effects play a prominent role in the junction room temperature resistance. Whereas our definition of the critical current density implies that this value is conserved throughout.

Josephson junction asymmetry

As we have written before, small junction asymmetry is critical for our system. Therefore, we characterized this value as $d_j = \frac{R_1 - R_2}{R_1 + R_2}$ and plot the result of this measurement on Fig. 3.56. Here, the x-axis shows d_j as a percentage. The lower it is, the better it is for the sample. As you can see, the best result is given by the *wafer-14* made according to the new recipe. In the case of this wafer, a large portion of the samples have a junction asymmetry of less than 2 percent.

There are two possible sources of this asymmetry: *(i)* different size of junctions, *(ii)* different properties of aluminum oxide at the same size. But according to SEM measurements, the ratio of the areas of the passages is much smaller than the ratio of their resistances. In addition, we found no dependence of d_j on the size of the junction being made, despite the fact that the smaller the junction area, the more difficult it is to make two identical ones. This leads us to assume that the improvement in terms of symmetry in the case of the new recipe is due to improved pumping with titanium evaporation rather than to improved fabrication resolution due to cold development.

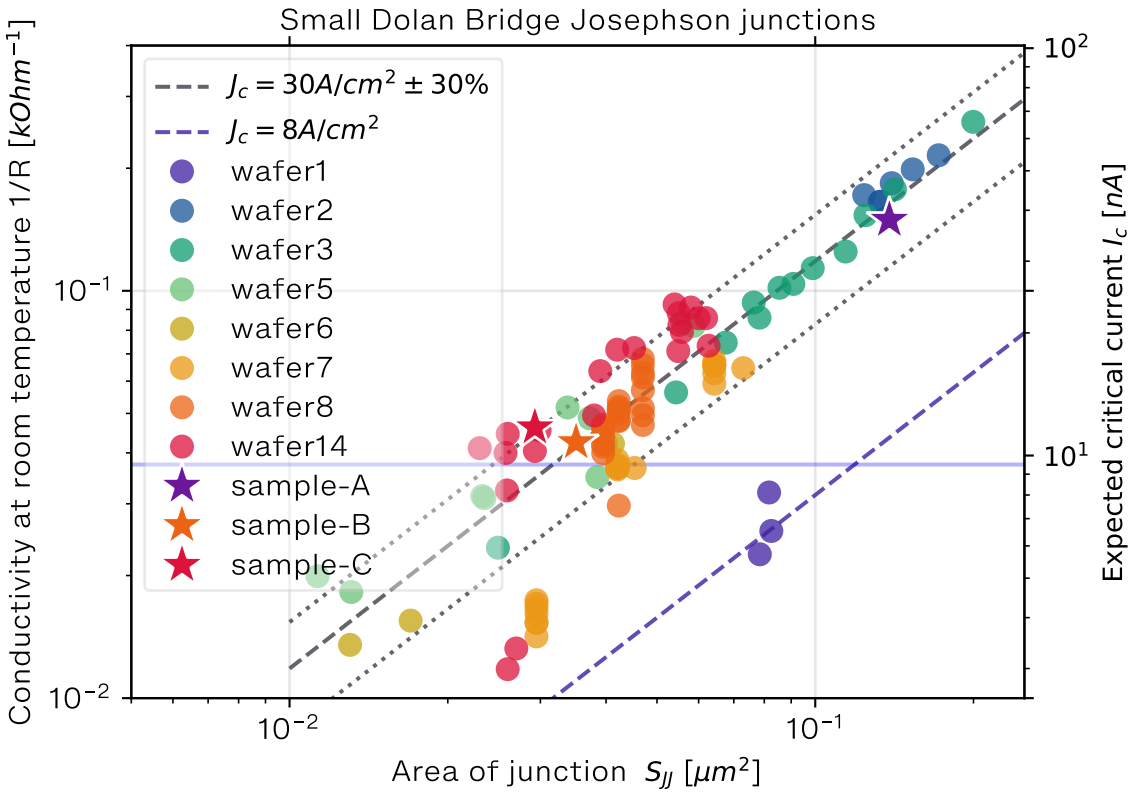

Figure 3.52: Dependence of conductivity of small junctions fabricated using Dolan Bridge technique (3.3.2) measured at room temperature versus area of this junction. Each point corresponds to one junction. Each color means a run of fabrication. A horizontal light blue dashed line correspond to a target value. The stars indicate the samples that were eventually loaded into the fridge and measured. Both scales are logarithmic. The dashed line indicates the line corresponding to a critical current density of $30A/cm^2$*, and the dotted lines correspond to* J_c *of 21 and 39* A/cm^2 *(30% deviation). Purple points and line indicates junctions obtained in the first fabrication cycle where oxidation was performed at* $1.5mbar$ *oxygen pressure in the chamber. All others were fabricated at a standard oxygen pressure of* $5mbar$*.*

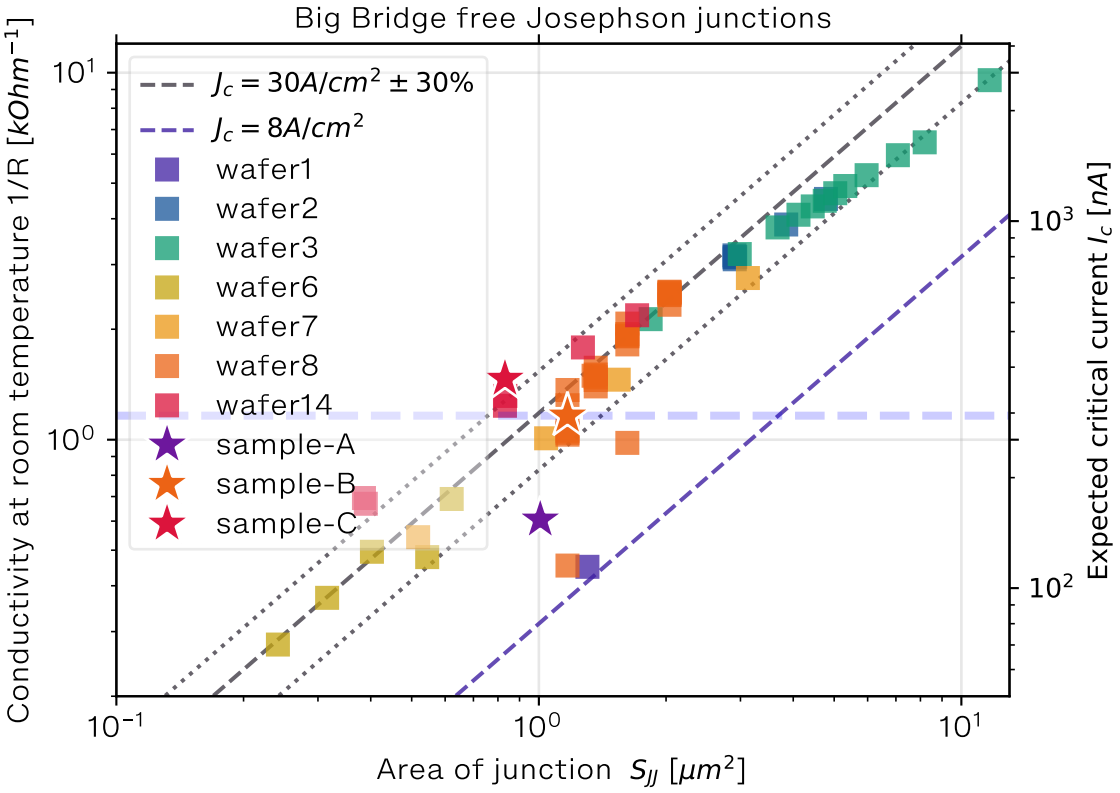

Figure 3.53: Dependence of conductivity of big junctions fabricated using Bridge Free technique (3.3.1). A horizontal light blue dashed line correspond to a target value. The stars indicate the samples that were eventually loaded into the fridge and measured. Both scales are logarithmic. The dashed line indicates the line corresponding to a critical current density of $30A/cm^2$, and the dotted lines correspond to J_c of 21 and 39 A/cm^2 (30% deviation).

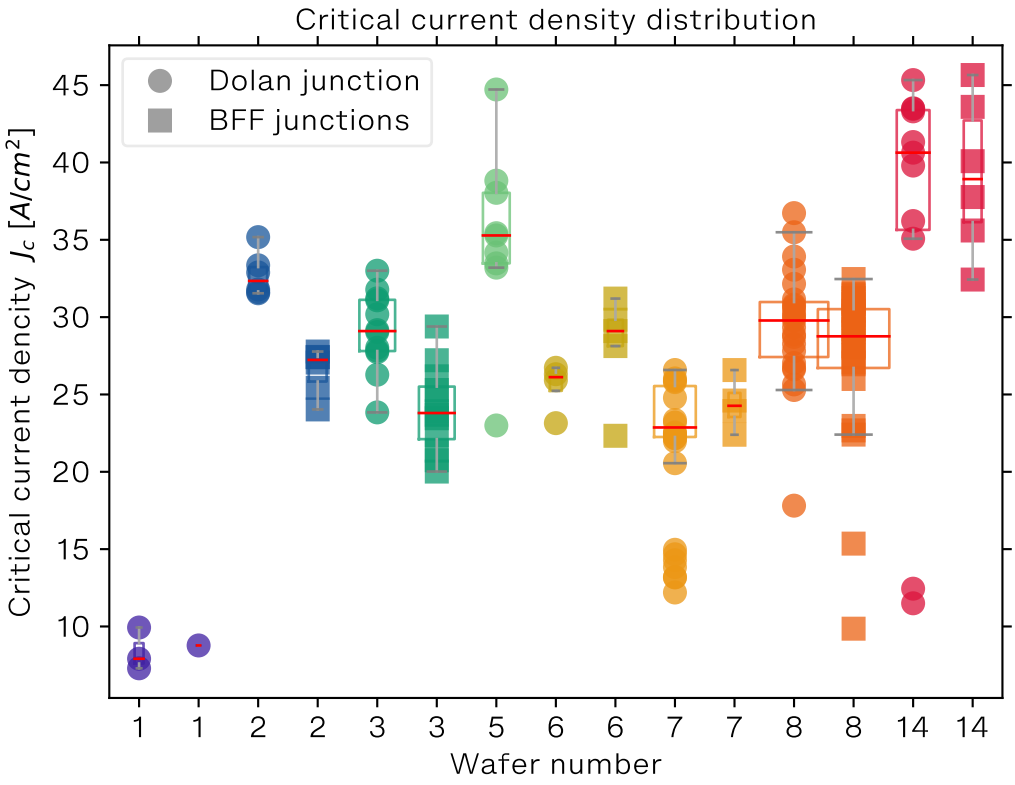

Figure 3.54: Scatter of J_c values within and between wafers. Each point corresponds to a Josephson junction. Junctions made by Dolan bridge or Bridge free technique are marked with a round or square marker, respectively. Each color and box-and-whiskers plot corresponds to a wafer (fabrication run). To calculate J_c, we divided the I_c value obtained from the Ambeokar-Boratov formula by the junction area measured with SEM. The width of the box corresponds to the number of points on which this graph was plotted.

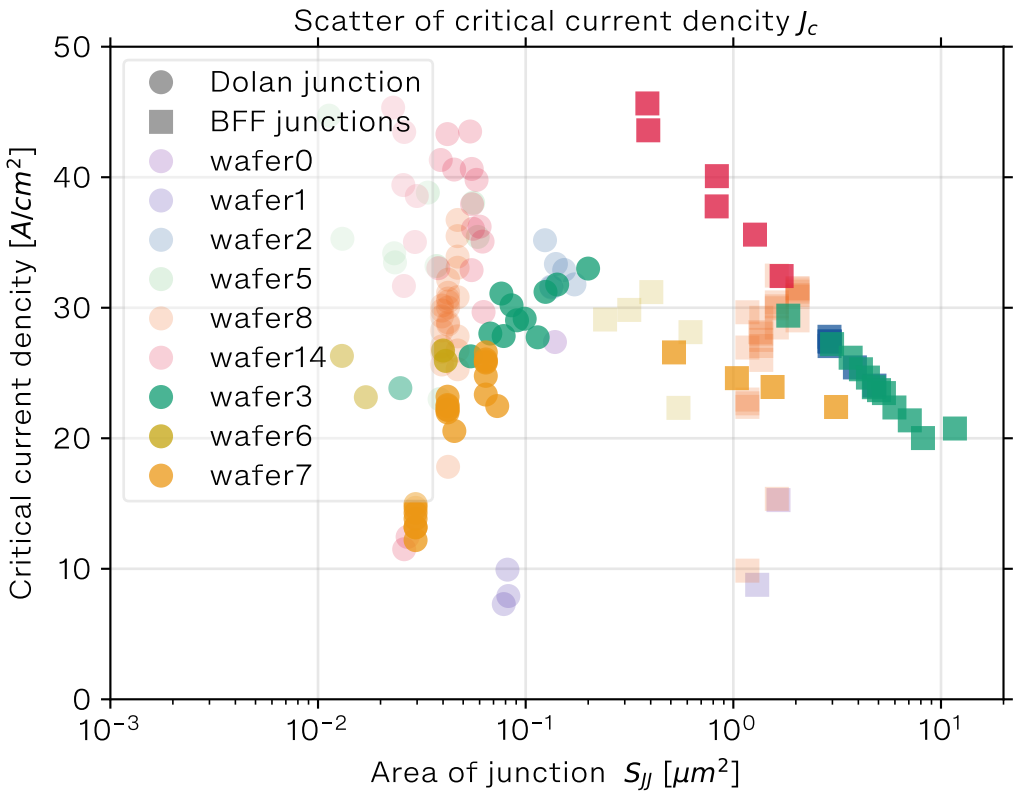

Figure 3.55: Dependence of the critical current density J_c on the junction area. Both Dolan Bridge (round markers) and Bridge Free (square markers) junctions are included.

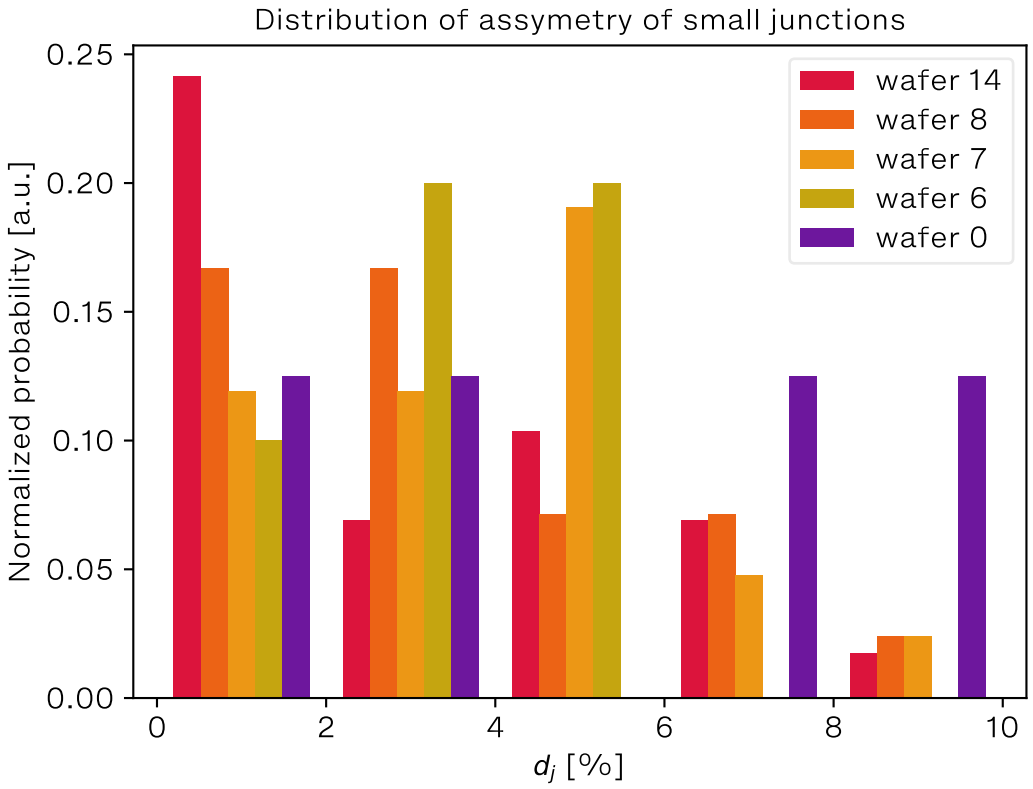

Figure 3.56: Distribution of asymmetry of small junction on different fabrication runs. This parameter we define as $d_j = \frac{R_1 - R_2}{R_1 + R_2}$*. The y-axis is given in conditional units and denotes the probability of a value having a given value.*

3.8.2. Measurements on real qubits

Once we are convinced that the test structures give promising results at room temperature, we move on to direct measurements of the junctions embedded in the real qubits in the dilution refrigerator. The following values were obtained for *sample-B* from *wafer8* and *sample-C* from *wafer14*.

3.9. Chapter key points

We began this chapter by setting a goal: to make a quality transmon molecule with the given electrical parameters. And we came to the logical conclusion of the chapter by making sure, after analyzing the DC-measurements, that we have two new samples with suitable parameters at our disposal. *Sample-B* was made according to the standard recipe, and *Sample-C* according to a new recipe that included etching in hydrofluoric acid, cold development, and a different evaporation protocol and liftoff. The capacitances were set for the most part by the design of the large pads and laid down in the design discussed in the previous chapter. However, the critical currents of the Josephson junctions depended entirely on the fabrication process. Considerable work was done to achieve an exact match of the critical currents of the large and small junctions to those specified in the task, revising some older models and creating a new fabrication recipe. Studies have also been conducted on some associated adverse effects described in section 3.5.

For a smoother entry for readers who are unfamiliar with this topic, the essence of all the processes taking place was described in detail. For those who are familiar with nanofabrication of superconducting circuits, many technical details have been added in this chapter, which may be useful or interest them.

Chapter 4.

Experimental setup

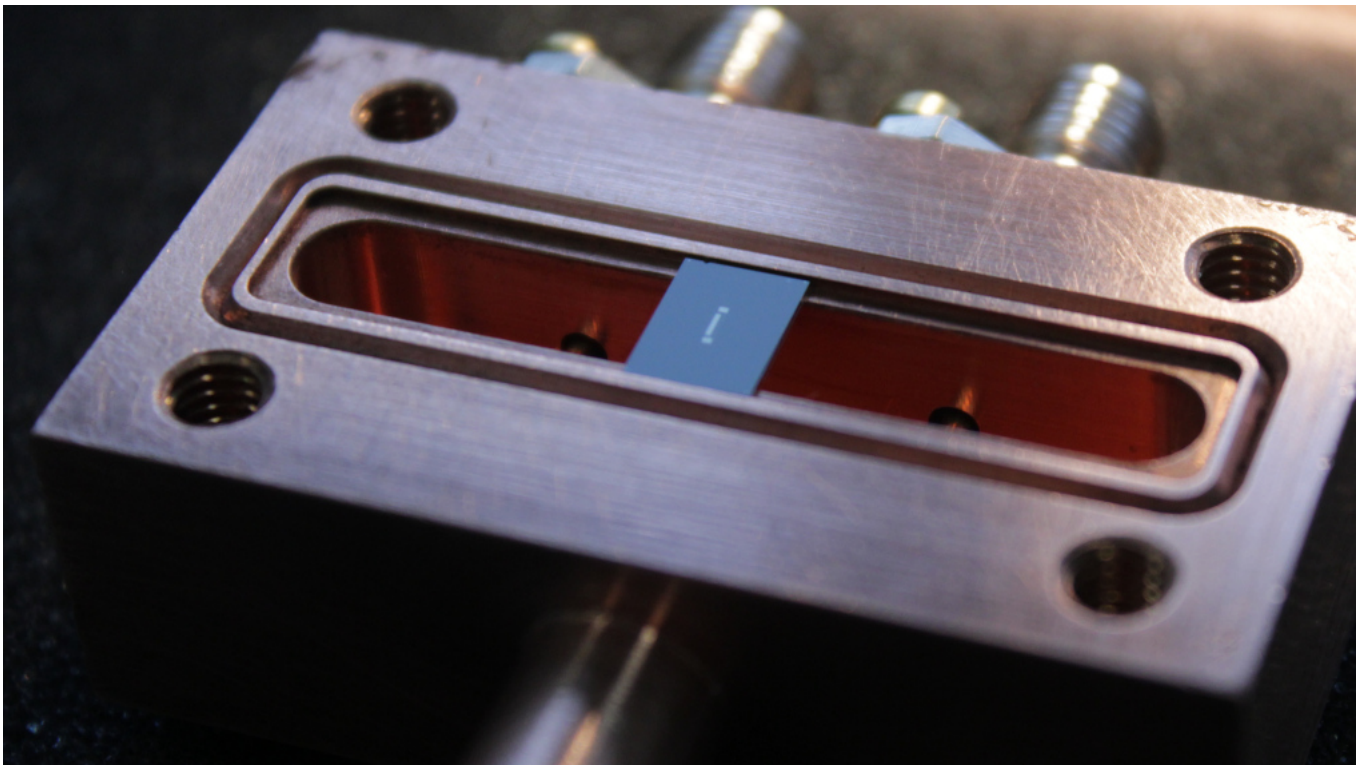

Figure 4.1: Sample-A *placed in copper 3D-cavity before cooling down.*

In this chapter we describe the laboratory setup we use to characterize the samples *Sample-A*, *Sample-B*, *Sample-C*. We will describe different parts of setup: the cryogenic part, the shielding, and a microwave scheme. Our description will be based on PhD thesis of Remy Dassonneville [84], who has assembled this setup. My contribution was mainly related to the software and recomposition of a room temperature part of microwave setup.

4.1. Cryogenic part

We will first describe the components of the setup that operate at extremely low temperatures (mostly 0.02 K). We will start our description with the dilution refrigerator that ensures the cooling process. Then we will discuss ways to isolate the

system from different types of noise. Finally, we will describe the low-temperature microwave setup.

4.1.1. Dilution refrigerators

Nowadays, the most widely used and conventional way to cool down superconducting circuits is dilution refrigeration. This method is used by numerous scientific groups and commercial companies working in a field of quantum computation [146]. The availability of off-the-shelf refrigerators on the market has significantly lowered the entry threshold into the field of superconducting quantum circuits: Bluefors™, Janis™, Oxford Instruments™.

The dilution refrigeration method was initially proposed by H. London, G.R. Clarke, E. Mendoza in 1962 [147]. They have used a liquefied mixture of two helium isotopes ^4He and ^3He. ^3He enters the cryostat from the room-temperature part and cools down to few Kelvin by liquid ^4He bath. Then ^3He cools down to 1 Kelvin entering the vacuum chamber due to volume expansion, and liquefies. After passing through the capillary system, the liquid ^3He cools to a few hundred millikelvins and enters the mixing chamber - the coldest part of the system with temperature of 10-20 millikelvin. In this chamber, two phases of ^3He-^4He mixture are separated by a phase barrier.

The phase diagram is shown on Fig. 4.2. One phase consists of pure ^3He and another one is a dilute phase with only 6.6% of ^3He (the rest is ^4He). The heat which is necessary to dilute ^3He is taken from the mixing chamber, which cools down the entire setup.

In modern dilution refrigerators, the closed-cycle is used. The pure ^3He is pumped out from the mixing chamber and then reintroduced into the system to close the loop. It is possible due to the fact that ^3He is easier to evaporate at low pressures than ^4He. Another improvement which is done in modern commercial refrigerators is based on using the Pulse tube ("dry"-system) instead of liquid ^4He-bath ("wet"-system) which removes the need for weekly ^4He transfers.

The operational principle of dilution refrigerators is also described in Oxford Instruments instruction [148] and a book of Probell [149].

In my work I have used two different dilution fridges: a) - "wet" system built in Institute Neel, Grenoble; b) - "dry" system - "Bluefors LD-250"

4.1.2. Isolating quantum system from the environment

For any quantum information processing, the qubit must be well isolated from the environment because any sort of interaction is provoking the leakage of quantum information (decoherence).

This includes protecting it from the thermal noise, magnetic field, cosmic rays and electrical noise from the wires. In following subsections, we will describe various solutions to isolate the quantum system.

Suppression of the thermal noise

To minimize the probability of spontaneous excitation of qubit by the thermal noise, the sample is thermalized at $20mK$ temperature.

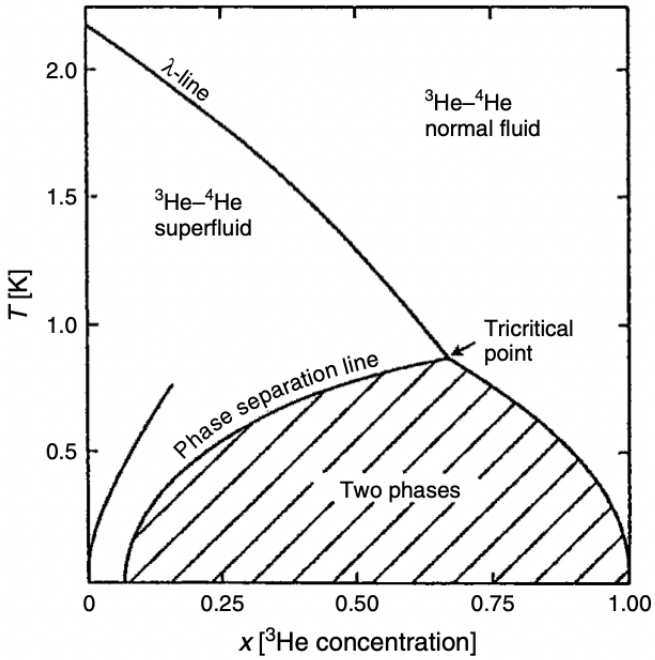

Figure 4.2: Phase diagram for a mixture of ^4He - ^3He at the saturated vapor pressure. X-axis shows concentration of ^3He isotope, when Y-axis shows temperature of mixture [150].

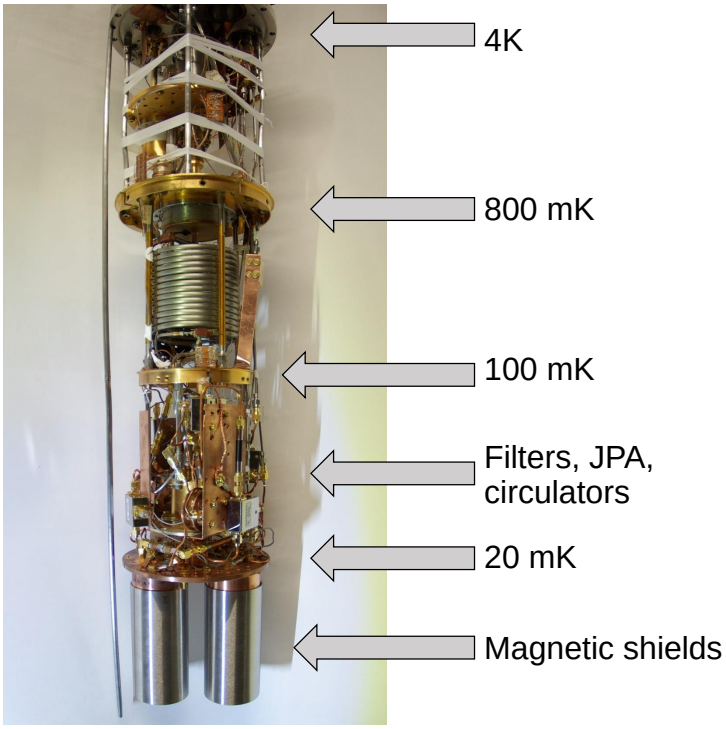

Figure 4.3: Photo of dilution refrigerator, used in this work.

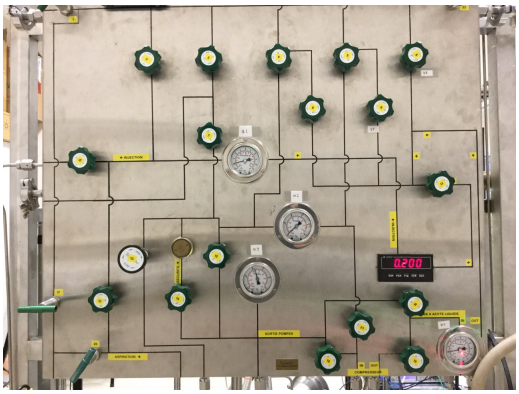

Figure 4.4: Photography of the control panel of the dilution refrigerator used in this work. This system was developed at the Neel Institute in Granoble.

However, the input and output signal cables can introduce the thermal radiation from the room-temperature environment. The attenuation chain is a standard solution to protect the sample from thermal noise coming from the input line. However, it lowers not only the noise, but also the signal itself. We apply an increased power of signal to compensate the chain of attenuators.

It is not only room temperature environment which produces the unwanted thermal radiation, but any part of the dilution fridge at temperature higher than $20mK$. To distribute the attenuators in the chain one must take into account that each attenuator, thermalized with a temperature higher than $20mK$, is also a source of thermal noise by itself. The best solution would be placing all the attenuators on the lowest temperature plate. But this decision is limited by the cooling power of the fridge, which should compensate for the additional heating. That is why a distribution of the attenuators in chain is an optimization to be solved.

An attenuator can work effectively if the level of noise added by it does not exceed the level of noise passing through it. The target of the entire attenuation chain is reducing the total noise, coming to the sample at the level of $20mK$ temperature noise. In our case, we have used $20dB$ of attenuation at $4K$ and $40dB$ attenuation at $20mK$ plate (See Fig. 4.3). The detailed calculations of thermal noise in a given scheme as well as the attenuation values can be found in [84, 89]. More information and theoretical estimations of incoming thermal noise for can be found in papers [136, 145].

The model which is applied is based on Johnson-Nyquist white noise approximation with a quantum correction to spectral density. According to these calculations, the thermal noise has a temperature around $20mK$. This proves that thermal radiation does not affect qubit decoherence significantly.

However, we can not solve the problem of thermal radiation from the output line using the method described above. Since the attenuators will destroy the weak signal from qubit, we use a chain of isolators (or circulators with $50Ohm$ terminations) instead. They are directional components with isolation around $-18dB$. In our case we use two circulators between amplification chain and $20mK$ setup as well as an additional circulator between 3D cavity and Josephson Parametric Amplifier (JPA) (see scheme 4.5 for the details).

Magnetic shielding

There are different sources of external magnetic field: Earth magnetic field, various ferromagnetic materials used in building, even some components used inside the dilution fridge like microwave circulators or nickel connectors.

There are two problems which external magnetic field brings. One relates to the constant part of this field, and another - to its fluctuations.

Since we tune the qubit frequency by applying magnetic flux into the SQUID, the additional constant magnetic field will add unwanted flux, which we would need to compensate. The fluctuations of magnetic field will change the flux in the SQUID randomly causing a qubit frequency fluctuations and as a result decoherence.

A general approach to suppress the magnetic field is using a μ-metal shield made of material with very high permeability (for example, permalloy).

In addition, to better suppress the variation component of the magnetic field we add a superconducting shield, which eliminate the magnetic field fluctuations due to the Meissner effect [151].

In this work, we have used three magnetic shields. First, the entire dilution fridge is covered by a large μ-metal shield that is $2mm$ thick, provided by Meca Magnetic company. Second, the $800mK$ still screen is entrapped in one layer of Metglas ribbon, attached with aluminum tape. Finally, the cylinder μ-metal shield of $1.5mm$ from "Magnetic shield Ltd" is fixed around a copper screen surrounding the 3D cavity with sample at base temperature (See Fig. 4.3).

Reduction of ionizing radiation

An effect of ionizing radiation on decoherence of superconducting qubits was recently investigated [42, 152, 153]. Cosmic rays can be a source of ionizing radiation which is very difficult to avoid. The ionizing radiation can break Cooper-pairs in superconducting material, producing quasiparticles. These quasiparticles lead to errors of qubits which cannot be corrected by error-correction protocols due to the fact that these errors are correlated.

The only way to avoid ionizing radiation is putting heavy-metal thick shields between the source and the object. Operating in a deep-underground cryostat covered by a thick shield made of lead or depleted uranium would be the best, though inconvenient, solution.

In this work we have not applied any additional shielding since comparatively low T_1 levels of *Sample-A* made this problem negligible. We have focused on improving the readout and relaxation time of the qubit by modifying its design and fabrication process.

IR shielding

The IR radiation can penetrate to the 3D cavity either through isolation material of coaxial cable, or through seams in the shields. The IR radiation penetrating through coaxial cables will be stopped by low-pass filters placed on $20mK$ the plate. To avoid IR photons coming from seams in the shields, we use highly reflective mirrors on the outer side of the $4K$ shield and black coating on the internal side of the $20mK$ shield. The black coating is prepared as mixture of silicon balls, carbon powder and Stycast®

epoxy. This material efficiently absorbs IR photons that are usually presented into the shield, preventing the quasiparticles bursts as was discussed in [154, 155].

Filtering of cables

Assuming that the sample is well isolated from any external electromagnetic field, we focus on the noise from signal wires. As we discussed above, we are using a chain of attenuators on the input line to suppress the thermal noise. On the output line, the chain of microwave isolators plays the similar role.

However, the high frequency photons ($> 20GHz$) can pass through these devices, since they were designed for different radiofrequency ranges. To stop the high frequency radiation, we use tubular low-pass filters K&L 6L250-00089 on all lines which enter the refrigerator. In some cases we have replaced the K&L filters by other filters made in our lab, which absorbs IR-radiation and microwave above $10GHz$ In addition, in some experiments to suppress a low-frequency noise we have added a DC-block on the input and output lines.

More detailed explanation of problems of noise and filtering can be also found in PhD thesis of Sebastian Leger [145]. For the spectroscopy experiments on *Sample-B* we have used a distributed attenuator, described in this thesis. This is a thin coaxial cable with a good thermal contact along its entire length due to the strong attachment provided by silver epoxy paste. It has been proven [145] that this cable can effectively suppress the high frequency noise.

4.1.3. Low temperature microwave setup

In this subsection, I will describe the microwave setup working at low temperature. Its scheme is presented in Fig. 4.5.

The signal of qubit pump and readout enters the refrigerator by the input line and passes through the chain of attenuators described above. After being filtered by a low-pass filter, it enters the 3D cavity The signal of qubit pump interacts with the qubit mode, but does not pass through the resonator being filtered. The readout signal interacts with the polariton mode and exits the resonator through the output port due to a stronger coupling in comparison to the input port. After the readout signal leaves the cavity, it passes through the circulator which prevents the thermal noise from penetrating the cavity. Then the signal passes through the directional coupler and another circulator to enter the Josephson Parametric Amplifier (JPA). The amplified signal reflected by JPA returns to the circulator where it is redirected to the HEMT amplifier through the filter. As a result, the readout signal carrying the information about qubit state returns to the room temperature scheme, where it can be analyzed.

The JPA pump wave enters the refrigerator and passes through another chain of attenuators and a filter. It comes to the $-20dB$ port of directional coupler, which allows it to go only in one direction - left-to-right. Then this wave passes through the circulators to the JPA and pumps it. However, due to the leakage, this wave can also partially reach the 3D cavity. To suppress it, we apply destructive interference. For that we introduce a JPA compensation wave which follows the similar line and enters another $20dB$ port of the directional coupler. Then the compensation wave can only go in right-to-left direction and compensate the unwanted JPA pump wave. The detailed description of the procedure used to set the precise parameters for the compensation tone is presented in [84].

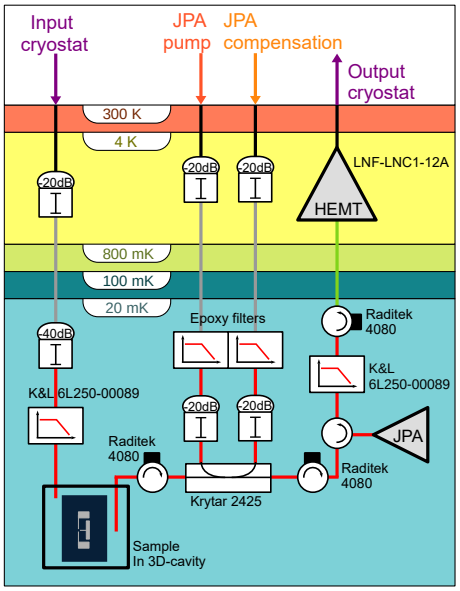

Coaxial cable	Reference	Inner Conductor	Dielectric	Outer conductor	Attenuation at 10GHz (dB/m)
	UT-85B-SS	Copper-Beryllium	PTFE	Stainless steel	5
	UT-085SS-SS	Stainless steel	PTFE	Stainless steel	13
	SC-219/50-SC	Oxygen free copper	PTFE	Stainless steel	5
	NbTi085/50	Niobium-Titanium	PTFE	Niobium-Titanium	0.4

Figure 4.5: Low temperature microwave setup.

JPA for *Sample-A*

The JPA operates at $20mK$ with an effective noise temperature of about $500mK$. It is used as a first amplifier, which allows us to reduce the effective noise temperature and achieve a high readout resolution of the qubit state. We use the JPA in a phase-sensitive mode [156] which requires the frequency of JPA pump equal to amplified signal frequency and the stable phase difference between the signal and the pump. To avoid a phase noise, we use the same microwave generator to pump the JPA and to produce the readout signal. If the amplified signal is in-phase with JPA pump, the amplification will be maximum.

In this work for measurements of *Sample-A* I have used the JPA described in [84]. This JPA is represented by an array of 80 SQUIDs forming a non-linear $\lambda/4$-resonator. The operating frequency can be tuned by external flux in range from $6.3GHz$ to $7.4GHz$. The maximum gain was measured to be $25dB$. The JPA has a large bandwidth of $45MHz$ in a regime of $20dB$ gain. This device was provided by Luca Planat. A similar device was also described in the following papers [157], [136].

TWPA for *Sample-B*

For measuring *Sample-B* I was using a reversed Kerr Traveling-Wave Parametric Amplifier (reversed Kerr TWPA) provided by Luca Planat, Martina Esposito and Arpit Ranadive [158]. This device presents a new phase matching mechanism based on the sign reversal of the Kerr nonlinearity. According to this paper, the reverse Kerr TWPA device has a bandwidth equal to $4GHz$, tunability of the amplification band equal to $8GHz$, and saturation $-98dBm$ at $20dB$ gain. The new TWPA provides a high gain in a broadband range, which can be tuned *in-situ*. The gain as a function of frequency is presented in Fig. 4.7 for three different frequencies of pump. A scheme of this device is given in Fig. 4.6. It consists of a long chain of superconducting nonlinear

asymmetric inductive elements (SNAILs) fabricated by double-angle evaporation of aluminum on the silicon substrate. These structures are covered by a layer of dielectric (alumina) and a ground conductor (gold).

In our measurements, we pump TWPA at a frequency far detuned from the 3D cavity frequency. That is why we do not need to apply a compensation wave in comparison to using JPA in a phase sensitive mode. We were using pump frequency $f_{TWPA} = 9.469GHz$ to achieve a gain of $G = 20dB$.

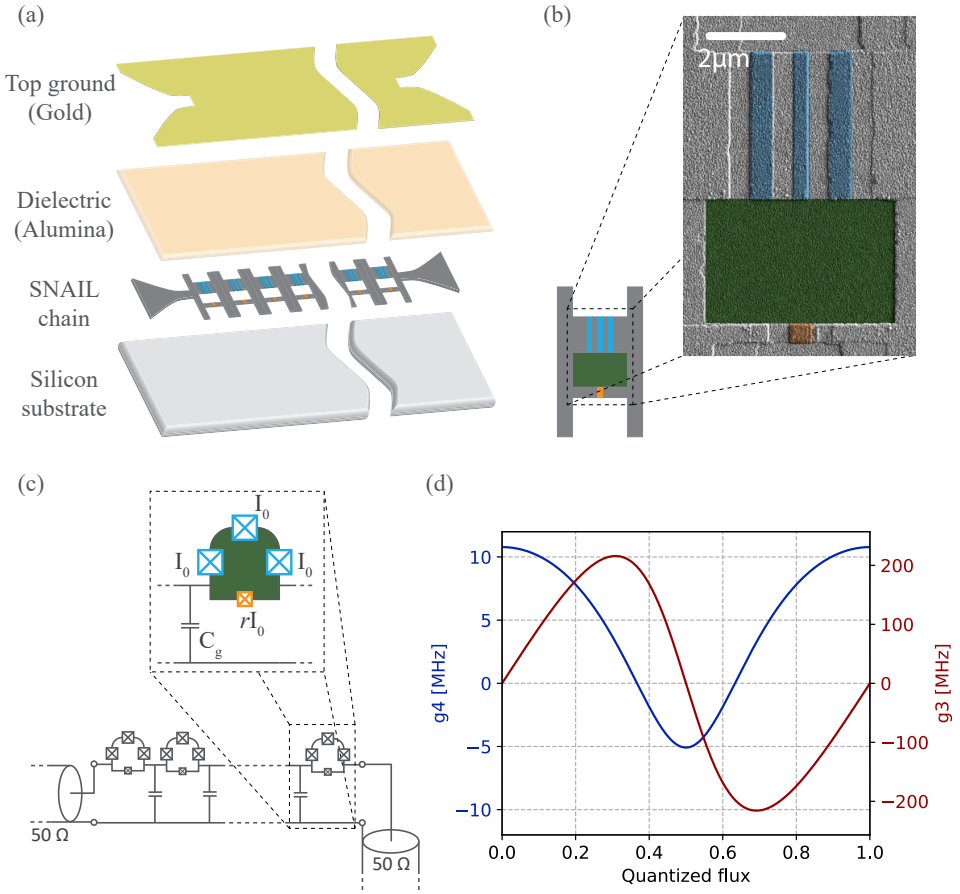

Figure 4.6: Pictures of reversed Kerr TWPA which was used for measuring Sampl-B. *a) - Presentation of materials used for producing the device; b) - SEM picture of one SQUID; c) - Electric scheme of the reversed Kerr TWPA; d) - Nonlinear coefficients g_3 and g_4 as a function of the external magnetic flux calculated using the device parameters obtained from the linear characterization (see [158])*

4.2. Microwave setup at room-temperature

To excite the qubit and readout its state, we need to prepare a π-pulse and a readout pulse. We also need to get the information about the qubit's state from an amplified readout pulse. In case of *Sample-A* we apply the scheme described in Fig. 4.8. This scheme has already been described in detail in [84], [89]. For *Sample-B* and *Sample-C* only minor changes were introduced: SSB and a filter on a qubit channel

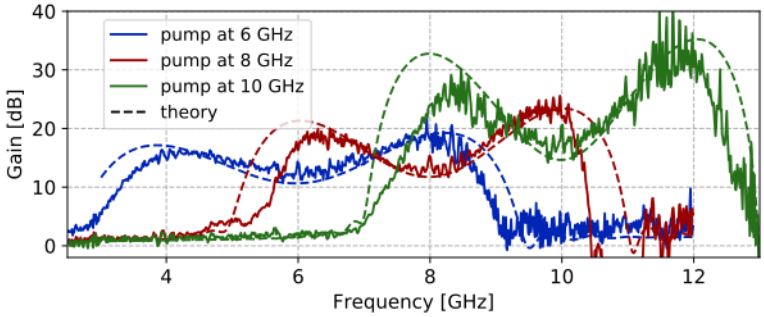

Figure 4.7: Typical gain profile of the Kerr TWPA device. It is tuned to operate at external magnetic flux $\Phi/\Phi_0 = 0.5$ and pumped at different frequencies. For more details, see [158].

were replaced by ones with lower frequencies. The JPA with its circulator were replaced by a TWPA. This way the connection of elements became serial: 3D-cavity, isolators, TWPA, HEMT, output of the refrigerator.

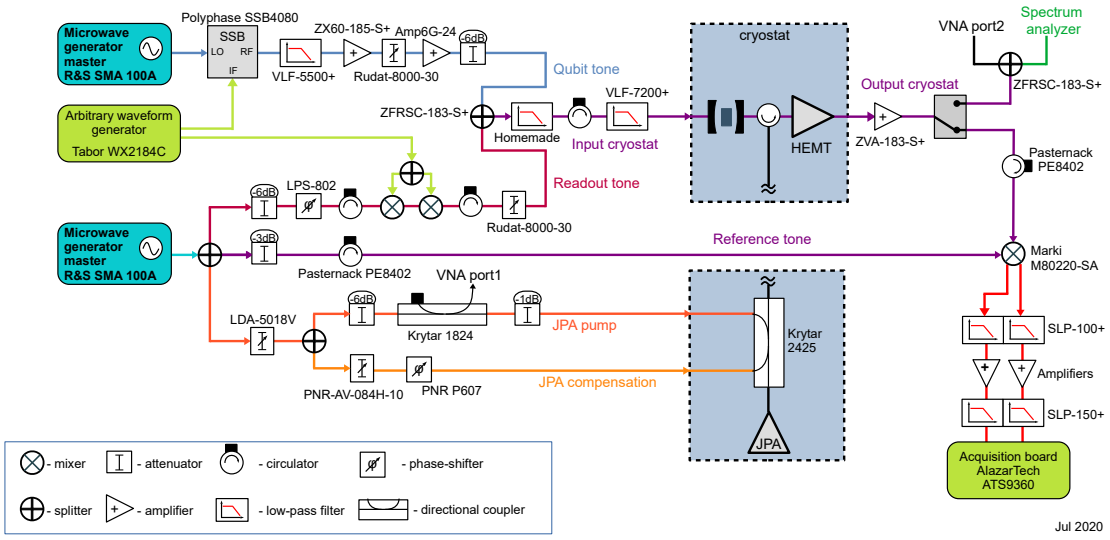

Figure 4.8: Room-temperature microwave setup scheme for time-domain measurements. The elements placed inside the dilution fridge are not depicted on this scheme, but can be found in Fig. 4.5.

4.2.1. Microwave scheme description

We use two microwave generators to produce two frequencies: the resonant frequency of the qubit and the resonant frequency of the polariton. After modulation, signals of both frequencies are merged in a splitter and sent to a refrigerator input.

Preparation of readout pulse

For readout signal, we apply an amplitude modulated by a pair of microwave mixers. We use two of them to improve the isolation in closed state (up to $\approx -70dB$). To send the readout signal, we need to apply a step-like signal to IF port of both mixers to open and close them back after readout time T_{read}.

Preparation of π-pulse

For a qubit pump signal, we use a single-sideband (SSB) modulation. We use a higher sideband to avoid the qubit excitation caused by imperfect isolation when there is no modulation applied. To prepare a π-pulse, we send a modulated sinusoidal signal on the IF-port of SSB-modulator. The modulated signal is produced by an Arbitrary Waveform Generator (AWG).

Two room temperature amplifiers are introduced to increase the pump pulse power so that the π-pulse time is reduced. In our experiments with *Sample-A* the π-pulse duration was usually around $30ns$, when the shape of the pulse was Gaussian. In case of *Sample-B* the π-pulse duration was extended to around $100ns$ with a Gaussian shape for the pulse.

Acquisition of readout pulse

In our measurements on the output of the refrigerator, we receive the readout signal after it was amplified by JPA (or TWPA), HEMT-amplifier and a room temperature amplifier. To analyze the received readout signal, we send it to the RF port of the IQ-mixer (Marki IQ4509LXP) at the same time sending a duplicating reference signal to the LO-port. As a result, we demodulate the readout signal, receiving an I and Q low frequency signals. These I and Q signals pass through low-pass filters and amplifiers before measurement in an $1GS/s$ acquisition board.

Pumping of JPA or TWPA

We need to vary the power of readout pulse in the experiments. However, JPA is very sensitive to changes in the power of the pump. Using the single microwave generator for both JPA pump and readout signal, we fix its power and add two programmable attenuators on both channels. This allows us to separately control the power with $0.1dB$ step in case of using JPA. In case of TWPA we use two microwave generators which eliminates this problem by default.

To set the power of JPA pump, we measure the JPA gain by VNA as a function of power. To set the TWPA parameters, we also measure its gain by VNA, but vary power and frequency of pump. We use a directional coupler to connect the source port of VNA to the JPA pump port of the refrigerator, and a microwave switch to connect VNAs input port to the output of the refrigerator. We also use copper cables to avoid phase instability between JPA pump wave and readout signal.

Compensation of JPA pump

To suppress the wave which goes from JPA to 3D-cavity, we use destructive interference. It is done by sending a compensation wave to the directional coupler.

To adjust the compensation wave power and phase, we use a precise manual variable attenuator and phase-shifter. To check the result of compensation, we use a spectrum analyser. We tune attenuation and phase-shift on the compensation line until the peak of pump frequency disappears on the spectrum.

Programmable attenuators

In addition to the programmable attenuator on JPA pump line, we also use programmable attenuators on readout and qubit pump lines. This way we can easily control the power of readout and π-pulse without affecting the JPA and mixers calibration.

Phase of readout signal

Since we use JPA in phase-sensitive mode, the phase between readout signal and JPA pump is important to control. To be able to control it, we add a phase-shifter on the readout line. When JPA is activated, we run Single-Shot readout experiments varying the phase of a readout signal. As soon as the phase is set, the signal resolution and fidelity of readout increase. To automate the process of phase shifting, I have also replaced the manual phase-shifter by a programmable one.

Filters

In addition to filters that we have used on $20mK$ the plate to remove the high-frequency noise, we use other microwave filters at room temperature. We use two low-pass filters at the entrance of refrigerator and another low-pass filter on the channel of qubit pump to cut all frequencies higher than needed. For samples of new design *Sample-B* and *Sample-C* the cut frequency of high-pass filter was changed, since the qubit resonance frequency was lowered.

Circulators

We use circulators with $50Ohm$ terminations to let the wave pass only in one direction. This allows us to avoid unwanted standing waves in the scheme and prevents the waves from entering back into microwave generators.

4.2.2. My contributions to the microwave setup

During my PhD I have applied some changes to the initial microwave setup trying to improve it.

Fixing leakages

During measuring excitation number in the polariton I have found that the wave of readout frequency can overcome closed mixers and enter the 3D-cavity populating the polariton. Several SMA-cables were leaky and I have replaced them. This has shown a positive effect on T_2 decoherence time of the qubit. During the reassembling of the entire room temperature microwave setup, I have strongly attached each cable to prevent the phase noise, improving the JPA stability (see the photo of reassembled microwave scheme in Fig. 4.9).

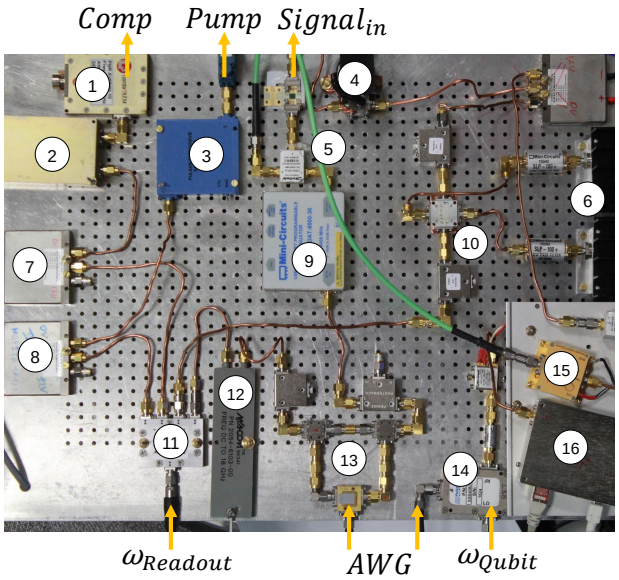

Figure 4.9: Photo of microwave scheme used for the measurements. 1) - manually adjustable attenuator for compensation line; 2) - manually adjustable phase-shifter for compensation line; 3) - analog adjustable attenuator for pump line; 4) - room temperature amplifier with radiator; 5) - splitter uniting qubit pump and readout lines; 6) - filters and amplifiers of I Q signals; 7) - microwave switch of compensation line; 8) - microwave switch of JPA pump line; 9) - Programmable attenuator for readout line; 10) - IQ-mixer; 11) - 4-channel splitter; 12) - manual phase-shifter of readout line; 13) - pair of mixers of readout line; 14) - SSB modulator of qubit pump line; 15) - Amplifier of qubit pump line; 16) - Programmable attenuator of qubit pump line. May of 2019

Programmable phase-shifter

The manual phase-shifter of the readout line was not precise, making it difficult and time-consuming to find a correct phase for the readout and set the JPA. After I have replaced it by a programmable one, the process of setting JPA became much faster and more precise.

Improved JPA pump

I have changed the microwave cicuit by placing the programmable attenuator before the splitter of JPA pump and compensation lines. This way it controls both power of pump and compensation wave. As a result, after adjusting the power, there is less change needed to adjust the compensation.

I have also replaced the programmable attenuator of JPA pump by another one to decrease the step of attenuation from $0.25dB$ to $0.1dB$.

VNA and Spectrum analyser connection

In the beginning of my PhD, I have had to disconnect the SMA cables each time I wanted to check the gain of JPA and quality of destructive interference. It was inconvenient, affected the cable lifetime and could slightly change the phase. To simplify this process and prepare the future automation, I have added a microwave switch after fridge output and amplifier. To be able to control the state of this switch from the computer, I assembled a simple Arduino-based switch controller which receives commands by USB. I have also written the Python driver to include this device into the environment.

4.3. Software part of setup

4.3.1. Python

To control the setup we use Python, which is a free open-source interpreted language. During my work, I have used mainly Python of 2.7 version.

4.3.2. QTLab

We have used QTLab - an IPython-based measurement environment written by Reinier Heeres, Pieter de Groot, and Martijn Schaafsma. However, this project is not updated since 2015. This made us to decide to implement the QCoDeS framework for future experiments.

There are three main classes: Instruments, Data and Plots. Each instrument object is related to each physical device. Though, some virtual instruments can be created to represent a small setup of physical instruments for a given task. During previous stages of the PhD project, the entire setup was represented by a single virtual instrument to simplify the user experience.

4.3.3. My contribution to the code

At the beginning of my work, to run any measurement, it was necessary to edit a script and set all the variables related to the measurement manually. The problem was that there are many of them. For example, in case of single-shot readout there are frequencies, powers, durations of π-pulse and readout pulse as well as many more technical parameters. These values were usually not given, but taken from other measurements (like Rabi and Ramsey experiments or spectroscopy). This increased the probability of a mistake.

Functions instead of scripts

I have decided to replace these scripts by callable functions or class methods. This way, the results of one measurement could become a parameter of a function call for another measurement, which reduced the probability of human error and allowed further automation of the experiment.

Automation of experiment

Using functions instead of scripts, I was able to run long series of measurements by varying different parameters and plotting them automatically. However, the main goal was to build the system which would be able to collect a feedback and optimize the input parameters automatically. This was done for the measurements that were conducted most frequently.

For example, I have made a function which is able to find a sweetspot by varying the magnetic field and measuring the spectroscopy. After it calibrates the pi-pulse by conducting Rabi-measurements series and adjusts the qubit frequency by conducting Ramsey-measurements. This process could be automated further, if the JPA would not require manual compensation adjustments.

Data analysis

The next subsection consists of very technical details, you don't have to read it to understand the rest of the text. However, for those interested, we have saved it here.

To make the automated process work, the functions should be able to return the correct value based on analysis of the measurement data even in presence of noise. To achieve this goal, I improved the programs of analysis of the measurement data. I was able to achieve a good fit of Rabi and Ramsey oscillations under almost any conditions.

Another part of the work was making fully automated analysis of single-shot readout data. The library devoted to this analysis can be found in my https://github.com/qc-coder/SingleShotReadout [159].

During the single-shot readout experiment, four readout pulses were sent: *I* - initialization readout pulse; *II* - readout of prepared $|g\rangle$-state; *III* - another initialization readout pulse; *IV* - readout of prepared $|e\rangle$-state. The resulting data consist of four pairs of I and Q values. After a series of measurements more than 10000 points were recorded. Our goal is to match these points to actual states of qubit.

First, we analyze the data given by readout pulses *II* and *IV*. We calculate the mean values of these results to define the centers of blobs by method "centers_two_blobs()".

After we change the basis from I,Q to I',Q' for both centers to have the same Q' which maximizes the resolution on I' axis by method "make_norm_data_from_raw()".

Second, we set a threshold which separates the points corresponding to $|g\rangle$-state from the ones corresponding to $|e\rangle$-state. To set the threshold, we apply a method "set_best_threshold()" which optimizes its possible values to maximize the fidelity of a measurement.

Third, we do the postselection of the data by method "make_postselected_data_from_norm(). We discard the entire data point, if the result of initializing (I or III) readout pulse is recognized as $|e\rangle$-state. In this case, the initialization is considered as failed.

Finally, we calculate the readout fidelity and generate the histogram plots with and without postselection of the results. During this process, they are fitted by double Gaussian to analyze the sources of errors. I have also automated the fitting and plotting so that all graphs are plotted in the correct axes and conveniently display the results. This allowed me to avoid the situation, when I have to manually correct small phase deviations without knowing the precise experiment result.

4.4. Chapter key points

In this chapter, we have described all parts of our measurement setup. Firstly, we introduced the low-temperature components as well as the cryogenic setup. Secondly, we described the schemes and devices used to protect the setup from external influences/ Then the parametric amplifiers were described: the JPA and the TWPA devices. After, we presented the microwave scheme for pulse preparation and measurement. Finally, my contributions to the setup and corresponding software were listed.

Chapter 5.

Measurements – Results

This chapter is devoted to microwave measurements of three samples with transmon molecules. It is divided into subsections according to the type of measurements taken.

(i) First, we will discuss microwave spectroscopy performed by single-tone and two-tone measurements. We will determine the frequencies of the qubit and polaritons. Using these frequencies, we will extract the electrical parameters of our system and compare them with the target values and electrical parameters of earlier generations of transmon molecules. The acquired data will be used as important feedback to improve the fabrication process and design of next qubits.

(ii) The second section is devoted to the study of qubit coherence through time-domain microwave measurement. The main focus will be on measuring times T_1, T_2 and T_{Rabi} under different conditions. With these studies, we aim to estimate how coherence times have evolved through the design modifications and a new fabrication recipe described in the Chapter 2 and Chapter 3, respectively.

(iii) Finally, in the third section, we will continue time-domain measurements with the goal of studying our original qubit readout. It presents the results of a single-shot qubit readout. We will also quantify its fidelity and its quantum nondemolition as well as present quantum trajectories. This data will be compared to the state-of-the-art solutions in the field of cQED systems obtained using dispersive readout with integrated Purcell filter. It will allow us to estimate the prospects of transmon molecules with cross-Kerr coupling for quantum computation.

5.1. Introducing three samples (”A”,”B”,”C”)

During my PhD work, I studied three different samples. The first sample, *Sample-A* was fabricated by Remy Dassonneville during his PhD project and has already been described in the following works [84], [85]. This sample has demonstrated high fidelity and fast readout performance. However, several problems were detected. This system had a low relaxation time (3.3 μs) which limited the fidelity of readout and its application for quantum information processing. In addition, high non-linearity of ancilla mode prevented the increase of readout speed by increasing the readout power. To face these challenges, the second and third samples (*Sample-B*, *Sample-C*) were created by the author of the manuscript. In this work, they are described for the first time. In *Sample-B* a new circular design was applied, described in detail in Chapter 2 - ”Engineering of transmon molecule”. The design changes were implemented based on the studies of *Sample-A* in order to improve the coherence times of the qubit. To

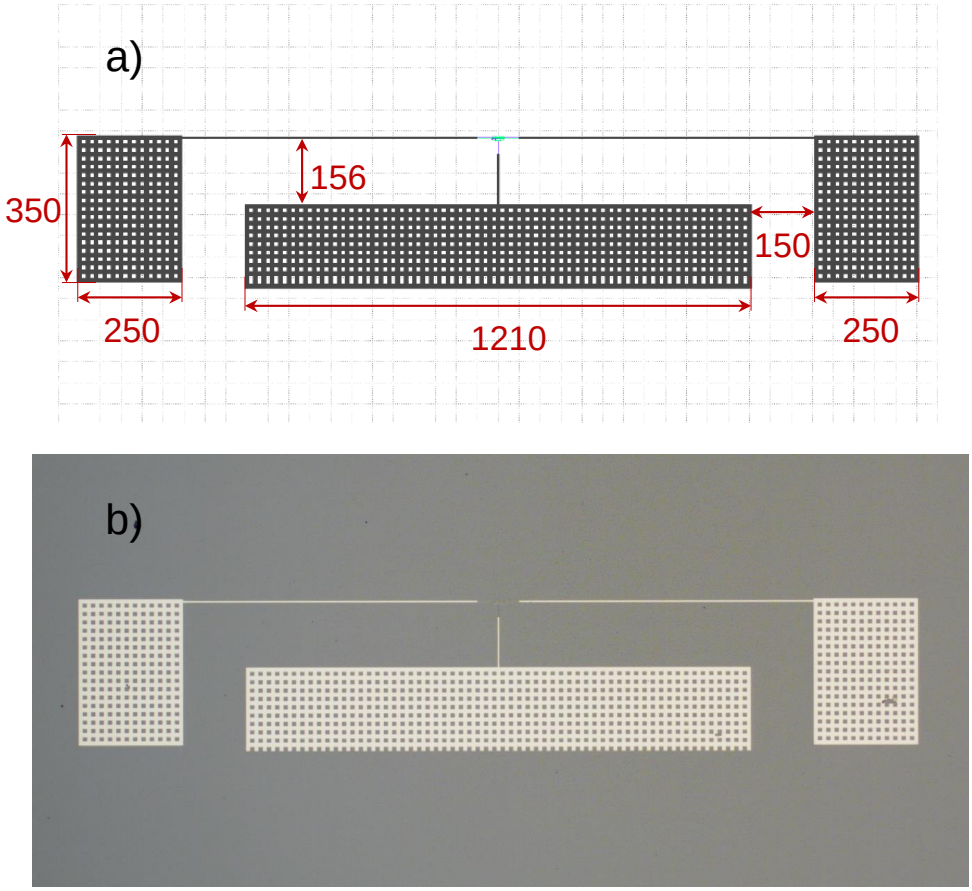

Figure 5.1: a) - Design of Sample-A*, projected by Remy Dassonneville. All sizes are given in μm. The width of wires is $4\mu m$. The size of holes is $10x10\mu m$. b) - Optical microscopy of* Sample-A *after measurements.*

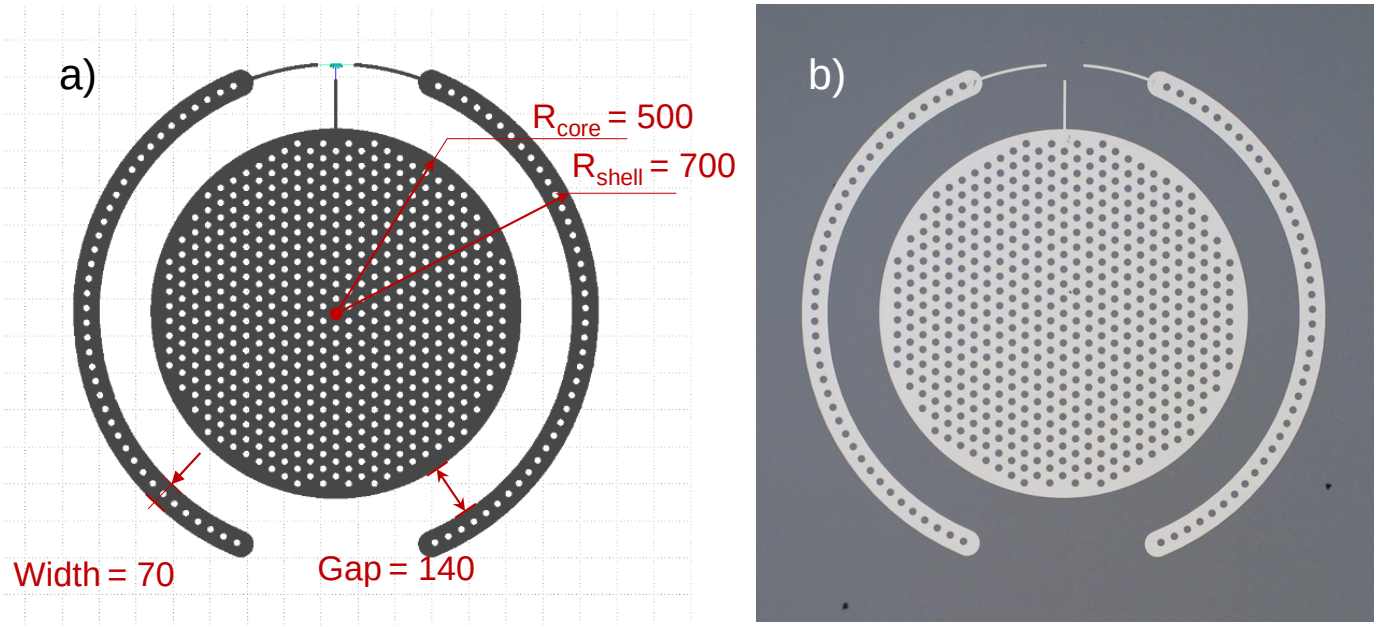

Figure 5.2: a) - Design of Sample-B, *projected by me during my PhD. All sizes are given in μm. The width of wires is $8\mu m$. The diameter of holes is $20\mu m$. b) - Optical microscopy of* Sample-B.

realize *Sample-B*, we kept the standard fabrication recipe developed for *Sample-A*. Consequently, we were able to evaluate the improvements of the qubit and redout properties due to only the design modification. Next step was the *Sample-C* for which an improved fabrication recipe was applied in addition to the previous design optimization.

Sample-A is the first generation of 3D transmon molecules. At this time, the purpose of *Sample-A* was to implement transmon molecules in 3D architecture and to demonstrate the novel readout through polariton.

Sample-B was the second transmon molecule generation. Its main goals were: *(i)* to minimize the residual transverse coupling by using the circular shape of the pads reducing the dipole momentum of the qubit; *(ii)* to explore new readout possibilities in the case of a less nonlinear ancilla; *(iii)* to increase the detuning between the qubit and the polariton readout frequency. As previously stated, the new design described in Chapter 2 was used to produce this sample.

Sample-C was based on the same design as *Sample-B*. The goal of this third-generation was to extend the coherence times of the transmon molecule based on the optimized fabrication recipe described in Chapter 3.

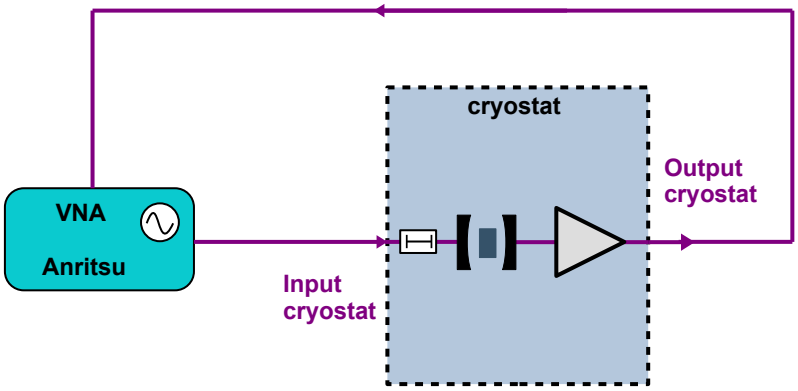

Figure 5.3: Simple single-tone spectroscopy measurement scheme. The VNA sends the probe signal through the coaxial cable to the input port of the fridge. The microwave signal propagates through a series of attenuators inside the refrigerator and reaches the entrance of the 3D-cavity with the sample inside. A part of the probe signal which passes through the cavity comes out through the output port. (The cavity ports are designed to stimulate the signal to leave the cavity through the output port, not through the input port.) The probe signal amplifies and returns to the input port of VNA to get analyzed.

5.2. Spectroscopy of polaritons and qubit

In this section, we will present measurements using continuous microwave spectroscopy. These measurements are made at the beginning in order to characterize the circuit and determine the frequencies of the qubit and the readout modes.

5.2.1. Single-tone spectroscopy

In order to implement single-tone spectroscopy, we connect a vector network analyzer (VNA) to the setup as it is shown in the Fig. 5.3. We measure the transmission of a continuous microwave signal propagating through a 3D cavity interacting with the transmon molecule. Technically, VNA compares the signal passing through the setup with the reference input signal. It measures the transmission coefficient in amplitude and phase. The signal sent by the VNA is called the probe signal. By varying the frequency of the probe signal, we can observe a peak in amplitude in transmission and a strong phase variation that corresponds to the resonant frequency of the 3D-cavity.

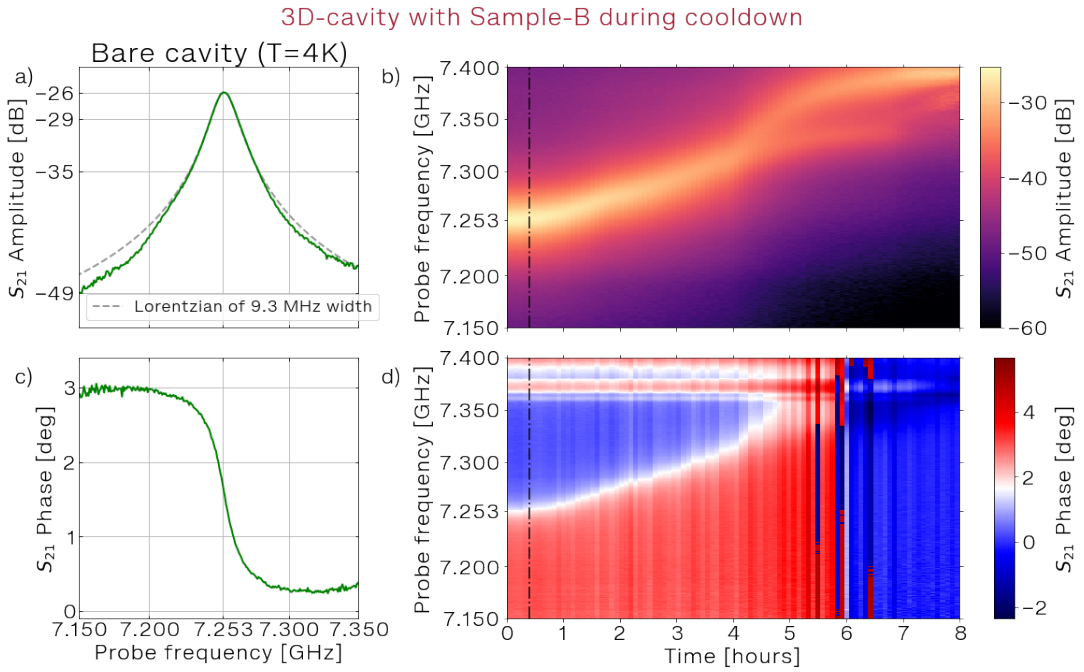

Figure 5.4: a), c) - Single-tone spectroscopy of the bare 3D-cavity measured at 4K. S_{21} amplitude and S_{21} phase are shown in a) and c) as a function of probe frequency. The green line shows measurement data, and the dashed gray line depicts the fit of the Lorentzian function. The extracted resonant frequency is 7.253 GHz and the full width at half maximum equals to 9.3 MHz. b), d) - Single-tone spectroscopy as a function of time, recorded as the temperature decreased from 4K to 50mK. The amplitude (orange to purple) and the phase change (red to blue) are plotted versus probe frequency and time in b) and d), respectively.

Bare 3D-cavity at 4K

At temperatures above the critical superconductivity temperature of aluminum, we measure the bare 3D-cavity frequency. The copper cavity's own resonant mode interacts with the silicon chip inside. However, at 4K the interaction with the aluminum microstructure can be neglected since the circuit remains highly resistive. The result of single-tone spectroscopy at around 4K is shown on Fig. 5.4. The frequency of the peak is around $7.253GHz$ and corresponds to the TE_{101} mode of this cavity with a silicon chip inserted inside.

When the temperature decreases below the critical temperature, the phase transition of aluminum to superconductivity occurs. The modes of the qubit and ancilla associated

with the aluminum device emerge. Because of the strong coupling, the ancilla and cavity form two polaritons.

During cooling, we observe the shift in the resonant frequency (see Fig. 5.4 b) and d)). The shift in the resonant frequency is caused by the appearance of polariton resonances, which can be seen. In Fig. 5.5 we observe two polaritons measured at a very low temperature ($T \approx 30mK$).

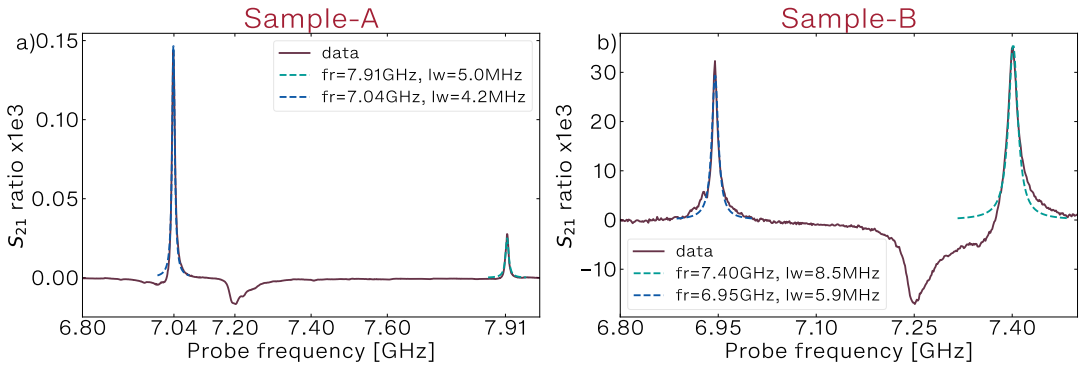

Figure 5.5: Single-tone spectroscopy of two polaritons measured at low temperature ($T \approx 30mK$) a) - Sample-A *and b)* - Sample-B. *Both plots depict the transmission of signal amplitude as a linear ratio vs frequency at zero magnetic flux. We observe the two peaks which fit the Lorentzian curves at frequencies of* $7.04GHZ \pm 1MHz$ *and* $7.91GHz \pm 1MHz$ *for* Sample-A *and* $6.95GHz \pm 1MHz$ *and* $7.40GHz \pm 1MHz$ *for* Sample-B.

Polariton spectroscopy vs magnetic flux

To investigate the polaritons frequency as function of magnetic flux, we sweep the external magnetic field during single-tone spectroscopy. The result is presented in Fig. 5.6. Fig. 5.6 (a) and (b) show measured amplitude of transmitted signal. Each of the plots has the probe frequency on the vertical axis and the magnetic flux $\frac{\Phi}{\Phi_0}$ on the bottom horizontal axis. The supply current corresponding to this flux is indicated on the upper axis. The two resonant peaks are observed as two maxima of amplitude. They correspond to the two polariton mode realized by the hybridization of the 3D-cavity and the ancilla mode of the transmon molecule. These peaks show a strong dependence on the external magnetic field. We observe a slow envelope in the frequencies versus flux of both polaritons, modulated by rapid periodic oscillations. Since the transmon molecule contains superconducting loops, we can change its characteristics by applying an external magnetic field, thus influencing the polariton frequency. The larger one, associated with the qubit, causes fast oscillations of the polariton, whereas small loops of the chain of SQUIDs constituting the inductor are responsible for the slow change of polariton frequency. We observe a little shift between zero of current (on top axis) and zero of magnetic flux (on bottom axis). This is explained by residual environmental magnetic field which remains despite the magnetic shields. (Notice that magnetic field of the Earth is around 25-65 μT) [160], [161].

It is in the local maxima of polaritons that the so-called sweet-spots are located. In these points, the system is less sensitive to magnetic noise. Therefore, it is preferable to measure at these flux values to maximize the coherence time of the qubit. In addition,

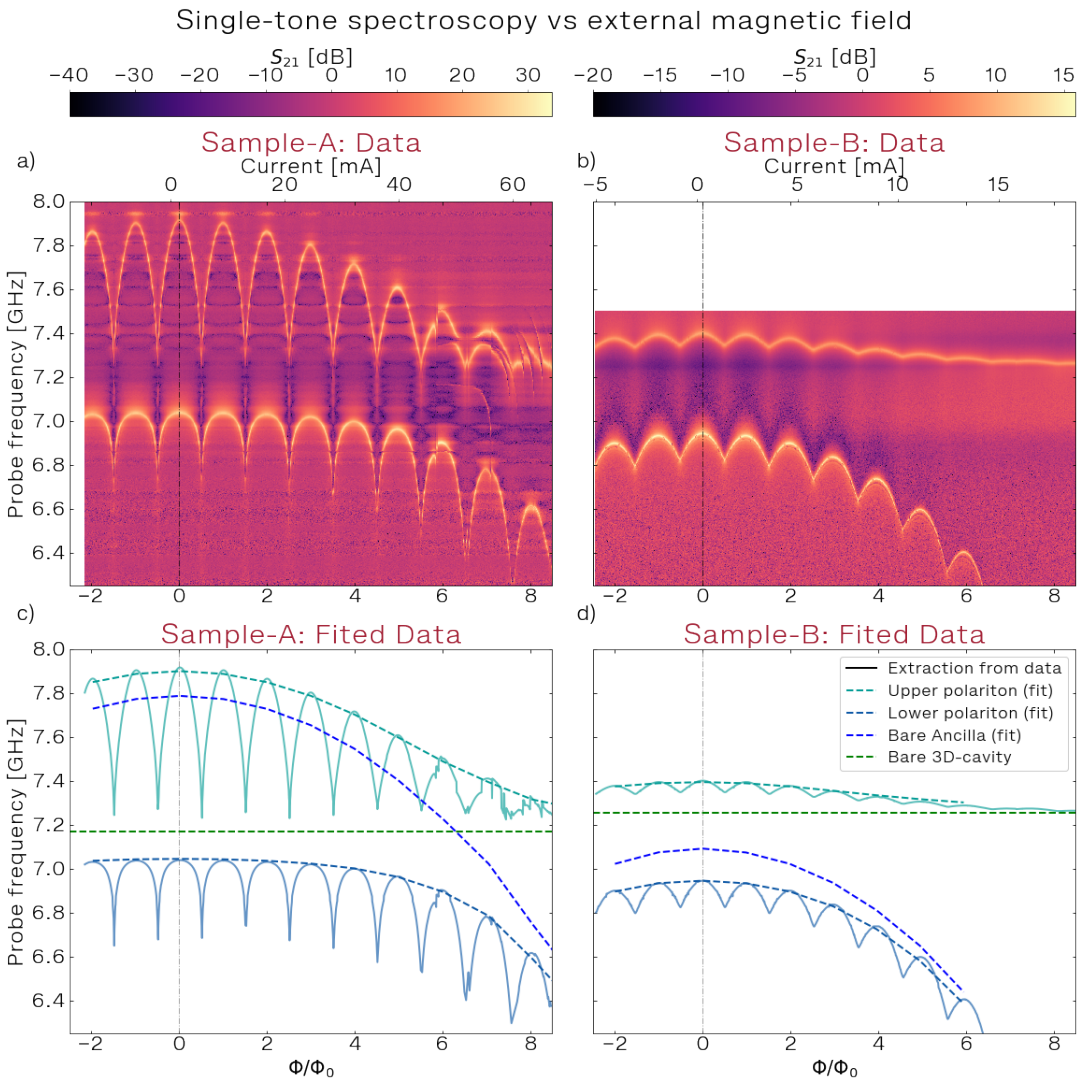

Figure 5.6: Single-tone spectroscopy vs external magnetic field. To generate the magnetic field, we apply a current through a coil of superconducting wire located near the cavity. On the Y axis is the frequency of the VNA. The bottom axis corresponds to the dimensionless magnetic flux passing through the large loop of our transmon molecule, corresponding to the qubit $\frac{\Phi}{\Phi_0}$*, where* $\Phi_0 = 2.067 \cdot 10^{-15} Wb$ *is a magnetic flux quantum. We will continue to use this designation throughout. The top axis corresponds to the current going through the magnetic coil, which is required for this flux.*

in the transmon molecule it is necessary to carry out measurements in the sweet-spots in order to fulfill the symmetry conditions to maximize the cross-Kerr coupling and to cancel additional coupling [90].

Fig. 5.6 (c) and (d) show fits of this data. Solid lines correspond to values of amplitude peaks extracted from the data. Green horizontal dashed line shows the frequency of bare cavity, measured at 4K. The blue line depicts the frequency of bare ancilla. Sea-color and steel-color dashed lines correspond to extracted polaritons frequencies.

To fit these curves, we used the protocol described in detail in [85]. From the single-tone spectroscopy, we obtain frequencies of two polaritons and bare cavity: $\overline{\omega_l}$, $\overline{\omega_u}$ and ω_c. From these values, we calculate the frequency of ancilla when qubit is in ground state: $\overline{\omega_a} = \overline{\omega_l} + \overline{\omega_u} - \omega_c$. Using the formula due to the strong transverse coupling between ancilla and cavity modes:

$$\omega_{u,l}^2 = \frac{\omega_a^2 + \omega_c^2}{2} \pm \frac{1}{2}\sqrt{(4g_{ac})^2\omega_a\omega_c + (\omega_a^2 - \omega_c^2)^2} \tag{5.1}$$

we extracted ancilla-cavity coupling $g_{ac}^A/2\pi$=295 MHz for *Sample-A* and $g_{ac}^B/2\pi$=209 MHz for *Sample-B* from the polaritons anti-level crossing. The bare ancilla frequency is given by: $\omega_a' = \overline{\omega_a} - g_{zz}$. g_{zz}, the ancilla-qubit cross-Kerr coupling is fitted from magnetic flux dependence of χ - cross-Kerr coupling strength between qubit and two polaritons.

The next step is to extract the weight angle θ, given by $\theta = \frac{1}{2}\arctan\left(\frac{2g_{ac}}{\omega_a - \omega_c}\right)$ which reflects the proportion of ancilla and cavity in each polariton. The extracted θ as a function of magnetic flux is presented on Fig. 5.7. The more this angle is close to 90° the more the lower polariton is ancilla-like, and the upper polariton is cavity-like. Inversely, when θ is close to 0° the lower polariton is more cavity-like, and the upper polariton ancilla-like. In case of *Sample-A* the value of θ is crossing value of 45° at the degeneracy point where the frequency of ancilla crosses the frequency of cavity. After that, the polaritons can be said to exchange roles. Indeed, if at zero magnetic flux, the upper polariton is more represented by ancilla than cavity. For magnetic flux greater than five, the upper polariton becomes more cavity-like. *Sample-B* behave differently because the frequency of bare ancilla is always lower than the frequency of bare cavity. This makes that the upper polariton is always more cavity-like, while the lower polariton - more ancilla-like.

Single-tone polariton spectroscopy vs power. Polariton Lamb shift

We study the modification of the mode of the polariton when the power of the probe signal increases. We need this measurement to rationally select the power of the probe signal. For this purpose, we choose the sweet spot corresponding to zero magnetic flux and conduct single-tone spectroscopy by increasing the probe power. The result of this measurement is plotted in Fig. 5.8 (a). The graph shows the amplitude of transmitted signal as a function of frequency and probe power.

At low power (Fig.5.8 b)), we observe two resonant peaks at about $7GHz$ and $7.6GHz$, well-fitted by a Lorentz function. As the probe power increases, the two polariton modes shift toward lower frequencies. At high power around $-55dBm$ (Fig.5.8 c), the two transmission peaks disappear and are replaced by a single Lorentzian peak at frequency of $7.17GHz$. This corresponds to the bare cavity frequency.

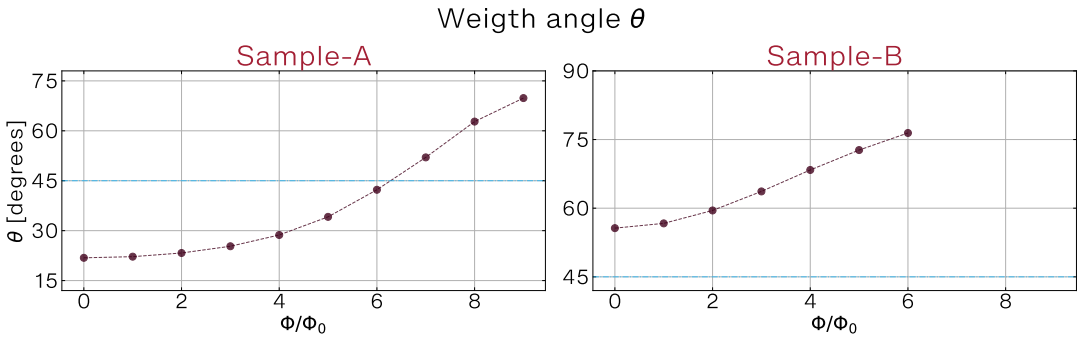

Figure 5.7: Weight angles between ancilla and cavity as function of integer value of magnetic flux. The range of values of this parameter lies within $0°$ *to* $90°$ *A* $45°$ *degree horizontal line correspond to the situation, where the polariton is maximally hybridized between the ancilla and the cavity.*

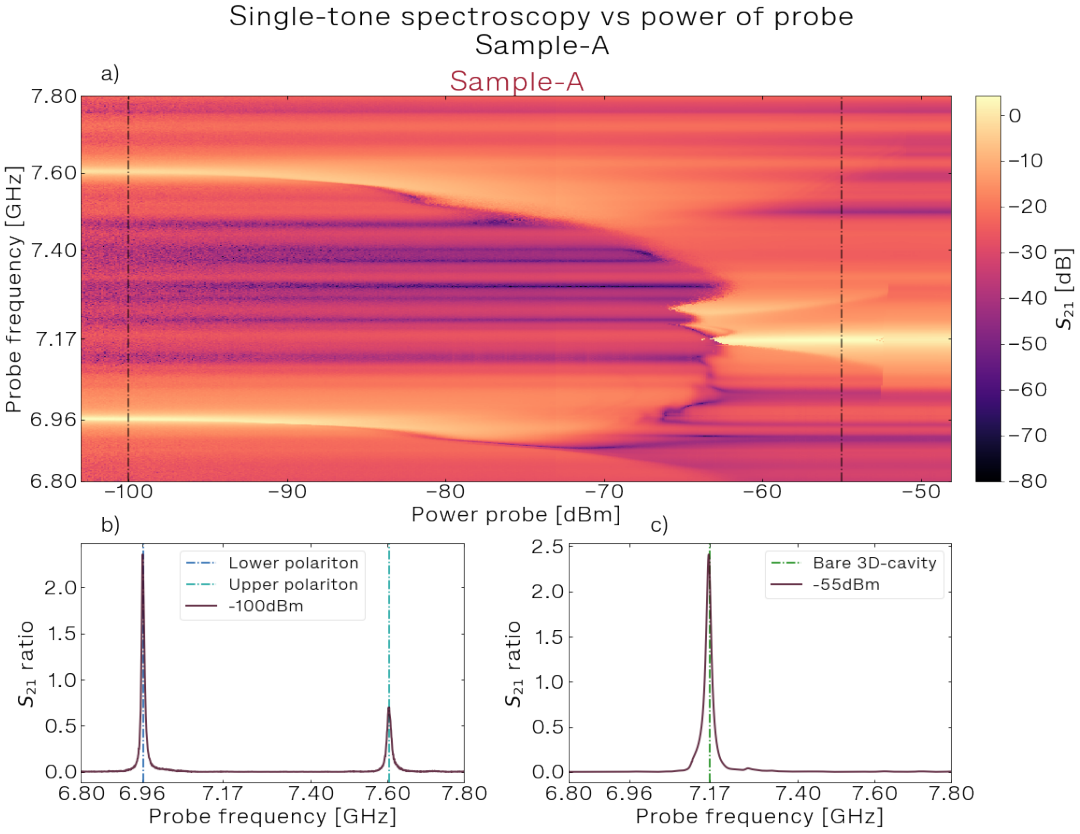

Figure 5.8: a) - Single-tone spectroscopy as a function of probe power and frequency for Sample-A*. The experiment was provided with applied external magnetic flux equal to* $5\Phi_0$*. On the X-axis, the power of the probe estimated at the entrance of the 3D-cavity. The Y axis is the frequency of the probing signal sent by the VNA. The color bar reflects the amplitude of the probe signal transmission. b), c) - Single-tone spectroscopy at given powers of probe (-100 dBm and -55 dBm, respectively). Here and after, measurements are made at zero magnetic flux, unless otherwise indicated.*

With the increase of power, the non-linearity of ancilla causes the Lamb shift of the polariton.

When the signal power at the resonator input exceeds a value of approx. $-55dBm$ the two polariton peaks disappear, and we observe a single peak corresponding to the bare 3D-cavity frequency. At this power level, the oscillating current in the circuit reaches the critical current value, and switches the circuit from superconducting to the normal state.

In the following measurements, we will use a probe signal power that does not cause significant frequency shift.

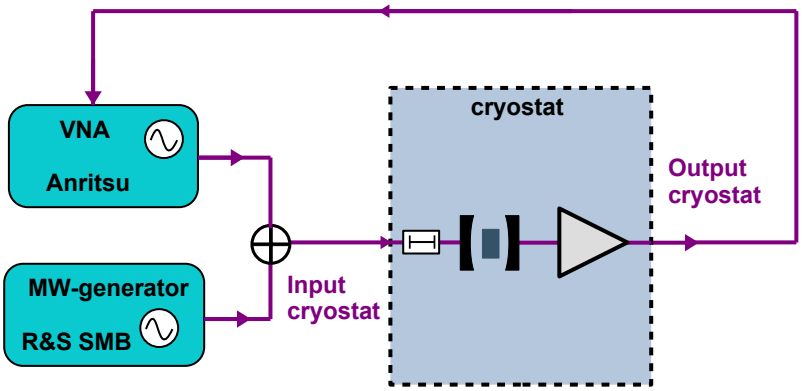

Figure 5.9: Schematic of a two-tone spectroscopy measurement. We use a microwave splitter to add the probe signal from the VNA and the pump signal from the microwave generator. Both signals are fed to the first pore of the resonator. Then the output signal is amplified and fed to the VNA input.

5.2.2. Two-tone spectroscopy

Our next goal is to perform measurements of the qubit mode of the transmon molecule. Since the qubit frequency lies far from the cavity frequency, we do not see it directly. Indeed, the cavity acts as a filter, preventing from transmission any signal far detuned from its resonant frequency. To measure qubit frequency, two-tone spectroscopy is performed. For this measurement, we add a second microwave source in addition to the initial VNA setup as shown on Fig. 5.9. The signal produced by this source is called pump signal and will excite the qubit. The VNA signal we will call probe signal.

Qubit frequency

We observe a frequency shift of the resonator when the qubit changes its state. This shift occurs due to our cross-Kerr coupling [85]. To perform two-tone spectroscopy, we scan the frequency of the pump signal while continuing to measure the transmission of the probe signal through the cavity. The probe signal frequency is usually selected

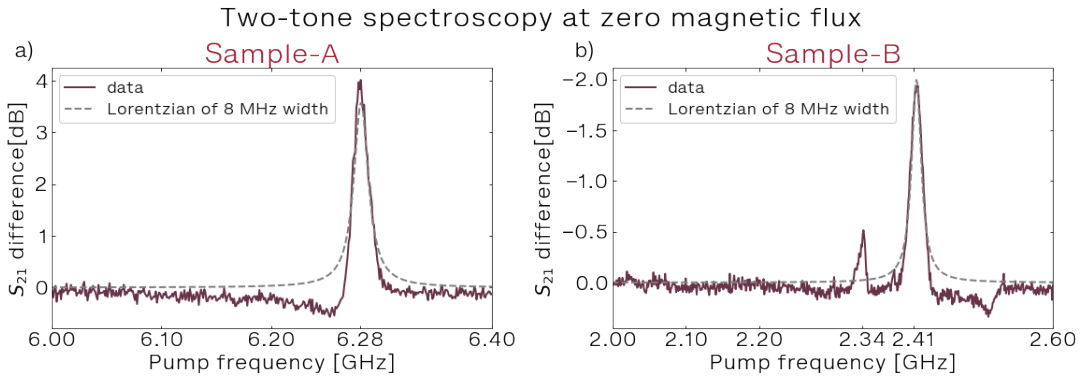

Figure 5.10: Result of two-tone spectroscopy experiment. On the X-axis, the frequency of the pump. The frequency probe was fixed in the vicinity of the resonance frequency of the polariton. On the Y axis is the amplitude of the probe frequency pass-through. It can be seen that when pump frequency reaches a certain value, the amplitude of probe frequency transmission changed. For Sample-A *the probe tone frequency was set to* $7.03GHz$*, which correspond to lower polariton frequency, and for* Sample-B *it was* $7.40GHz$ *,which correspond to upper polariton frequency. These values will continue to be used unless otherwise specified.*

close to the polariton resonance. When the pump frequency coincides with the qubit's frequency, the qubit is partially excited. This causes a shift in the polariton frequency. Consequently, a change is observed in the transmission as the pump frequency is swept while the probe frequency has been fixed (See Fig. 5.10).

This transmission change of the probe signal occurs when the pumping signal frequency matches the qubit transition. From these measurements, we have determined the transition frequency $|0\rangle \rightarrow |1\rangle$ of the qubit. The change in transmission is due to a shift in polariton frequency.

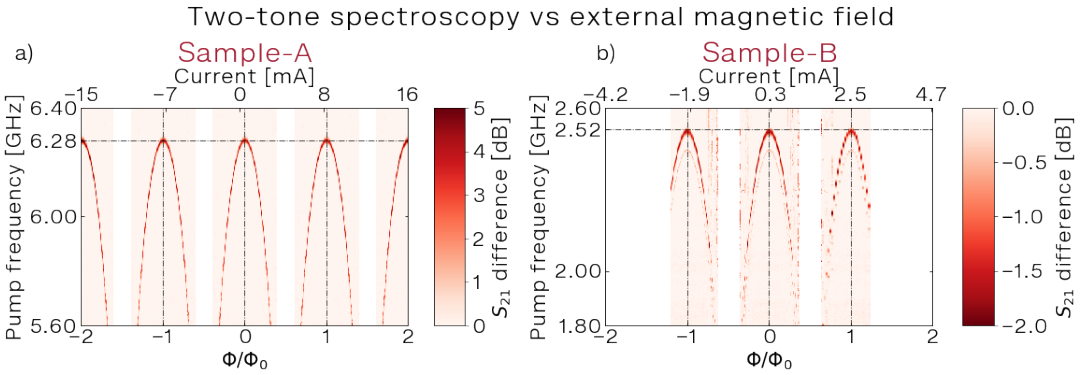

Figure 5.11: Two-tone spectroscopy vs magnetic flux made for Sample-A *a) and* Sample-B *b). Bottom axes show a magnetic flux, and top axes show the current in the coil, correspond to this flux. Left axis show pump frequency. The color corresponds to transmission amplitude of the probe signal.*

Qubit frequency vs magnetic flux

In Fig. 5.11 we plot the transmitted probe signal as function of the frequency pump and the magnetic flux. We observe the qubit resonance frequency, which strongly

depends on the magnetic field. Its maximum is around $6.29GHz$ for *Sample-A* and $2.52GHz$ for *Sample-B*. Qubit frequency behaves periodically, and its maximums are almost the same. The period of this dependence is around $7.7 \pm 0.05\ mA$ for *Sample-A* and $2.18 \pm 0.02\ mA$ for*Sample-B*. We have already observed the same periodicity through the polariton's frequency versus magnetic field. However, since the frequency of the qubit is more sensitive to the magnetic field than the polariton frequency, we accurately determine the current value for the sweet spot by looking for the maximum qubit frequency.

This period corresponds to a magnetic flux passing through the big loop of the transmon molecule. For *Sample-A* it corresponds to $1\Phi_0$ per $7.7mA$. From this periodic magnetic flux, we establish the law between magnetic flux passing through the circuit loop and the electric current in the magnetic coil. For *sample-A* area of the big loop is about $S_{Loop_Q} = 5\mu m \times 28\mu m$. For *sample-B* the area of this loop was $S_{Loop_Q} = 5\mu m \times 32\mu m$. Since the two coils were different, we can not compare the maximum values' periodicity of the two samples.

The offset of current for zero magnetic flux was estimated as $280\ \mu A \pm 10\ \mu A$ for *Sample-A* and $292\ \mu A \pm 10\ \mu A$ for *Sample-B*. The reason of this offset were already discussed in comments to Fig.5.6. Since the magnetic flux passing through a big loop of transmon molecule equal to one magnetic flux quantum corresponds to a coil current of about $870\mu A$, we can estimate the residual magnetic field in the sample to be around $2\mu T$.

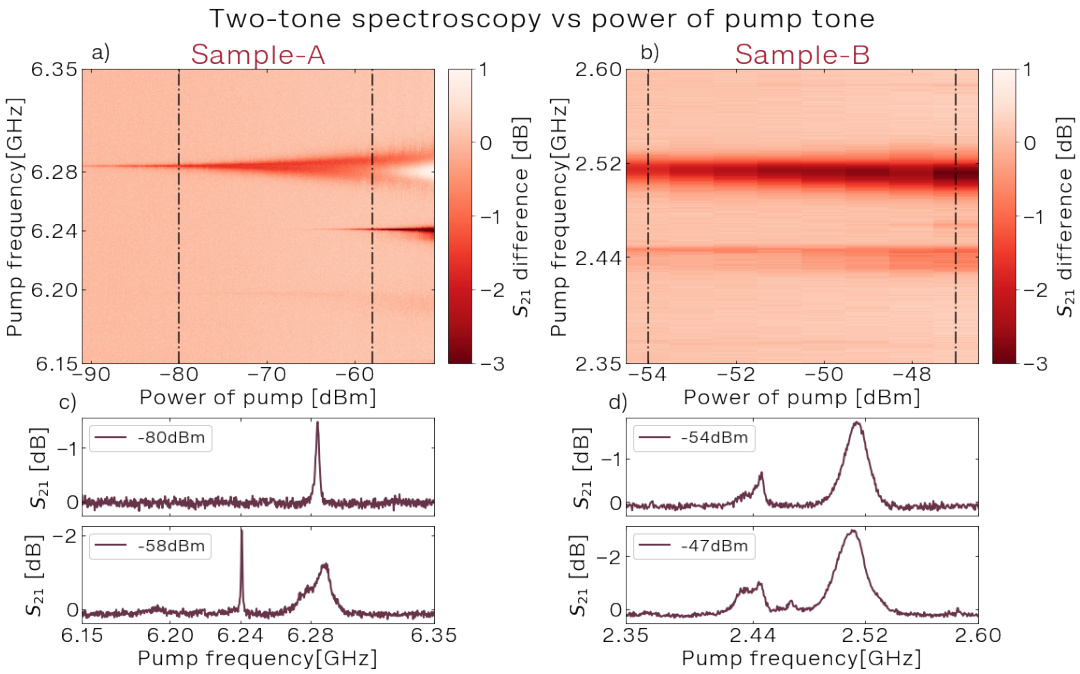

Figure 5.12: a), b) - Two-tone spectroscopy as a function of power and frequency of pump tone. As the power increases, there are more transitions between the energy levels of the qubit. Due to this, it is possible to extract values of qubit anharmonicity α_q. c), d) - Two-tone spectroscopy at a given pump powers. The frequencies of the peaks are $6.24GHz$ and $6.29GHz$ for Sample-A *and $2.44GHz$ and $2.52GHz$ for* Sample-B.

Qubit frequency vs power of pump

To extract the anharmonicity of the qubit mode, we probe higher-order transitions. For this purpose, we increase the pump signal power until we find other peaks. A second peak corresponding to transition frequency $|1\rangle \rightarrow |2\rangle$ appears first.

This transition is possible due to the probability of qubit being observed in state $|1\rangle$ as a result of thermalization.

We observe this transition in *Sample-B* (Fig. 5.12 (b) and (d)) but not in *Sample-A* which had better thermal connection to the sample holder.

When the pumping power is high enough, the peak associated to the two-photon transition $|0\rangle \rightarrow |2\rangle$ is also detected (Fig. 5.12 (a) and (c)). This two-photon transition $\frac{\omega_{2,1}}{2}$ is located between the qubit transition $\omega_{0,1}$ and $\omega_{1,2}$ (see the small peak on Fig. 5.12 (d)). The anharmonicity of the qubit is extracted through the formula: $\alpha_q = \omega_{2,0} - 2\omega_{1,0}$. The anharmonicity of qubit α_q was defined as $-88MHz$ for *Sample-A* and $-76.2MHz$ for *Sample-B*.

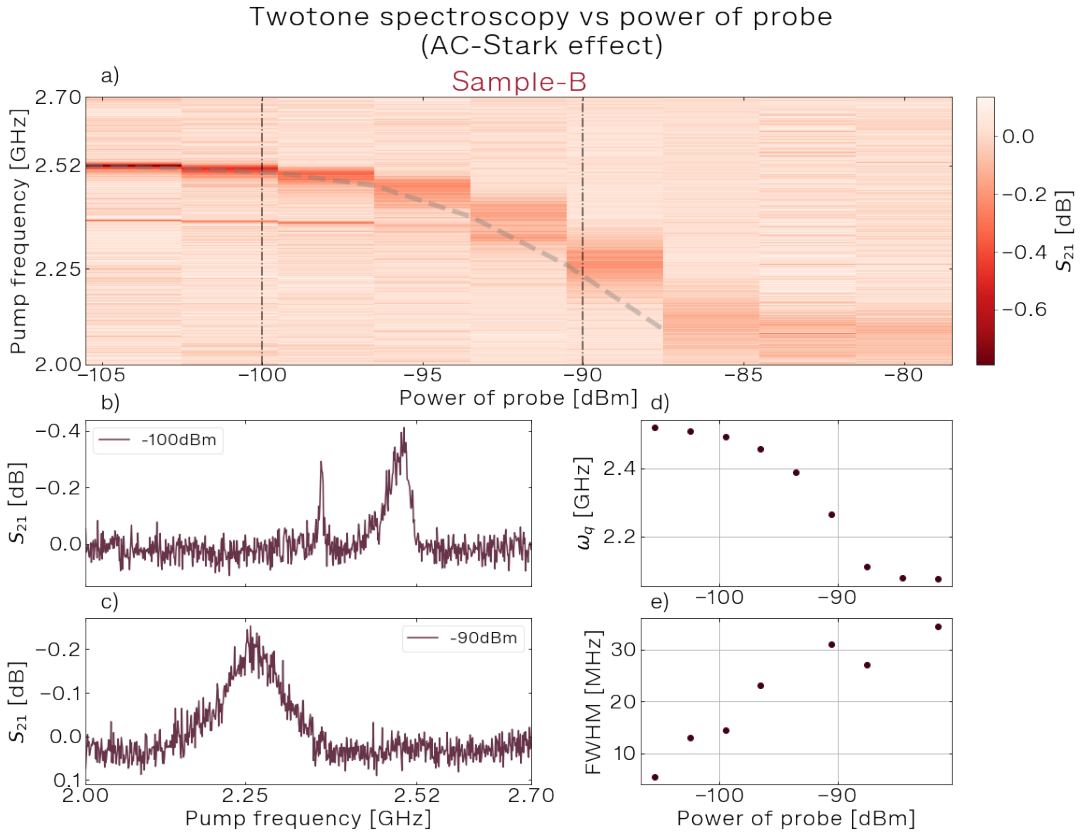

Figure 5.13: Broadening and frequency shift of the qubit's resonance peak as function of probe tone power. a) Two-tone spectroscopy as a function of power of probe (X-axis) and frequency of pump tone (Y-axis) for Sample-B*. b), c) - two-tone spectroscopy at given probe tone powers. d), e) - values of qubit frequency ω_q and linewidth of its peak as a function of probe power, extracted by fitting data by Lorenzian function. A grey dashed line shows the trend of qubit frequency shift.*

AC-Stark effect. Qubit frequency vs power of probe tone

Qubit AC-Stark shift is a frequency shift of the qubit induced by the occupation of the resonator mode by photons whose fluctuations of their number are also producing the qubit line broadening [162]. In our case, the role of the resonator will be played by a polariton.

We perform the two-tone spectroscopy measurements by increasing the power of a probe signal (Fig. 5.13). At low power of probe signal, we observe the two peaks. The peak of higher frequency corresponds to the qubit $|0\rangle \rightarrow |1\rangle$ transition. With the increase of probe power, we observe the decrease of frequency of the transition and broadening of the peak's linewidth.

The Fig. 5.13 d), e) show quantified values of qubit's peak frequency and linewidth as a function of probe power.

During other measurements, we aim not to increase the power of probe pulse higher than $-100dBm$ to avoid the unwanted AC-Stark effect.

5.2.3. Conclusions of spectroscopy measurements

Based on the results of spectroscopic studies, we were able to characterize *sample-B* and compare it with the target characteristics as well as with *sample-A*.

The precise parameters of *Sample-B* were estimated using numerical modeling by Cyril Mori during his master internship [163].

The extracted characteristics are included in Table 5.1. The four columns present *Sample-A*, the target value *Sample-B* and *Sample-C*, respectively. The target value has been defined in chapter 2 as the objective of *Sample-B* and *Sample-C* realization. As we can see from this table, the physical and the circuit parameters correspond reasonably well to the target values.

For the last sample *Sample-C* not all the parameters were extracted yet. We have measured frequencies of qubit and ancilla, and in the assumption that capacitance remains the same for the same design of aluminum pads, we extracted the expected E_j and L_a. That's why the color of these cells is blue.

5.3. Coherence times of qubit

In the following section, we focus on investigating the coherence times of the transmon molecule. We start with a brief description of a microwave measurement setup, which has been discussed in more detail in chapter 4. Next, we present the results of time-domain spectroscopy measurements: *(i)* we introduce T_{Rabi} and T_π, extracted by Rabi experiments; *(ii)* we measure the relaxation time T_1; *(iii)* we discuss the dephasing time T_2 obtained in Ramsey experiment and precisely calibrate the qubit frequency; *(iv)* we calibrate the number of polaritons n_{po} (Ramsey-Stark experiment). Finally, in this section, we discuss the results of the conditional transmission experiment and extract the cross-Kerr couplings χ between the qubit and polaritons. Throughout this section, we continue to compare the results of two samples, *Sample-A* and *Sample-B*. In addition, the first experimental results on *Sample-C* will also be presented for consideration.

All the following measurements were made at zero magnetic flux unless otherwise specified.

Value	*Sample-A*	Target	*Sample-B*	*Sample-C*
$\omega_Q/2\pi$ $[GHz]$	6.284	2.78	2.523	2.811
$\omega_A/2\pi$ $[GHz]$	7.78	7.35	7.092	6.692
$g_{ac}/2\pi$ $[MHz]$	295	> 100	290	246
$\alpha_q/2\pi$ $[MHz]$	-88	-77	-76.2	-
$U_A/2\pi$ $[MHz]$	-13.5	-1.3	-1.92	-
$g_{zz}/2\pi$ $[MHz]$	34.5	10.1	13.6	-
C_s $[fF]$	110	125	129	129
C_t $[fF]$	59.6	87	83.5	83.5
$E_j/2\pi\hbar$ $[GHz]$	29.2	7.3	5.76	6.91
L_A $[nH]$	5.32	2.66	3.59	3.87

Table 5.1: Spectroscopic and electrical characteristics' comparison between three samples and the target values. First the Sample-A *was measured, then the target parameters were chosen and* Sample-B *was developed. The blue color of text corresponds to the values which have been chosen or approximated, while black text is related to values which were extracted experimentally.*

In subsequent experiments, we used the lower polariton to readout qubit state of *Sample-A* and the upper polariton to readout qubit state of *Sample-B*, unless otherwise specified. It is based on the fact that the transmission rate increases with polariton's frequency approaching the bare cavity. As a result, the signal-to-noise ratio increases.

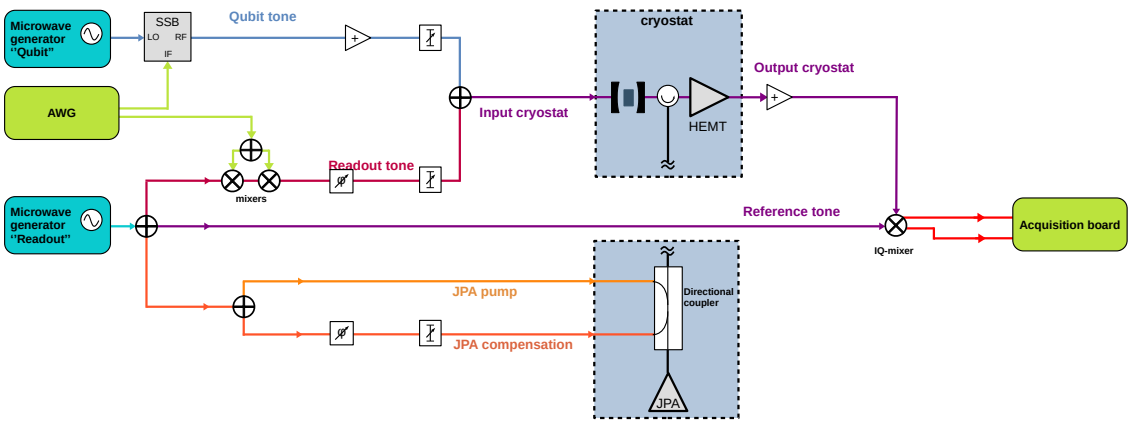

Figure 5.14: Simplified microwave setup to provide time-domain measurements.

5.3.1. Time-domain measurements setup

A brief description of time-domain microwave measurement setup is depicted by Fig. 5.14. For detailed description, see Chapter 4. To modulate the pump signal, a Single Sideband Modulator (SSB) is used. We also use two mixers to shape the probe signal in the time domain and an IQ-mixer for down-conversion of the probe signal to dc signal. After this down-conversion, the two voltage signals I and Q are amplified, filtered and sent to the acquisition board.

In all subsequent time-domain experiments, we measure the two voltages from

the IQ-mixer. In our measurement, these voltages correspond to the in-phase and quadrature components.

The two qubit states correspond to a point on the complex plane, given by its I and Q values.

In further discussion, we will stick to another value called "distance", which is more convenient to use if we focus on qubit state readout.

We define this value as:

$$D = \sqrt{(I - I_0)^2 + (Q - Q_0)^2}, \tag{5.2}$$

where I_0 and Q_0 correspond to base values of I and Q measured at the initial time $\tau = 0$.

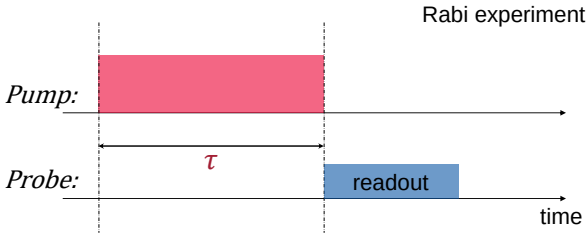

Figure 5.15: Pulse sequence for Rabi experiment. We apply a pump-pulse with variable duration τ to drive qubit Rabi-oscillations. Then we read out the state of qubit by applying a probe-pulse.

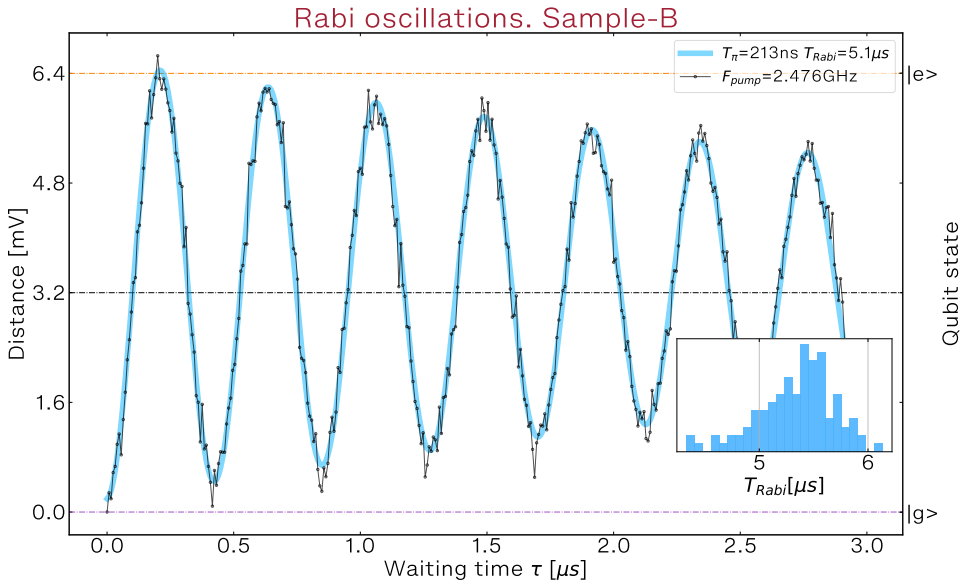

Figure 5.16: Rabi oscillations measured for Sample-B. *The duration of the pump-pulse τ is plotted along the X-axis. The Y-axis shows the distance defined in Formula 5.2. The result of the experiment averaged over a few thousands times is depicted by black points. The blue curve presents the fit of the data by exponentially decaying sine. The distribution of extracted T_{Rabi} is shown on a histogram in the right-low corner.*

5.3.2. Rabi experiment: T_{pi}, T_{Rabi}

The goal of the next experiment is to calibrate the π-pulse for further work, as well as to extract the T_{Rabi}, the decay time of the Rabi oscillation in order to characterize the system. Fig. 5.15 depicts a pulse sequence required to conduct this experiment. We send the pump tone of variable duration τ and immediately after we read out the qubit state by sending a probe pulse. This pulse sequence we repeat around 1000 times for each τ and average the results. The resonant microwave field of the pump causes Rabi oscillations of the qubit. Depending on the duration of this interaction, the final qubit state changes between pure $|g\rangle$ and $|e\rangle$ states passing through coherent superposition states. This process can be presented as rotation of the Bloch-sphere around the X-axis. The probability of qubit in state $|e\rangle$ is given by:

$$P_{|e\rangle}(\tau) = \frac{1}{2} \cdot (1 - cos(\Omega_{Rabi}\tau)) \cdot exp(-\frac{\tau}{T_{Rabi}}), \tag{5.3}$$

where the Rabi oscillation Ω_{Rabi} depends on the microwave pump amplitude field Ω_{field} through:

$$\Omega_{Rabi} = \sqrt{\Omega_{field}^2 + (\omega - \omega_Q)^2}. \tag{5.4}$$

An example of measured Rabi-oscillations is shown on Fig. 5.16. At the beginning, the state of the qubit is thermal and close to $|g\rangle$. Consequently, if we read out it at this time, we are likely to get a $|g\rangle$ state. Therefore, the point on the IQ-plane that we had measured when the duration of the pump-pulse was zero is close to state $|g\rangle$. It will be our reference point giving I_0, Q_0 for the distance. The increasing pump-pulse duration changes the position of the point on the IQ-plane. The distance between the initial state and the final state begins to grow. However, after reaching its maximum value, it plummets to almost zero. When the distance is maximal, it means that qubit reaches the $|e\rangle$-state. That duration of pump pulse, which corresponds to the maximum in distance, defines the pi-pulse. (The name π-pulse is given since the pulse of this duration produces a rotation of Bloch-vector on the Bloch sphere on the angle of π). In addition, we observe that the amplitude of oscillations decreases with the duration of the pump pulse. This decay is explained because the system is not isolated from the environment. Over time, the state of the qubit becomes more and more random, losing its coherence. From this experimental decay, we can determine the characteristic decay time of Rabi-oscillations T_{Rabi}.

We repeat this experiment, using different pump-frequencies, that is, with variable tuning between ω_q and ω_{pump}. The results of this variation are shown on Fig. 5.17 e), f) (for *Sample-A* and *Sample-B* respectively). On plots a), b), c), d) horizontal cross-sections of these pseudo-color plots are depicted. For instance, the pump frequency for a) and c) is $6.310GHz$, and $6.296GHz$, respectively. By comparing plots a) and c) we observe that the frequency of Rabi oscillation changes with the detuning. In our example, it drops by a factor of 1.7.

Fig. 5.17 (g) and (h) present the extracted frequency of Rabi-oscillations as a function of detuning fitted according to Formula 5.4. From this fit, we extract qubit frequency to be $6.297GHz$ and $2.475GHz$ for *Sample-A* and *Sample-B*, respectively. It leads to π-pulse duration T_π equal to 30 and 51 ns for a given pump amplitude. T_{Rabi} was also measured for both samples and is around $2.8\mu s$ and $5.3\mu s$.

We change the time of π-pulse by changing the power of the pump tone. Since the resolution of our arbitrary waveform generator is discrete with a limiting step of

$1ns$, we calibrate the pump power corresponding to a π-pulse to an integer number of nanoseconds.

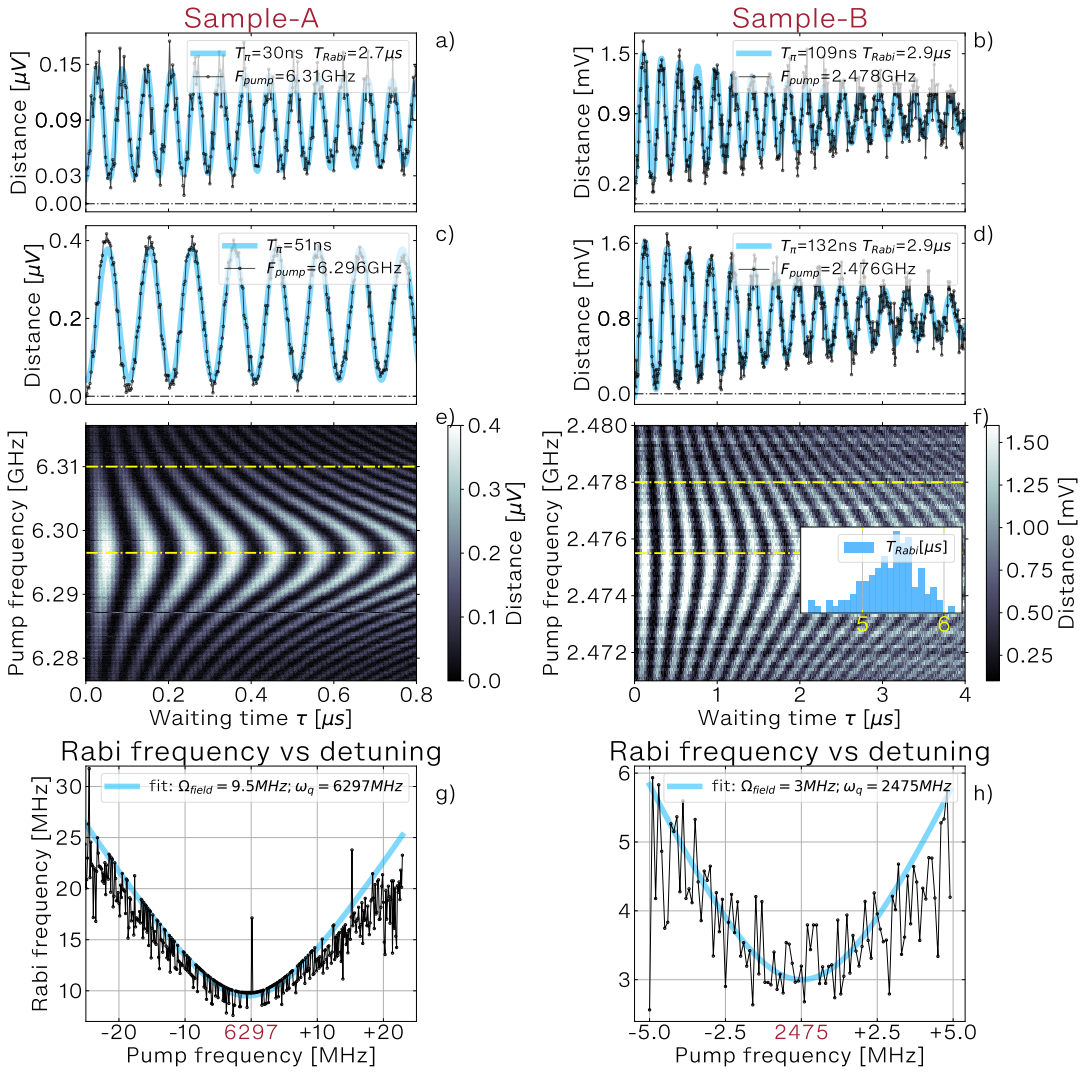

Figure 5.17: Rabi chevrons, resulting from measurements of Rabi oscillations as a function of pump frequency. Results of Sample-A *and* Sample-B *are demonstrated by the left and right columns, respectively. Plots a) and b) show the Rabi oscillations at the pump frequency* $10MHz$ *detuned from the qubit resonance frequency. Plots c) and d) show the Rabi oscillations at the pump frequency, matching the qubit resonance. We observe slower oscillations in this case. On the plots e) and f) the distance is depicted as a function of waiting time* τ *and pump frequency. Plots g) and h) show the Rabi frequency as a function of pump frequency. Black points represent the Rabi frequency extracted from Rabi oscillations. The blue curve depicts the fit of this data.*

5.3.3. Relaxation - T_1

The next experiment is devoted to measuring the relaxation time of the qubit. Fig. 5.18 shows the pulse sequence we apply for this experiment. The idea is to prepare a $|e\rangle$-state of a qubit through a π-pulse, wait for time τ and readout the qubit state. Based on average results, we measure the probability of qubit to keep its $|e\rangle$ state.

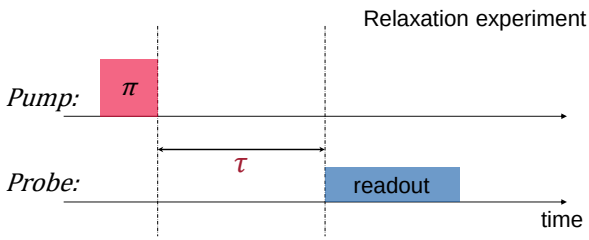

Figure 5.18: Pulse sequence for relaxation experiment We prepare a $|e\rangle$-state of the qubit by applying a π-pulse and making readout after a variable amount of time τ.

Fig. 5.20 shows the result of this experiment for both samples. To provide this experiment we average over 3000 readouts. We expect the qubit state to decay exponentially with time:

$$P_e(\tau) = e^{-\frac{\tau-\tau_0}{T_1}} \tag{5.5}$$

By fitting the experimental data, we extract $T_1^{(A)} = 3.4\ \mu s$ and $T_1^{(B)} = 15.1\ \mu s$ for *Sample-A* and *Sample-B*, respectively. However, the value of extracted T_1 fluctuates from one measurement to another [33]. To estimate this effect, we have repeated this measurement over a few hours to plot the histograms shown in Fig. 5.20 c), d). As we see, the distribution of resulting T_1 is almost Gaussian and has a deviation of about 15% in both cases. We also notice a slight improvement in relaxation time of *Sample-B*, when we move it from one dilution refrigerator to another. This we explain by the fact, that the second refrigerator has the better filtering microwave lines optimized for measuring qubits.

As we have mentioned before, the motivation of making a new generation of samples was mainly to improve the relaxation time. Judging by the experiment results, this goal is achieved.

5.3.4. Relaxation time as a function of magnetic flux

Trying to understand the reasons causing relatively low T_1 of *Sample-A* we provide relaxation experiments in different flux points. The results of this experiment for *Sample-A* and *Sample-B* are shown in Fig. 5.20. We have plotted both results along one Y-axis with *Sample-B* presented above *Sample-A*. For each magnetic flux, we have made more than one thousand T_1 measurements. For *Sample-A*, in Fig. 5.20 b), T_1 tends to decrease significantly with an increase of magnetic flux. This can be explained by the fact that with the increase in magnetic flux, ancilla frequency ω_a reduces, whereas the qubit frequency ω_q remains constant. This means that detuning Δ_{qa} is decreasing with increasing magnetic flux leading to a larger Purcell effect, if there is a residual transverse coupling.

Indeed, according to our initial hypothesis, due to the asymmetry of Josephson junctions and probably some misalignment of the sample inside 3D-cavity, some residual transverse coupling remains and produces the Purcell effect. This hypothesis was checked through Ansys HFSS modeling by Gonzalo Troncozo [164] during his master internship and by numerical modeling by Remy Dassonneville in his thesis [84]. Based on this, significant changes between *Sample-A* and *Sample-B* were introduced into sample design: the shape of pads of the transmon molecule was changed to a circular one to reduce the qubit dipole moment (see Chapter2 for details).

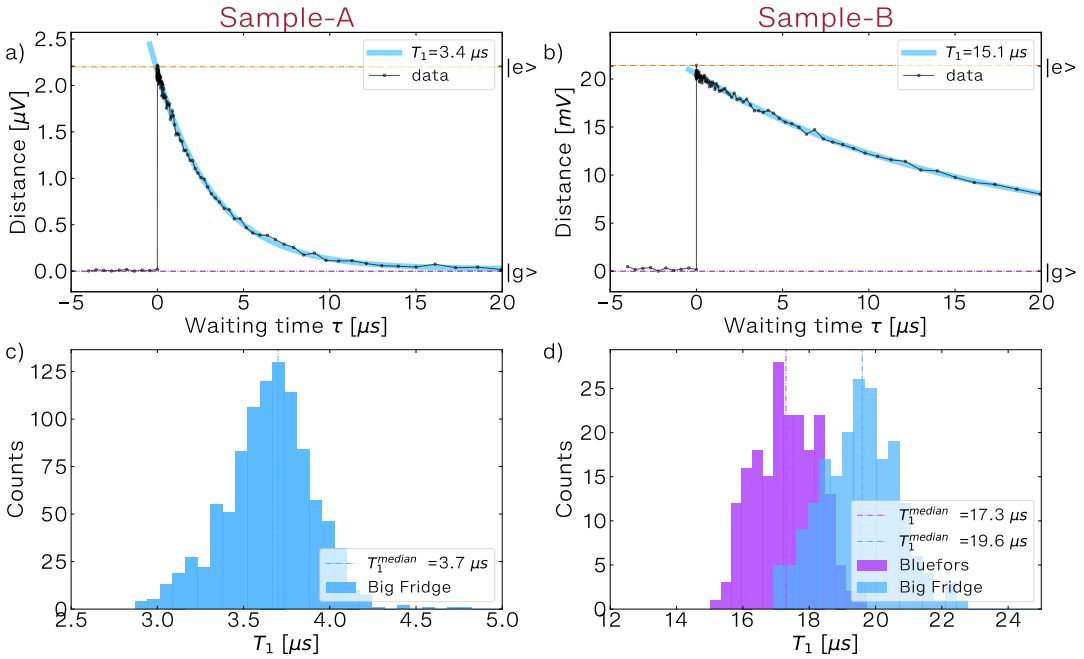

Figure 5.19: Plots a) and b) represent the result of the relaxation experiment for Sample-A *and* Sample-B*, respectively. The waiting time between π-pulse and readout pulse τ is plotted along the X-axis. The Y-axis shows the distance value. Black points show the experiment result averaged over thousands times. The blue curve shows the exponential decay fit of the data. The legend shows values of T_1, extracted from the fit. The purple and orange horizontal dashed lines reflect the minimum and maximum values of the distance. The minimum and maximum distance values correspond to qubit states $|g\rangle$ and $|e\rangle$, respectively. Plots c) and d) show the distribution of T_1 values for* Sample-A *and* Sample-B*, respectively. These values are extracted from a thousand repetitions of the relaxation experiment (each experiment includes a few thousand of averaging). The X-axis reflects the T_1 value and the Y-axis shows the number of counts. Vertical dashed lines represent the median values of registered T_1. Blue and purple histograms correspond to the experiments conducted in two different refrigerators.*

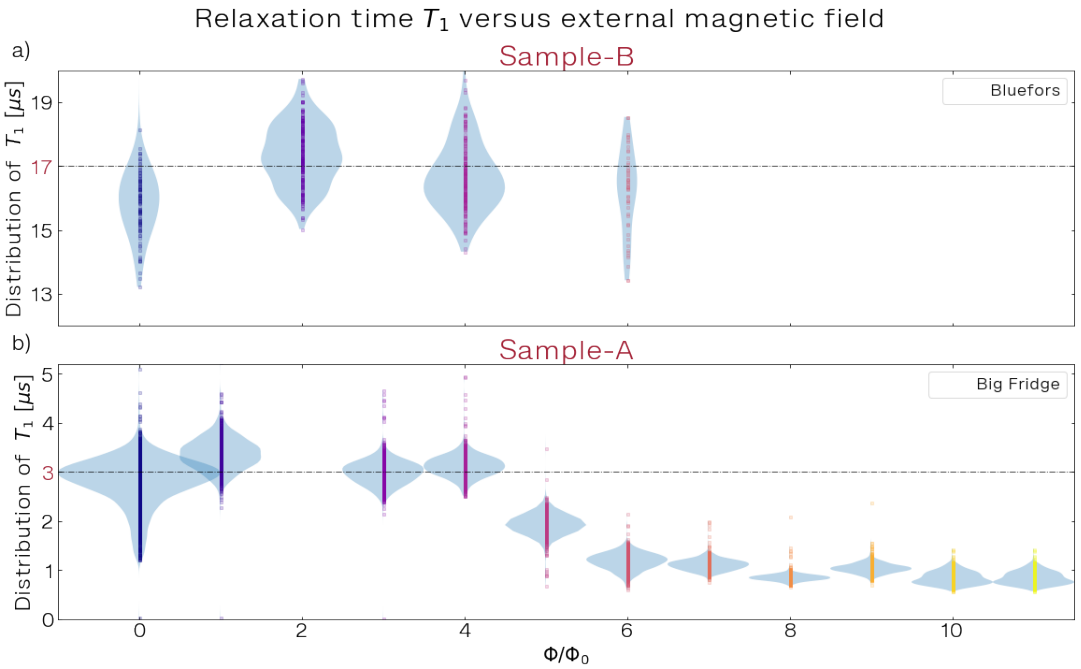

Figure 5.20: T_1 distribution is depicted as a function of magnetic flux for Sample-B *and* Sample-A*. The inverse of plots is made to keep the consistency of the Y-axes. The shape of the "violin" plots reflects the distribution of results for T_1 measurements.*

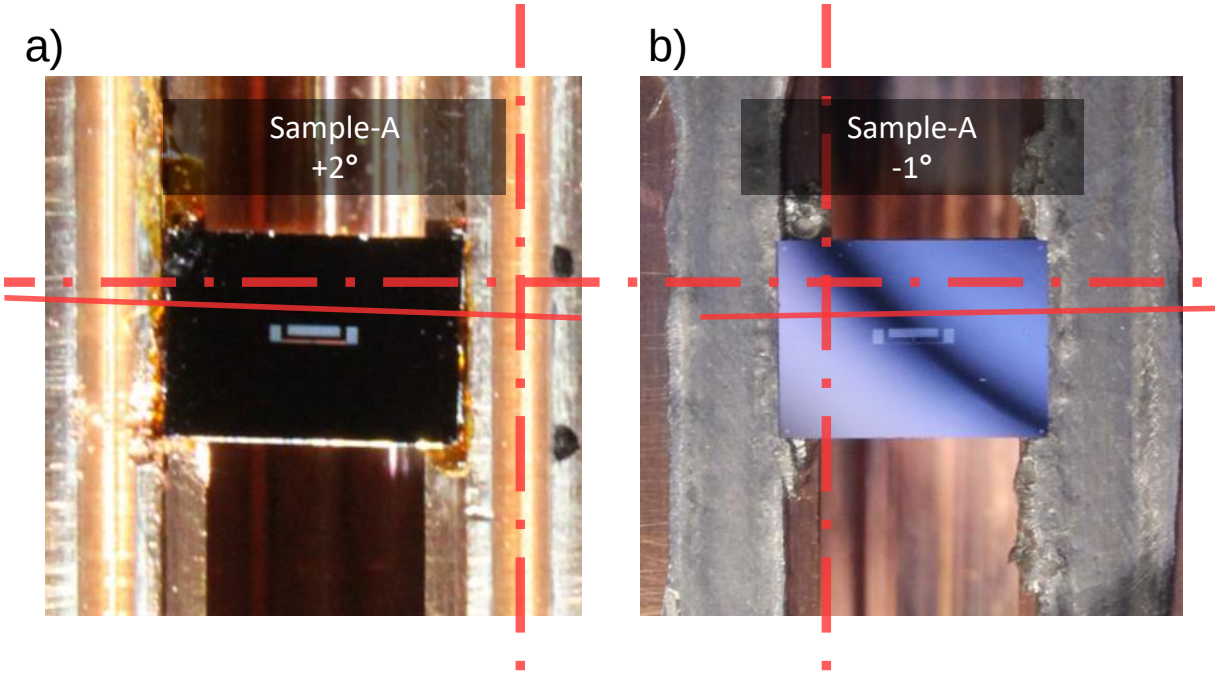

Figure 5.21: Photo of Sample-A *before and after rotation in 3D-cavity, which was made to correct the angle of sample misalignment. See plots a) and b), respectively. The red dashed lines represent the correct angle of 90°, in comparison to the actual angle reflected by the solid red line. The angle was corrected from +2° to the target value of −1° to compensate the Josephson junctions' asymmetry.*

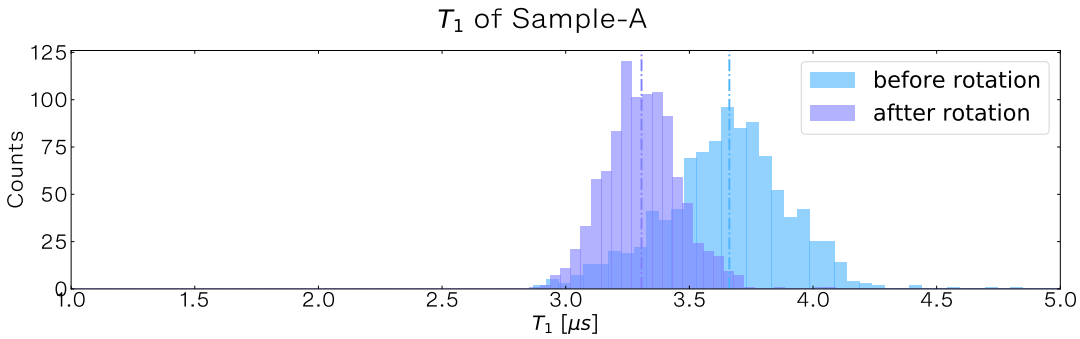

Figure 5.22: Results of statistical measurements of relaxation time for Sample-A *before and after rotation in cavity. We see that median value of T_1 was slightly changed. Both experiments were conducted 1000 times with averaging over 2000 samples. The time period between the two experiments equals to 3.5 months. (The first experiment was provided on 18 February 2020, and the second one on 8 June of 2020.)*

Through systematic HFSS simulations we have demonstrated the following [164]: *(i)* the quality factor of qubit mode depends strongly on both the misalignment of the sample within the 3D-cavity and the asymmetry of the small Josephson junctions, *(ii)* asymmetry of transitions can in principle be compensated by a small change in the angle of rotation of the sample and vice versa. For each value of the resulting asymmetry of junctions, the sample rotation angle was calculated to compensate the asymmetry and maximize the quality factor of qubit mode.

From this study, we have tried to rotate the sample inside the cavity at a given angle, trying to compensate the asymmetry of our circuit. The result of this experiment is shown in Fig. 5.21. After opening the cavity, the angle of sample misalignment was measured. The angle was $+2°$. After removing the sample carefully, we changed the angle of misalignment to $-1°$. This angle was estimated according to HFSS modeling with motivation to compensate for the asymmetry of junctions. Nevertheless, no significant difference in T_1 was observed after this manipulation. The median value of T_1 has even decreased from 3.6 μs to around 3.3 μs. This change can be related to degradation of the chip with time. Indeed, four months have passed between the two experiments, and most of the time the sample was stored in a dilution fridge at room temperature because of COVID lockdown in France.

5.3.5. Improved relaxation time with a new nanofabrication recipe

We observed a significant improvement in the T_1 for *Sample-C* comparing to *Sample-C*. Despite the considerable variation, it almost never fell below 50 μs and the median value lie around 122 μs. The measurements of this sample, and samples from the same fabrication run, will be continued. At this point we suspect that this new nanofabrication recipe has improved the relaxation time as we had hoped to start developing it.

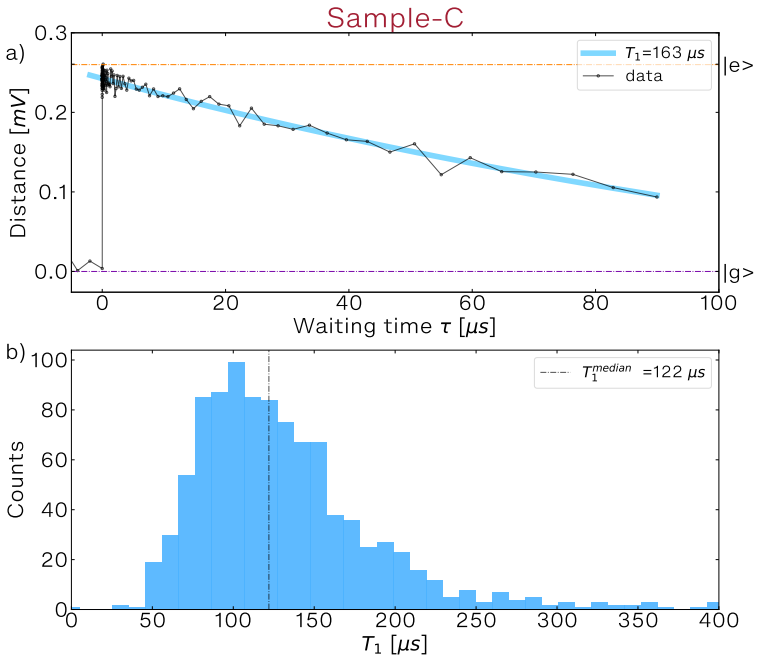

Figure 5.23: Recent result of relaxation time measurement for Sample-C*, which was fabricated by the same design as* Sample-B*, but using a new fabrication recipe.*

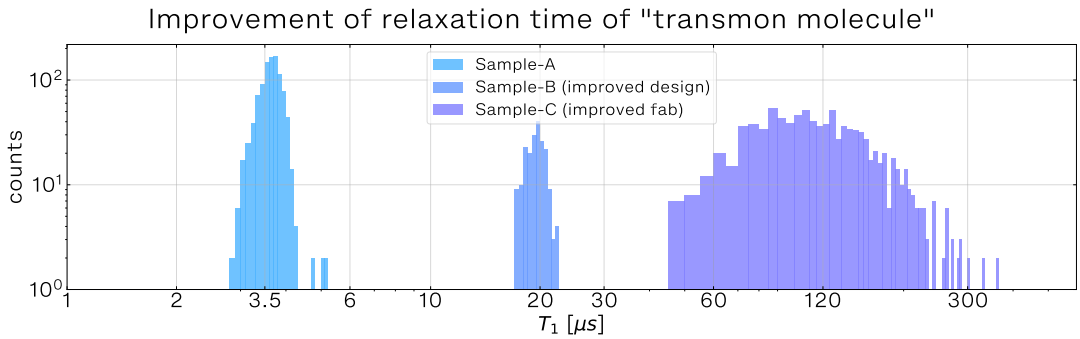

Figure 5.24: Comparison of relaxation time results over three samples. The bottom axis is logarithmic and correspond to T_1.

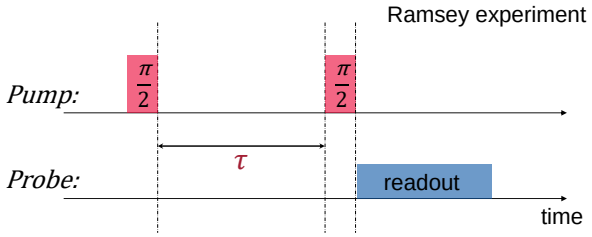

Figure 5.25: Pulse sequence for Ramsey experiment. We prepare a mixed state $|\psi\rangle = \frac{|g\rangle+|e\rangle}{\sqrt{2}}$ by applying a $\frac{\pi}{2}$-pulse. After waiting the variable amount of time τ we apply another $\frac{\pi}{2}$-pulse and readout the state of qubit.

5.3.6. Ramsey experiment

Ramsey interferometry [165] is a precise method to define a qubit frequency ω_q, and to measure intrinsic coherence time T_2 or T_{Ramsey}.

Conditions of the Ramsey experiment

To conduct the Ramsey experiment, we use $\frac{\pi}{2}$-pulses instead of π-pulses, which we have applied in the previous two experiments. Thus, we reduce the duration of the pump-pulse by a factor of two, keeping its power constant.

The pulse sequence for Ramsey-experiment is shown on Fig. 5.25. Assuming that initially the qubit is in $|g\rangle$-state and $\frac{\pi}{2}$-pulse is perfect. The pulse prepares a new qubit state $|\psi\rangle = \frac{|g\rangle+|e\rangle}{\sqrt{2}}$. The latter corresponds to the point on the equator of the Bloch-sphere. After a variable amount of time, we apply another $\frac{\pi}{2}$-pulse and project the qubit state on the Z-axis of the Bloch sphere. If there was no detuning $\Delta_{pump,q} = 0$ between the pump-tone and the qubit frequency, as well as no coherence losses, the qubit would be in $|e\rangle$-state after the pulse sequence. However, when the detuning $\Delta_{pump,q}$ is not zero, there will be a pulse delay between the qubit evolution and the pump mictowave. If the second $\frac{\pi}{2}$-pulse was applied after a time which corresponds to a phase difference of π, it will also rotate the Bloch-vector to $|g\rangle$-state instead of $|e\rangle$-state. As a result, we see oscillations on Fig. 5.26 a), c) whose frequency is directly given by the detuning $\Delta_{pump,q}$.

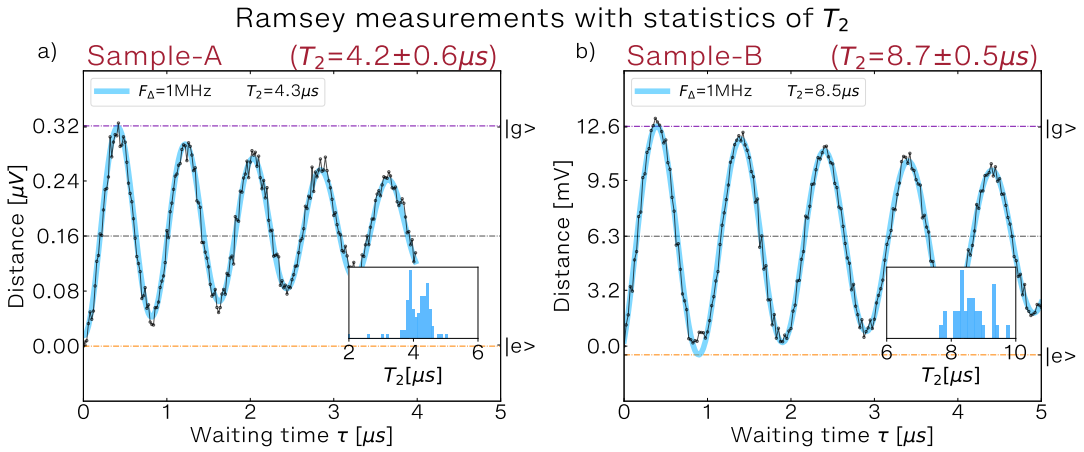

Figure 5.26: Results of Ramsey experiments for Sample-A *on plot a) and* Sample-B *on plot b). The bottom axis shows the waiting time τ. The left axis displays the distance between the point on the IQ-plane corresponding to the state measured at $\tau = 0$ and the new measured point. Black points depict the data measured in the experiment. The blue line corresponds to fit by Formula 5.6. The histograms of extracted T_2 are also shown in sub axes of each plot.*

Results of Ramsey experiment

To explain the damping of the oscillations we need to take into account the decoherence of a qubit, which can lead to fluctuations of phase as well as fluctuations of energy (angles ϕ and Θ on the Bloch-sphere, respectively).

To fit the data we have measured in this experiment, we use the following equations:

$$P_{|e\rangle}(\tau) = \frac{1}{2} \cdot \left[1 - \sin\left(\tau\Omega_{Ramsey}\right) \cdot e^{-\frac{\tau}{T_2}}\right] \tag{5.6}$$

$$\Omega_{Ramsey} = \sqrt{(\omega_{pump} - \omega_q)^2} \tag{5.7}$$

As a result, we define decoherence time for *Sample-A* and *Sample-B* to be equal to $T_2^A = 4.2 \pm 0.6\mu s$ and $T_2^B = 8.7 \pm 0.5\mu s$ by making statistical investigation.

Ramsey fringes

To see how the Ramsey oscillations behave with a change of detuning $\Delta_{pump,q}$ we provide a series of experiments with the variation of pump frequency ω_{pump} (see Fig. 5.27). Looking at plots a) and c), which correspond to different ω_{pump}, we see that the frequency of oscillations has changed. Applying the formula 5.7, we calculate the exact frequency of qubit ω_q with high precision. Knowing that with $\omega_{pump}/2\pi = 6.310GHz$ we had $\Omega_{Ramsey}/2\pi = 14MHz$ and with $\omega_{pump}/2\pi = 6.3GHz$ we had $\Omega_{Ramsey}/2\pi = 4MHz$ we calculate, that $\omega_q/2\pi = 6.300 - 0.004 = 6.296GHz$

On Fig. 5.27 b) we see how Ramsey oscillations behave with the change of the detuning (so-called Ramsey fringes). When the pump frequency reaches the value of 6.296 GHz, we stop observing oscillations. On Fig. 5.27 d) we plot the extracted Ω_{Ramsey} for each pump frequency and then fit it by formula 5.7. This gives us a more precise value of $\omega_q/2\pi = 6.29573GHz \pm 20kHz$.

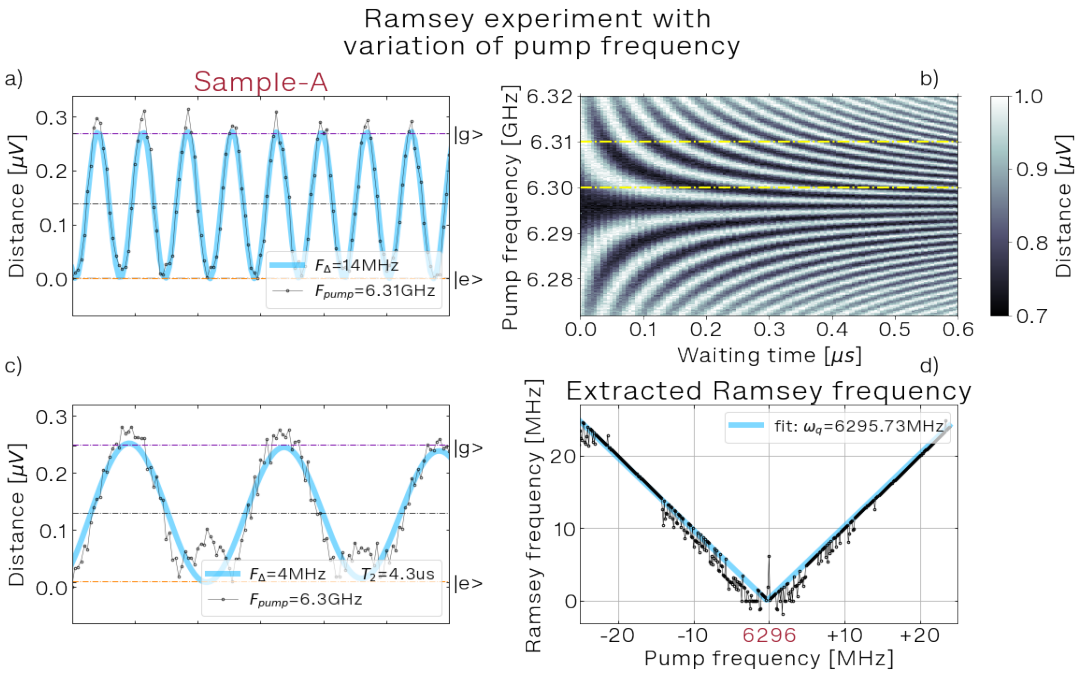

Figure 5.27: Ramsey's experiment with a variation of pump frequency. The black points correspond to data. The light-blue color correspond to the fit of the data. a), c) - Ramsey oscillations at pump frequencies 6.31 GHz and 6.30 GHz. b) - distance from the initial state on the IQ-plane as a function of waiting time and pump frequency. d) - extracted Ω_{Ramsey} as a function of detuning between pump and qubit frequencies.

Value	*Sample-A*	*Sample-B*	**Sample-C*
T_1 $[\mu s]$	3.7 ±0.3	19.6 ±1.8	120.0 ±60.0
T_2 $[\mu s]$	4.2 ±0.6	8.7 ±0.6	3.7 ±1.0
T_ϕ $[\mu s]$	10 ±4	11 ±2	4 ±2
T_{Rabi} $[\mu s]$	2.7±0.5	5.4 ±0.4	1.5 ±1

Table 5.2: Characteristic coherence times

We have also provided measurements of T_2 for *Sample-B* with different magnetic flux. The result is shown on Fig. 5.28. We see that in case of *Sample-B*, T_2 is not significantly affected by the change of magnetic flux, at least up to $\Phi/\Phi_0 = 6$.

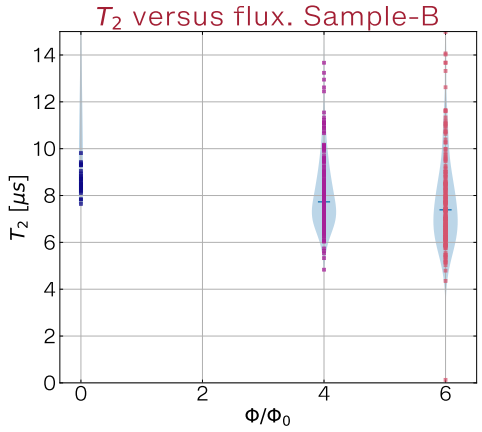

Figure 5.28: T_2 vs magnetic flux for Sample-B. *For three values of magnetic flux, the distribution of extracted T_2 is plotted as a violin plot. The dots are placed on top, representing the exact values of extracted T_2.*

5.3.7. Coherence times of transmon molecule

We summarize the coherence times we have measured for two generations of transmon molecules, *Sample-A* and *Sample-B*, in a Table 5.2. Having measured the relaxation and decoherence times T_1 and T_2 we can also calculate pure dephasing time T_ϕ using next equation [166]:

$$\frac{1}{T_2} = \frac{1}{2T_1} + \frac{1}{T_\phi} \tag{5.8}$$

5.3.8. Photon number calibration

The Ramsey-Stark experiment allowed us to calibrate the number of excitations in a polariton mode n_{ph} at the given power of readout pulse (probe). Hereafter, I will name excitations in polariton modes as "photon". In addition to this, we can extract values of polariton decay rate k and the cross-Kerr shift χ between polariton and qubit.

The pulse sequence that we use for this experiment is shown on Fig. 5.29. We repeat the same experiment as a Ramsey one, described above, but now we populate the polariton mode by photons applying a "population"-pulse with the same frequency

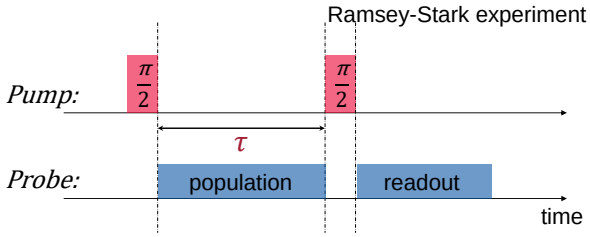

Figure 5.29: Pulse sequence for Ramsey-Stark experiment. It is almost similar to the pulse sequence for the Ramsey experiment shown in Fig. 5.25, but between a pair of $\frac{\pi}{2}$-pulses we send a probe tone to populate the polariton mode by photons. In our case, the amplitude of population-pulse was equal to the amplitude of readout pulse for consistency reasons.

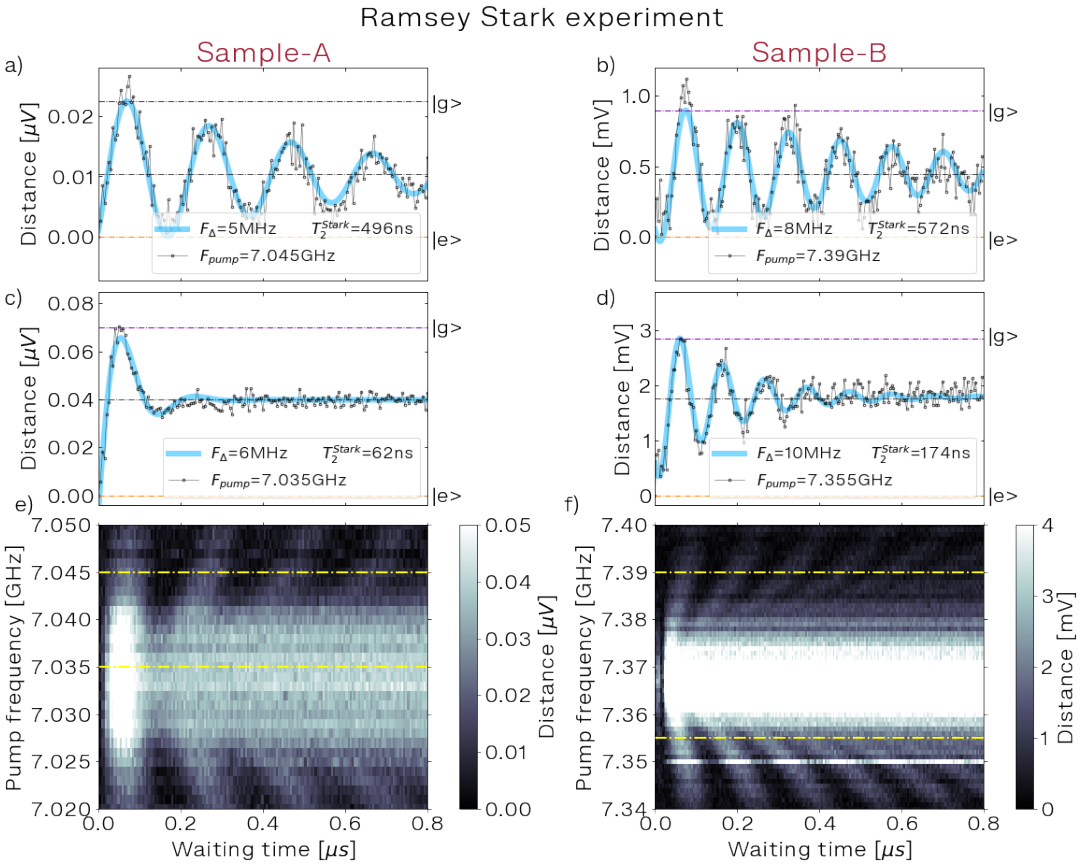

Figure 5.30: The left axis of these plots correspond to distance at IQ-plane between signals of initial and new states. Plots a) and b) are Ramsey oscillations obtained with a probe frequency detuned from the resonance of polariton when plots c) and d) are taken closer to resonance. The bottom axes of all charts show waiting time τ between two $\frac{\pi}{2}$-pulses. All the left part is devoted to Sample-A*, and the right part - to* Sample-B*. The e) and f) charts show how Ramsey-Stark oscillations behave with a variation of probe frequency (left axis), false color corresponds to distance. Yellow dashed lines on plots e) and f) correspond to cross-sections shown on the plots above.*

as the probe. Probe frequency, we vary around resonance of polartion. The closer the probe frequency is to the resonance of polariton - the more photons will be excited. Pump frequency is always constant in these experiments, and taken for having a significant detuning $\Delta_{Pump,q}$ to see the Ramsey oscillations. The results of these series of experiments are shown in Fig. 5.30. Ramsey-Stark oscillations are shown of plots a), b), c) and d). Plots on the left are devoted to *Sample-A* and right plots for *Sample-B*.

We observe that oscillations are damped. The damping factor is indicated as the variable T_2^{Stark}. These values are much less than T_2, measured in Ramsey experiment and strongly depend on probe frequency. The probe frequency which we used for these experiments is specified in legend. We also see that frequency of oscillations changes with variation of probe frequency.

To see this tendency more clear, we made plots e) and f), which show a distance as a function of probe frequency $\omega_{probe}/2\pi$ and waiting time τ between $\frac{\pi}{2}$-pulses. The yellow dashed lines correspond to the plots above. We see that near polariton resonance frequency, the oscillations are no more visible because of high damping. We also see that frequency of oscillations is increasing with decreasing of detuning between probe and polariton frequencies $\Delta_{probe,Pol} \to 0$. By fitting this data, we obtain T_2^{Stark} and ω_{Stark} as a function of probe frequency and probe amplitude.

On Fig. 5.31 a), b) the extracted dephasing rate $\Gamma_d = \frac{1}{T_2^{Stark}}$ is plotted as a function of probe frequency (bottom axis) for *Sample-A* and *Sample-B* respectively. Plots on Fig. 5.31 c) and d) show ω_{Stark} as a function of probe frequency. We repeated this series of experiment with different power of probe pulse at the entrance of 3D-cavity. This power is indicated in the legend in Fig. 5.31.

The process of calibration n_{ph} is well described in the thesis of Quentin Ficheux [167]. We have directly applied his calculation to our experimental setup. The decay coherence rate Γ_d and the frequency shift ω_{Stark} when the polariton mode of frequency $\omega_{Polariton}$ is probed by a coherent field of frequency ω_{probe} and an amplitude ϵ_{probe} are given by a Formulas 5.9, 5.10.

$$\Gamma_d(\omega_{probe}) = -\frac{8k\chi^2|\epsilon_{probe}|^2}{(k^2 + 4(\omega_{probe} - \omega_{polariton})^2 - \chi^2)^2 + 4\chi^2k^2} \tag{5.9}$$

$$\omega_{stark}(\omega_{probe}) = \frac{4\chi^2|\epsilon_{Probe}|^2 \cdot (k^2 + 4(\omega_{probe} - \omega_{polariton})^2 - \chi^2)}{(k^2 + 4(\omega_{probe} - \omega_{polariton})^2 - \chi^2)^2 + 4\chi^2k^2} \tag{5.10}$$

Here k is the decay rate of the polariton mode and χ is the cross-Kerr coupling between polariton and qubit. The polariton number inside the polariton mode (hereafter we call it photon) is given by:

$$n_{ph}(\omega) = \frac{k^2 + \chi^2}{2k\chi^2} \cdot \Gamma_d(\omega_{probe}) \tag{5.11}$$

The curves shown on Fig. 5.31 a), b) are fitted by Eq. 5.9, and curves from plot c), d) are fitted by Eq. 5.10. From the fits, the polariton line width k, qubit induced shift χ and drive strength $|\epsilon|^2$ can be extracted.

Using formula 5.11 we can obtain the number of photons in a polariton mode. The results are given in Table 5.3.

The maximum of number of photons n_{ph} for a given probe amplitude is achieved when the probe frequency matches the polariton. We have plotted as a function of expected input power in graphs e) and f) of Fig. 5.31. We see that the number of

Value	*Sample-A*	*Sample-B*
$k\ [MHz]$	15 ±1.8	22 ±0.5
$\chi\ [MHz]$	7.8 ±0.3	9.0 ±0.2
$\omega_c\ [MHz]$	7033.8 ±0.2	7370.0 ±0.2

Table 5.3: Extracted parameters from the Ramsey-Stark experiment

photons that we extract from the Ramsey-Stark experiment grows proportionally to the power of the probe pulse. We expect this dependence to be linear and fit this data by linear expression. As soon as we plot it in semi-log axis (bottom axis is in dBm), the dependence looks like exponential grow when it is linear.

We found that data of number of photons are better fitted by $n_{ph}^{A} = 0.54P_{in}^{[pW]} + 0.04$ for *Sample-A* and $n_{ph}^{A} = 0.91P_{in}^{[pW]} + 0.09$, where estimated input power is taken in picowatts for convenience. This gives us a calibration between the power we send to our microwave setup and the number of photons that we have in the polariton mode during readout of qubit.

We can also notice here a difference between factors of proportionality between two samples. This can be explained by different line width of polaritons in these two cases, and in addition the estimation of the input power can include some error (the microwave scheme was changed between two series).

The additive constant used in the fit law reflects an expected number of photons in polariton with no probe pulse applied. According to our fit curves, this value is around 0.05-0.10 photons in average.

As we have calibrated number of photons in the polariton mode for given powers of probe tone, we can predict the photon number for larger probe amplitude, making an assumption of linear behavior of the system. This assumption stops to be true when we enter a regime of nonlinear respond of the polariton. But we still will use the parameter of expected number of photons as if it would have stayed linear. To highlight this approximation, we will use a notation expected number of photons n_{ph}^{*} instead of calibrated number of photons n_{ph}.

5.4. Qubit state readout via cross-Kerr coupling

In this section, we will now focus in more detail on the qubit state readout. First, the effect of the qubit state on the polariton transmission will be demonstrated. Then the best single-shot readout results for both samples will be presented. We will discuss the sources of readout errors and the effect of readout pulse duration and power on these errors. Next, we will evaluate the QNDness of our measurement by performing two consecutive readout pulses for sample-B. Finally, we discuss the results of quantum trajectory measurements for sample-A, extracting parameters such as decay and excitation rates, QNDness, and effective temperature.

5.4.1. Conditional transmission of polariton

Our first experiment will be devoted to measuring the transmission of polariton as a function of frequency and power of the probe pulse. The results of these experiments will give us the polariton resonance shift due to qubit state. This will give us the

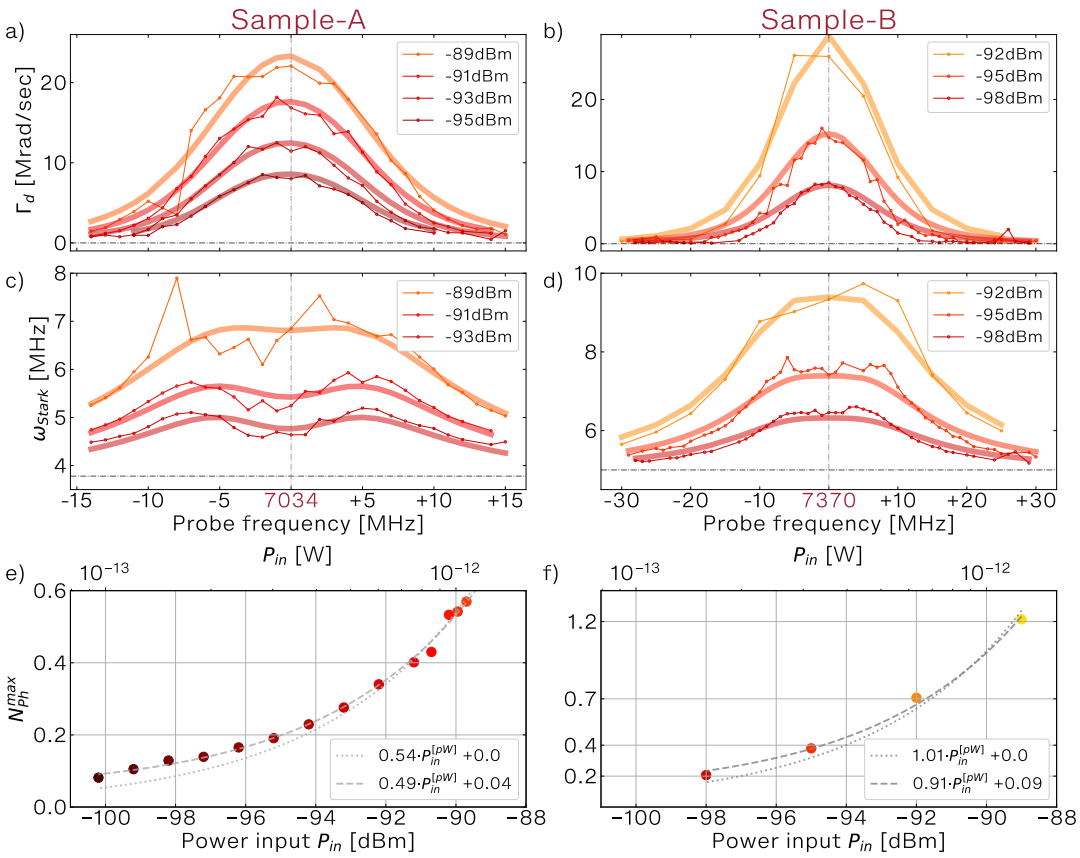

Figure 5.31: Calibration of number of photons in polariton. On plots a) and b) the dephasing rate $\Gamma_p = \frac{1}{T_2^S tark}$ *is depicted for* Sample-A *and* Sample-B *as a function of probe frequency. Plots c) and d) show Ramsey-Stark oscillations frequencies* ω_{stark} *as a function of probe frequency. Each color from dark-red to yellow reflects different power of probe tone on the input of 3D-cavity. Lines with round points reflects the experiment data, when solid thick lines correspond to fitting curves. Plots e) and f) show the number of photons extracted by formula 5.11 as a function of input power when the probe frequency is in resonance to the polariton mode. The bottom axis show power at the input of 3D-cavity in dBm, when the top axes show the same value in watts. The gray dashed lines represent linear dependence: with zero additive constant and with non-zero additive constant.*

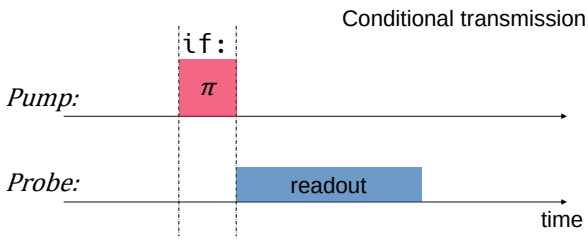

Figure 5.32: Schematic of a polariton conditional transmission measurement. We use two types of sequence (which is hinted by text 'if:' on the plot): in a half of experiments we apply a π-pulse to excite the qubit and in another half we don't do it. Then we immediately make a readout of the qubit state by applying a probing pulse of $500ns$ duration. We repeat this pair of measurements 1000-3000 times and average the result. We wait for a few hundreds of microseconds before repeating this sequence to let the system relax.

cross-Kerr coupling strength between qubit and polariton - χ. We will also find the conditions for readout pulse to maximize the recognition of qubit state.

To provide this experiment, we measure the spectroscopy of polariton conditioned on the state of qubit. The pulse sequence is presented in Fig.5.32. Duration of π-pulse is taken from Rabi experiment and consists of $30ns$ and $100ns$ for *Sample-A* and *Sample-B*, respectively. This pulse sequence is performed for different probe frequencies leading to spectroscopy depending on the qubit state as shown in Fig. 5.33 a) and b).

Conditional spectroscopy

Fig. 5.33 (a) shows amplitude of polariton transmission, when Fig. 5.33 (b) corresponds to phase. Distance is shown in Fig. 5.33 (c). Amplitude and phase are calculated from I and Q signals through $Amp = \sqrt{I^2 + Q^2}$ and $Phase = \arctan \frac{Q}{I}$.

From Fig. 5.33 (a) we see that both amplitude curves have a resonance peak associated to polariton frequency. The resonance frequency of polariton is different for different states of qubit. Similarly, the phase presents a drop at the polariton resonance, and this drop is shifted when the qubit state is changed. This frequency shift is caused by cross-Kerr coupling between qubit and polariton. Due to the cross-Kerr shift, we were able to perform two-tone spectroscopy described in section 5.2.2.

Extraction of cross-Kerr shift χ

From these conditional spectroscopes, we extract the cross-Kerr shift at different magnetic fluxes for lower and upper polariton. Results of this extraction for both *sample-A* and *sample-B* are shown in Fig. 5.34 left and right plots, respectively. We see that in case of *Sample-A* the two curves corresponding to cross-Kerr couplings χ between qubit and upper or lower polariton present an intersection. It appears at the same magnetic flux when bare ancilla frequency crosses bare cavity frequency and weight angle θ crosses a value of 45° (see Fig. 5.7). This only happens in case of *Sample-A*.

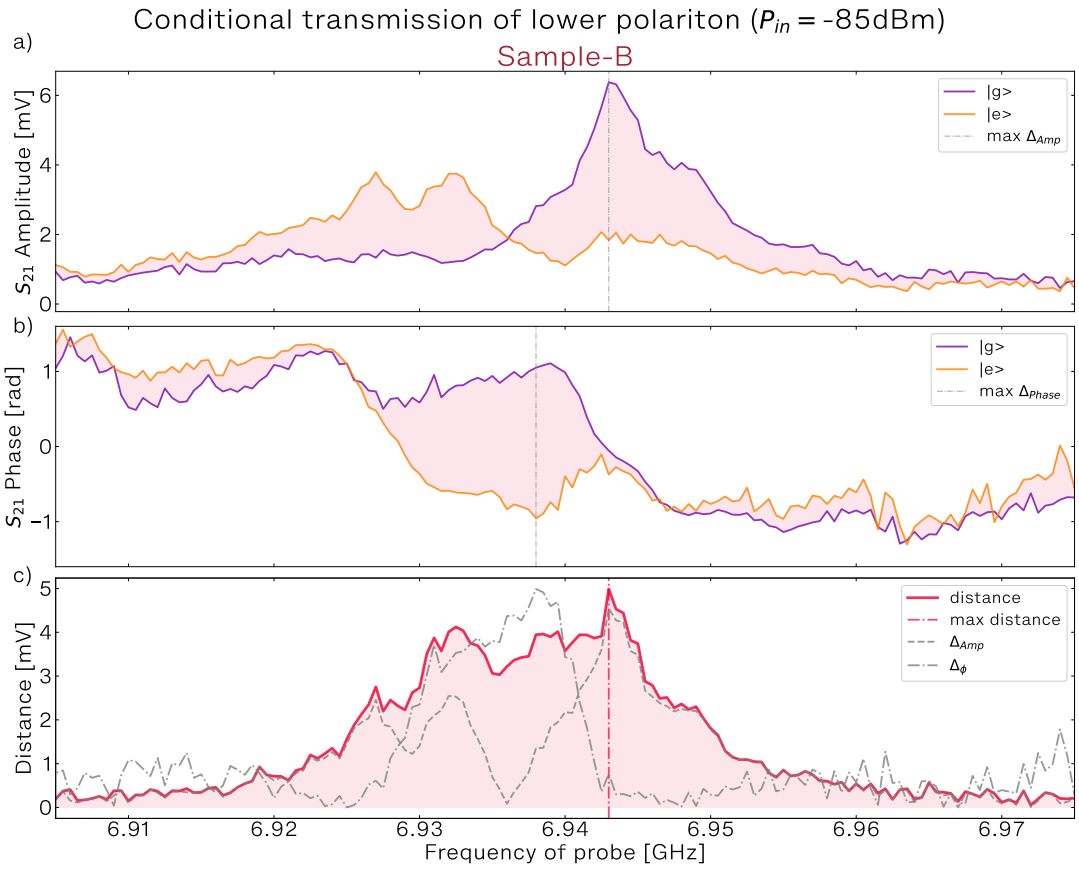

Figure 5.33: Conditional spectroscopy of polariton as a function of probe-frequency (bottom axis). Plots (a) and (b) show amplitude and phase of transmitted signal, and plot (c) shows distance D value (See 5.3.1). Purple color correspond to the data measured without applying of π-pulse, so we expect qubit to be in $|g\rangle$-state. Orange color correspond to measurement done after pi-pulse, which excites qubit to $|e\rangle$-state. The shaded pink area shows the difference between obtained after applying π-pulse or not.

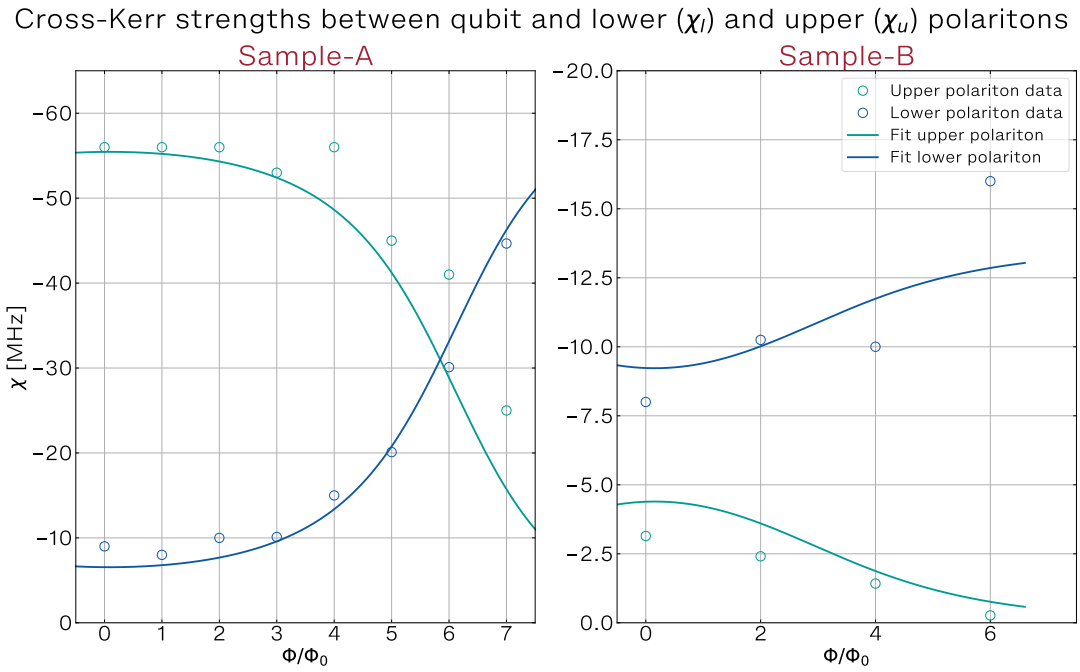

Figure 5.34: Cross-Kerr polariton shift χ extracted from conditional spectroscopy as a function of external magnetic flux. Sea-color correspond to upper polariton and steel-color correspond to lower polariton.

Conditional spectroscopy as a function of probe power

Fig. 5.35 shows amplitude (left column), phase (middle column) and distance (right column) as a function of probe frequency at three different powers of probe pulse. The first row corresponds to $-89dBm$ probe power, the second to $-85dBm$ and the third to $-77dBm$. By comparing amplitudes phases of transmitted signal (plots Fig. 5.35 (a, d, g)) and (plots Fig. 5.35 (b, e, h)) we see that value of cross-Kerr shift does not change much. However, the line shapes of resonance peaks are not Lorentzian anymore at probe power of $-77dBm$. Also, we see that the two peaks corresponding to $|g\rangle$ and $|e\rangle$ states are shifted to lower frequencies when the power is increased.

These effects were well explained and modeled by Remy Dassonneville, Thomas Ramos and Juan Jose Garcia Rippol and published in thesis of Remy Dassonneville (Chapter 8.5) and [84] and are due to the non-linearity of the polariton, induced by non-linearity of ancilla. According to their work these effects are related to non-linearity of polariton, induced by non-linearity of ancilla, which is well modeled by Duffing oscillator.

Concerning distance as a function of probe frequency (See Fig. 5.35 (c, f, i), we see that it increases with power of probe pulse. This is expected due to the fact that the number of photons n_{ph} in the polariton increases. We also see that sometimes distance has two local maxima. This is due to the fact that there are two resonance peaks - one correspond to $|g\rangle$-state of qubit and one to $|e\rangle$-state.

The distance as a function of probe frequency and power is shown in Fig. 5.36. The larger the distance is, the better is the readout performance due to a larger signal-to-noise ratio. By increasing the probe power, the distance increases but the polariton resonance peak shifts to lower frequency. This behavior is the same for both samples. However, there is a difference: in case of *Sample-A* distance maximum more

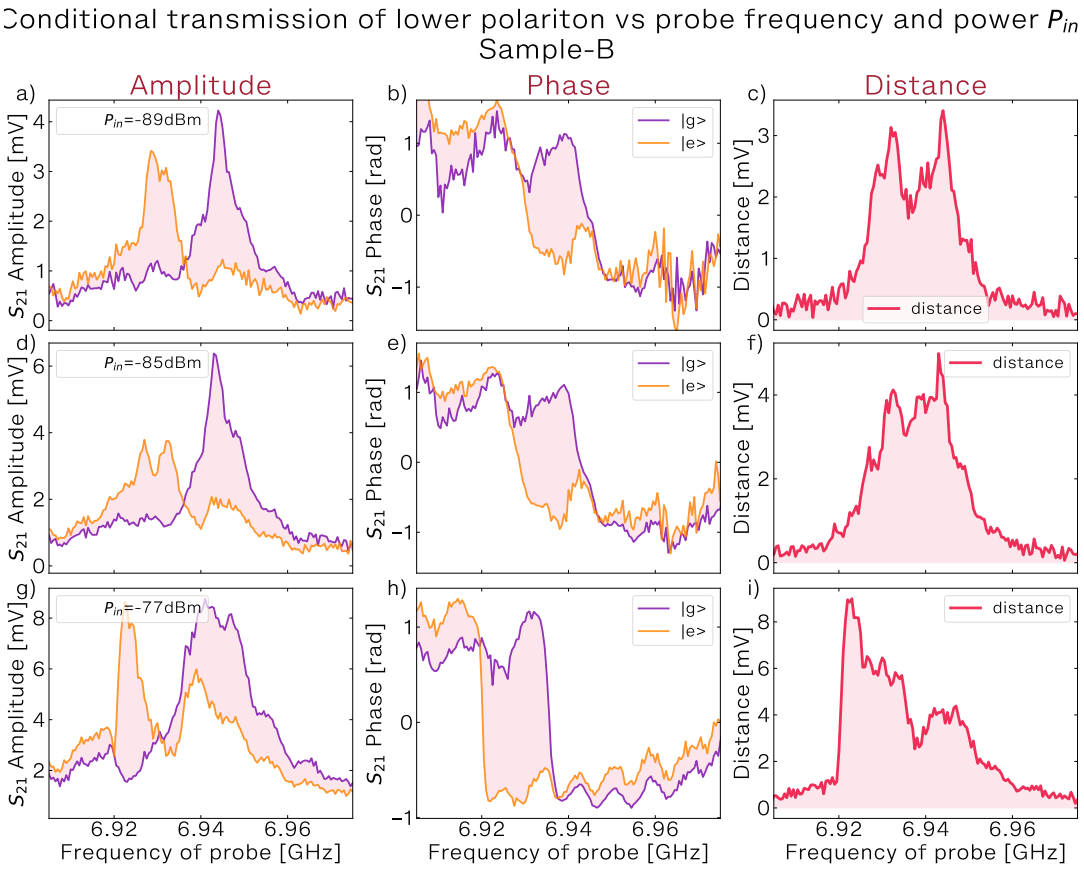

Figure 5.35: Conditional transmission amplitude (left column), phase (middle column) and distance (right column) as a function of probe frequency (bottom axis) at different power of probe pulse. The probe power is specified in the legend of the left plot of each row. Purple color correspond to the data measured without applying of π-pulse, so we expect qubit to be in $|g\rangle$-state. Orange color correspond to measurement done after pi-pulse, which excites qubit to $|e\rangle$-state. The shaded pink area shows the difference between obtained after applying π-pulse or not.

tends to split on two maxima. Such splitting not observed in *Sample-B*. Also, the growth of distance with increase of power has a limitation for *Sample-A*, but we have not observed it for *Sample-B*. This fact can be explained by the lower non-linearity of the polariton due to the lower anharmonicity of the ancilla embedded in the *Sample-B* design. In addition, the value of distance in *Sample-B* is about 5-10 times higher than in *Sample-A* (note the values corresponding to the color in both cases). This effect we explain by the fact that the transmission of the polariton is significantly higher, which results from resonance conditions of ancilla and cavity.

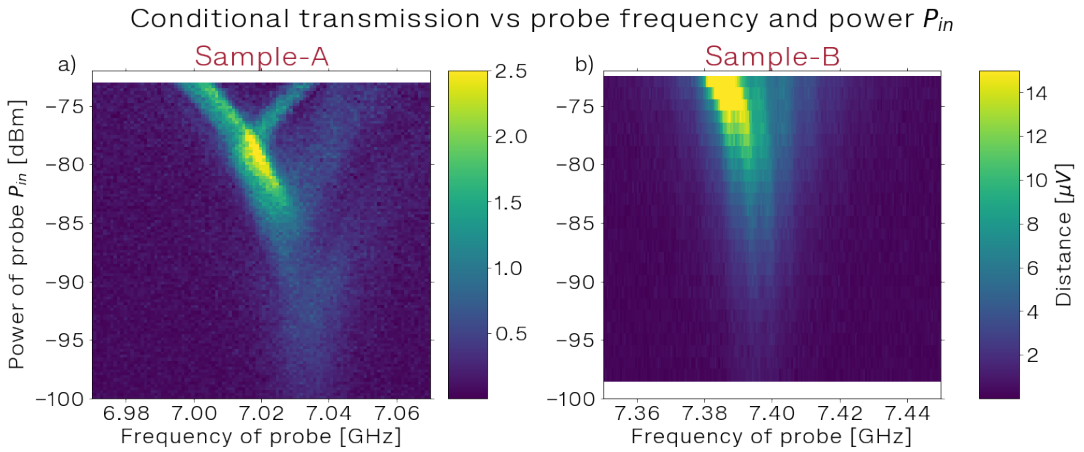

Figure 5.36: Distance measured by conditional spectroscopy as a function of power (lef axis) and frequency (bottom axis) of probe for Sample-A *(on the left) and* Sample-B *(on the right).*

5.4.2. Single-shot readout

By single-shot projective readout we mean the experiment, which allows discriminating qubit state by one measurement. Each execution of the pulse sequence shown will give us knowledge of qubit state. This means that we don't need to average the signal obtained from multiple repetitions of the pulse sequence anymore. According to quantum mechanics, even an ideal projective measurement will give a probabilistic result if one will measure a quantum state $|\psi\rangle = \alpha\,|g\rangle + \beta\,|e\rangle$ with the probability of $|\alpha|^2$ and $|\beta|^2$ to measure the $|g\rangle$ and $|e\rangle$ states, respectively. Therefore, we will need to repeat many times the measurements to estimate these probabilities. However, in case of measuring the pure states ($|\psi\rangle = |g\rangle$ or $|\psi\rangle = |e\rangle$), a simple measurement will be enough to determine the quantum state. Nevertheless, the single-shot readout have a non-zero probability of error, which is related to measurement setup. Even by measurement of pure state, $|g\rangle$ we can obtain an answer $|e\rangle$ sometimes. To express the magnitude of this error, the fidelity of the measurement F is defined:

$$F = 1 - \frac{P_{e|g} + P_{g|e}}{2}, \tag{5.12}$$

where $P_{i|j}$ is a probability of reading the state i when it is actually j.

The ability to make single-shot readout with high fidelity is critically important for real-time quantum feedback schemes, which uses for example in quantum error correction [168] [169], teleportation [170] and state initialization [171] as well as in some fundamental quantum physics studies [172] [173].

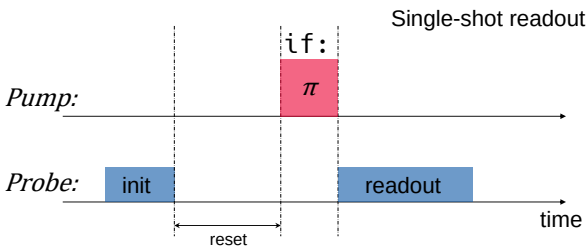

Figure 5.37: Pulse sequence to perform a single-shot readout. The pi-pulse is conditional now, because we skip it in half cases, when we wish to prepare state $|g\rangle$, and apply in another half cases, when wish to prepare $|e\rangle$-state.

The pulse sequence that we use to implement single-shot readout is shown in Fig. 5.37. In this sequence, first we send an initializing pulse on probe frequency to populate the polariton by photons. This probe pulse realizes the first measurement, which projects qubit to one of the pure states. Then we wait few hundreds of nanoseconds to relax the state of polariton. After, depending on which state we want to prepare, we apply a π-pulse to excite qubit or not. And finally, we apply the readout pulse of the probe frequency. We recover the measurement signals after both initialization and readout probe pulses. When the first initialization pulse gives us a signal related to $|e\rangle$ state, we ignore the following readout. This selection method corrects errors caused by a bad initialization of state. This process we call postselection.

Best achieved fidelity

The best results in terms of single-shot readout fidelity, that we have achieved on transmon molecules, are presented in Fig. 5.38. In Fig. 5.38 a), b) scattering diagrams of I' and Q' results are shown for qubit prepared in $|g\rangle$ or $|e\rangle$ states. Histograms presented in Fig. 5.38 c), d) show a distribution of measured points along the I'-axis after preparation of $|g\rangle$ or $|e\rangle$-state (purple and orange color respectively).

The data for *Sample-A*, shown in this Fig. 5.38 a), c) is obtained with readout pulse of duration $138ns$ and power of $-95.2dBm$ at probe frequency of $7.032GHz$ which is close to lower polariton resonance. To excite qubit the Gaussian-shape π-pulse with duration $26ns$ was used at frequency $6.2841GHz$. Before implementing these pulses, we have waited for $500ns$ after initialization pulse of the same parameters as a readout pulse.

For the single-shot readout of *Sample-B*, which result is shown on Fig. 5.38 (b, d) we used a readout pulse with duration $150ns$ and power of $-81dBm$ at probe frequency $7.344GHz$, which is close to upper polariton frequency. We sent a square-shape pulse with $118ns$ duration at pump frequency of $2.475799GHz$ in case we wish to prepare excited state. We waited for $150ns$ after initialization pulse for implementing a readout pulse.

We observe that the measurement values of the different states $|g\rangle$ and $|e\rangle$ are well separable for both samples. We can notice that blobs, which correspond to *Sample-A* are squeezed. This is an effect of using Josephson Parametric Amplifier (JPA). In case of *Sample-B* we have used a Travelling Wave Parametric Amplifier (TWPA), which is not phase sensitive and does not produce squeezing. On scattering diagram of *Sample-B* in Fig. 5.38 b), we see that orange blob, which correspond to the $|e\rangle$-state

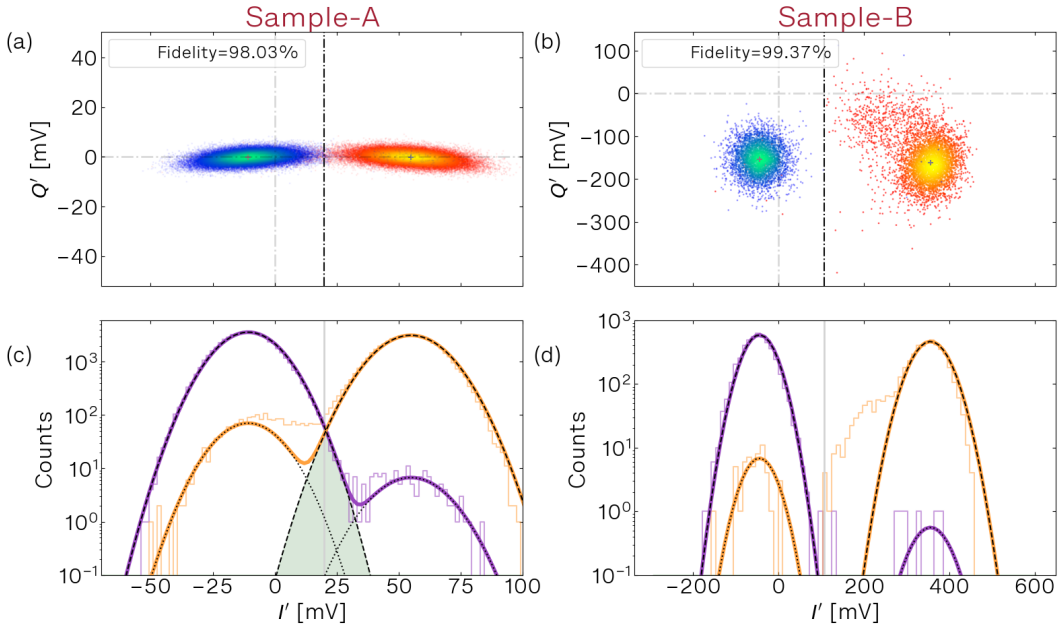

Figure 5.38: Single-shot readout results with the best fidelity achieved on each sample. a), c) - scattering diagrams with progressive color - more brightness means more dot density. We rotate a basis of complex plane around (0,0), which is equal to changing the initial phase ϕ. As a result, we have replaced the IQ-basis by a new one - $I'Q'$. The bottom and left axis correspond to the new values I' and Q', which form a new basis rotated with respect to I and Q so that all information about the qubit state is contained in I'. The dashed black line shows a threshold value. Figures b), d) shown histograms, plotted along I'-axis. The left axis is logarithmic and corresponds to the number of counts. The orange and purple step-like line shows the distribution of counts along I'-axis for prepared $|e\rangle$ and $|g\rangle$-states, respectively. A solid line of the same color shows the fit of these distributions by double Gaussian function. Dashed and dotted black lines show fit of counts distribution by single Gaussian functions corresponded to expected and unexpected states, respectively. The green area marks an overlap between two Gaussian fits, which lead to error due to limited SNR.

of qubit is slightly spread. This we explain by slight overload of TWPA by signal amplitude. This is observed only on a blob of $|e\rangle$-state, because amplitude (distance between center of blob and point $(0, 0)$) is bigger in that case.

Sources of errors

To understand the readout errors, we analyzed the histograms in Fig. 5.38 (c, d) by fitting both of them by double Gaussian function. There are two types of error of single-shot measurement. *(i)* First is related to Signal-to-Noise ratio (SNR) and cause an overlap of two Gaussian. This overlap is marked as a green area on the plot. If one particular measurement give us the value covered by this area - we are not able to say, which state qubit has. This error we call an overlap error ϵ_o *(ii)* Second error is due to transition between qubit states. In that case we can exactly measure the state of the qubit, but it is not the state, that was prepared. This can happen either because of wrong preparation of the state, or because qubit changed its state during the measurement. The state change can be either spontaneous, or induced by the readout pulse. In these cases, the measurement is not called Quantum Non-Demolition (QND) anymore. We will call decay errors $\epsilon_{|e\rangle}$ the errors of single-shot readout when we expected the state $|e\rangle$, but got an answer $|g\rangle$. And otherwise we call the excitation errors $\epsilon_{|g\rangle}$ of getting $|g\rangle$, when we expect to get $|e\rangle$.

We see that histograms on Fig. 5.38 c) corresponding to *Sample-A* presents an overlap, leading to overlap error. Moreover, there are second Gaussian, related to transition errors (both decay and excitation). On plot Fig. 5.38 d) situation is much better: there is no overlap visible between two Gaussian, and we see only one second Gaussian, related to decay error.

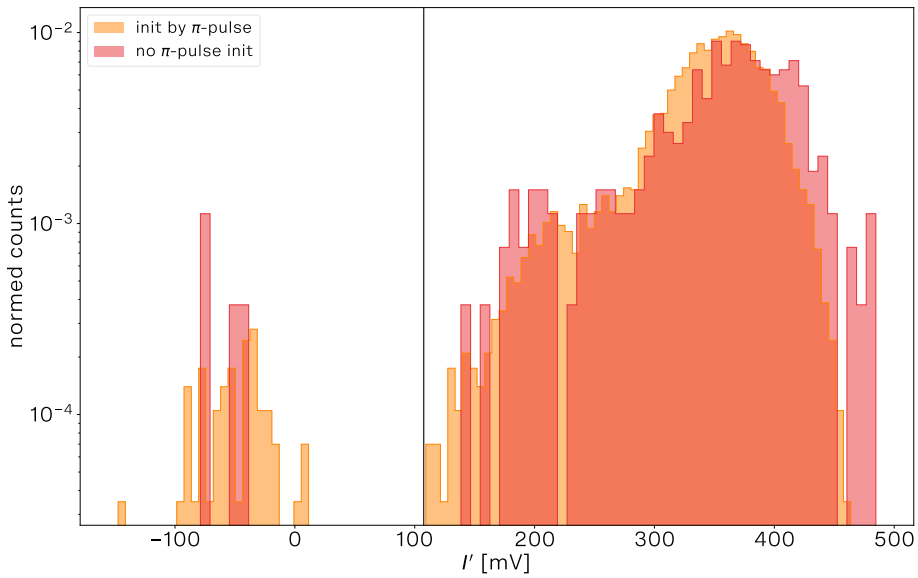

Figure 5.39: Normalized histograms showing single-shot readout results after two different ways of preparation an $|e\rangle$-state of qubit: by applying a π-pulse after getting $|g\rangle$-state from initializing pulse (orange histogram) and by simply readout the state after getting $|e\rangle$-state from initializing pulse (red histogram).

Value	*Sample-A*	*Sample-B*
F [%]	98.03	99.37
$\epsilon_{\|e\rangle}$ [%]	3.42	1.11
$\epsilon_{\|g\rangle}$ [%]	0.52	0.15
ϵ_o [%]	0.2	0.00006
discard [%]	1.85	6.51

Table 5.4: Fidelity results.
Value F correspond to fidelity of single-shot readout. An $\epsilon_{|e\rangle}$ is an error of measuring $|e\rangle$-state, same as $\epsilon_{|g\rangle}$ is an error of measuring $|g\rangle$-state. An ϵ_o is an error of overlap, caused by limited SNR. The last line shows the amount of discarded measurements due to the postselection.

Some deviation from the fit of measuring excited state (orange line) in case of *Sample-A* (Fig. 5.38 c)) can be explained by the following: if qubit was in the state $|e\rangle$ at the beginning of the measurement, but changed its state to $|g\rangle$ in the middle of readout, the readout signal changes with time. By integrating the received signal over time of the readout pulse, the average value is somewhere in between the two Gaussian. This explanation agrees well with the fact that this deviation is stronger when the duration of the reading pulses are longer.

In case of *Sample-B* (Fig. 5.38 d)) the explanation for the fit deviation from Gaussian is different. As we said before, in this case we work in conditions of a little overloading the TWPA by the readout pulse, which produce more scattering around.

Comparison of single-shot readout results

In a Table 5.4 we list the errors extracted from data shown on Fig. 5.38. We see that the total error $\epsilon_{tot} = 1 - F$ achieved with *Sample-B* is three times less than the total error shown by *Sample-A*. The error of overlap ϵ_o is not a limiting factor anymore in case of *Sample-B*. We also see a reduction of both types of transition errors $\epsilon_{|e\rangle}$ and $\epsilon_{|g\rangle}$. In both cases, the main limiting factor of fidelity is $\epsilon_{|e\rangle}$. This error is mainly caused by relaxation time of qubit T_1, but can be also due to decay induced by the readout pulse or due to not perfect $|e\rangle$-state preparation.

For *Sample-A* with, $T_1 = 3.3\mu s$ we expect an error $\epsilon_{|e\rangle}$ of $3.7\% \pm 0.3\%$ for *Sample-A* due to natural decay, given a value of $T_1 = 3.7 \pm 0.3\mu s$ and readout time $T_{read} = 138ns$. These expectations are in good agreement with the value obtained.

In case of *Sample-B* we expect an error due to the natural relaxation around $0.75\% \pm 0.08\%$ taking into account $T_1 = 20 \pm 2\mu s$ and $T_{read} = 150ns$. But in fact the decay error is around, 1.1% which is 1.5 times more than expected. This can be explained by the longer the duration (T_π=118ns) of the π-pulse in case of *Sample-B*. Calculating an expected decay error for waiting time around, $210ns = T_{read} + 0.5T_\pi$ we got an error about $1.05\% \pm 0.1\%$. This calculation is in good agreement with extracted value. Nevertheless, part of this error may also be caused by a non-ideal π-pulse.

Alternative way of $|e\rangle$-state preparation

In order to check whether the readout error can be attributed to π-pulse performance, we have used another method of $|e\rangle$-state preparation in addition to the

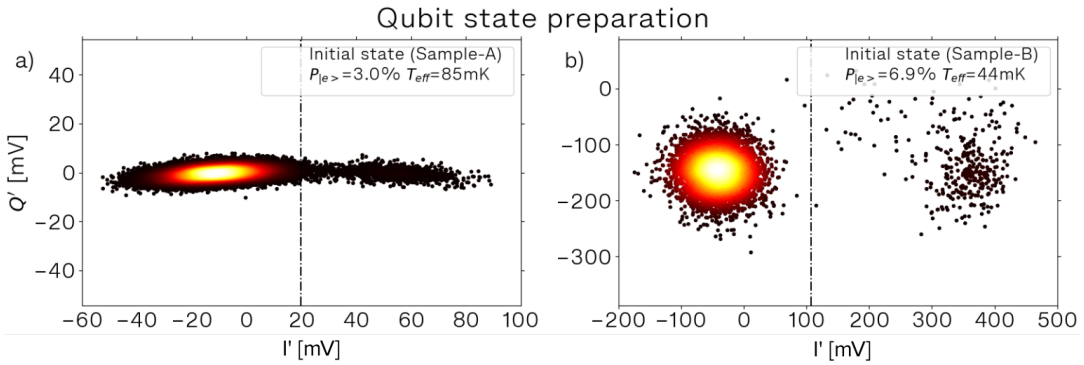

Figure 5.40: Result of initializing pulse showing an initial thermal state of qubit. In case of Sample-A *measured with JPA - a), and in case of* Sample-B *measured with TWPA - b).*

traditional way described above. We have applied the same pulse sequence as demonstrated in Fig. 5.37. However, in this approach we have used the data which were normally discarded during the post-selection process. To this group of results belong the cases when initialization readout pulse returned a $|e\rangle$-state. This occurs relatively rarely - about 1% of all cases, since the thermal state of the qubit is closer to the $|g\rangle$-state than to the $|e\rangle$-state. As a result, we have randomly initialized a $|e\rangle$-state of a qubit without using a π-pulse.

The results are demonstrated in Fig. 5.39. We have registered significantly better state distribution, which means that the readout error can be partially explained by π-pulse infidelity. However, we have to take into account that the amount of statistics is much less in this case (only 330 points against 4680 points), which makes the final conclusion more complex.

Effective temperature

Another possible reason for the readout error can be explained by the high effective temperature of qubit T_{eff}.

The results of measuring thermal state of *Sample-A* and *Sample-B* are shown on Fig. 5.40 (a) and (b), respectively. Probability of measuring $|e\rangle$-state instead of $|g\rangle$-state is about 3% for *Sample-A* and almost 7% for *Sample-B*. By taking into account frequency of qubit for both cases, we calculated T_{eff} to be $85.4mK$ and $44.2mK$ for *Sample-A* and *Sample-B*, respectively. More detailed information is shown in Table 5.5. We calculated a temperature which would excite the qubit using equation The effective temperature T_{eff} of qubit has been extracted from probability of qubit to be in $|e\rangle$-state $P_{|e\rangle}$ using Bose-Einstein distribution

$$f_{BE}(\omega_q) = \frac{1}{\exp\frac{\hbar\omega_q}{k_B T} - 1} \tag{5.13}$$

We noticed that the $|e\rangle$-state population is higher for *Sample-B* despite the fact that T_{eff} is twice lower. This is explained by the much lower energy of the qubit of *Sample-B* which is $T_q = 121mK$ in temperature unity.

$$T_q = \hbar\omega_q / k_B \tag{5.14}$$

Value	*Sample-A*	*Sample-B*
$\omega_q/2\pi$ [GHz]	6.284	2.523
T_q [mK]	302	121
$P_{\|e\rangle}$ [%]	3.0	6.9
T_{eff} [mK]	85.4	44.2
T_{eff}/T_q [%]	28	37

Table 5.5: Comparison of the thermal populations of qubit. The first line shows frequency of qubit. The second line is the calculated value of temperature, which would excite our qubit T_q. The third line shows measured probability of qubit to be in excited state. A fourth line is calculated T_{eff}, which our qubit has.

Because the excitation temperature T_q is lower for *Sample-B*, the qubit of this sample is more sensitive to the environment temperature.

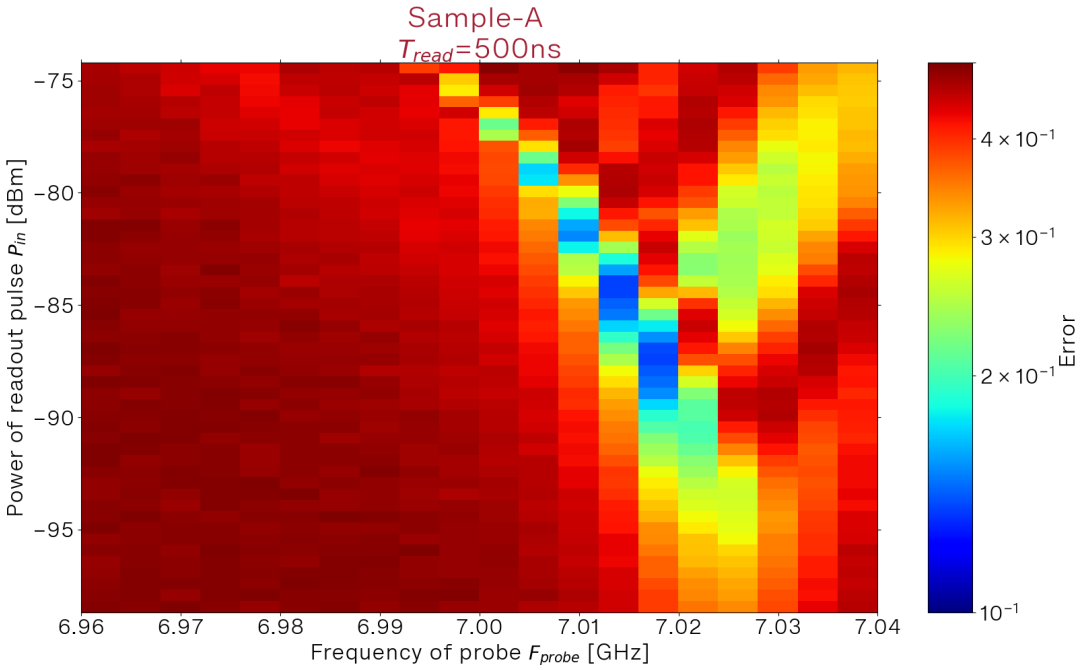

Figure 5.41: Error as function of power (bottom axis) and frequency (left axis) of the readout pulse. Blue color correspond to lower error (and higher fidelity). Dark red color shows zones, where qubit states are indistinguishable.

Fidelity as a function of readout pulse properties

A lot of work has been done to achieve optimal single-shot readout shown in Fig. 5.38. First, π-pulse must be optimized to have precise frequency and duration. Moreover, readout pulse also need to be adjusted in terms of frequency, duration and power. Frequency of readout should be chosen so that the distance D is maximal. But as we have seen in Fig. 5.36 the frequency maximizing the distance is also a function of power. Fig. 5.41 shows fidelity as a function of frequency and power of readout pulse for *Sample-A*. The measurement was done with JPA off with a duration $T_{read} = 500ns$. By comparing Fig. 5.38 showing distance and Fig. 5.41 showing error

of readout ϵ_{tot} we see, that usually the best fidelity can be achieved in that conditions, where distance is maximal.

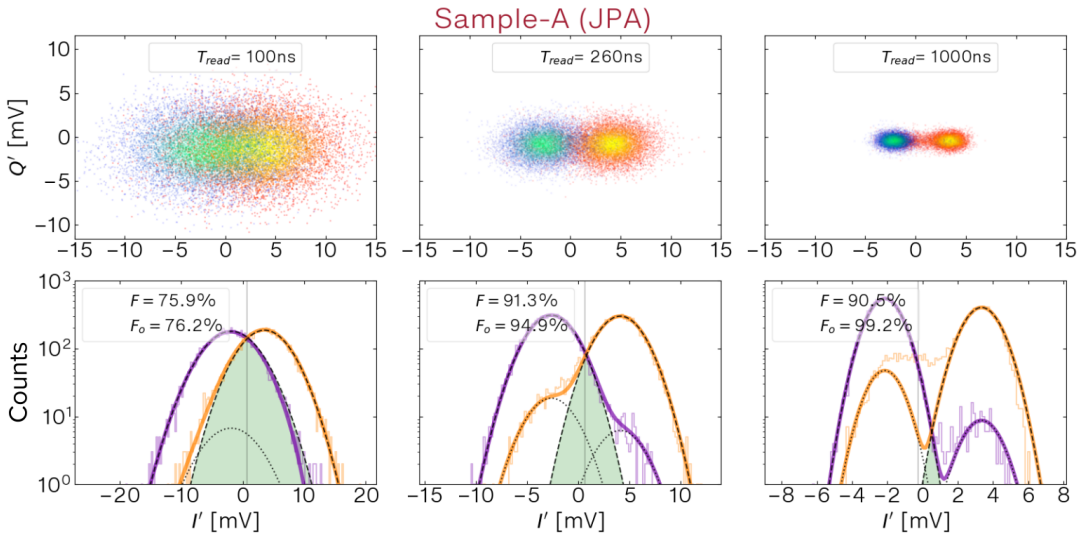

Figure 5.42: Three examples of single-shot readout with variation of readout pulse duration. Bottom axes correspond to I' values, which carry information about qubit state. Top three plots show scattering diagrams of single-shot readout. Its left axes correspond to Q' values. The low three plots show histograms plotted along I'-axis. Its left axes show number of counts in logarithmic scale. Green shade areas show the overlap of two Gaussian fits.

There is usually a trade-off between power and duration of the readout pulse. On the one hand, to maximize SNR (and minimize an overlap error ϵ_o) we would like to maximize both power P_{in} and duration T_{read}. On the other hand, if the duration of readout pulse is too long - we will get a big decay error due to the finite relaxation time T_1. Differently, when the power is too high, it can induce additional transition errors. Indeed, qubit is affected by high photon number stored in the readout mode.

To illustrate this trade-off, we plot the single-shot readout results of three different T_{read} of *Sample-A* on Fig. 5.42. We can see that as the duration of the readout pulse, and hence the time of signal acquisition, increases, the size of the spots decreases, while the positions of the centers remain constant. So the overlap error is decreasing due to better SNR. However, looking on histograms we see growing of secondary Gaussian, which is the result of qubit state transitions during measurement. We see, that decay occurs more often than excitations, but both processes exists. In conclusion, the optimal situation is when the readout time is chosen so that overlap error ϵ_o is comparable to transition errors $\epsilon_{|e\rangle,|g\rangle}$.

A more detailed analysis of variation with change of T_{read} is presented in Fig. 5.43, where the horizontal axis corresponds to T_{read}. By looking on projection of blobs in Fig.5.43 a), we see that full separation of blobs reached after $T_{read} > 400ns$. The distance between blob centers reach a constant value for $T_{read} > 150ns$. Looking on Fig.5.43 b), we observe middle figure we see that at the point of intersection of blue (distance) and black (noise) lines intersect the Signal-to-Noise ratio (red line) reaches value of 0 dB. We see that noise (equal to size of blob) reduces as square root with T_{read}. The distance seems to stay stable with T_{read} after reaching the plateau with only a small reduction. The analysis of errors of the readout is presented in Fig.5.43

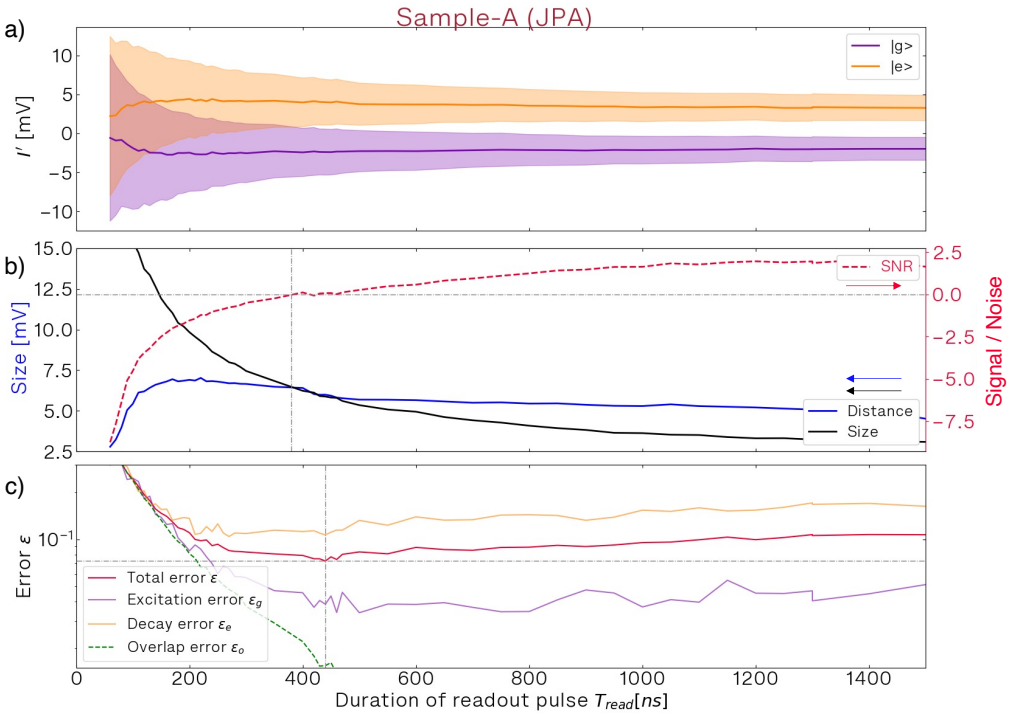

Figure 5.43: Projection of histogram, signal, noise, SNR and fidelity as a function of readout pulse duration. The top figure shows positions of centers and edges of blobs, projected onto I' axis. Measured distances between centers and sizes of blobs we plot on the middle figure as blue and black line. The red line on the middle figure shows SNR in dB. Grey dashed axes show the level of 0dB SNR and the point, when this value reaches. The lowest figure shows the total error ϵ_{tot} (red line), decay error $\epsilon_{|e\rangle}$ (orange line) and excitation error ϵ_{ketg} (purple line). The left axis is logarithmic. A green dashed line corresponds to overlap error ϵ_o A gray dashed vertical line shows T_{read}, where the lowest ϵ_{tot} reached.

c). For short readout time, the total error ϵ_{tot} is limited by overlap error ϵ_o (green dashed line). However, for T_{read} larger than $150ns$ the total error does not follow the curve of overlap error anymore and reaches a plateau. At this point, the total error is limited by transition errors $\epsilon_{|e\rangle}$, $\epsilon_{|g\rangle}$. We also notice that error due to decay is bigger than error related to excitations. And, with increasing of duration of readout T_{read} both transition errors grows.

Regarding the dependence of the fidelity of a single-shot readout on the power of the readout pulse, with *Sample-A* we met the similar compromise. We see that with increasing of power we reduce an overlap error ϵ_o by increasing distance between blobs, and keeping the noise at the same level. But by increasing the power, more and more transition errors occur due to qubit transitions induced by the readout pulse.

We have also found that at some critical power (above typically $-87dBm$) errors increase very abruptly. Soon after that, the JPA stop to be stable. We think, that this transitions of qubit due to increase of photon number in the polariton can be caused by residual Purcell effect due to residual transverse coupling of our qubit to the cavity mode or (and) nonlinear response of polariton because of ancilla nonlinearity.

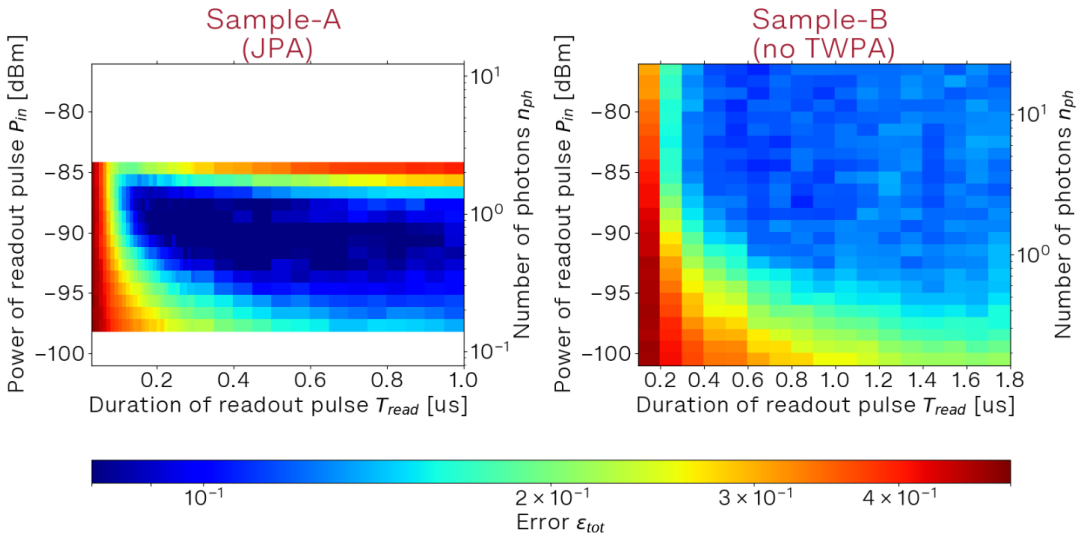

Figure 5.44: Total error ϵ_{tot} as a function of power (left axis) and duration (bottom axis) of readout pulse for sample-A *(on the left) and* Sample-B *(on the right). Blue regions corresponds to small error of readout ϵ_{tot}.*

When we were designing *Sample-B* our targets were a reduction of ancilla nonlinearity and getting rid of residual transverse coupling. The comparison of ϵ_{tot} of *Sample-A* and *Sample-B* on Fig. 5.44 as a function of T_{read} and P_{in} shows that much higher power of readout pulse can be achieved in *Sample-B*. As we discussed already, if power P_{in} and duration T_{read} of the readout pulse is too small, we are limited by overlap error because of low SNR. But in case of *Sample-A* we clearly see that possible power P_{in} is limited by value around $-85dBm$, which correspond to 1-2 photons inside polariton. Close to this value, transition errors start to grow very fast with a power and limit the fidelity. However, in case of *Sample-B* we haven't observed such problem. This allowed us to reach higher fidelity, being limited by only T_1 of qubit. We only stop increasing the power when we start to overload the TWPA. However, this does not affect the quality of qubit state separation.

We notice that in Fig. 5.44, the left plot was done using JPA, when the result

on the right picture was obtained without JPA or TWPA. This difference explains why the total error is less in the left plot. However, the behavior of transition errors as a function of readout power of both samples remained the same with or without additional amplifier.

In conclusion, we demonstrate that using pure cross-Kerr coupling to read the qubit state has helped us to overcome the trade-off between SNR and transition errors induced by readout.

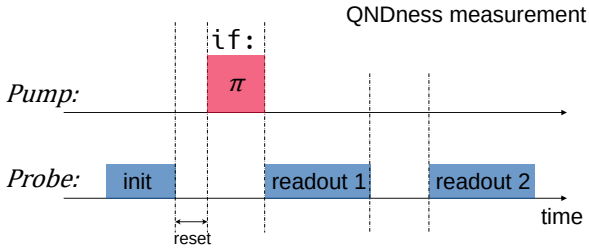

Figure 5.45: Pulse sequence for direct QNDness measurement. After initialization of qubit by applying a pulse at probe frequency, we prepare $|e\rangle$-state by sending a π-pulse or keep the state to be $|g\rangle$. Then we realize two successive measurements with a pause between them.

5.4.3. QND readout by serial readout pulses

Ideal projective measurement changes the quantum state of the system to one of its pure state and gives us information about which state it was. After the measurement, the quantum system remains in this state that we have measured. It is on this fact the quantum Zeno effect [174] [175] is based. This paradox of quantum mechanics describes the situation when a quantum system can be prevented from changing its metastable state by frequent measurements.

However, when the measurement itself is invasive, it can disturb the system so much that its state can change to another one. When the measurement is delicate enough to not perturbate a qubit and its state remains the same after measurement, we call this measurement a Quantum Non-Demolition (QND) readout. Since we use cross-Kerr coupling in our system, we expect to have a readout with high QNDness.

The logical way of characterization of the QNDness would be to repeat the readout of qubit state right after previous readout and compare the two successive results. This idea was used in Boulant *et al* [176] and Touzard *et al* [177]. To provide this measurement we applied a series of pulses shown in Fig. 5.45. By this way, we obtain results from two successive single-shot readouts, which are plotted in Fig. 5.46. In these measurements, we did not apply postselection. We expect all the points of left plot to be in bottom-left quadrant, which means that both readout give us a $|g\rangle$-state and all the points of right plot to be in top-right quadrant, which means that both readout give us a $|e\rangle$-state. The diametrically opposite points (top-right quadrant of left picture and bottom-left quadrant of right picture) show the cases when the state was wrongly prepared. However, the states stays conserved between the two readouts. We observed this situation because postselection was not applied. The QNDness characterizes the number of matching pairs of readouts.

This measurement was done before we installed a TWPA, explaining why SNR is not perfect. Even so, the power of readout is quite high and correspond to about $n_{ph} = 15$ photons inside the polariton. For better extraction of QNDness we use double threshold for the state definition. All the points, which are in gray zones, are considered as questionable and therefore ignored. But even with this approach, we are not immune to very few false hits in the red quadrants because of SNR. However, on the right plot we definitely observe too many points in the bottom-right quadrant, which could not be explained by low SNR. This means that after applied π-pulse, our first measurement gave us $|e\rangle$, but the second one gave $|g\rangle$ states.

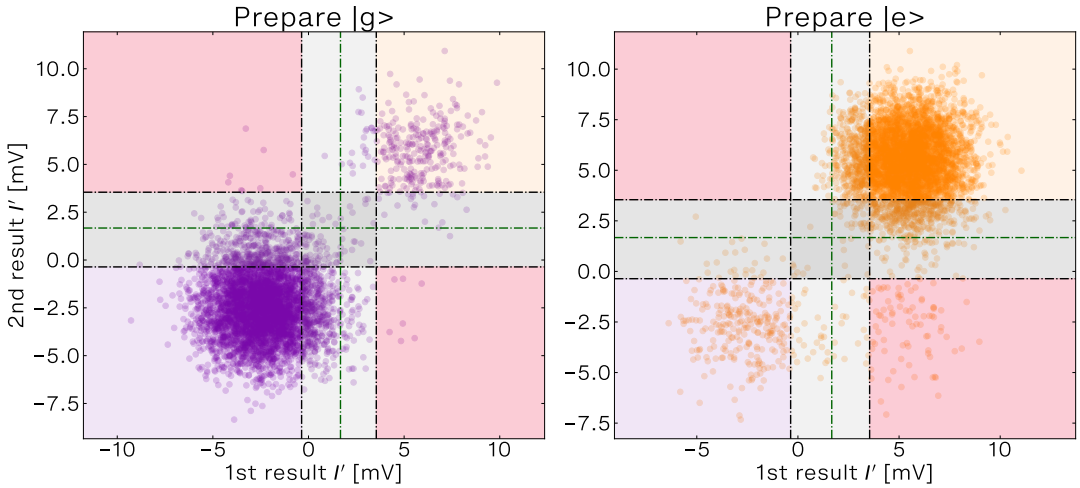

Figure 5.46: The results of measuring prepared $|g\rangle$ and $|e\rangle$ states two times in series. Low axis correspond to first readout, and left axis correspond to second readout. Both axes show an I' value, which is related to qubit state. The green dashed line shows the level of threshold. Black dashed lines show the levels of double threshold. If the point is in the bottom-left quadrant, it means that we have obtained $|g\rangle$-state after both readout signals. A top-right quadrant shows results of measuring $|e\rangle$ by both pulses. The rest two quadrants colored in red, because it contains points, which show the pair of measurements, which gave different results. If the point is in the bottom-right quadrant, it means that the first readout gave us a $|e\rangle$-state, but the second readout gave $|g\rangle$-state. So we register a case of decay than. Top-left quadrant consist of cases of measuring $|g\rangle$-state by first readout, and $|e\rangle$ by second one. The power of the readout pulse is $P_{in} = -78dBm$, which correspond to $n_{ph} = 14.5$ photons in polariton.

Probability of changing qubit state

To characterize the obtained result, we define four probabilities $P_{g\to g}$, $P_{g\to e}$, $P_{e\to e}$, $P_{e\to g}$ by next formulas:

$$P_{i\to j} = \frac{N_{i\to j}}{N_{i\to i} + N_{i\to j}} \tag{5.15}$$

where $N_{i\to j}$ is a number of cases of measuring state $|i\rangle$ by first pulse and state $|j\rangle$ by second one. The results of these probabilities is shown in Fig. 5.47.

We see that in most of the cases we got the same answer of both readout pulses ($P_{g\to g}$ and $P_{e\to e}$). But there is a probability of qubit state to be changed from $|e\rangle$ to $|g\rangle$ around $P_{e\to g} = 1\%$. This probability can be explained by natural decay of qubit.

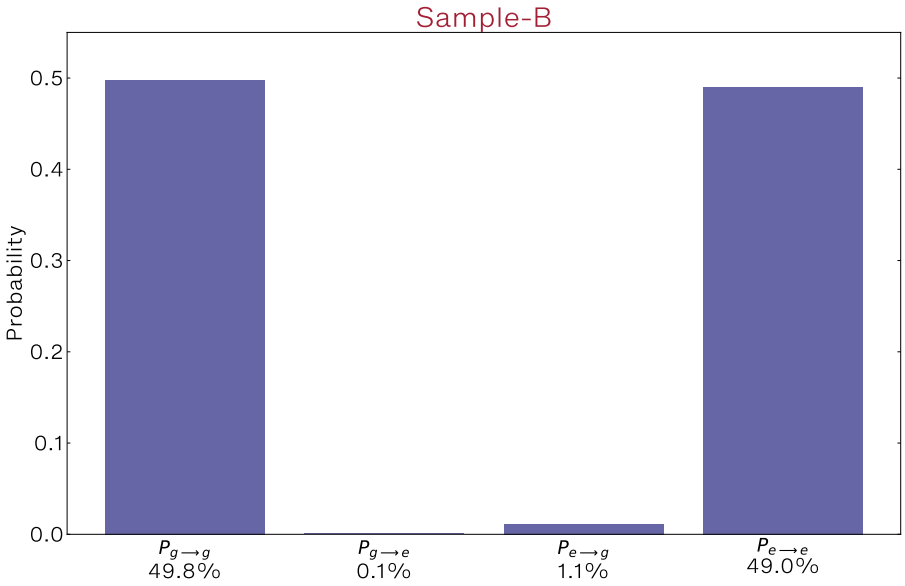

Figure 5.47: The result of two consecutive single-shot measurements of the qubit of Sample-B. *The bottom axis has four different cases, labeled as $P_{i\to j}$. This notification means that first single-shot readout gave us state $|i\rangle$, and second on gave us $|j\rangle$. The left axis shows the probability of each case.*

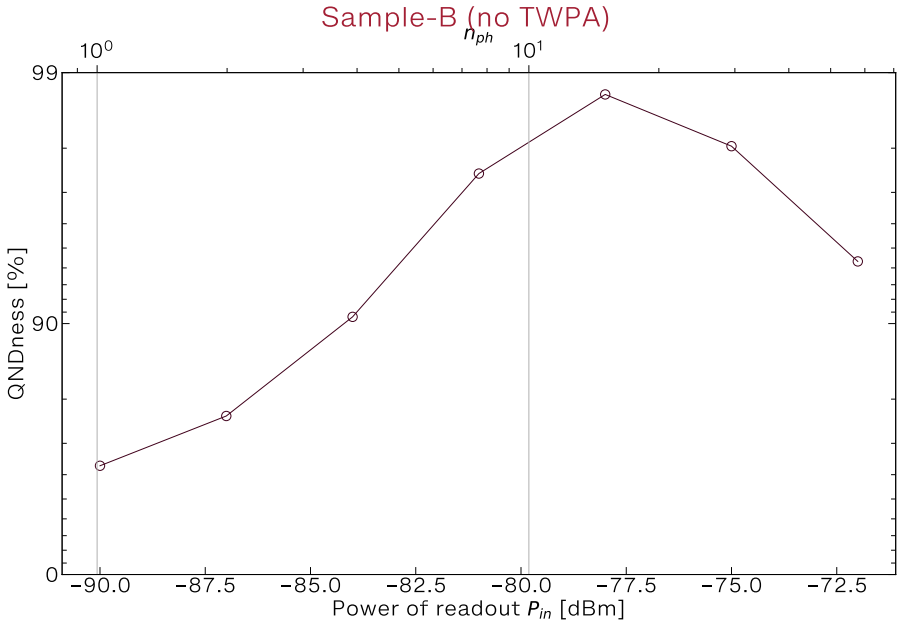

Figure 5.48: QNDness as a function of power of readout pulse. The left axis is logarithmic and shows the measured QNDness. Bottom axis correspond to power at the entrance of 3D-cavity P_{in}. The top axis shows the number of photons n_{ph}, which correspond to this power.

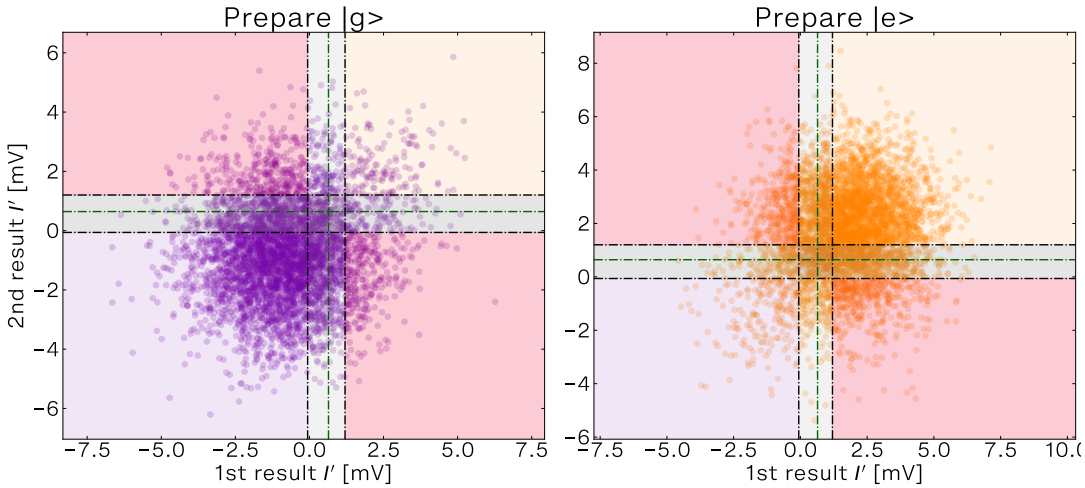

Figure 5.49: The results of measuring prepared $|g\rangle$ and $|e\rangle$ states two times in series at a power of $P_{in} = -87dBm$ and $n_{ph} = 3.2$. Because of very low SNR, we can not extract the right value of QNDness even by using double threshold.

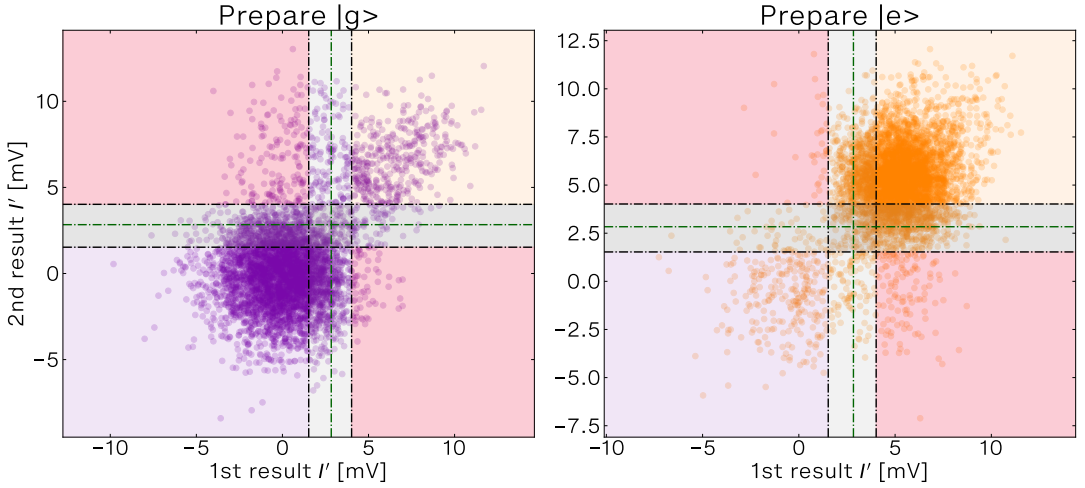

Figure 5.50: The results of measuring prepared $|g\rangle$ and $|e\rangle$ states two times in series at a power of $P_{in} = -72dBm$, which correspond to number of photons in polariton as high as $n_{ph} = 58$. Because of very low SNR, we can not extract the right value of QNDness even by using double threshold.

With duration of readout $T_{read} = 150ns$ and waiting time $T_{between} = 150ns$, we expect a probability of natural decay around $1.4\% \pm 0.15\%$, because $T_1 = 20\mu s \pm 2\mu s$.

A small probability around 0.1% of measuring state $|e\rangle$ after reading state $|g\rangle$ can be explained by error of state registration due to small SNR. Looking at the scattering diagram of Fig. 5.46 left, it doesn't seem that there is an additional blob in the top-left quadrant. It is more likely due to the big blob in the bottom-left quadrant. But to confirm or deny this, additional measurements must be taken with bigger number of statistics. We also expect that repeating this measurement using TWPA will give a more clear result because of much higher SNR, which we already have seen in Fig. 5.38.

After calculating the value of QNDness by,

$$P_{QND} = \frac{P_{g\to g} + P_{e\to e}}{2} \tag{5.16}$$

we obtain a QNDness of the measurement, $P_{QND} = 98.8\%$. This value includes natural decay of qubit. This high QNDness was obtained when the readout power is around, $-78dBm$ corresponding to about $n_{ph} = 15$ and the readout duration about $T_{read} = 150ns$.

As we have demonstrated, the QND error of 1.2% can be fully attributed to natural decay of qubit, which proves the possibility of non-demolition readout based on cross-Kerr coupling.

QNDness as a function of power

It is interesting to study how the QNDness is affected by variation of power of the readout. In Fig. 5.48, extracted QNDness is plotted as a function of readout power. We notice that at low power, extracted QNDness is quite small. This effect is explained by very low SNR at this power due to the absence of Josephson amplifier. (To understand, it is enough to have a look at Fig. 5.49.) Increasing the readout power leads to an increase of QNDness. It does not mean, that real QNDness of measurement is increasing, it is just our ability of extraction it improves. At the power of $P_{in} = -78dBm$, which corresponds to $n_{ph} = 14.5$ photons in polariton we achieve a maximum of QNDness at the level of 98.8 %. Then by continuing to increase the number of photons in polariton the QNDness starts to reduce. We are not surprised by the fact that QNDness of the measurement reduces by increasing the power. Indeed, the more photons we put into the polariton the more it will interact with the qubit. At the power of $P_{in} = -75dBm$, which correspond to, $n_{ph} = 29$ we have measured $P_{QND} = 98.0\%$. At twice higher power $P_{in} = -72dBm$ and $n_{ph} = 58$ the QNDness drop to $P_{QND} = 94.3\%$ (see corresponding scattering diagrams in Fig. 5.50).

Therefore, our measurement is affected by power of readout pulse.

Nevertheless, we got a very high QNDness at quite high power, corresponding to about 15 photons in the polariton mode. Even higher power corresponding to almost 60 photons does not destroy QNDness completely, but just reduces it to 94%. We can expect to reach even better QNDness at lower n_{ph} if we improve the SNR by using a TWPA.

5.4.4. QNDness from quantum trajectories

In this subsection, we will show the results of measuring quantum trajectories. Using the obtained trajectories, we will calculate a QNDness of qubit in presence of readout pulse.

This big series of experiments were only done for *Sample-A* and not repeated for *Sample-A* up to this moment. All the data analysis of quantum trajectories was done with the help of master internship student Timothée Guerra, whom I co-supervised. The approaches of analyzing for this data was first described in more details in his master thesis [178].

For better understand qubit behavior and investigate the effect of the measurement on qubit state as a function of parameters of the readout, we provided series of quantum trajectory experiments with different power during a very long readout time. The target of recording a trajectory is to observe and characterize quantum jumps of the qubit. The notion of quantum jumps was introduced by Bohr in 1913 [179] [180].

A quantum trajectory is a result of a continuous measurement of a qubit state. To record a trajectory, we use the pulse sequence depicted in Fig. 5.51. In half of the scenarios we keep the qubit in its thermal state close to $|g\rangle$, and in another half we excite the qubit by applying a π-pulse. Right after that, a very long readout pulse of given power with a duration $10\mu s$ is applied. Then we acquire the signal of I any Q channels. It is recorded every nanosecond, since the frequency of our acquisition board is $1GS/s$. To obtain enough statistics, we repeat this measurement over and over with a delay time of $800\mu s$ to let qubit to relax back to thermal state.

Same as we did for single-shot readout, we rotate the IQ-basis to keep all the meaningful signal in one signal called I'. An example of measured raw trajectory with I' (blue) and Q' (orange) is shown in Fig. 5.52 (a). This example was recorded with a power of readout corresponded to $n_{ph} = 6.4$. By observing the I' voltage jumps, we can detect the qubit jumps from one state to another.

To improve the signal over noise of the trajectory, an averaging was applied. By averaging, we mean division the curve on segments consist of N_{aver} a number of points and replacing each segment by the average value of this set of points. This way, the total number of points in trajectory reduces by a factor N_{aver}, but the quality of signal improves. More precisely, the level of noise is reduced by the square root of the averaging number. However, applying an averaging is equivalent to low-pass filtering, leading to remove high frequency signals. This way all the jumps which happening faster than average frequency are removed from the trajectory.

The result of averaging over $50ns$ is shown in Fig. 5.52 (b). Now we can clearly see four quantum jumps on this curve. The next step is to extract a state sequence of qubit as a function of time for each individual trajectory. This task is similar to what we did for single-shot readout, when we used the threshold value to define the qubit state. This time we will use an approach of double threshold, same as Daniel Huber Slichter did in his thesis [132]. This approach includes memory of previous state to define a new one and behaves as a hysteric "Schmitt trigger".

- If the voltage point is above a higher threshold value, state is defines as $|e\rangle$.
- If the voltage is below the lower threshold value, the state is defines as $|g\rangle$.
- If the voltage is between lower and higher threshold, we do not trust this value and define the state to be equal to previous.

This approach helps to avoid false jump detections.

To define these two thresholds, we use an approach described below. For each power of readout we measured a set of $N_{traces} = 2000$ trajectories of $T_{traj} = 10\mu s$ duration with $f_S = 1GS/s$ rate. Each trajectory is composed of a sequence of voltage values I'. The total number of points we collect for a given power is as big as $N_{points} = \frac{N_{traces} \cdot T_{traj}}{N_{aver}} \times f_S = \frac{2 \cdot 10^3 \cdot 10^{4-5}}{N_{aver}} \times 10^9$. Taking the number of averages N_{aver} from 50 to 500, the total number of points is $N_{points} = 4 \cdot 10^4 - 4 \cdot 10^5$.

To analyze the distribution of these voltages, we compute a histogram based on all these points. An example of this histogram is shown in Fig. 5.53 a). It is made for power of readout corresponding to $n_{ph} = 6.4$ with averaging of $N_{aver} = 50$. The histogram is composed by two Gaussian distributions. This two Gaussian are shown as solid lines of blue and red colors. The sum of these two Gaussian is indicated by a black solid line, which perfectly fits the measured distribution. This result is expected, because we expect qubit to be either in state $|g\rangle$ or in $|e\rangle$ which is depicted by color of fits. Using the knowledge of correlation between state of qubit and distribution of possible voltages we measure, we can define two threshold values V_h and V_l as follows:

$$V_{mid} = \frac{\mu_e + \mu_g}{2} \qquad V_h = \frac{\mu_{mid} + \mu_e}{2} \qquad V_l = \frac{\mu_{mid} + \mu_g}{2} \tag{5.17}$$

where μ_g/e is a mean value of the Gaussian related to $|g\rangle$ and $|e\rangle$, respectively and $\mu_{mid} = \frac{\mu_{|g\rangle} + \mu_{|e\rangle}}{2}$.

Once the two thresholds V_h and V_l are defined, we can process each individual trajectory to extract the actual state of the qubit as a function of time. An example of resulting state recognition from individual trajectory is shown in Fig. 5.53 b) as a gray step-like line. From this knowledge about the state of qubit as a function of time, we can calculate the probabilities $P_{e \to g}$ and $P_{g \to e}$ of qubit to change its state from one measuring point to another. Based on these probabilities, we can obtain the QNDness of the measurement from Eq. 5.16.

The calculated probabilities will depend on power of readout and readout duration, which depends on N_{aver}. We calculated the value of QNDness as function of variation of N_{aver} and plot it in Fig. 5.54. All curves present a maximum except the black one, which corresponds to the highest power of readout. The increase of QNDness with growth of N_{aver} is explained by improving of distinguishability (similar to SNR) with more averaging of signal. The more power, the faster the good resolution is achieved. On the other hand, the longer the measurement continues, the more likely the state of the qubit will change. This can happen either because of the effect of the measurement on the qubit or because of natural decay or excitation. We notice that QNDness depends strongly on the power of readout or number of photons polariton n_{ph}. If this value is too high, QNDness drops quickly by increasing of the readout duration time. But below this high value of power, we see the positive effect of increasing the power. Indeed, this increase leads to high distinguishability, which can be achieved with shorter readout times. It is important to be able to read out the state in shorter time, because then the probability of natural decay or excitation is lower. The best QNDness that we achieve on *Sample-A* was equal to $P_{QND} = 98.5\%$ for $n_{ph} = 6.4$. As a comparison, Touzard *et al* had reported almost the same a QNDness of 98.4% in [177].

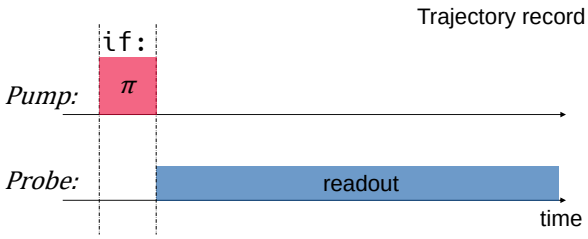

Figure 5.51: Pulse sequence for recording a quantum trajectory. For half of the cases, we apply the π-pulse to excite the qubit $|e\rangle$-state. After we send a readout pulse of a long duration ($> 10\mu s$). As soon as the acquisition board starts receiving a signal, we record the sequence of points with a periodicity of $1ns$. We save the values of I and Q as a function of time, which represents a single quantum trajectory.

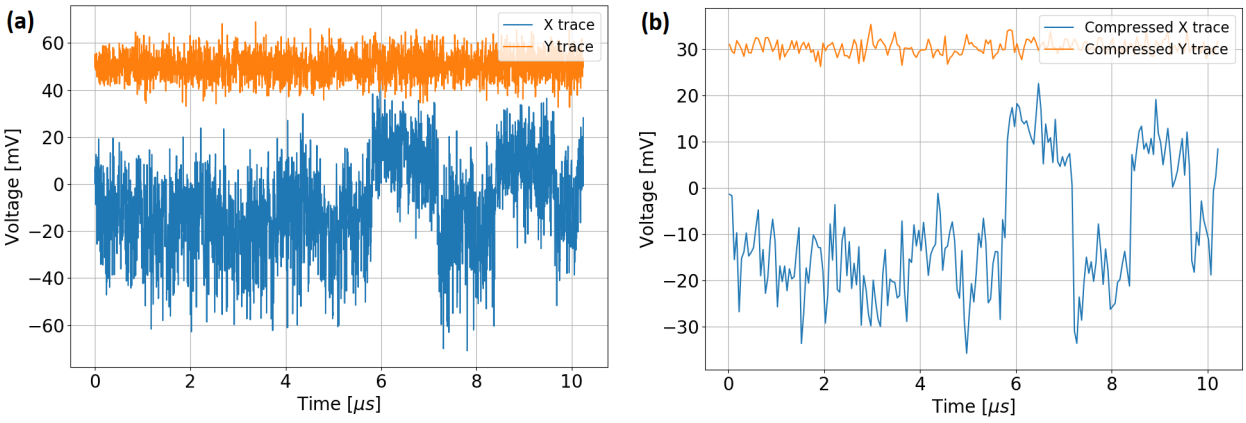

Figure 5.52: Example of a quantum trajectory. The bottom axis shows time in microseconds. The left axis corresponds to the voltage of the received signal. The blue curve is a value of signal I' of the rotated basis. Orange curve is a value of Q'. The plot shows (a) a raw signal, (b) a "compressed" trajectory after averaging. Measurement made on Sample-A *with JPA.*

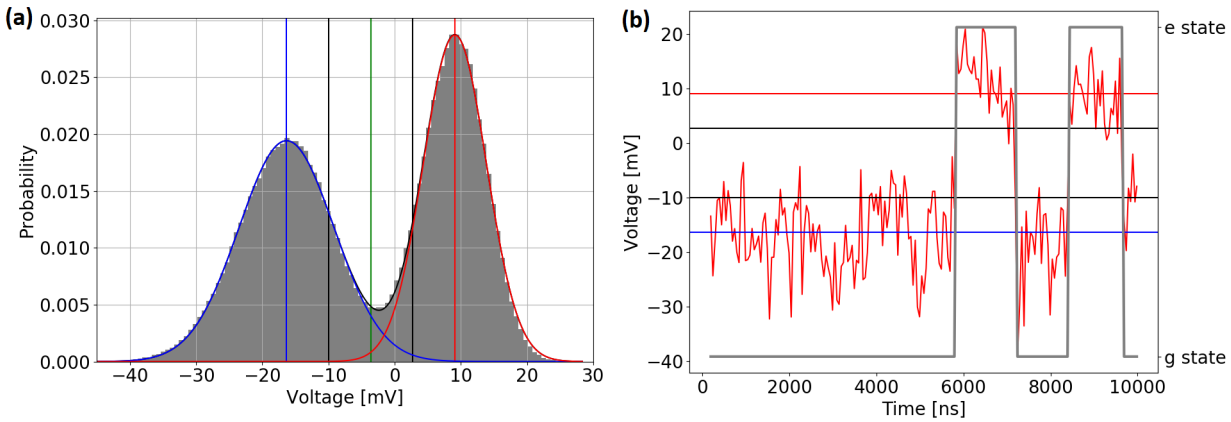

Figure 5.53: To define the thresholds, separating $|g\rangle$ and $|e\rangle$ states, we plot the distribution of all trajectory results. The gray histogram of plot (a) shows the probability of the normalized signal I' (Y-axis) to have a given voltage (X-axis), based on the distribution of points in all collected trajectories. All trajectories were taken with power of readout $n_{ph} = 6.4$. The blue and red curves correspond to Gaussian fits of $|g\rangle$ and $|e\rangle$ states. The vertical gray lines show the new double threshold values, defined from the histogram by equations 5.15, using values of μ_g, μ_e, μ_{mid} (represented by vertical lines in blue, red and green colors). Plot (b) represents one randomly taken quantum trajectory measured by readout pulse of power $n_{ph} = 6.4$ (red curve). We wish to define the state of the qubit as a function of time. The X-axis corresponds to time, and the Y-axis corresponds to signal voltage of I' in a rotated basis. The red and blue horizontal lines depict the mean values of $|e\rangle$ any $|g\rangle$ qubit states. The two gray horizontal lines show the values of double threshold, which defines the qubit state. If the point of the red curve is below the lower threshold, we say, that qubit is in $|g\rangle$-state. If the point of the red curve is above the higher threshold, we say, that qubit is in $|e\rangle$-state. (We ignore the single points as fluctuations) Based on that we define binary function which correspond to qubit state (the gray step-like line).

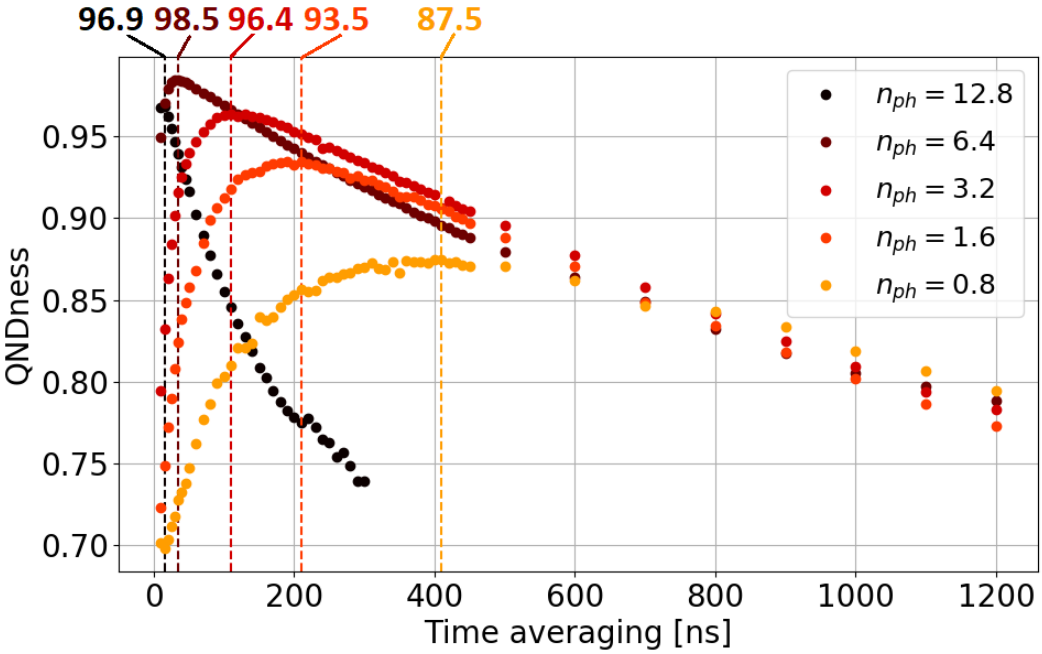

Figure 5.54: Calculated QNDness (Y axis) as a function of N_{aver} (X axis) for different power of the readout (shown by color). Vertical colored dashed lines show the averaging coefficient which gave the maximum value of QNDness for a given power. Values of maximum QNDness are indicated above. Measurement conducted on Sample-A *using JPA.*

5.4.5. Extraction of decay and excitation rate values from individual trajectories

This subsection analyzes the same set of data as in the previous subsection, focusing on extraction of excitation and decay rates $\Gamma_\uparrow$, $\Gamma_\downarrow$ in the presence of a readout pulse. These values characterize internal physical processes that affect the resulting QNDness of readout.

As we have shown before, we can measure the quantum trajectory of the qubit and extract the state of the qubit as a function of time (See Fig. 5.53 (b)). The gray line depicts qubit quantum jumps from $|g\rangle$ the $|e\rangle$ state and *vice versa*. This is a stochastic process related to the qubit T_1 by the following equation [167]:

$$T_1 = \frac{1}{\Gamma_\uparrow + \Gamma_\downarrow}. \tag{5.18}$$

An effective temperature experienced by qubit can be also calculated from the parameters $\Gamma_\downarrow$ and $\Gamma_\downarrow$ by [143]:

$$\frac{\Gamma_\uparrow}{\Gamma_\downarrow} = \exp -\frac{\hbar\omega_q}{k_B T_{eff}}, \tag{5.19}$$

where ω_q is the resonant qubit frequency and k_B is the Boltzmann constant.

In order to investigate the effect of a readout pulse on decay $\Gamma_\downarrow$ and excitation $\Gamma_\uparrow$ rates, as well as on the effective temperature T_{eff}, we extract these values from trajectories measured by readout pulses of different power. We extract these values using two different methods. We compare the results with each other and with T_1 of qubit which was not affected by readout (See section 5.3). We also compare an

effective temperature T_{eff} with the temperatures' data from a single-shot measurement and the thermometer of a dilution fridge.

As mentioned above, we use two approaches to extract the decay and excitation rates. The first is based on recording individual cases of qubit jumps and calculating their probability. The second involves averaging all obtained trajectories and analyzing the changes in the averaged value over time.

Extraction of jump rates from exponential decay

For each individual trajectory, we obtain a sequence of qubit states as a function of time. From this sequence, we see how long the qubit remains in each state before the next jump. The duration of a given state preservation are called Δt_g^i or Δt_e^i for the state $|g\rangle$ or, $|e\rangle$ respectively. By measuring the duration of the preservation of each state of a qubit, we plot the distribution of these durations. However, we should not include the last duration into account due to the fact, that it is interrupted by the end of the measurement pulse. The obtained distribution of durations Δt is plotted in Fig. 5.55 (a). The distribution on picture (a) should follow an exponential distribution. After fitting the histograms by this distribution, we extract jump rates for given $n_{ph} = 3.2$ and $N_{aver} = 200$. The rates are $\Gamma_\downarrow = 0.67\mu s^{-1}$ $\Gamma_\uparrow = 0.20\mu s^{-1}$. This approach is similar to the one applied by Gusenkova *et al* in [181].

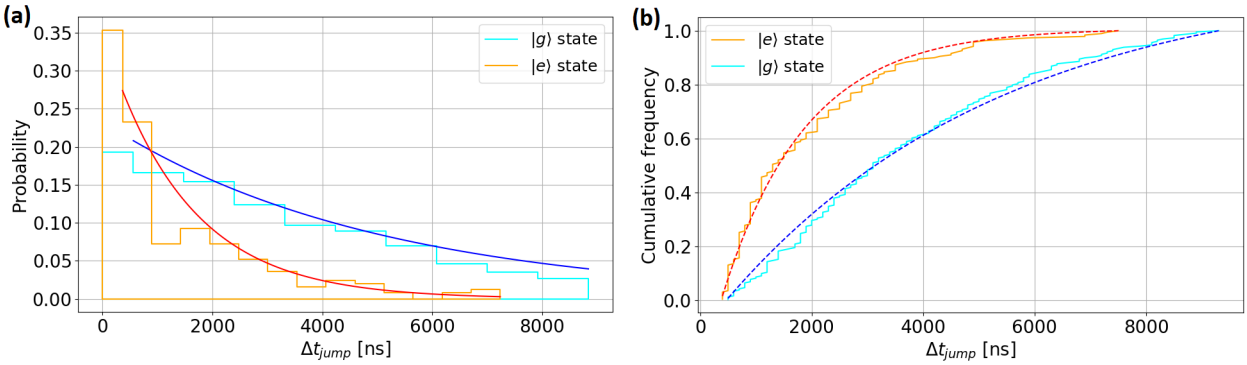

Figure 5.55: (a) Distributions of duration times that qubit remains in $|g\rangle$ (light blue step-like line) and $|e\rangle$ (orange step-like line) states. Fit by exponent is shown as solid lines of red and blue colors for $|e\rangle$ and $|g\rangle$ states, respectively. (b) Cumulative distributions of durations built for the same data and their fit.

Because our target was to automate the process of extraction of jump rates for variable N_{aver} and power n_{ph}, we had to choose the width of the bins of the histogram before fitting. There are several approaches to make it algorithmically: Freedman-Diaconis rule [182], the Shimazaki and Shinomoto's choice [183] and the Surge's formula [184]. However, neither of these approaches guarantees the accuracy of the fit.

To simplify the task of fitting the data, we switch to cumulative distribution function (CDF) of the data. This function reflects the probability of the measured value being less than the set value. The advantage of this function is that in this case, the width of bins is less significant. Fig. 5.55 (b) depicts the cumulative distribution of the same data. We use it to fit the data in most cases.

Extraction of jump rates from master equations

In this approach, we average all the individual trajectories to obtain an average signal as a function of time. In this way, we process results of individual trajectories as an ensemble. Using the state sequences from individual trajectories, we can compute the probability of qubit to be in state $|g\rangle$ or $|e\rangle$ at each point of time. These probabilities are given by:

$$P_e(t) = \frac{N_e(t)}{N_e(t) + N_g(t)}, \qquad P_g(t) = \frac{N_g(t)}{N_e(t) + N_g(t)}. \tag{5.20}$$

Assuming that qubit has only two possible quantum states $|g\rangle$ and $|e\rangle$ these probabilities follow the master equations:

$$\frac{dP_e}{dt} = -\Gamma_\downarrow P_e(t) + \Gamma_\uparrow P_g(t), \qquad \frac{dP_g}{dt} = +\Gamma_\downarrow P_e(t) - \Gamma_\uparrow P_g(t). \tag{5.21}$$

The solutions can be computed based on the fact that the sum of the probabilities equals one ($P_e + Pg = 1$):

$$P_e(t) = p_0^e \cdot e^{-(\Gamma_\downarrow + \Gamma_\uparrow)t} + \frac{\Gamma_\uparrow}{\Gamma_\downarrow + \Gamma_\uparrow}\left[1 - e^{-(\Gamma_\downarrow + \Gamma_\uparrow)t}\right], \tag{5.22}$$

$$P_g(t) = (1 - p_0^e) \cdot e^{-(\Gamma_\downarrow + \Gamma_\uparrow)t} + \frac{\Gamma_\downarrow}{\Gamma_\downarrow + \Gamma_\uparrow}\left[1 - e^{-(\Gamma_\downarrow + \Gamma_\uparrow)t}\right], \tag{5.23}$$

where p_0^e is the probability of qubit to be in $|e\rangle$ state at $t = 0$. We apply these equations to fit the data shown in Fig. 5.56. We see that data curves are in good agreement with fits based on formulas 5.22 and 5.23.

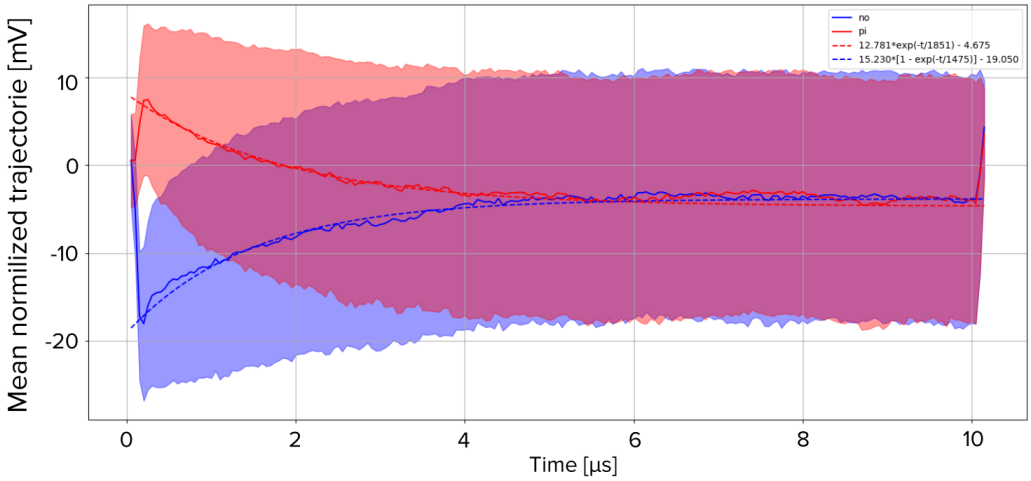

Figure 5.56: Averaged values of many trajectories with averaging factor $N_{qver} = 50$ when the number of photons was equal to $n_{ph} = 6.4$. Red curve and red shade are respectively the average and the standard deviation of all trajectories after t he $|e\rangle$ state preparation by a π-pulse, same for blue curve and shade for $|g\rangle$ state.

Jump rates as a function of readout power

As discussed above, we have conducted a series of trajectory measurements with variation of readout power. These measurements were done to analyze how QNDness depends on variation of power. We have extracted the jump rates $\Gamma_\uparrow$ and $\Gamma_\downarrow$ as a function of power. To extract the jump rates, we are using both methods described above (See subsections 5.4.5 and 5.4.5).

To compare the outcome of both methods, we analyze three different sets of trajectories measured at 3 different readout powers. In all cases these trajectories were analyzed with variation of number of averaging. The results are shown in Fig. 5.57. All the plots show the excitation and decay rates as a function of number of averaging. The graphics in the left column depict the first method of extraction of exponential decay fit. The plots in the right column are devoted to the method of extraction from master equations.

Both methods lead to comparable results and are useful for extraction of jump rates. Though, the master equation's method depends less on number of averaging and provides a more stable result.

We extract the jump rates applying both methods with variation of power and plot them in a single Fig. 5.58. We are using optimal number of averaging for both methods.

As one can see, the excitation rate (red line) tends to increase with increase of photon number. We see this tendency using both methods. However, for a number of photons lower than 4 the significant difference between the two methods is observed. It can be explained by low signal-to-noise ratio

An unexpected result relates to the fact that the decay rate (blue line) does not depend strongly on a number of photons. This, in turn, leads to an interesting effect taking place when the number of photons exceeds 6.4. In this regime the decay rate becomes lower than the excitation rate (inversion of populations) which signals the appearance of the negative temperature in our system. This fact is yet to be explained, which makes it a promising research venue for further work.

The ability of measuring quantum trajectories is a powerful tool to investigate qubit behavior in time. Its potential may be discovered in future experiments with systems consisting of more than one qubit. In our case, we were able to verify the possibility of measuring quantum trajectories, extracting QNDness and jump rates of the qubit. The most remarkable result is the high QNDness value. In addition, an inversion of population was found when a high number of photons in the cavity was reached. Thus, effect seems to be waiting to analyze and understand but in first it is important to reproduce it in another sample. Maybe some kind of similar effect was observed and described in the paper [185]

5.5. Chapter key points

In this chapter we present results of microwave measurements for three samples: *Sample-A*, *Sample-B*, *Sample-C*.

As the spectroscopic measurements of the *"Sample-A"* and *"Sample-B"* demonstrated, we had achieved the goal which was set in Chapter 2. The frequencies of the qubit and ancilla, as well as their anharmonicity are in good agreement with the target ones.

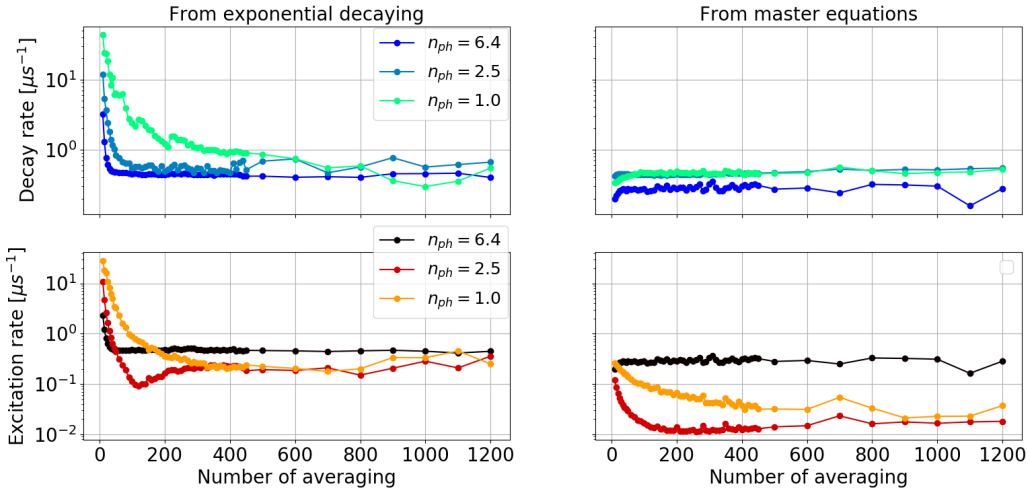

Figure 5.57: Extracted jump rates (left logarithmic axis) as a function of N_{aver} parameter (bottom axis). The top pair of plots corresponds to decay rates $\Gamma_{\downarrow}$ and the bottom pair of plots represents the excitation rates $\Gamma_{\uparrow}$. Results depicted for different power of readout are shown by different colors. The left pair of plots corresponds to values extracted from exponential decaying. The right pair of plots shows extraction from master equations.

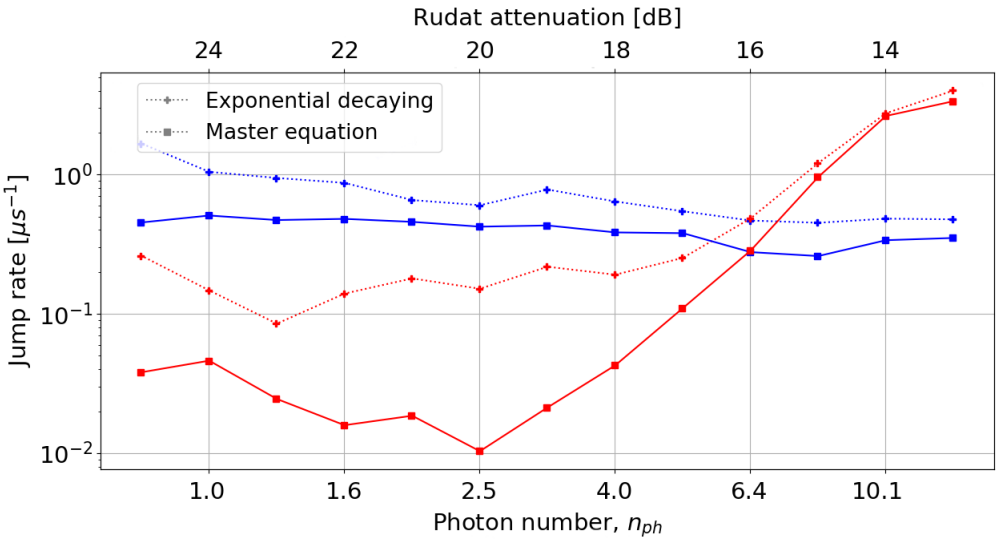

Figure 5.58: Extracted jump rates of decay $\Gamma_{\downarrow}$ (blue) and excitation $\Gamma_{\uparrow}$ (red) of the qubit in presence of readout signal as a function of its power. Square markers and solid lines illustrate the result of applying the master equation method. Diamond markers and dashed lines show values extracted by exponential decaying method. The bottom axis reflects the number of photons n_{ph} into polariton. Top axis shows an additional attenuation at room temperature. The left logarithmic axis shows jump rate.

During the qubit coherence time experiments, a five-time increase in T_1 was found in *"Sample-B"* compared to *"Sample-A"*. This demonstrates the benefits of the new design for a transmon molecule. However, it is difficult to judge the proportional contribution of each of the changes made. The preliminary data obtained from the *"Sample-C"* also look promising and demonstrate the validity of a new recipe presented in the Fabrication Chapter 3. However, this needs to be confirmed in further experiments.

As it was supposed, due to the increase in the qubit lifetime, we have succeeded in expanding possible limits of readout fidelity for the transmon molecule. For the *"Sample-B"* the results of a single-shot readout demonstrated the fidelity as high as 99.4% with readout pulse time of $150ns$. The fidelity values remain high within a broad range of variations in duration and power of readout pulse, which was not observed in the case of *"Sample-A"*.

The QNDnees of 98.8% was measured without TWPA which means that it can be improved by including TWPA to improve single-to-noise ratio.

The obtained results demonstrated the prospects of using transmon molecules built on pure cross-Kerr coupling for the readout. This would allow us to overcome such limitations as Purcell-effect and number of photons in cavity. Measurements of *"Sample-C"* preliminary show the decay time T_1 as high as 120 μs which proves the possibility of a better readout fidelity for transmon molecules. However, this particular result must be repeated.

Chapter 6.

Conclusions and Perspectives

6.1. Conclusions

In this manuscript, I experimentally investigated an innovative qubit based on non-perturbative *cross-Kerr* coupling called "transmon molecule". It consists of two inductively coupled transmons and has two orthogonal modes: *ancilla* and *qubit* coupled by a direct *cross-Kerr* coupling. The first generations of these devices were introduced before in the following papers: [89, 82, 83, 84, 85]. My work was focused on investigation of qubit readout via this *cross-Kerr* coupling as opposed to the conventional *transverse* coupling. This coupling allows the high-fidelity and QND qubit readout, because it ensures a complete absence of the Purcell effect and tolerance to the readout power. Moreover, the strength of the *cross-Kerr* coupling does not depend on the detuning between qubit and readout frequencies, which makes it very useful for the readout purpose. A sample with this structure was put into a 3D-cavity in a way to couple only the ancilla mode to the cavity field. The frequency of ancilla was designed to be close to the resonant frequency of the 3D cavity. Since the ancilla and the cavity are coupled and put into resonance, two hybridized modes - polaritons - appear. They inherit the direct non-perturbative *cross-Kerr* coupling with the qubit. In addition, they are coupled to external microwave field and can be used for readout.

We characterized the first generation of transmon molecule - *Sample-A* - by measuring its single-shot readout fidelity, quantum trajectories, coherence times and spectroscopy. To have a good reference point of the readout power, the number of excitations in the polariton was calibrated using series of Ramsey-Stark experiments with different power of readout signal. The parameters of the single-shot readout were optimized to achieve the maximum fidelity with the Josephson Parametric Amplifier (JPA) developed by Luca Planat [157]. An extensive work had been done to adjust the phase, power, frequency and duration of readout pulse, calibrate the π-pulse and optimize power, frequency and phase of JPA pump and compensation. A Gaussian π-pulse was implemented to excite the $|e\rangle$ state of qubit without exciting higher qubit states. The ancilla anharmonicity and the detuning between qubit and ancilla were varied by external magnetic field. To automate analysis of single-shot readout data, a Python library was created.

The best single-shot readout fidelity for *Sample-A* was equal to $F = 0.5(P_{e|g}+P_{g|e}) = 98.03\%$, where $P_{i|j}$ is a probability to find a qubit in a state $|i\rangle$ after preparation in $|j\rangle$. We found the fidelity of single-shot readout to be high, but limited by a significantly low relaxation time $T_1 \sim 3.3\mu s$. A negative correlation between measured relaxation

time and the detuning between ancilla and qubit was observed. We hypothesized a Purcell effect caused by the residual *transverse* coupling, which could result from either asymmetry of Josephson junctions, or sample misalignment in the cavity. To compensate the asymmetry of Josephson junctions, the *Sample-A* was rotated inside the cavity on a precisely chosen angle. As a result, a change in relaxation time was observed, but it was not significant enough to draw the final conclusion. This led us to considering other ways to protect the transmon molecule from the Purcell effect caused by *transverse* coupling.

Another line of research was related to measurements of quantum trajectories. To better characterize the behavior of the qubit in presence of excitation in polariton, a series of trajectory recording experiments was performed. The QNDness of the readout, as well as the probability of decay and excitation of qubit as a function of readout power, were extracted. The best QNDness was measured to be $QND = 98.5\%$. In addition, an unexpected effect of population inversion at high power was observed: the excitation rate was increasing with readout power, but the decay rate remained stable. This preliminary result needs to be reproduced in another sample before pushing interpretations.

To improve these results, a new generation of transmon molecule was introduced - *Sample-B*. The new set of parameters have been chosen, and the geometry has been changed to minimize the dipole moment, as well as to optimize an electric field distribution. The microscopic pictures of this new design are presented in Fig. 6.1. Due to the axial symmetry of this shape, the dipole moment related to qubit mode is suppressed, which eliminate the *transverse* coupling between qubit and cavity (see Fig. 6.1 d)). In the Table 6.1 these chosen target parameters as well as experimentally extracted parameters of *Sample-A* and *Sample-B* are presented. According to the measurements of *Sample-A* its parameters (column 1) was not perfect, and we have chosen a new target parameters by using a dedicated optimization algorithm (column 2). After a new design was optimized to reach these target values. As we can see from the table, the resulting values of new *Sample-B* (column 3) are very close to the target ones, which means the success of simulations, design and fabrication steps. This means that we successfully reached the target. To automate a generation of the design, a Python script was written. The main goal was to increase the relaxation time T_1 to prove the prospects of a new cross-Kerr based readout. Since the *cross-Kerr* coupling is tolerant to detuning between qubit and polariton, the detuning was extensively increased to avoid Purcell effect even under conditions of residual *transverse* coupling. The ancilla anharmonicity was reduced to make it less sensitive to the readout power. Another Python optimization script was written to optimize the values of electrical parameters for the transmon molecule circuit. To reduce the residual *transverse* coupling, the dipole moment related to qubit mode was reduced and a new circular geometry for the pads inspired from [99] was proposed. HFSS finite element simulations of electric fields allowed to reduce the amplitude of qubit electric field and to reach the target values for the capacitances.

During the nanofabrication stage of my PhD work, the fabrication recipe was optimized. To fabricate the *Sample-B*, I implied several minor changes and significantly improved the recipe for *Sample-C*. For *Sample-B* the improvements included optimization of a polymer mask deposition, calibration of the electron-beam doses and investigation of the resulting areas of Josephson junctions as a function of input parameters using a scanning electron microscope. For *Sample-C* the residual polymer

Value	*Sample-A*	Target	*Sample-B*
$\omega_Q/2\pi$ $[GHz]$	6.284	2.78	2.523
$\omega_A/2\pi$ $[GHz]$	7.78	7.35	7.092
$g_{ac}/2\pi$ $[MHz]$	295	> 100	290
$\alpha_q/2\pi$ $[MHz]$	-88	-77	-76.2
$U_A/2\pi$ $[MHz]$	-13.5	-1.3	-1.92
$g_{zz}/2\pi$ $[MHz]$	34.5	10.1	13.6
C_s $[fF]$	110	125	129
C_t $[fF]$	59.6	87	83.5
$E_j/2\pi\hbar$ $[GHz]$	29.2	7.3	5.76
L_A $[nH]$	5.32	2.66	3.59

Table 6.1: Spectroscopic and electrical characteristics' comparison between three samples and the target values. First the Sample-A *was measured, then the target parameters were chosen and* Sample-B *was developed. The blue color of text corresponds to the values which have been chosen or approximated, while black text is related to values which were extracted experimentally.*

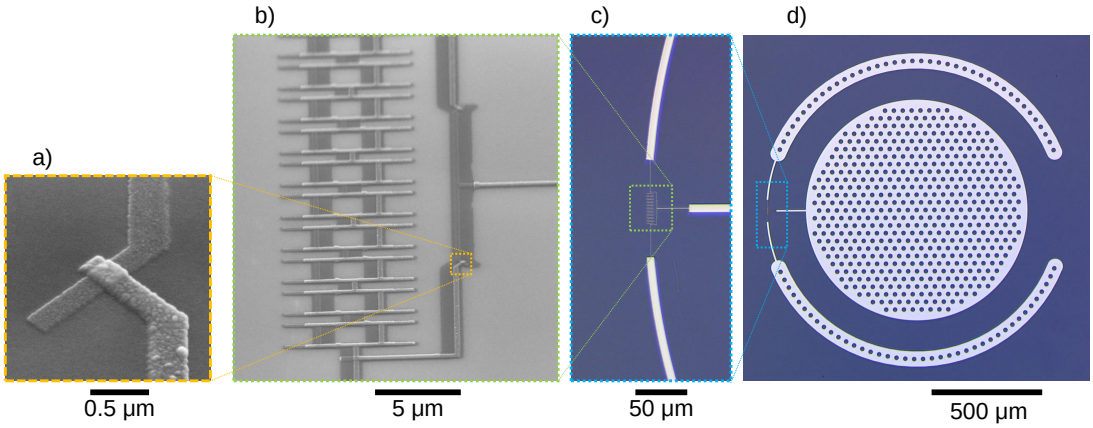

Figure 6.1: Illustration of a transmon molecule with new circular geometry of the pads. a, b) - scanning electron microscopy of the Josephson junctions; c, d) - optical microscopy of the pads.

Reference	Fidelity	Duration	T_1	QND	Coupling
Jeffrey et al 2014 [73]	98.0%	$140ns$	$10\mu s$	missing	transverse
Walter et al 2017 [69]	99.1 – 99.6%	$48-88ns$	$7.6\mu s$	missing	transverse
Sunada et al. 2022 [76]	99.1%	$40ns$	$17\mu s$	98.1%	transverse
Ikonen et al 2018 [186]	93.4%	$400ns$	$3\mu s$	missing	longitudinal
Touzard et al 2018 [177]	97.8%	$750ns$	$90 - 190\mu s$	98.4%	longitudinal
Dassonneville et al 2018 [85]	97.4%	$50ns$	$3.3\mu s$	99% ± 0.6%	cross-Kerr
This work	99.4%	$150ns$	$19.6\mu s$	98.8%	cross-Kerr

Table 6.2: Results of state-of-the-art qubit readout for three different coupling types between the qubit and readout modes.

film around the junctions was analyzed, and a cold development process was applied to avoid it. The source of a problem with a quality of aluminum in our cleanroom was solved by reducing the power of ultrasonication during the lift-off. Several new steps were introduced into the recipe to further improve the substrate quality, such as hydrofluoric etching of silicon oxide and titanium sublimation pumping of the chamber before the aluminum evaporation. These improvements contributed to reduction of the amount of TLS.

To evaluate the impact of applied changes on the target parameters, several measurements were conducted. *Sample-B* was measured to analyze the new design, and *Sample-C* - to test major changes in the fabrication recipe. Both samples have demonstrated significant progress. In case of *Sample-B* the relaxation time was improved in more than 5 times in comparison to *Sample-A* and reached $T_1 = 20\mu s$. As a result, a single-shot readout was applied with fidelity as high as 99.37%. The readout fidelity has also shown insensitivity to the increase of readout power. The QNDness of *Sample-B* was measured to be 98.8%. The preliminary measurements of *Sample-C* have demonstrated the average relaxation time equal to $T_1 = 120\mu s$. However, more investigation needs to be done to confirm it. To put these results in the context of the state-of-the-art qubit readout we put it in the Table 6.2. As one can see, the readout fidelity results in our case are similar to the best results achieved for transverse coupling.

In conclusion, this work explores the benefits of *cross-Kerr* coupling for the improved readout of qubit. We achieved better results of high-fidelity quantum-non-demolition readout for new generation of transmon molecules, provided by design optimization and nanofabrication improvements. This circuit may be considered as a promising element for future superconducting quantum processor units, since it allows overcoming the fundamental limitations of *transverse* coupling scheme. In particular, it does not require Purcell filters and creates a possibility of quantum non-demolition readout even under high readout power. Its benefits require further investigation, which may focus on reproducing the results of a fabrication recipe and developing a two-qubit gate based on the transmon molecule.

6.2. Prospects

Future milestones

To prove the ability of a transmon molecule to be used in quantum processor units, several milestones should be reached. First, the two-qubit gates between two transmon molecules should be developed. Second, multiplexing readout should be demonstrated. Third, it is important to test the functioning of a transmon molecule in 2D architecture. Though it was already shown in [89, 82, 83], higher decoherence times are necessary to be achieved. For that purpose, the nanofabrication process needs to be further improved in the planar geometry.

Improvements of nanofabrication

To sustain a reproduction of the improved nanofabrication recipe is a primary step for further development of this project. The results to be verified include the quality of a substrate surface, reproducibility of similarity of Josephson junctions, the quality of aluminum pads and absence of residual aluminum in the areas around junctions. All measurements should be based on scanning electron microscopy - SEM. This new recipe needs to be standardized

To additionally improve the nanofabrication process and to increase the T_1 several ideas can be proposed. First, it would be useful to switch to "Manhattan-style" junctions to make the Josephson junctions more similar. Second, to make the junctions even more similar, the laser annealing can be used to adjust the junctions' size [187]. Third, to produce large aluminum surfaces, the liftoff technique should be replaced by etching gaps in the aluminum film that completely covers the wafer. This method has shown a better quality of interface between aluminum and silicon substrate. Finally, the materials of fabrication can be reviewed: replacing the aluminum by niobium for the pads is a common technique of increasing relaxation time of the qubit. After the recent article which have shown a significant improvement of transmon T_1 a tantalum is becoming a new popular solution [188].

Other improvements

There is a possibility to replace the SQUID-chain by a nanowire to produce the inductance in the transmon molecule. This approach looks promising, since it reduces the number of Josephson junctions in the system.

Using DRAG-pulse for exciting the qubit and CLEAR-pulse for the readout can also help to improve the initialization and the readout performance.

Bibliography

[1] McKinseyCompany. Quantum computing: An emerging ecosystem and industry use cases. (December), 2021.

[2] Paul Benioff. The computer as a physical system: A microscopic quantum mechanical Hamiltonian model of computers as represented by Turing machines. *Journal of Statistical Physics*, 22(5):563–591, 1980.

[3] U. Manin. *Computable and not computable*. Soviet radio, Moscow, 1980.

[4] Richard P. Feynman. Simulating Physics with Computers. *Department of Physics, California Institute of Technology*, 21:467–488, 1981.

[5] Stephen Wiesner. Conjugate coding. *ACM SIGACT News*, 15(1):78–88, 1983.

[6] Seth Lloyd. A potentially realizable quantum computer. *Science*, 261(5128):1569–1571, 1993.

[7] Y. Nakamura, Yu. A. Pashkin, and J. S. Tsai. Coherent control of macroscopic quantum states in a single-cooper-pair box. *Nature*, 398(6730):786–788, Apr 1999.

[8] Morten Kjaergaard, Mollie E. Schwartz, Jochen Braumüller, Philip Krantz, Joel I.-J. Wang, Simon Gustavsson, and William D. Oliver. Superconducting qubits: Current state of play. *Annual Review of Condensed Matter Physics*, 11(1):369–395, Mar 2020.

[9] J. M. Raimond, M. Brune, and S. Haroche. Manipulating quantum entanglement with atoms and photons in a cavity. *Rev. Mod. Phys.*, 73:565–582, Aug 2001.

[10] Igor Ryabtsev, Denis Tretyakov, and Ilya Beterov. Applicability of rydberg atoms to quantum computers. *Journal of Physics B Atomic and Molecular Physics*, 38:421–436, 01 2005.

[11] M. Saffman, T. G. Walker, and K. Mølmer. Quantum information with Rydberg atoms. *Reviews of Modern Physics*, 82(3):2313–2363, 2010.

[12] M. Saffman. Quantum computing with atomic qubits and Rydberg interactions: Progress and challenges. *Journal of Physics B: Atomic, Molecular and Optical Physics*, 49(20), 2016.

[13] C. S. Adams, J. D. Pritchard, and J. P. Shaffer. Rydberg atom quantum technologies. *Journal of Physics B: Atomic, Molecular and Optical Physics*, 53(1):1–24, 2020.

[14] Daniel Loss, David P DiVincenzo, and P DiVincenzo. Quantum computation with quantum dots. *Phys. Rev. A*, 57(1):120–126, 1997.

[15] Siying Wang, Claudia Querner, Tali Dadosh, Catherine H. Crouch, Dmitry S. Novikov, and Marija Drndic. Collective fluorescence enhancement in nanoparticle clusters. *Nature Communications*, 2(1):364–368, 2011.

[16] G. J. Milburn. Photons as qubits. *Physica Scripta T*, T137, 2009.

[17] Rosa Brouri, Alexios Beveratos, Jean-Philippe Poizat, and Philippe Grangier. Photon antibunching in the fluorescence of individual color centers in diamond. *Opt. Lett.*, 25(17):1294–1296, Sep 2000.

[18] L. Childress, M. V. Gurudev Dutt, J. M. Taylor, A. S. Zibrov, F. Jelezko, J. Wrachtrup, P. R. Hemmer, and M. D. Lukin. Coherent dynamics of coupled electron and nuclear spin qubits in diamond. *Science*, 314(5797):281–285, 2006.

[19] Lov K. Grover. A fast quantum mechanical algorithm for database search. *STOC '96: Proceedings of the twenty-eighth annual ACM symposium on Theory of Computing*, pages 212–219, 1996.

[20] Peter W. Shor. Polynomial-time algorithms for prime factorization and discrete logarithms on a quantum computer. *SIAM Journal on Computing*, 26(5):1484–1509, 1997.

[21] Martin Gardner. Mathematical Games: A new kind of cipher that would take millions of years to break. *Scientific American*, 237(August):120–124, 1977.

[22] Frank Arute, Kunal Arya, Ryan Babbush, Dave Bacon, Joseph C. Bardin, Rami Barends, Rupak Biswas, Sergio Boixo, Fernando G.S.L. Brandao, David A. Buell, Brian Burkett, Yu Chen, Zijun Chen, Ben Chiaro, Roberto Collins, William Courtney, Andrew Dunsworth, Edward Farhi, Brooks Foxen, Austin Fowler, Craig Gidney, Marissa Giustina, Rob Graff, Keith Guerin, Steve Habegger, Matthew P. Harrigan, Michael J. Hartmann, Alan Ho, Markus Hoffmann, Trent Huang, Travis S. Humble, Sergei V. Isakov, Evan Jeffrey, Zhang Jiang, Dvir Kafri, Kostyantyn Kechedzhi, Julian Kelly, Paul V. Klimov, Sergey Knysh, Alexander Korotkov, Fedor Kostritsa, David Landhuis, Mike Lindmark, Erik Lucero, Dmitry Lyakh, Salvatore Mandrà, Jarrod R. McClean, Matthew McEwen, Anthony Megrant, Xiao Mi, Kristel Michielsen, Masoud Mohseni, Josh Mutus, Ofer Naaman, Matthew Neeley, Charles Neill, Murphy Yuezhen Niu, Eric Ostby, Andre Petukhov, John C. Platt, Chris Quintana, Eleanor G. Rieffel, Pedram Roushan, Nicholas C. Rubin, Daniel Sank, Kevin J. Satzinger, Vadim Smelyanskiy, Kevin J. Sung, Matthew D. Trevithick, Amit Vainsencher, Benjamin Villalonga, Theodore White, Z. Jamie Yao, Ping Yeh, Adam Zalcman, Hartmut Neven, and John M. Martinis. Quantum supremacy using a programmable superconducting processor. *Nature*, 574(7779):505–510, 2019.

[23] IBM Quantum web-page.

[24] Rigetti Forest web-site.

[25] Amazon Bracket web-site.

[26] Azure Quantum web-site.

[27] IQM web-site.

[28] D-WAVE web-site.

[29] David P. DiVincenzo. The physical implementation of quantum computation. *Fortschritte der Physik*, 48(9-11):771–783, 2000.

[30] K Lee Geerlings. Improving Coherence of Superconducting Qubits and Resonators. 2013.

[31] Clemens Müller, Jürgen Lisenfeld, Alexander Shnirman, and Stefano Poletto. Interacting two-level defects as sources of fluctuating high-frequency noise in superconducting circuits. *Physical Review B - Condensed Matter and Materials Physics*, 92(3):1–14, 2015.

[32] Alexander Bilmes, Serhii Volosheniuk, Jan David Brehm, Alexey V. Ustinov, and Jürgen Lisenfeld. Quantum sensors for microscopic tunneling systems. *npj Quantum Information*, 7(1):1–12, 2021.

[33] P. V. Klimov, J. Kelly, Z. Chen, M. Neeley, A. Megrant, B. Burkett, R. Barends, K. Arya, B. Chiaro, Yu Chen, A. Dunsworth, A. Fowler, B. Foxen, C. Gidney, M. Giustina, R. Graff, T. Huang, E. Jeffrey, Erik Lucero, J. Y. Mutus, O. Naaman, C. Neill, C. Quintana, P. Roushan, Daniel Sank, A. Vainsencher, J. Wenner, T. C. White, S. Boixo, R. Babbush, V. N. Smelyanskiy, H. Neven, and John M. Martinis. Fluctuations of Energy-Relaxation Times in Superconducting Qubits. *Physical Review Letters*, 121(9):22–25, 2018.

[34] Conal E. Murray. Material matters in superconducting qubits. *Materials Science and Engineering R: Reports*, 146, 2021.

[35] Dominik Szczęśniak and Sabre Kais. Magnetic flux noise in superconducting qubits and the gap states continuum. *Scientific Reports*, 11(1):1–7, 2021.

[36] J. M. Gambetta, A. A. Houck, and Alexandre Blais. Superconducting qubit with purcell protection and tunable coupling. *Physical Review Letters*, 106(3):1–4, 2011.

[37] B. G. Christensen, C. D. Wilen, A. Opremcak, J. Nelson, F. Schlenker, C. H. Zimonick, L. Faoro, L. B. Ioffe, Y. J. Rosen, J. L. Dubois, B. L.T. Plourde, and R. Mcdermott. Anomalous charge noise in superconducting qubits. *Physical Review B*, 100(14), 2019.

[38] E. M. Purcell.

[39] A. A. Houck, J. A. Schreier, B. R. Johnson, J. M. Chow, Jens Koch, J. M. Gambetta, D. I. Schuster, L. Frunzio, M. H. Devoret, S. M. Girvin, and R. J. Schoelkopf. Controlling the spontaneous emission of a superconducting transmon qubit. *Physical Review Letters*, 101(8), aug 2008.

[40] G. Catelani, R. J. Schoelkopf, M. H. Devoret, and L. I. Glazman. Relaxation and frequency shifts induced by quasiparticles in superconducting qubits. *Physical Review B - Condensed Matter and Materials Physics*, 84(6):1–24, 2011.

[41] K. Serniak, M. Hays, G. De Lange, S. Diamond, S. Shankar, L. D. Burkhart, L. Frunzio, M. Houzet, and M. H. Devoret. Hot Nonequilibrium Quasiparticles in Transmon Qubits. *Physical Review Letters*, 121(15):157701, 2018.

[42] Antti P. Vepsäläinen, Amir H. Karamlou, John L. Orrell, Akshunna S. Dogra, Ben Loer, Francisca Vasconcelos, David K. Kim, Alexander J. Melville, Bethany M. Niedzielski, Jonilyn L. Yoder, Simon Gustavsson, Joseph A. Formaggio, Brent A. VanDevender, and William D. Oliver. Impact of ionizing radiation on superconducting qubit coherence. *Nature*, 584(7822):551–556, 2020.

[43] M. H. Devoret and R. J. Schoelkopf. Superconducting circuits for quantum information: An outlook. *Science*, 339(6124):1169–1174, 2013.

[44] John Clarke and Frank K. Wilhelm. Superconducting quantum bits, 2008.

[45] Y. Nakamura, C. D. Chen, and J. S. Tsai. Spectroscopy of energy-level splitting between two macroscopic quantum states of charge coherently superposed by josephson coupling. *Phys. Rev. Lett.*, 79:2328–2331, Sep 1997.

[46] Y Nakamura, Yu A Pashkin, and J S Tsai. Nat Coherent Control of Macro States. 398(April), 1999.

[47] T. P. Orlando, J. E. Mooij, Lin Tian, Caspar H. Van Der Wal, L. S. Levitov, Seth Lloyd, and J. J. Mazo. Superconducting persistent-current qubit. *Physical Review B - Condensed Matter and Materials Physics*, 60(22):15398–15413, 1999.

[48] M. Grajcar, A. Izmalkov, E. Il'ichev, Th Wagner, N. Oukhanski, U. Hübner, T. May, I. Zhilyaev, H. E. Hoenig, Ya S. Greenberg, V. I. Shnyrkov, D. Born, W. Krech, H. G. Meyer, Alec Maassen Van Den Brink, and M. H.S. Amin. Low-frequency measurement of the tunneling amplitude in a flux qubit. *Physical Review B - Condensed Matter and Materials Physics*, 69(6):9–11, 2004.

[49] F. W. Putnam. American Association for the Advancement of Science. *Science*, 5(124):760–761, 1897.

[50] John M. Martinis, S. Nam, J. Aumentado, and C. Urbina. Rabi oscillations in a large josephson-junction qubit. *Phys. Rev. Lett.*, 89:117901, Aug 2002.

[51] K. B. Cooper, Matthias Steffen, R. McDermott, R. W. Simmonds, Seongshik Oh, D. A. Hite, D. P. Pappas, and John M. Martinis. Observation of Quantum Oscillations between a Josephson Phase Qubit and a Microscopic Resonator Using Fast Readout. *Physical Review Letters*, 93(18):1–5, 2004.

[52] E. Hoskinson, F. Lecocq, N. Didier, A. Fay, F. W.J. Hekking, W. Guichard, O. Buisson, R. Dolata, B. MacKrodt, and A. B. Zorin. Quantum dynamics in a camelback potential of a dc SQUID. *Physical Review Letters*, 102(9):1–4, 2009.

[53] D. Vion, A. Aassime, A. Cottet, P. Joyez, H. Pothier, C. Urbina, D. Esteve, and M. H. Devoret. Manipulating the quantum state of an electrical circuit. *Science*, 296(5569):886–889, 2002.

[54] A. Fay, E. Hoskinson, F. Lecocq, L. P. Lévy, F. W. J. Hekking, W. Guichard, and O. Buisson. Strong tunable coupling between a superconducting charge and phase qubit. *Phys. Rev. Lett.*, 100:187003, May 2008.

[55] V. V. Ryazanov, V. A. Oboznov, A. Yu. Rusanov, A. V. Veretennikov, A. A. Golubov, and J. Aarts. Coupling of two superconductors through a ferromagnet: Evidence for a π junction. *Phys. Rev. Lett.*, 86:2427–2430, Mar 2001.

[56] Jens Koch, Terri M. Yu, Jay Gambetta, A. A. Houck, D. I. Schuster, J. Majer, Alexandre Blais, M. H. Devoret, S. M. Girvin, and R. J. Schoelkopf. Charge-insensitive qubit design derived from the Cooper pair box, 2007.

[57] Vladimir E. Manucharyan, Jens Koch, Markus Brink, Leonid I. Glazman, and Michel H. Devoret. Coherent oscillations between classically separable quantum states of a superconducting loop. 2009.

[58] J. A. Schreier, A. A. Houck, Jens Koch, D. I. Schuster, B. R. Johnson, J. M. Chow, J. M. Gambetta, J. Majer, L. Frunzio, M. H. Devoret, S. M. Girvin, and R. J. Schoelkopf. Suppressing charge noise decoherence in superconducting charge qubits, 2008.

[59] Martin Sandberg, Michael R. Vissers, Thomas A. Ohki, Jiansong Gao, José Aumentado, Martin Weides, and David P. Pappas. Radiation-suppressed superconducting quantum bit in a planar geometry. *Applied Physics Letters*, 102(7), 2013.

[60] R. Barends, J. Kelly, A. Megrant, D. Sank, E. Jeffrey, Y. Chen, Y. Yin, B. Chiaro, J. Mutus, C. Neill, P. O'Malley, P. Roushan, J. Wenner, T. C. White, A. N. Cleland, and John M. Martinis. Coherent josephson qubit suitable for scalable quantum integrated circuits. *Physical Review Letters*, 111(8):1–5, 2013.

[61] Vladimir E. Manucharyan, Jens Koch, Leonid I. Glazman, and Michel H. Devoret. Fluxonium: Single cooper-pair circuit free of charge offsets. *Science*, 326(5949):113–116, 2009.

[62] Nathanaël Cottet, Haonan Xiong, Long B. Nguyen, Yen Hsiang Lin, and Vladimir E. Manucharyan. Electron shelving of a superconducting artificial atom. *Nature Communications*, 12(1):1–7, 2021.

[63] Aaron Somoroff, Quentin Ficheux, Raymond A. Mencia, Haonan Xiong, Roman V. Kuzmin, and Vladimir E. Manucharyan. Millisecond coherence in a superconducting qubit. 1, 2021.

[64] András Gyenis, Agustin Di Paolo, Jens Koch, Alexandre Blais, Andrew A. Houck, and David I. Schuster. Moving beyond the Transmon: Noise-Protected Superconducting Quantum Circuits. *PRX Quantum*, 2(3):1–14, 2021.

[65] Alexandre Blais, Arne L. Grimsmo, S. M. Girvin, and Andreas Wallraff. Circuit quantum electrodynamics. *Reviews of Modern Physics*, 93(2):25005, 2021.

[66] Xiu Gu, Anton Frisk Kockum, Adam Miranowicz, Yu xi Liu, and Franco Nori. Microwave photonics with superconducting quantum circuits. *Physics Reports*,

718-719:1–102, 2017. Microwave photonics with superconducting quantum circuits.

[67] Alexandre Blais, Ren Shou Huang, Andreas Wallraff, S. M. Girvin, and R. J. Schoelkopf. Cavity quantum electrodynamics for superconducting electrical circuits: An architecture for quantum computation. *Physical Review A - Atomic, Molecular, and Optical Physics*, 69(6), 2004.

[68] E.T. Jaynes and F.W. Cummings. Comparison of quantum and semiclassical radiation theories with application to the beam maser. *Proceedings of the IEEE*, 51(1):89–109, 1963.

[69] T. Walter, P. Kurpiers, S. Gasparinetti, P. Magnard, A. Potočnik, Y. Salathé, M. Pechal, M. Mondal, M. Oppliger, C. Eichler, and A. Wallraff. Rapid High-Fidelity Single-Shot Dispersive Readout of Superconducting Qubits. *Physical Review Applied*, 7(5):1–11, 2017.

[70] D. H. Slichter, R. Vijay, S. J. Weber, S. Boutin, M. Boissonneault, J. M. Gambetta, A. Blais, and I. Siddiqi. Measurement-induced qubit state mixing in circuit QED from Up-converted dephasing noise. *Physical Review Letters*, 109(15):1–5, 2012.

[71] Daniel Sank, Zijun Chen, Mostafa Khezri, J. Kelly, R. Barends, B. Campbell, Y. Chen, B. Chiaro, A. Dunsworth, A. Fowler, E. Jeffrey, E. Lucero, A. Megrant, J. Mutus, M. Neeley, C. Neill, P. J.J. O'Malley, C. Quintana, P. Roushan, A. Vainsencher, T. White, J. Wenner, Alexander N. Korotkov, and John M. Martinis. Measurement-Induced State Transitions in a Superconducting Qubit: Beyond the Rotating Wave Approximation. *Physical Review Letters*, 117(19), nov 2016.

[72] Raphaël Lescanne, Lucas Verney, Quentin Ficheux, Michel H. Devoret, Benjamin Huard, Mazyar Mirrahimi, and Zaki Leghtas. Escape of a Driven Quantum Josephson Circuit into Unconfined States. *Physical Review Applied*, 11(1):1, 2019.

[73] Evan Jeffrey, Daniel Sank, J. Y. Mutus, T. C. White, J. Kelly, R. Barends, Y. Chen, Z. Chen, B. Chiaro, A. Dunsworth, A. Megrant, P. J. O'Malley, C. Neill, P. Roushan, A. Vainsencher, J. Wenner, A. N. Cleland, and John M. Martinis. Fast accurate state measurement with superconducting qubits. *Physical Review Letters*, 112(19), may 2014.

[74] Eyob A. Sete, John M. Martinis, and Alexander N. Korotkov. Quantum theory of a band-pass Purcell filter for qubit readout. *Physical Review A - Atomic, Molecular, and Optical Physics*, 92(1), jul 2015.

[75] H. J. Mamin, E. Huang, S. Carnevale, C. T. Rettner, N. Arellano, M. H. Sherwood, C. Kurter, B. Trimm, M. Sandberg, R. M. Shelby, M. A. Mueed, B. A. Madon, A. Pushp, M. Steffen, and D. Rugar. Merged-Element Transmons: Design and Qubit Performance. *Physical Review Applied*, 16(2):1–8, 2021.

[76] Yoshiki Sunada, Shingo Kono, Jesper Ilves, Shuhei Tamate, Takanori Sugiyama, Yutaka Tabuchi, and Yasunobu Nakamura. Fast readout and reset of a superconducting qubit coupled to a resonator with an intrinsic purcell filter, 2022.

[77] Nicolas Didier, Jérôme Bourassa, and Alexandre Blais. Fast Quantum Nondemolition Readout by Parametric Modulation of Longitudinal Qubit-Oscillator Interaction. *Physical Review Letters*, 2015.

[78] Steven Touzard, A. Kou, N. Frattini, V. Sivak, S. Puri, A. Grimm, L. Frunzio, Shyam Shankar, and M. Devoret. Gated conditional displacement readout of superconducting qubits. pages 1–17, 09 2018.

[79] Baptiste Royer, Arne L. Grimsmo, Nicolas Didier, and Alexandre Blais. Fast and high-fidelity entangling gate through parametrically modulated longitudinal coupling. *Quantum*, 1, 2017.

[80] F. Lecocq, J. Claudon, O. Buisson, and P. Milman. Nonlinear coupling between the two oscillation modes of a dc squid. *Phys. Rev. Lett.*, 107:197002, Nov 2011.

[81] I. Diniz, E. Dumur, O. Buisson, and A. Auffèves. Ultrafast quantum nondemolition measurements based on a diamond-shaped artificial atom. *Phys. Rev. A*, 87:033837, Mar 2013.

[82] É. Dumur, B. Küng, A. K. Feofanov, T. Weissl, N. Roch, C. Naud, W. Guichard, and O. Buisson. V-shaped superconducting artificial atom based on two inductively coupled transmons. *Phys. Rev. B*, 92:020515, Jul 2015.

[83] Etienne Dumur, Bruno Kung, Alexey Feofanov, Thomas Weissl, Yuriy Krupko, Nicolas Roch, Cecile Naud, Wiebke Guichard, and Olivier Buisson. Unexpectedly allowed transition in two inductively coupled transmons. *IEEE Transactions on Applied Superconductivity*, page 1–1, 2016.

[84] Remy Dassonneville. Qubit readouts using a transmon molecule in a 3D circuit quantum electrodynamics architecture. *Thesis*, 2019.

[85] R. Dassonneville, T. Ramos, V. Milchakov, L. Planat, Dumur, F. Foroughi, J. Puertas, S. Leger, K. Bharadwaj, J. Delaforce, C. Naud, W. Hasch-Guichard, J. J. García-Ripoll, N. Roch, and O. Buisson. Fast High-Fidelity Quantum Nondemolition Qubit Readout via a Nonperturbative Cross-Kerr Coupling. *Physical Review X*, 10(1):1–17, 2020.

[86] Xin Wang, Adam Miranowicz, and Franco Nori. Ideal quantum nondemolition readout of a flux qubit without purcell limitations. *Phys. Rev. Applied*, 12:064037, Dec 2019.

[87] J. Q. You and Franco Nori. Pokemon: Protected logic qubit derived from the 0-π qubit, 2021.

[88] Yufeng Ye, Kaidong Peng, Mahdi Naghiloo, Gregory Cunningham, and Kevin P. O'Brien. Engineering Purely Nonlinear Coupling with the Quarton. 2020.

[89] Etienne Dumur. A V-shape superconducting artificial atom for circuit quantum electrodynamics. *Thesis*, page 233, 2015.

[90] F. Lecocq, I. M. Pop, I. Matei, E. Dumur, A. K. Feofanov, C. Naud, W. Guichard, and O. Buisson. Coherent frequency conversion in a superconducting artificial atom with two internal degrees of freedom. *Physical Review Letters*, 108(10):1–5, 2012.

[91] ANSYS. Ansys HFSS.

[92] Vladimir Milchakov. Github: Transmon molecule optimization of electric parameters, June 2019.

[93] John M. Martinis, K. B. Cooper, R. McDermott, Matthias Steffen, Markus Ansmann, K. D. Osborn, K. Cicak, Seongshik Oh, D. P. Pappas, R. W. Simmonds, and Clare C. Yu. Decoherence in josephson qubits from dielectric loss. *Physical Review Letters*, 95(21), nov 2005.

[94] Hanhee Paik, D. I. Schuster, Lev S. Bishop, G. Kirchmair, G. Catelani, A. P. Sears, B. R. Johnson, M. J. Reagor, L. Frunzio, L. Glazman, S. M. Girvin, M. H. Devoret, and R. J. Schoelkopf. Observation of high coherence in Josephson junction qubits measured in a three-dimensional circuit QED architecture. may 2011.

[95] C. Wang, C. Axline, Y. Y. Gao, T. Brecht, Y. Chu, L. Frunzio, M. H. Devoret, and R. J. Schoelkopf. Surface participation and dielectric loss in superconducting qubits. *Applied Physics Letters*, 107(16):162601, Oct 2015.

[96] Jay M. Gambetta, Conal E. Murray, Y.-K.-K. Fung, Douglas T. McClure, Oliver Dial, William Shanks, Jeffrey W. Sleight, and Matthias Steffen. Investigating surface loss effects in superconducting transmon qubits. *IEEE Transactions on Applied Superconductivity*, 27(1):1–5, Jan 2017.

[97] J. Wenner, R. Barends, R. C. Bialczak, Yu Chen, J. Kelly, Erik Lucero, Matteo Mariantoni, A. Megrant, P. J. J. O'Malley, D. Sank, A. Vainsencher, H. Wang, T. C. White, Y. Yin, J. Zhao, A. N. Cleland, and John M. Martinis. Surface loss simulations of superconducting coplanar waveguide resonators. *Applied Physics Letters*, 99(11):113513, Sep 2011.

[98] Xuegang Li, Yingshan Zhang, Chuhong Yang, Zhiyuan Li, Junhua Wang, Tang Su, Mo Chen, Yongchao Li, Chengyao Li, Zhenyu Mi, Xuehui Liang, Chenlu Wang, Zhen Yang, Yulong Feng, Kehuan Linghu, Huikai Xu, Jiaxiu Han, Weiyang Liu, Peng Zhao, Teng Ma, Ruixia Wang, Jingning Zhang, Yu Song, Pei Liu, Ziting Wang, Zhaohua Yang, Guangming Xue, Yirong Jin, and Haifeng Yu. Vacuum-gap transmon qubits realized using flip-chip technology. *Applied Physics Letters*, 119(18):1–9, 2021.

[99] Jochen Braumüller, Martin Sandberg, Michael R. Vissers, Andre Schneider, Steffen Schlör, Lukas Grünhaupt, Hannes Rotzinger, Michael Marthaler, Alexander Lukashenko, Amadeus Dieter, Alexey V. Ustinov, Martin Weides, and David P. Pappas. Concentric transmon qubit featuring fast tunability and an anisotropic magnetic dipole moment. *Applied Physics Letters*, 108(3), 2016.

[100] J. Rahamim, T. Behrle, M. J. Peterer, A. Patterson, P. A. Spring, T. Tsunoda, R. Manenti, G. Tancredi, and P. J. Leek. Double-sided coaxial circuit QED with out-of-plane wiring. *Applied Physics Letters*, 110(22), 2017.

[101] Vladimir Milchakov. Github: Database of calculated values of cs and ct from eigenmodes obtained in hfss with variation of geometric sizes, June 2019.

[102] Johannes Heinsoo, Sinan Inel, David Janzso, Máté Jenei, Janne Kotilahti, Alessandro Landra, Caspar Ockeloen-Korppi, Jukka Räbinä, and Niko Savola. Kqcircuits, June 2021.

[103] Vladimir Milchakov. Github: Automatic generating the .gds files with transmon molecule designs, March 2021.

[104] A.Abrikosov. Magnetic properties of superconducting alloy films. *J. Phys. Chem. Solids.*, 2(3):199–208, 1957.

[105] Frederick S. Wells, Alexey V. Pan, X. Renshaw Wang, Sergey A. Fedoseev, and Hans Hilgenkamp. Analysis of low-field isotropic vortex glass containing vortex groups in YBa2Cu3O7-x thin films visualized by scanning SQUID microscopy. *Scientific Reports*, 5(i):1–5, 2015.

[106] Oliver Dial, Douglas T. McClure, Stefano Poletto, G. A. Keefe, Mary Beth Rothwell, Jay M. Gambetta, David W. Abraham, Jerry M. Chow, and Matthias Steffen. Bulk and surface loss in superconducting transmon qubits. *Superconductor Science and Technology*, 29(4):1–4, 2016.

[107] William D. Oliver and Paul B. Welander. Materials in superconducting quantum bits. *MRS Bulletin*, 38(10):816–825, 2013.

[108] G. Calusine, A. Melville, W. Woods, R. Das, C. Stull, V. Bolkhovsky, D. Braje, D. Hover, D. K. Kim, X. Miloshi, D. Rosenberg, A. Sevi, J. L. Yoder, E. Dauler, and W. D. Oliver. Analysis and mitigation of interface losses in trenched superconducting coplanar waveguide resonators. *Applied Physics Letters*, 112(6), 2018.

[109] Alexander P.M. Place, Lila V.H. Rodgers, Pranav Mundada, Basil M. Smitham, Mattias Fitzpatrick, Zhaoqi Leng, Anjali Premkumar, Jacob Bryon, Andrei Vrajitoarea, Sara Sussman, Guangming Cheng, Trisha Madhavan, Harshvardhan K. Babla, Xuan Hoang Le, Youqi Gang, Berthold Jäck, András Gyenis, Nan Yao, Robert J. Cava, Nathalie P. de Leon, and Andrew A. Houck. New material platform for superconducting transmon qubits with coherence times exceeding 0.3 milliseconds. *Nature Communications*, 12(1), 2021.

[110] Sami Franssila. Introduction to Microfabrication. *Introduction to Microfabrication*, 2010.

[111] Daniel Bratton, Da Yang, Junyan Dai, and Christopher K. Ober. Recent progress in high resolution lithography. *Polymers for Advanced Technologies*, 17(2):94–103, 2006.

[112] Rajesh Menon, Amil Patel, Dario Gil, and Henry I. Smith. Maskless lithography. *Materials Today*, 8(2):26–33, 2005.

[113] Ampere A. Tseng, Kuan Chen, Chii D. Chen, and Kung J. Ma. Electron beam lithography in nanoscale fabrication: Recent development. *IEEE Transactions on Electronics Packaging Manufacturing*, 26(2):141–149, 2003.

[114] Klaus D. Sattler. *Handbook of Nanophysics Nanoelectronics and Nanophotonics*. CRC Press, 217.

[115] Bin Yu, Leland Chang, Shibly Ahmed, Haihong Wang, Scott Bell, Chih Yuh Yang, Cyrus Tabery, Chau Ho, Qi Xiang, Tsu Jae King, Jeffrey Bokor, Chenming Hu, Ming Ren Lin, and David Kyser. FinFET scaling to 10 nm gate length. *Technical Digest - International Electron Devices Meeting*, pages 251–254, 2002.

[116] G. J. Dolan. Offset masks for lift-off photoprocessing. *Applied Physics Letters*, 31(5):337–339, 1977.

[117] Florent Lecocq, Cécile Naud, Ioan M. Pop, Zhi-Hui Peng, Iulian Matei, Thierry Crozes, Thierry Fournier, Wiebke Guichard, and Olivier Buisson. Novel E-beam lithography technique for in-situ junction fabrication: the controlled undercut. 1:1–5, 2011.

[118] Florent Lecocq, Ioan M. Pop, Zhihui Peng, Iulian Matei, Thierry Crozes, Thierry Fournier, Cécile Naud, Wiebke Guichard, and Olivier Buisson. Junction fabrication by shadow evaporation without a suspended bridge. *Nanotechnology*, 22(31), 2011.

[119] Liming Ren and Baoqin Chen. Proximity effect in electron beam lithography. *International Conference on Solid-State and Integrated Circuits Technology Proceedings, ICSICT*, 1:579–582, 2004.

[120] D. F. Kyser and N. S. Viswanathan. Monte Carlo Simulation of Spatially Distributed Beams in Electron-Beam Lithography. *J Vac Sci Technol*, 12(6):1305–1308, 1975.

[121] Harry Levinson. *Principles of lithography: Third edition*. 01 2011.

[122] Morten Kjaergaard, Mollie E Schwartz, Jochen Braumüller, Philip Krantz, Joel I Wang, Simon Gustavsson, and William D Oliver. Superconducting Qubits: Current State of Play. pages 369–395, 2019.

[123] R. Dolata, H. Scherer, A. B. Zorin, and J. Niemeyer. Single-charge devices with ultrasmall Nb/AlO x/Nb trilayer Josephson junctions. *Journal of Applied Physics*, 97(5), 2005.

[124] Alexander Stehli, Jan David Brehm, Tim Wolz, Paul Baity, Sergey Danilin, Valentino Seferai, Hannes Rotzinger, Alexey V. Ustinov, and Martin Weides. Coherent superconducting qubits from a subtractive junction fabrication process. *Applied Physics Letters*, 117(12), 2020.

[125] J. Niemeyer and V. Kose. Observation of large dc supercurrents at nonzero voltages in Josephson tunnel junctions. *Applied Physics Letters*, 29(6):380–382, 1976.

[126] J. M. Kreikebaum, K. P. O'Brien, A. Morvan, and I. Siddiqi. Improving wafer-scale Josephson junction resistance variation in superconducting quantum coherent circuits. *Superconductor Science and Technology*, 33(6), 2020.

[127] Ke Zhang, Meng Meng Li, Qiang Liu, Hai Feng Yu, and Yang Yu. Bridge-free fabrication process for Al/AlOx/Al Josephson junctions. *Chinese Physics B*, 26(7), 2017.

[128] X. Wu, J. L. Long, H. S. Ku, R. E. Lake, M. Bal, and D. P. Pappas. Overlap junctions for high coherence superconducting qubits. *Applied Physics Letters*, 111(3):2015–2018, 2017.

[129] A. Potts, G. J. Parker, J. J. Baumberg, and P. A.J. De Groot. CMOS compatible fabrication methods for submicron Josephson junction qubits, 2001.

[130] Jan Goetz. The Interplay of Superconducting Quantum Circuits and Propagating Microwave States. *Thesis*, 2017.

[131] Gary H. Bernstein, Davide A. Hill, and Wen Ping Liu. New high-contrast developers for poly(methyl methacrylate) resist. *Journal of Applied Physics*, 71(8):4066–4075, 1992.

[132] Daniel Huber Slichter. Quantum Jumps and Measurement Backaction in a Superconducting Qubit. *Angewandte Chemie International Edition, 6(11), 951–952.*, 2011.

[133] David Isaac Schuster. Circuit Quantum Electrodynamics. Technical report, 2007.

[134] S. Yanai and G. A. Steele. Observation of enhanced coherence in Josephson SQUID cavities using a hybrid fabrication approach. pages 1–31, 2019.

[135] I. M. Pop, T. Fournier, T. Crozes, F. Lecocq, I. Matei, B. Pannetier, O. Buisson, and W. Guichard. Fabrication of stable and reproducible submicron tunnel junctions. *Journal of Vacuum Science & Technology B, Nanotechnology and Microelectronics: Materials, Processing, Measurement, and Phenomena*, 30(1):010607, 2012.

[136] Luca Planat. Resonant and traveling-wave parametric amplification near the quantum limit. *Thesis*, 2020.

[137] Wenchuang (Walter) Hu, Koshala Sarveswaran, Marya Lieberman, and Gary H. Bernstein. Sub-10 nm electron beam lithography using cold development of poly(methylmethacrylate). *Journal of Vacuum Science & Technology B: Microelectronics and Nanometer Structures*, 22(4):1711, 2004.

[138] Sub-10 nm electron beam lithography using cold development of poly(methylmethacrylate). *Journal of Vacuum Science & Technology B: Microelectronics and Nanometer Structures*, 22(4):1711, 2004.

[139] L. E. Ocola and A. Stein. Effect of cold development on improvement in electron-beam nanopatterning resolution and line roughness. *Journal of Vacuum Science & Technology B: Microelectronics and Nanometer Structures*, 24(6):3061, 2006.

[140] Bryan Cord, Jodie Lutkenhaus, and Karl K. Berggren. Optimal temperature for development of poly(methylmethacrylate). *Journal of Vacuum Science & Technology B: Microelectronics and Nanometer Structures*, 25(6):2013, 2007.

[141] Vinay Ambegaokar and Alexis Baratoff. Tunneling between superconductors. *Physical Review Letters*, 11(2):104, 1963.

[142] K. Gloos, R. S. Poikolainen, and J. P. Pekola. Wide-range thermometer based on the temperature-dependent conductance of planar tunnel junctions. *Applied Physics Letters*, 77(18):2915–2917, 2000.

[143] Julien Claudon. *Oscillations cohérentes dans un circuit quantique supraconducteur : le SQUID dc.* Theses, Université Joseph-Fourier - Grenoble I, September 2005.

[144] Javier Puertas Martínez. Probing light-matter interaction in the many-body regime of superconducting quantum circuits. *Thesis*, 2018.

[145] Sebastien Leger. Quantum Electrodynamics of a Josephson junction coupled to a strongly dissipative environment. *Thesis*, 2021.

[146] S. Krinner, S. Storz, P. Kurpiers, P. Magnard, J. Heinsoo, R. Keller, J. Lütolf, C. Eichler, and A. Wallraff. Engineering cryogenic setups for 100-qubit scale superconducting circuit systems. *EPJ Quantum Technology*, 6(1), 2019.

[147] H. London, G. R. Clarke, and Eric Mendoza. Osmotic pressure of He3 in liquid He4, with proposals for a refrigerator to work below 1°K. *Physical Review*, 128(5):1992–2005, 1962.

[148] Principles of dilution refrigeration - a brief technology guide.

[149] F. Pobell. *Matter and Methods at Low Temperatures.* Springer Berlin Heidelberg, 2007.

[150] Alecsandro Roberto Lemos Francisco. *The Art of Crogenics*, volume 53. 2013.

[151] W. Meissner and R. Ochsenfeld. Ein neuer Effekt bei Eintritt der Supraleitfähigkeit. *Die Naturwissenschaften*, 21(44):787–788, 1933.

[152] C. D. Wilen, S. Abdullah, N. A. Kurinsky, C. Stanford, L. Cardani, G. D'Imperio, C. Tomei, L. Faoro, L. B. Ioffe, C. H. Liu, A. Opremcak, B. G. Christensen, J. L. DuBois, and R. McDermott. Correlated charge noise and relaxation errors in superconducting qubits. *Nature*, 594(7863):369–373, 2021.

[153] L. Cardani, F. Valenti, N. Casali, G. Catelani, T. Charpentier, M. Clemenza, I. Colantoni, A. Cruciani, G. D'Imperio, L. Gironi, L. Grünhaupt, D. Gusenkova, F. Henriques, M. Lagoin, M. Martinez, G. Pettinari, C. Rusconi, O. Sander, C. Tomei, A. V. Ustinov, M. Weber, W. Wernsdorfer, M. Vignati, S. Pirro, and I. M. Pop. Reducing the impact of radioactivity on quantum circuits in a deep-underground facility. *Nature Communications*, 12(1):13–18, 2021.

[154] R. Barends, J. Wenner, M. Lenander, Y. Chen, R. C. Bialczak, J. Kelly, E. Lucero, P. O'Malley, M. Mariantoni, D. Sank, H. Wang, T. C. White, Y. Yin, J. Zhao, A. N. Cleland, John M. Martinis, and J. J.A. Baselmans. Minimizing quasiparticle generation from stray infrared light in superconducting quantum circuits. *Applied Physics Letters*, 99(11):1–4, 2011.

[155] J. J.A. Baselmans and S. J.C. Yates. Long quasiparticle lifetime in aluminum Microwave Kinetic Inductance Detectors using coaxial stray light filters. *AIP Conference Proceedings*, 1185:160–163, 2009.

[156] Carlton M. Caves. Quantum limits on noise in linear amplifiers. *Physical Review D*, 26(8):1817–1839, 1982.

[157] Luca Planat, Rémy Dassonneville, Javier Puertas Martínez, Farshad Foroughi, Olivier Buisson, Wiebke Hasch-Guichard, Cécile Naud, R. Vijay, Kater Murch, and Nicolas Roch. Understanding the Saturation Power of Josephson Parametric Amplifiers Made from SQUID Arrays. *Physical Review Applied*, 11(3):1–14, 2019.

[158] Arpit Ranadive, Martina Esposito, Luca Planat, Edgar Bonet, Cécile Naud, Olivier Buisson, Wiebke Guichard, and Nicolas Roch. A reversed Kerr traveling wave parametric amplifier. 2021.

[159] Vladimir Milchakov. Github: Analysis of single shot readout data, June 2019.

[160] National centers for environmental information. https://www.ngdc.noaa.gov/geomag/faqgeom.shtml. [Online].

[161] Leonid Antsfeld and Boris Chidlovskii. Magnetic Field Sensing for Pedestrian and Robot Indoor Positioning. 2021.

[162] D. I. Schuster, A. Wallraff, A. Blais, L. Frunzio, R. S. Huang, J. Majer, S. M. Girvin, and R. J. Schoelkopf. Ac Stark shift and dephasing of a superconducting qubit strongly coupled to a cavity field. *Physical Review Letters*, 94(12):1–4, 2005.

[163] Cyril Mori. QND readout of superconducting qubits. *Master Thesis*, 2021.

[164] Gonzalo Troncozo Fernandez-Bada. Superconducting V-shape circuit in a 3D cavity. *Master Thesis*, 2018.

[165] Norman F. Ramsey. A molecular beam resonance method with separated oscillating fields. *Physical Review*, 78(6):695–699, 1950.

[166] G. Ithier, E. Collin, P. Joyez, P. J. Meeson, D. Vion, D. Esteve, F. Chiarello, A. Shnirman, Y. Makhlin, J. Schriefl, and et al. Decoherence in a superconducting quantum bit circuit. *Physical Review B*, 72(13), Oct 2005.

[167] Quentin Ficheux. *Quantum Trajectories with Incompatible Decoherence Channels*. Theses, École normale supérieure - ENS PARIS, December 2018.

[168] David P. DiVincenzo. Fault-tolerant architectures for superconducting qubits. *Physica Scripta T*, T137, 2009.

[169] R. Barends, J. Kelly, A. Megrant, A. Veitia, D. Sank, E. Jeffrey, T. C. White, J. Mutus, A. G. Fowler, B. Campbell, Y. Chen, Z. Chen, B. Chiaro, A. Dunsworth, C. Neill, P. O'Malley, P. Roushan, A. Vainsencher, J. Wenner, A. N. Korotkov, A. N. Cleland, and John M. Martinis. Superconducting quantum circuits at the surface code threshold for fault tolerance, 2014.

[170] Teleporting an unknown quantum state via dual classical and Einstein-Podolsky-Rosen channels. *Physical Review Letters*, 70(13):1895–1899, 1993.

[171] J. E. Johnson, C. MacKlin, D. H. Slichter, R. Vijay, E. B. Weingarten, John Clarke, and I. Siddiqi. Heralded state preparation in a superconducting qubit, 2012.

[172] Markus Ansmann, H. Wang, Radoslaw C. Bialczak, Max Hofheinz, Erik Lucero, M. Neeley, A. D. O'Connell, D. Sank, M. Weides, J. Wenner, A. N. Cleland, and John M. Martinis. Violation of Bell's inequality in Josephson phase qubits. *Nature*, 461(7263):504–506, 2009.

[173] B. Hensen, H. Bernien, A. E. Dreaú, A. Reiserer, N. Kalb, M. S. Blok, J. Ruitenberg, R. F.L. Vermeulen, R. N. Schouten, C. Abellán, W. Amaya, V. Pruneri, M. W. Mitchell, M. Markham, D. J. Twitchen, D. Elkouss, S. Wehner, T. H. Taminiau, and R. Hanson. Loophole-free Bell inequality violation using electron spins separated by 1.3 kilometers. *Nature*, 526(7575):682–686, 2015.

[174] Wayne M. Itano, D. J. Heinzen, J. J. Bollinger, and D. J. Wineland. Quantum Zero effect. *Physical Review A*, 41(5):2295–2300, 1990.

[175] R. POOL. Quantum Pot Watching: A test of how observation affects a quantum system verifies theoretical predictions and proves the truth of an old maxim. *Science*, 246(4932):888–888, 1989.

[176] N. Boulant, G. Ithier, P. Meeson, F. Nguyen, D. Vion, D. Esteve, I. Siddiqi, R. Vijay, C. Rigetti, F. Pierre, and M. Devoret. Quantum nondemolition readout using a Josephson bifurcation amplifier. *Physical Review B - Condensed Matter and Materials Physics*, 76(1), 2007.

[177] S. Touzard, A. Kou, N. E. Frattini, V. V. Sivak, S. Puri, A. Grimm, L. Frunzio, S. Shankar, and M. H. Devoret. Gated Conditional Displacement Readout of Superconducting Qubits. *Physical Review Letters*, 122(8):80502, 2019.

[178] Timothee Guerra. Quantum non-demolition measurements in a superconducting qubit. *Master Thesis*, 2020.

[179] Bohr Niels. On the construction of atoms and molecules. *The London, Edinburgh and Dublin Philosophical Magazine and Journal of Science*, 26(151):1–25, 1913.

[180] N Bohr. The trilogy: On the constitution of atoms and molecules. *Niels Bohr Collected Works*, 2(C):159–233, 1981.

[181] Daria Gusenkova, Martin Spiecker, Richard Gebauer, Madita Willsch, Dennis Willsch, Francesco Valenti, Nick Karcher, Lukas Grünhaupt, Ivan Takmakov, Patrick Winkel, Dennis Rieger, Alexey V. Ustinov, Nicolas Roch, Wolfgang

Wernsdorfer, Kristel Michielsen, Oliver Sander, and Ioan M. Pop. Quantum Nondemolition Dispersive Readout of a Superconducting Artificial Atom Using Large Photon Numbers. *Physical Review Applied*, 15(6):1–15, 2021.

[182] David Freedman and Persi Diaconis. On the histogram as a density estimator:L2 theory. *Zeitschrift für Wahrscheinlichkeitstheorie und Verwandte Gebiete*, 57(4):453–476, 1981.

[183] Hideaki Shimazaki and Shigeru Shinomoto. A method for selecting the bin size of a time histogram. *Neural Computation*, 19(6):1503–1527, 2007.

[184] American Statistical Association Stable. The Choice of a Class Interval Author(s): Herbert A . Sturges Reviewed work (s). 21(153):65–66, 2012.

[185] U. Vool, I.M. Pop, K. Sliwa, B. Abdo, C. Wang, T. Brecht, Y.Y. Gao, S. Shankar, M. Hatridge, G. Catelani, M. Mirrahimi, L. Frunzio, R.J. Schoelkopf, L.I. Glazman, and M.H. Devoret. Non-poissonian quantum jumps of a fluxonium qubit due to quasiparticle excitations. *Physical Review Letters*, 113(24), Dec 2014.

[186] Joni Ikonen, Jan Goetz, Jesper Ilves, Aarne Keränen, Andras M. Gunyho, Matti Partanen, Kuan Y. Tan, Dibyendu Hazra, Leif Grönberg, Visa Vesterinen, Slawomir Simbierowicz, Juha Hassel, and Mikko Möttönen. Qubit measurement by multichannel driving. *Physical Review Letters*, 122(8), Feb 2019.

[187] Jared B. Hertzberg, Eric J. Zhang, Sami Rosenblatt, Easwar Magesan, John A. Smolin, Jeng-Bang Yau, Vivekananda P. Adiga, Martin Sandberg, Markus Brink, Jerry M. Chow, and Jason S. Orcutt. Laser-annealing josephson junctions for yielding scaled-up superconducting quantum processors. *npj Quantum Information*, 7(1), Aug 2021.

[188] Alexander P. M. Place, Lila V. H. Rodgers, Pranav Mundada, Basil M. Smitham, Mattias Fitzpatrick, Zhaoqi Leng, Anjali Premkumar, Jacob Bryon, Andrei Vrajitoarea, Sara Sussman, Guangming Cheng, Trisha Madhavan, Harshvardhan K. Babla, Xuan Hoang Le, Youqi Gang, Berthold Jäck, András Gyenis, Nan Yao, Robert J. Cava, Nathalie P. de Leon, and Andrew A. Houck. New material platform for superconducting transmon qubits with coherence times exceeding 0.3 milliseconds. *Nature Communications*, 12(1), Mar 2021.